Universitat Autònoma de Barcelona

Weak lensing in DES Y3: redshift distributions, shape catalogue, and mass mapping

Marco Gatti

ADVERTIMENT. L'accés als continguts d'aquesta tesi queda condicionat a l'acceptació de les condicions d'ús establertes per la següent llicència Creative Commons: http://cat.creativecommons.org/?page_id=184

ADVERTENCIA. El acceso a los contenidos de esta tesis queda condicionado a la aceptación de las condiciones de uso establecidas por la siguiente licencia Creative Commons: http://es.creativecommons.org/blog/licencias/

WARNING. The access to the contents of this doctoral thesis it is limited to the acceptance of the use conditions set by the following Creative Commons license: https://creativecommons.org/licenses/?lang=en

Weak lensing in DES Y3: redshift distributions, shape catalogue, and mass mapping

Author: Marco Gatti

Institut de Física d'Altes Energies (IFAE)

A thesis submitted for the degree of
Philosophae Doctor (PhD)

Department de Física
Universitat Autònoma de Barcelona

Thesis Advisor:

Dr. Ramon Miquel
Pascual

Thesis Co-Advisor:

Dr. Chihway Chang

Contents

Introduction and Motivation

In the last century, tremendous progresses have been made in the understanding of our Universe. The development of the theory of General Relativity by Einstein in 1915 gave us the tools to frame a mathematical description of our Universe; the observations that followed helped us identifying - and quantifying - the main ingredients of that mathematical framework. What is nowadays known as the standard cosmological model (or ΛCDM, presented in Chapter 1 of this thesis) is an incredibly simple yet effective model that depends on a handful of parameters and that is capable of explaining observational results spanning almost the whole lifetime of our Universe. These observational evidences include, for instance, the structure of the cosmic microwave background, the spatial distribution of galaxies on large scales, the accelerated expansion of the Universe. Despite its simplicity and effectiveness, however, the standard model is a reminder of our ignorance: in order to work it needs the addition of two components, the so called "dark matter" and "dark energy", which alone constitute ~ 95 per cent of the total energy-matter budget of our Universe. Their nature and origin are basically unknown, and investigating them with greater accuracy through better and more extensive observational campaigns is paramount.

Without any doubt galaxy surveys have been playing a key role fostering our understanding of the Universe. The spatial distribution of galaxies as a function of time can be revealing: galaxies are not simply randomly distributed, but they do cluster, and the amplitude and the characteristic scale of the clustering depends on the geometry, the growth of structure and the properties of the components of the Universe. In recent times, photometric galaxy surveys have become increasingly popular; not only do they allow to measure galaxy positions, but also to measure galaxy shapes. This is particularly relevant as it enables the measurement of (weak) gravitational lensing effects, which is the focus of Chapter 2 of this thesis. Gravitational lensing effects manifest themselves when the path followed by the light emitted

by background objects (e.g., galaxies) appears to be deflected due to some foreground mass, as predicted by the theory of General Relativity. The net effect is that the shape of the galaxies that we measure is slightly distorted. Gravitational lensing turned out to be a powerful probe of cosmology: it allows to indirectly trace the matter distribution of the Universe (which is mostly invisible to us, as it is mostly dark matter!), and it is sensitive to both the geometry of the Universe and to the history of structure growth.

The size of galaxy surveys have rapidly escalated with time, growing from thousands of galaxies of the first pioneering surveys to current and future surveys (DES, KIDS, HSC, LSST, Euclid, WFIRST), which map (or plan to map) a few hundreds million of galaxies. These ambitious programs have the potential to answer many open questions in Cosmology (or, depending on their results, to open new exciting scenarios, involving new physics beyond the standard cosmological model and the standard model of particle physics). In particular, this thesis focuses on the first three years of data from the Dark Energy Survey (DES Y3), which comprises 100 million galaxies observed in 5 different optical bands over 5000 square degrees of the southern hemisphere. DES and the data set used in this thesis are discussed in detail in Chapter 3, which together with Chapter 1 and 2 constitutes Part I of this thesis.

The scientifically positive outcome of DES and other photometric galaxy surveys goes hand in hand with a supreme understanding of the data, of the observational systematics affecting the measurements, and of the limits of the theoretical modelling of the observables. One of the main challenge of galaxy photometric surveys like DES is to correctly estimate the distance of the galaxies. Photometric surveys observe the galaxies in a limited number of broad optical bands, and the estimate of their *redshifts* is somewhat uncertain, which constitutes one of the main limiting factor of their copsmological analyses. Part II and its Chapter 4 are devoted to a new auxiliary technique recently developed that allows to infer (or calibrate) redshift distributions exploiting cross-correlation with small reference samples with secure redshifts. The so called "clustering-redshift" method is discussed in depth, as well as its role in the overall DES Y3 redshift calibration strategy.

Part III and Chapter 5 are devoted to another key aspect of photometric surveys, that enables the study of weak gravitational lensing: the shape catalogue. The official DES Y3 shape catalogue is presented, together with all the systematic tests performed to validate it such that it can be considered science-ready.

Last, part IV focuses on how to use weak gravitational lensing and the

DES Y3 shape catalogue to create weak lensing mass maps, i.e., maps of the mass distribution of the Universe. Chapter 6 discusses different map making techniques, whereas Chapter 7 presents a simulated cosmological analysis using the high order moments of the mass maps.

Part I

Preliminars

This first part contains all the theoretical background needed to understand the rest of the thesis. We start introducing the cosmological framework, followed by an introduction to weak gravitation lensing. We then introduce the Dark Energy Survey and give an overview of some of the main techniques and challenges to measure the large-scale structure of the Universe and weak gravitational lensing effects.

Chapter 1

Cosmological Background

1.1 The cosmological principle and the expanding Universe

According to the "cosmological principle", the Universe is homogeneous and isotropic, i.e. there is no preferred direction or preferred position. The cosmological principle is a statement about reference systems: homogeneity translates into the invariance of the laws under spatial translations, while isotropy translates as invariance under rotations of our reference system. Homogeneity and isotropy are backed up by observations at large scales ($\sim 100\ h^{-1}$ Mpc), but they start to break down at smaller scales, due to structure formation.

While the Universe might look the same regardless of the position of the observer, it does not look the same as time evolves. The "Big Bang Theory" and the realisation of the expansion of the Universe made that point clear: the geometry of the Universe is not "static", but evolves with time, and with it, distances.

If a homogeneous, isotropic, static Universe would be described by a Minkowski space-time with a natural choice of coordinate systems $\xi^\alpha = (-ct, x_1, x_2, x_3)$, this is no longer the case for an expanding Universe. It is preferred to introduce the transformation of coordinates[1] $\chi^i = \chi^i(\xi^j)$ such that $(x_1, x_2, x_3) = a(t)(\chi_1, \chi_2, \chi_3)$, or in vectorial form,

$$\vec{r} = a(t)\vec{\chi}. \tag{1.1}$$

[1]Greek indices run on all the components of the 4-vectors, while roman indices (e.g., i) run on the spatial part of the 4-vectors only.

The factor $a(t)$ is the "scale factor" and describes the homogenoeus and isotropic expansion of the Universe. It is customary to take $a(t_0) = 1$ with t_0 the present time. We shall refer to the spatial part of the new coordinate systems $\vec{\chi}$ as "comoving coordinates", while we shall refer to the spatial part of the Minkowski coordinates as "physical" or "proper" coordinates. The difference between the two systems of coordinates is that comoving coordinates do not see the expansion of the Universe, i.e. the comoving distance between two objects is constant with time. This is not true for the physical distance: two objects with a given physical distance today would have been closer in the past.

1.2 The FLWR metric

In general relativity, the metric tensor $g_{\alpha,\beta}$ determines the intrinsic properties of a metric space[2], i.e., it allows to compute the distance between vectors $\vec{A} \cdot \vec{B} \equiv g_{\alpha,\beta} A^\alpha B^\beta$ (where the sum over repeated greek indices is implicit).

To derive the metric of a given space-time, one should solve Einstein's field equations, which also contain information about the energy-density content of the Universe. Historically, this is not how the metric of the Universe (the Friedmann-Lemaitre-Robertson-Walker or FLWR metric) was derived. The FLRW metric followed from geometrical considerations on how to compute distances in a homogeneous, isotropic and expanding space-time. For a flat Universe, it readily follows from the coordinate transformation in Eq. 1.1, by considering $g_{\alpha\beta} = \partial\xi^\alpha/\partial x^\mu \xi^\beta/\partial x^\nu \eta_{\alpha\beta}$ with $\eta_{\alpha\beta} = diag(-1, 1, 1, 1)$ the metric tensor of the flat Minkowski space-time. For a curved space-time with curvature K, it reads:

$$g_{\mu\nu} = \begin{pmatrix} -1 & 0 & 0 & 0 \\ 0 & a^2 & 0 & 0 \\ 0 & 0 & a^2 f_K(\chi)^2 & 0 \\ 0 & 0 & 0 & a^2 f_K(\chi)^2 \end{pmatrix}, \tag{1.2}$$

In the above, we adopted spherical coordinates for the spatial part of the metric $\xi^\mu = (ct, \chi, \theta, \phi)$[3]. The term f_K depends on the curvature K of the

[2] A metric space is a set together with a metric on the set. The metric is a function that defines a concept of distance between any two members of the set (Wikipedia).

[3] One adopts the following coordinates transformation for the spatial coordinates: $x = a\chi \sin\theta \sin\phi$, $y = a\chi \sin\theta \cos\phi$, $z = a\chi \cos\theta$.

Universe:

$$f_K = \begin{cases} \frac{1}{\sqrt{K}} \sin\left(\sqrt{K}\chi\right) & K > 0 \\ \chi & K = 0 \\ \frac{1}{\sqrt{-K}} \sinh\left(\sqrt{-K}\chi\right) & K < 0 \end{cases} \tag{1.3}$$

In a closed Universe $K > 0$, whereas in a open Universe $K < 0$. We note that the FRLW metric implicitly relies on Weyl's principle, which states that in cosmology the world lines of fluids form a spacetime-filling family of non-intersecting geodesics converging towards the past[4].

The FLRW metric breaks down at small scales, due to the failure of the cosmological principle at scales $< 100\ h^{-1}$ Mpc due to structure formation. To describe the Universe when it departs from homogeneity, the metric is usually perturbed (see § 1.6).

1.3 The Standard Cosmological Model

1.3.1 Friedmann Equations

The cosmological principle, together with the Friedmann equations, are the pillars of the Standard Cosmological model. The two Friedmann equations directly stem from the Einstein field equations once the FLRW metric (and, therefore, the cosmological principle) is assumed. We start from the Einstein field equations:

$$G_{\mu\nu} = \frac{8\pi G}{c^4} T_{\mu\nu}. \tag{1.4}$$

The Einstein equations pinpoint the interplay between the geometry of space-time (left-hand side) and its energy content (right-hand side). In particular, in Eq. 1.4, $G_{\mu\nu}$ is the Einstein tensor, which depends on the geometry of the space time (i.e., the metric), and $T_{\mu\nu}$ is the stress-energy tensor, which depends on the energy content of the space-time and it describes the source of the gravitational field. The Einstein tensor is better expressed in terms of the Ricci curvature tensor $R_{\mu\nu}$ and the Ricci scalar R:

$$G_{\mu\nu} = R_{\mu\nu} - \frac{1}{2} g_{\mu\nu} R + \Lambda g_{\mu\nu}. \tag{1.5}$$

[4]In other terms, this implies that the world lines should be everywhere orthogonal to a family of spatial hyperslices. This imposes $g_{0i} = 0$. The cosmological principle, together with the spatial curvature of the Universe, take part in modelling the spatial part of the metric. For a historical introduction to Weyl's principle in Cosmology see, e.g., Rugh & Zinkernagel (2010).

The Ricci tensor is linear in the second derivatives of the metric $g_{\mu\nu}$ and non linear in the first derivatives[5]. The Ricci scalar R is defined as $R = R^{\alpha}_{\alpha}$. Finally, Λ is a constant term that in Cosmology has a specific role, and it is referred to as the "cosmological constant"[6].

In our case, the Einstein tensor $G_{\mu\nu}$ is fully determined by the choice of the FLRW metric. The Ricci tensor has as components:

$$R_{00} = -3\frac{c^{-2}\ddot{a}(t)}{a(t)}, \tag{1.6}$$

$$R_{0i} = 0, \tag{1.7}$$

$$R_{ij} = \frac{c^{-2}\ddot{a}(t)a(t) + 2c^{-2}\dot{a}(t)^2 + 2K}{a(t)^2} g_{ij}. \tag{1.8}$$

In the above equations, the symbol " $\dot{}$ " refers to the differentiation with respect to physical time t. We note that $R_{0i} = 0$ is a consequence of Weyl's principle, and $R_{ij} \propto g_{ij}$ stems from having assumed isotropy and homogeneity. As for the Ricci scalar, it reads:

$$R = 6\frac{c^{-2}\ddot{a}(t)a(t) + c^{-2}\dot{a}(t)^2 + K}{a(t)^2}. \tag{1.9}$$

The stress-energy tensor behaves similarly to the Ricci tensor in terms of components. Its formal definition for a homogeneous and isotropic fluid at equilibrium is:

$$T_{\alpha\beta} = [\rho(t)c^2 + p(t)]u^{\alpha}u^{\beta} + p(t)g_{\alpha\beta}, \tag{1.10}$$

with $p(t)$ being the pressure, $\rho(t)$ the density and $u^{\alpha} = \frac{dx^{\alpha}}{cd\tau}$ the 4-velocity[7]. Since in an inertial, comoving frame $u^{\alpha} = (1, 0, 0, 0)$, it follows that the components of the stress-energy tensor are:

$$T_{00} = \rho(t)c^2, \tag{1.11}$$

[5]Ricci tensor is formally defined as the contracted form of the Riemann tensor $R_{\alpha\mu\beta\nu}$, i.e. $R_{\mu\nu} = g^{\alpha\beta}R_{\alpha\mu\beta\nu}$. The Riemann tensor is also referred to as the curvature tensor, as it vanishes in a flat spacetime. Its dependence on the derivatives of the metric can be understood looking at its definition: $R_{\alpha\beta\mu\nu} = \Gamma^{\alpha}_{\beta\nu,\mu} - \gamma^{\alpha}_{\beta\mu,\nu} - \Gamma^{\alpha}_{\kappa\nu}\Gamma^{\kappa}_{\beta\mu} + \Gamma^{\alpha}_{\kappa\mu}\Gamma^{\kappa}_{\beta\nu}$, where we have introduced the Christoffel's symbols $\Gamma^{\alpha}_{\beta\nu} = \frac{1}{2}g^{\nu\sigma}\left[g_{\mu\nu,\lambda} + g_{\lambda\nu,\mu} - g_{\lambda\mu,\nu}\right]$. The notation "$_{,\lambda}$" indicates differentiation with respect to the variable x^{λ}.

[6]This nomenclature is used specifically in Cosmology. More generally, Einstein field equations always admit the additional term $\Lambda g_{\mu\nu}$ under the condition of Λ to be small, such that the 00 component of the equations in the weak field limit reduces to the Newtonian case.

[7]τ is the proper time defined as $d\tau^2 = g_{\mu\nu}dx^{\mu}dx^{\nu}$.

$$T_{0i} = 0, \tag{1.12}$$

$$T_{ij} = p(t) g_{ij}. \tag{1.13}$$

We can now derive the Friedmann equations, which relate the geometry of the Universe to its content in the framework of General Relativity. The first Friedmann equation corresponds to the 00 component of the Einstein field equation:

$$-3\frac{c^{-2}\ddot{a}(t)}{a(t)} + 3\frac{c^{-2}\ddot{a}(t)a(t) + c^{-2}\dot{a}(t)^2 + K}{a(t)^2} - \Lambda = \frac{8\pi G}{c^2}\rho(t), \tag{1.14}$$

$$\frac{\dot{a}(t)^2}{a(t)^2} = \frac{8\pi G}{3}\rho(t) + \frac{\Lambda c^2}{3} - \frac{Kc^2}{a(t)^2}. \tag{1.15}$$

We can now introduce the Hubble rate

$$H(t) \equiv \frac{\dot{a}(t)}{a(t)}, \tag{1.16}$$

which is defined as the rate of expansion of the Universe. With this definition, the first Friedman equation reads:

$$H(t)^2 = \frac{8\pi G}{3}\rho(t) + \frac{\Lambda c^2}{3} - \frac{Kc^2}{a(t)^2}. \tag{1.17}$$

This equation shows how the expansion rate of the Universe is determined by both the geometry of the Universe and its total energy density $\rho(t)$.

The second Friedman equation follows from the spatial components of the Einstein field equations:

$$\left(-2\frac{c^{-2}\ddot{a}(t)}{a(t)} - \frac{c^{-2}\dot{a}(t)^2 + K}{a(t)^2} + \Lambda\right) g_{\mu\nu} = \frac{8\pi G}{c^4} p(t) g_{\mu\nu}, \tag{1.18}$$

which, combined with Eq. 1.15, leads to

$$\frac{\ddot{a}(t)}{a(t)} = -\frac{4\pi G}{3}\left(\rho(t) + \frac{3p(t)}{c^2}\right) + \frac{\Lambda c^2}{3}. \tag{1.19}$$

In the Einstein field equations, the cosmological constant Λ has been introduced as part of the Einstein tensor, on the left-hand side of Eq. 1.4; in this respect, it can be interpreted as an intrinsic geometrical feature of the

space-time. However, we can also incorporate it in the energy content of the Universe by the following transformation:

$$\rho(t) \to \rho(t) + \frac{\Lambda c^2}{8\pi G} \tag{1.20}$$

$$p(t) \to p(t) - \frac{\Lambda c^2}{8\pi G} \tag{1.21}$$

This is equivalent to consider the cosmological constant as a "fluid" with density ρ_Λ and pressure p_Λ, such that $p_\Lambda = -\rho_\Lambda c^2$. We can rewrite the Friedmann equations as:

$$H(t)^2 = \frac{8\pi G}{3}\rho(t) - \frac{Kc^2}{a(t)^2}., \tag{1.22}$$

$$\frac{\ddot{a}(t)}{a(t)} = -\frac{4\pi G}{3}\left(\rho(t) + \frac{3p(t)}{c^2}\right). \tag{1.23}$$

Eq. 1.23 is also referred to as "acceleration equation", and it indicates that the acceleration of the expansion of the Universe is determined both by the energy density and the pressure of the fluids filling the Universe. In particular, the relation between density and pressure (determined by the equation of state) is crucial: depending on the signs of $\rho(t)$ and $p(t)$, the acceleration of the Universe can be either positive ore negative (i.e. it would be a deceleration[8]).

Finally, at any moment of the cosmic time, we can also define a "critical density", which is the density needed for the Universe to be flat ($K = 0$):

$$\rho_{\text{crit}} \equiv \frac{3H(t)^2}{8\pi G}. \tag{1.24}$$

We note that in the density term ρ we included all the forms of matter and energy present in the Universe, as we will specify better in the next subsection.

1.3.2 Energy Evolution

The stress-energy tensor describes the energy content of the Universe. In general relativity, it obeys the following conservation law:

$$T^\mu_{\nu;\mu} \equiv T^\mu_{\nu,\mu} + \Gamma^\mu_{\alpha\mu}T^\alpha_\mu - \Gamma^\mu_{\alpha\mu}T^\alpha_\mu = 0, \tag{1.25}$$

[8]One can define a "deceleration parameter" $q_0 \equiv -\ddot{a}(t_0)/(a(t_0)H_0^2)$. Current constraints from type Ia supernovae show that $q_0 \approx -0.6$, hence the Universe expansion is accelerating.

where $\Gamma^{\mu}_{\alpha\mu}$ are Christofell's symbols. The $\nu = 0$ component of the above system of equations is equivalent to continuity equation, while the spatial part is equivalent to the Euler equation. Let us focus on the $\nu = 0$ component. By substituting the non-vanishing Christoffel's symbols, it reads:

$$\frac{\partial \rho}{\partial t} + 3\frac{\dot{a}}{a}\left(\rho + \frac{P}{c^2}\right) = 0. \tag{1.26}$$

The continuity equation allows to derive the evolution of the energy density with time. In cosmology, we approximate all the components of the Universe by fluids obeying a simple equation of state:

$$p(t) = w\rho(t)c^2, \tag{1.27}$$

with w constant. Such equation of state is normally used to describe diluted fluids with no torsion. The continuity equations can be therefore rewritten as:

$$\frac{d\rho}{\rho} = -3(1+w)\frac{da}{a}. \tag{1.28}$$

Solving the continuity equation and the Friedmann equations, assuming the Universe is made up of only one fluid obeying a simple equation of state, leads to:

$$\rho(a) = \rho_0 a^{-3(1+w)}, \tag{1.29}$$

$$a(t) = a_0 t^{2/[3(1+w)]}. \tag{1.30}$$

Depending on the equation of state, the density and scale factor have a different evolution with cosmic time. The standard cosmological model considers as constituents of our Universe the following:

- non-relativistic massive particles, where non relativistic means their random thermal motion is much slower than the speed of light. Such fluid follows the law of a perfect gas:

$$P = \frac{\rho}{\mu}k_B T = \frac{\rho\langle v^2\rangle}{3} \rightarrow w = \frac{\langle v^2\rangle}{3c^2} \approx 0, \tag{1.31}$$

  where k_B is the Boltmann's constant and μ is and μ is the average atomic weight of the gas considered. This equation follows from the relation between the temperature T of the gas and its thermal velocity v: $3kT = \mu\langle v^2\rangle$. This implies that non-relativistic fluids are characterised by an equation of state with $w = 0$. Non-relativistic matter includes baryonic and dark matter, and it will be referred to generically as "matter".

- Relativistic, massless particles. Photons and other massless particles are characterised by
$$P = \frac{\rho c^2}{3} \rightarrow w = \frac{1}{3}. \tag{1.32}$$
We will refer to relativistic particles as "radiation".

- Dark energy. It is defined as a substance characterised by an equation of state:
$$P = w\rho c^2, \text{ with } w < 1/3. \tag{1.33}$$
Dark Energy causes the Universe to expand, as it would cause the sign of the right-hand side of the acceleration equation (Eq. 1.23) to be positive. The cosmological constant Λ, with $w = -1$, is a special case of dark energy.

Using (Eq. 1.29), we can compute the evolution of each component of the Universe:

$$p = w\rho c^2 \begin{cases} \text{Matter} & w_m = 0 & \rho_m = \rho_{m,0} a^{-3} \\ \text{Radiation} & w_r = \frac{1}{3} & \rho_r = \rho_{r,0} a^{-4} \\ \Lambda & w_\Lambda = -1 & \rho_\Lambda = \rho_{\Lambda,0} \\ \text{Dark Energy} & w_{\text{de}} = w(a) < -\frac{1}{3} & \rho_{\text{de}} = \rho_{\text{de},0} a^{-3[1+w(a)]} \end{cases} \tag{1.34}$$

The standard cosmological model includes, as components of the Universe, matter (mostly cold, non-relativistic dark matter), radiation and dark energy in the form of the cosmological constant, and it is referred to as the ΛCDM model, which is considered the benchmark model in cosmology. Due to the different evolution of these components, the Universe has seen different "epochs" where each of this component was the dominant constituent of the Universe (see Fig. 1.1).

If a more general form of dark energy than Λ is considered, the model is referred to as wCDM model. In the most general form, the dark energy equation of state can assume any parametric form $w(a)$, but it is usually described in terms of the lowest order Taylor expansion of $w(a)$:

$$w(a) = w_0 + (1 - a)w_a + O(1 - a)^2. \tag{1.35}$$

We can now solve the first Friedmann equation (Eq. 1.17) for a generic wCDM Universe:

$$H^2 = H_0 \left(\frac{\Omega_{m0}}{a^3} + \frac{\Omega_{r0}}{a^4} + \frac{\Omega_{\text{de}0}}{a^{3[1+w(a)]}} + \frac{\Omega_K}{a^2} \right), \tag{1.36}$$

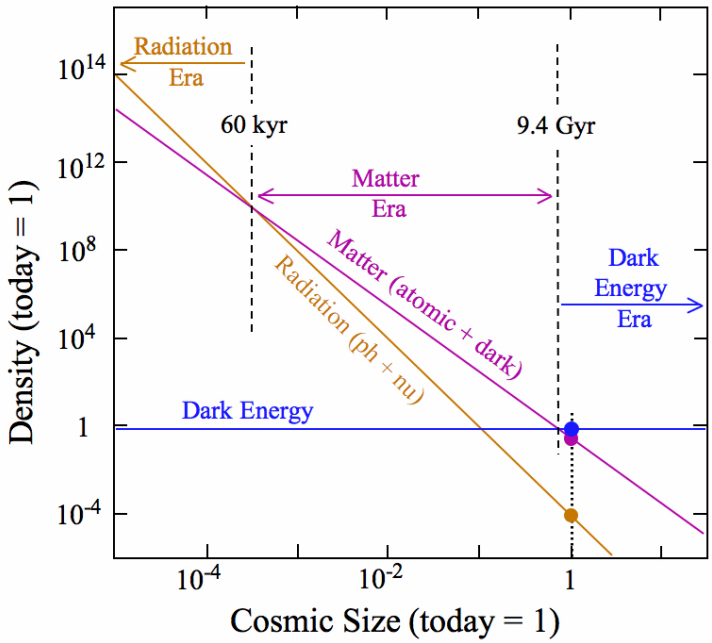

Figure 1.1: Density evolution for the different components of the Universe in a ΛCDM model. The dots represent the values of the density as measured today. Source: http://people.virginia.edu/dmw8f/

having defined the cosmological parameters Ω_i as:

$$\Omega_i \equiv \frac{\rho_{i,0}}{\rho_{\mathrm{crit},0}}, \tag{1.37}$$

and $\rho_K = \frac{Kc^2}{H_0^2} = \rho_0 - \rho_{\mathrm{crit},0}$, where $\rho_0 = \rho_{m,0} + \rho_{r,0} + \rho_{\mathrm{de},0}$ is the total density today (by definition, in a flat Universe, $\rho_0 = \rho_{\mathrm{crit},0}$). The parameters Ω_i form a minimum set of "cosmological parameters" that describes the Universe content today. The goal of modern cosmology is to measure these parameters to exquisite precision. Current experiments placed percent-level constraints on many of those (Table 1.1). In the next years the level of accuracy of the measurement of these parameters will further increase, helping shedding light on the nature of dark matter and dark energy, which is still one of the fundamental questions in cosmology today.

Table 1.1: Cosmological parameters from *Planck* (Planck Collaboration, 2018). The parameter h is the Hubble constant H_0 in units of 100 km/s/Mpc. The total matter $\Omega_{m,0}$ is further divided into a dark matter only component and a baryonic $\Omega_{b,0}$ component. The radiation density is computed from the temperature of the CMB $T = 2.7255 \pm 0.0006K$ and it is usually considered fixed in cosmological analysis (due to the high precision of its measurement). The curvature parameter value has been obtained combining with the data from BAO.

parameter	*Planck* TT,TE,EE+lowE+lensing
h	0.674 ± 0.005
$\Omega_{m,0}$	0.315 ± 0.007
$\Omega_{b,0}h^2$	0.0224 ± 0.0001
$\Omega_{\Lambda,0}$	0.685 ± 0.007
$\Omega_{r,0}$	$4.18343 \cdot 10^{-5}$
Ω_K	0.0007 ± 0.0019 (+BAO)

1.4 Distances

1.4.1 Redshift in Cosmology

The term "redshift" refers to a phenomenon where electromagnetic radiation emitted from an object is subject to an increase in wavelength (as opposed to "blueshift", where the wavelength diminishes). It is formally defined as the fractional difference between the observed and emitted wavelengths:

$$1 + z \equiv \frac{\lambda_{\mathrm{o}}}{\lambda_{\mathrm{e}}}. \tag{1.38}$$

Every cosmological object, except for the ones in our neighbourhood where peculiar velocity is dominant with respect to the cosmological expansion, are subject to redshift. This is a consequence of the Doppler effect: because of the expansion of the Universe, every objects is receding from us, thus causing the light emitted to become redder to the observer.

Given a distant galaxy, the comoving distance travelled by light is:

$$\chi = \int_{t_{\mathrm{e}}}^{t_{\mathrm{o}}} c\frac{dt}{a(t)}. \tag{1.39}$$

Suppose now that the light is emitted with wavelength λ_{e} and observed with wavelength λ_{o}. As the distance travelled by two wave crests is the same, it follows that:

$$\int_{t_{\mathrm{e}}}^{t_{\mathrm{o}}} c\frac{dt}{a(t)} = \int_{t_{\mathrm{e}}+\frac{\lambda_o}{c}}^{t_{\mathrm{o}}+\frac{\lambda_o}{c}} c\frac{dt}{a(t)}, \tag{1.40}$$

which can be re-written subtracting the quantity $\int_{t_e+\frac{\lambda_e}{c}}^{t_o} c\frac{dt}{a(t)}$:

$$\int_{t_e}^{t_e+\frac{\lambda_e}{c}} c\frac{dt}{a(t)} = \int_{t_o}^{t_o+\frac{\lambda_e}{c}} c\frac{dt}{a(t)}. \tag{1.41}$$

Each integral is computed over the time passed between two wave crests, at the position of the emitter and the observer. In such a small fraction of time, one can consider $a(t)$ constant, as the Universe did not have enough time to expand. It follows that:

$$\frac{\lambda_e}{a(t_e)} = \frac{\lambda_o}{a(t_o)}. \tag{1.42}$$

Following the definition of redshift (Eq. 1.38), and that the scale factor at present time is assumed to be $a(t_o) = 1$, it follows that:

$$1 + z = \frac{1}{a(t)}. \tag{1.43}$$

This last equation relates the redshift to the scale factor of the Universe; in other words, observing shifts in the spectral lines of distant object reveals the relative size of the Universe at the time the light was emitted.

1.4.2 Angular diameter and luminosity distance

In cosmology, there exist different ways to estimate the distance of an object. The choice of coordinate system defined in § 1.1 naturally suggests the use of the comoving distance (which remains constant as the Universe expands) as fundamental distance. The comoving distance can be related to redshift if the expansion of the Universe, described by $H(z)$, is known. It follows from Eq. 1.39 and Eq. 1.43 that the distance of an object located at a scale factor a is:

$$\chi(a) = \int_{t(z)}^{t_o} c\frac{dt}{a(t)} = \int_a^1 c\frac{da}{a^2 H(a)} = \int_0^z c\frac{dz}{H(z)}, \tag{1.44}$$

where we also used the definition of the Hubble constant $H(z)$ (Eq. 1.16). Unfortunately, we cannot directly measure the comoving distance of an object from observations. Usually, the comoving distance of an object is inferred from its redshift and once the cosmological model (and its parameters) are known.

If we knew *a priori* the size or the luminosity of an object, however, we could estimate more directly its distance from us. In particular, it is useful to introduce two other distances, the "angular diameter distance" and the "luminosity distance", which are more directly constrained by observations.

Let us assume we know the physical size[9] ℓ of an object and that, when we observe it, it subtends an angle $\Delta\theta$ in the sky. Its size can also be expressed as the infinitesimal line element between the extremities of the object:

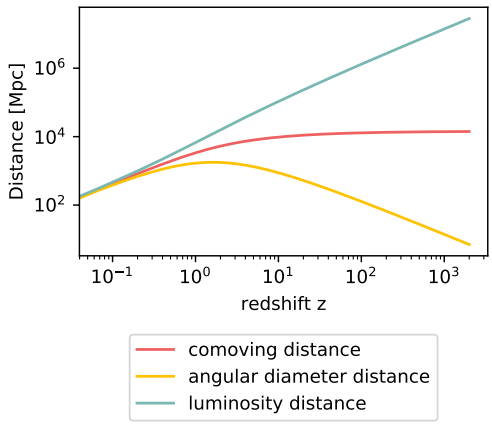

Figure 1.2: Angular diameter, luminosity and comoving distance as a function of redshift for a Planck cosmology.

$$\ell = \sqrt{ds^2} = a(t_e) f_K(\chi_e) \Delta\theta, \tag{1.45}$$

where we assumed $dt = d\phi = d\chi = 0$. We define the angular diameter distance as:

$$D_A \equiv \frac{\ell}{\Delta\theta} = a(t_e) f_K(\chi_e), \tag{1.46}$$

which becomes:

$$D_A = \frac{f_K(\chi_e)}{1 + z_e}. \tag{1.47}$$

We remind that for a flat Universe, $f_K(\chi_e) \to \chi_e$, such that $D_A = \frac{\chi_e}{1+z_e}$. The angular diameter distance is very similar to the comoving distance at low redshift, but it decreases by a factor $1 + z$ at high redshift. In a flat Universe, this implies that objects at high redshift appears larger than if they were located at intermediate redshift.

The other useful distance in cosmology is the "luminosity distance", which comes into play whenever the luminosity of an object is known *a priori*. In a Minkwoski Universe, the luminosity of an emitting source and the measured flux are related by:

$$F = \frac{L}{4\pi d_e^2}, \tag{1.48}$$

[9]We assume ℓ to be the size of the object in the plane perpendicular to the line of sight.

were d_e is the distance to the emitting source[10]. In an expanding Universe, however, both the distance and the luminosity vary as a function of cosmic time. The luminosity, in particular, varies because the energy of the photons will be smaller by a factor $1+z$ since their emission due to the Universe expansion; moreover, the number of photons crossing a shell in a fixed time will also be smaller by a factor $1+z$ for the same reason[11]. The relation between the luminosity at the time of emission and at the time of observation is:

$$L_e = L_o(1+z)^2. \tag{1.49}$$

Since the area of a sphere at comoving distance $\chi(a)$ is $S = 4\pi f_K(\chi)^2$, the relation between observed flux and luminosity at the emission is:

$$F = \frac{L_e}{(1+z)^2 4\pi f_K(\chi)^2} = \frac{L_e}{4\pi D_L^2}. \tag{1.50}$$

With the luminosity distance D_L defined as:

$$D_L \equiv (1+z) f_K(\chi). \tag{1.51}$$

For a flat Universe, the luminosity distance reads $D_L \equiv (1+z)\chi$. Luminosity, angular diameter and comoving distances as a function of redshift are shown in Fig. 1.2

1.5 The cosmic microwave background

One of the consequences of the expansion of the Universe is that the Universe must have been much smaller in the past. This means that the Universe was also hotter than what it is today. Indeed, photons filling in the Universe are in thermal equilibrium at a given temperature T and are described by a Bose-Einstein distribution, which implies the following relation between the photons energy density and their temperature:

$$\rho_r \propto T_\gamma^4. \tag{1.52}$$

[10]This relations stems from the fact that the luminosity is defined as released energy per unit time $L \equiv \frac{dE}{dt}$, while the flux is released energy per unit time per unit area $F \equiv \frac{dE}{dtdA}$. Since the area considered here is a spherical shell around the source, Eq. 1.48 follows.

[11]First, one can note that the energy dE of a packet of photons is proportional to its frequency ν and inversely proportional to its wavelength λ. It follows from the definition of redshift that $1+z_e = \frac{\lambda_o}{\lambda_e} = \frac{\nu_e}{\nu_o} = \frac{dE_e}{dE_o}$. Also, the relation between frequency and time interval implies $\nu_o dt_o = \nu_e dt_e$ and $1+z_e = \frac{dt_o}{dt_e}$.

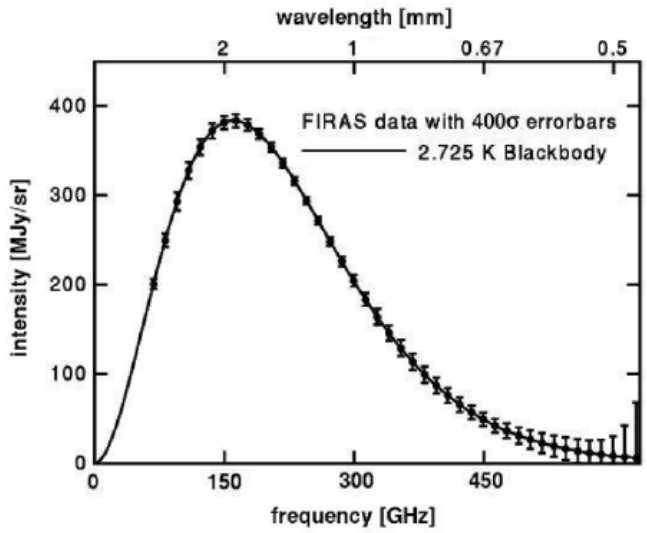

Figure 1.3: Intensity of CMB radiation as a function of wavelength and frequency for the COBE FIRAS experiment Mather (1994), and the best fit black body spectrum. Error bars are magnified by a factor of 400 in the plot.

As radiation evolves $\rho_r \propto a^{-4}$ (Eq. 1.34), it follows that the radiation filling the Universe must have been hotter in the past:

$$T_\gamma(a) = \frac{T_{\gamma,o}}{a^4}. \tag{1.53}$$

In the past, the temperature was high enough that photons were able to ionise light-weight atoms as hydrogen or helium, and the Universe was filled by a hot ionised plasma of particles and radiations. In such a hot plasma, ionised atoms were coupled with radiation through Thomson scattering, which implies that the mean free path per electron was extremely short, effectively making the Universe opaque. Moreover, any newly formed hydrogen atom was immediately ionised by ambient photons. In such state, photons were effectively at the thermodynamic equilibrium, which means their radiation could be completely characterised by a black body spectrum. As the Universe expanded, the temperature of the radiation dropped enough that ambient photons were no longer able to ionise hydrogen. As a result, the mean free path of photons increased, effectively making the Universe transparent. The leftover of this ancient radiation coming from the early Universe was firstly been observed by Penzias & Wilson (1965) in a single wavelength in the microwave range, and it has been referred

since then as the "Cosmic Microwave Background" (CMB). The confirmation that the CMB had a black body spectrum arrived with the launch of COsmic Background Explorer (COBE), which extended the measurement to a wide range of wavelengths (Fig. 1.3, Mather 1994), making it one of the observational pillars of the Big Bang theory.

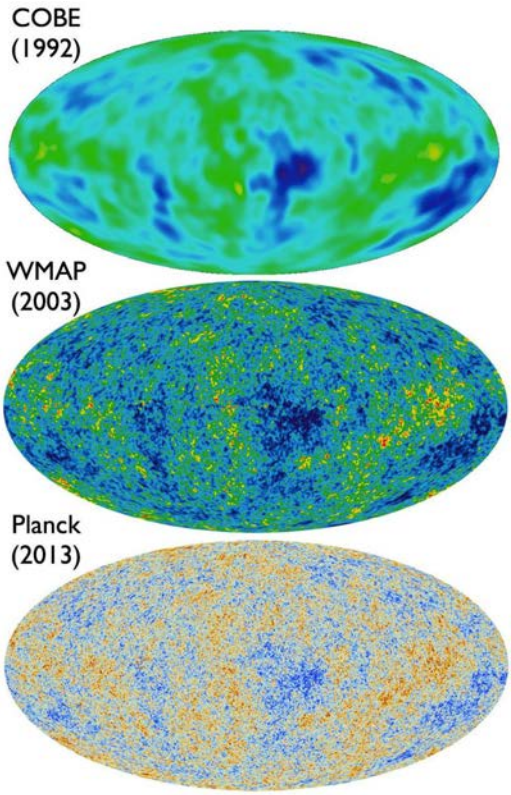

Figure 1.4: Anisotropies in the CMB temperature map (the color scales highlight fluctuations of the order 10^5), as observed with increasing resolution by COBE,WMAP and Planck.

After COBE, the CMB has been observed with greater accuracy by WMAP and more recently by Planck. It is now consolidated that the CMB radiation is a relic of the last scattering surface, which took place when the Universe was roughly 400,000 years old ($z \approx 1100$). The measured blackbody spectrum agrees with the one of radiation in thermal equilibrium at $T_o = 2.72548 \pm 0.00057K$ (Fixsen, 2009), which corresponds to a temperature of $\sim 3000K$ at the time of last scattering (Eq. 1.53).

The CMB constitutes the most perfect black body spectrum in nature, and it is perfectly homogeneous and isotropic at the percent level. Beyond the CMB monopole, however, the CMB is characterised by a number of anisotropies that carry a wealth of cosmological information. First of all, there exists an anisotropy of 1 part in 10^3 caused by the motion of Earth with respect to the CMB rest frame. This shows up as a dipole anisotropy, as one of the hemisphere of the CMB is slightly blueshifted (i.e., it is at higher temperature) and the other slightly redshifted (i.e., it is at lower temperature). Beyond this dipole anisotropy, further distortions appear at the level of 1 part in 10^5. These anisotropies are shown in Fig. 1.4, as observed with increasing resolution by COBE (Smoot, 1992), WMAP (Bennett, 2015) and Planck (Planck Collaboration, 2019). The origins of such fluctuations have

to be found in the quantum fluctuations in the very early stages of the Universe, and eventually led to the structures (galaxies, clusters of galaxies, filaments, etc.) we see today, through the process of gravitational collapse (generally referred to as structure formation). The statistical study of CMB anisotropy has been particularly prolific in the last two decades, as the CMB contains a wealth of cosmological information, providing accurate estimates of the cosmological parameters from the early moments of the Universe. In our standard cosmological model, the values of such parameters should not be different from the ones measured at later times. From this point of view, cosmological inferences from late Universe observables (like weak lensing) are particularly valuable, as they allow to stress-test the standard cosmological model at a different time of the life of the Universe.

1.6 Structure formation

The cosmological principle states the Universe is homogeneous and isotropic on large scales. This assumption (supported by observational evidences) clearly no longer holds on small scales: if we just look at our neighborhood (in space), we can see a large variety of galaxies of different sizes and masses. The presence of structures as galaxy groups, clusters or galaxy voids, or the CMB anisotropies we discussed above are clear examples of the break down of the cosmological principle on small scales.

The origin of the structures we see today dates back to the origin of the Universe, when the only inhomogeneities in the density field were on microscopic scales, due to quantum fluctuations. Such fluctuations are believed to have grown exponentially during the Inflationary epoch[12] (Guth, 1981). Indeed, without inflation, the microscopic quantum fluctuations would not be large enough to explain the amplitude of the CMB anisotropies we observe.

[12]The term "inflation" refers to a mechanism which is believed to have caused an accelerated expansion of the Universe during its early life. The inflationary theory has been developed to explain three major problems in Cosmology: the "flatness" problem (i.e., the fact our Universe is substantially flat), "the monopole problem" (i.e. the fact we do not observe magnetic monopoles in our Universe), and the "horizon problem" (i.e., the fact that the Universe observed at the time of the CMB is homogeneous and isotropic on very large scales that, without inflation, would have never been in casual contact with each other).

1.6.1 Linear evolution

The evolution of primordial inhomogeneities through cosmic time led to the structures we see today in the Universe. Describing the evolution of such fluctuations can be very complex at small scales, whereas at large scales it can be reasonably described by a linear theory. Most of the cosmological analyses take advantage of the large-scale regime, where linear theory can be used, and only marginally use small scales, due to the complex modelling of the observables.

For the case of a perfect fluid, a fluctuation $\delta\rho$ can grow according to the "gravitational Jeans instability": if the self-gravity of the fluctuation overtakes the stabilising effect of pressure, it will grow with time (in the sense that $\delta\rho$ will increase[13]).

The linear evolution of fluctuations can be obtained by perturbing the FLRW metric and the stress-energy tensor, and combining together the continuity equation, the Euler equation and the Poisson equation. Let us define the perturbed metric, perturbed 4-velocity and perturbed stress-energy tensor:

$$g_{\mu\nu} = \begin{pmatrix} -(1+\frac{2\Phi}{c^2}) & 0 & 0 & 0 \\ 0 & a^2(1-\frac{2\Phi}{c^2}) & 0 & 0 \\ 0 & 0 & a^2 f_K(\chi)^2(1-\frac{2\Phi}{c^2}) & \\ 0 & 0 & 0 & a_K^2(\chi)^2(1-\frac{2\Phi}{c^2}) \end{pmatrix}. \tag{1.54}$$

$$u^\alpha = \left(1 - \frac{\Phi}{c^2}, \frac{v^i}{a}\right), \tag{1.55}$$

$$T_{00} = \delta\rho c^2, \quad T_{ii} = \delta p, \quad T_0^i = (\rho c^2 + p)v^i, \tag{1.56}$$

where Φ is the Newtonian potential of the perturbation[14], v^i the peculiar velocity with respect to the expansion of the Universe, and $\delta\rho$ and δp perturbations to the density and pressure. Assuming stationarity ($g_{\alpha\beta,0} = 0$,

[13] One can have a rough idea of the phenomenon for a collisional fluid by defining the self-gravitation per unit mass force of a fluctuation of mass M and size λ as $F_g \sim \frac{GM}{\lambda^2} \sim G\rho\lambda$ and the pressure per unit mass as $F_p \sim \frac{p\lambda^2}{\rho\lambda^3} \sim \frac{v_s^2}{\lambda}$ with v_s speed of sound. By imposing $F_g > F_p$, one can see that fluctuations of scales $\lambda > \frac{v_s}{\sqrt{G\rho}}$ will increase. For a collisionless fluid (i.e., dark matter), v_s is substituted by v_*, the mean velocity dispersion of the fluid.

[14] The most general metric perturbed by scalar fields would be $g_{\alpha\beta} = diag\left[-\left(1+\frac{2\Psi}{c^2}\right), a^2\left(1-\frac{2\Phi}{c^2}\right), a^2 f_K(\chi)^2\left(1-\frac{2\Phi}{c^2}\right), a^2 f_K(\chi)^2\left(1-\frac{2\Phi}{c^2}\right)\right]$; however, in General Relativity, $\Psi = \Phi$.

$\Phi_{,0} = 0$), at first order the continuity and Euler equations[15] become:

$$u^0(\rho + \delta\rho)_{,0} = -\left(\rho + \delta\rho + \frac{p + \delta p}{c^2}\right)\left(\frac{u^0 v^i_{,i}}{a} + 3u^0 H\right), \tag{1.57}$$

$$\frac{\delta p_{,i}}{a} = -\left(\rho + \delta\rho + \frac{p + \delta p}{c^2}\right)\left(H v^i + v^i_{,0} + \frac{\Phi_{,i}}{a}\right). \tag{1.58}$$

Keeping only the first-order terms we obtain:

$$\rho\delta_{,0} = -\left(\rho + \frac{p}{c^2}\right)\left(\frac{v^i_{,i}}{a}\right), \tag{1.59}$$

$$\frac{\delta p_{,i}}{a} = -\left(\rho + \frac{p}{c^2}\right)\left(H v^i + v^i_{,0} + \frac{\Phi_{,i}}{a}\right). \tag{1.60}$$

We can also write the 00 component of the perturbed Einstein equations (which can be interpreted as the general relativity version of the Poisson equation):

$$\Phi_{,i,i} = 4\pi G a^2\left(\delta\rho + 3\frac{\delta p}{c^2}\right). \tag{1.61}$$

To obtain the equation describing the time evolution of fluctuations, we need to make explicit the equation of state of the fluid ($p = p(\rho)$), take the time derivative of Eq. 1.59 and combine with Eqs. 1.60, 1.61. For a dark matter dominated Universe, we obtain:

$$\ddot{\delta} + 2H\dot{\delta} - 4\pi G\bar{\rho}\delta = 0. \tag{1.62}$$

This differential equation has two solutions, one growing with time and one decaying. As we are interest in the growing mode, the general solution is usually written as:

$$\delta(\vec{x}, t) = \frac{D(t)}{D(t_0)}\delta(\vec{x}, t_0), \tag{1.63}$$

with $D(t)$ the "growth factor", which depends on the cosmological parameters. The above solution holds only when the Universe is completely made (or dominated) of dark matter: in practice, we would need to consider all the different components at the same time.

[15] The Euler equation is the spatial part of the stress-energy conservation law (Eq. 1.25).

1.6.2 Statistics of the matter density field

No theory can predict the exact value of the dark matter density field at every point of the space time, as the observable Universe is just one possible realisation of a random density field. We can, however, describe the properties of the random field: this can be achieved, for instance, measuring all the N-point correlation functions of the field. The first two relevant N-point correlation function are the 2-point and 3-point correlation functions (since the mean value of the density fluctuation field is expected to vanish):

$$\xi(\vec{x},\vec{y}) \equiv \langle \delta(\vec{x}), \delta(\vec{y}) \rangle = \xi(|\vec{x}-\vec{y}|), \tag{1.64}$$

$$\zeta(\vec{x},\vec{y},\vec{z}) \equiv \langle \delta(\vec{x}), \delta(\vec{y}), \delta(\vec{z}) \rangle = \zeta(|\vec{x}-\vec{y}|, |\vec{y}-\vec{z}|). \tag{1.65}$$

The 2-point (3-point) correlation function represents the probability of having two (three) density fluctuations $\delta(\vec{x}), \delta(\vec{y}$ ($\delta(\vec{z})$) at two (three) different locations with respect to a random distribution. The correlation functions depend on distance differences only due to the cosmological principle[16]. In the above equations, $\langle \cdot \rangle$ should formally be the "ensemble average": as we can only observe one Universe, this is substituted by a spatial average, due to the ergodic hypothesis[17].

Correlation functions are usually predicted from theoretical arguments starting from their Fourier transforms. We define the Fourier transform of the density contrast:

$$\tilde{\delta}(\vec{k}) = \int d^3k \delta(\vec{x}) e^{-i\vec{k}\vec{x}}. \tag{1.66}$$

$$\delta(\vec{x}) = \frac{1}{(2\pi)^3} \int d^3k \tilde{\delta}(k) e^{i\vec{k}\vec{x}}, \tag{1.67}$$

The Fourier transform of the 2-point and 3-point correlation functions read:

$$\xi(|\vec{x}-\vec{y}|) = \int d^3k P(|\vec{k}|) e^{i\vec{k}|\vec{x}-\vec{y}|}, \tag{1.68}$$

[16] We note that the cosmological principle holds as long as perturbation to the metric $\frac{2\Phi}{c^2}$ are small. Density fluctuations $\frac{\delta\rho}{\rho}$ can be larger than unity without violating the cosmological principle, as they are related to perturbations of the metric as $\frac{\Phi}{c^2} \sim \frac{\lambda}{ct}\frac{\delta\rho}{\rho}$, with λ the scale of the perturbation. Basically, unless we considered perturbations on scales comparable to the cosmological horizon $\sim ct$, the cosmological principle would still hold.

[17] This also means that the largest scales observable will be necessarily dominated by the variance of the field (referred to as "cosmic variance"), as we do not have enough realisations to average over.

$$\zeta(|\vec{x}-\vec{y}|,|\vec{y}-\vec{z}|) = \frac{1}{(2\pi)^3}\int d^3k \int d^3k' B(|\vec{k}|,|\vec{k'}|)e^{i(\vec{k}|\vec{x}-\vec{y}|+\vec{k'},|\vec{y}-\vec{z}|}, \quad (1.69)$$

where $P(k)$ and $B(k,k')$ are the power spectrum and the bispectrum, which obey the following relations:

$$\langle\tilde{\delta}(\vec{k})\tilde{\delta}(\vec{k'})\rangle = (2\pi^3)\delta_D(\vec{k}-\vec{k'})P(|\vec{k}|), \quad (1.70)$$

$$\langle\tilde{\delta}(\vec{k})\tilde{\delta}(\vec{k'})\tilde{\delta}(\vec{k''})\rangle = (2\pi^3)\delta_D(\vec{k}-\vec{k'}-\vec{k''})B(|\vec{k}|,|\vec{k'}|), \quad (1.71)$$

with δ_D the Dirac delta function.

The inflationary theory predicts that primordial fluctuations were mostly described by a Gaussian random field, and that the primordial power spectrum did not depend on a characteristic scale, i.e.:

$$P_0(k) = A_s k^{n_s}, \quad (1.72)$$

with n_s the power spectrum index. The inflationary theory predicts n_s to be very close to unity, with the latest measurement from Planck being $n_s = 0.9649 \pm 0.0042$ (TT + LowP, Planck Collaboration 2019). As long as the primordial density field is Gaussian, the primordial bispectrum (or, equivalently, the 3-point correlation function), does not add any valuable information to the 2-point correlation function. Indeed, the primordial bispectrum can be used as a test for primordial non Gaussianity (Meerburg et al., 2019).

The amplitude of the power spectrum cannot be predicted by theory, and it is usually constrained by observations. The amplitude is usually parameterised in terms of the quantity σ_8, which represents the square root of the variance of the density field in spheres of radius 8 h^{-1} Mpc scattered throughout the Universe:

$$\sigma_R^2 = \frac{1}{2\pi^2}\int dk k^2 P(k, z=0)\left[\frac{3j_1(kR)}{kR}\right]^2, \quad (1.73)$$

with $R = 8h^{-1}$ Mpc, $P(k, z=0)$ the power spectrum at present time and j_1 the spherical Bessel function of order 1. In practice, this implies the power spectrum has been smoothed using a spherical top-hat window function.

The matter power spectrum and bispectrum today are usually connected to the primordial power spectrum and bispectrum through the transfer function $T(k,z)$:

$$P(k,z) = T(k,z)^2 P_0(k), \quad (1.74)$$

$$B(k,z) = T(k,z)^3 B_0(k), \tag{1.75}$$

with the redshift part of the transfer function that can be expressed as:

$$T(k,z) = \frac{D(z)}{D(z=0)} a(z) T(k), \tag{1.76}$$

with $D(z)$ the growth factor introduced in Eq. 1.63. The transfer function encodes all the effects[18] that modify the linear growth of structures at different scales. It can be obtained by solving the equivalent of Eq. 1.62 but considering all the different components of the Universe (baryons, radiation, dark matter, dark energy). For a ΛCDM Universe, the resulting power spectrum and bispectrum correspond to a bottom-up scenario, where small structures form first and, by merging, subsequently form bigger structures.

1.6.3 Non-linear evolution

At small scales, the growth of fluctuations cannot be described by a linear theory. As soon as fluctuations are larger than $\delta \gtrsim 1$, linear theory becomes inadequate: the gravitational collapse proceed faster, and structures decouple from the evolution of the rest of the Universe, which proceeds following the linear theory. The standard approach to understand the non-linear evolution follows the "spherical collapse" model (Press & Schechter, 1974; Mo & White, 1996). Fluctuations δ exceeding a critical value δ_c form a bound structure that with time merges with neighbouring structures, forming bigger halos according to a hierarchical formation model. In this framework, baryons are caught by the gravitational potential of dark matter halos, initially in the form of hot spherical gaseous structures. Due to several cooling processes, these hot spherical gas structures collapse to cold proto-galactic disks, fostering the onsets of star forming processes.

The non-linear evolution is very complicated to predict from theoretical principles. Generally, it is common to use analytical fitting formulae obtained from high-resolution N-body simulation suites that encompass a

[18]Depending on the era of the Universe, we have: 1) the Meszaros effect, which is the stagnation of fluctuations of pressureless fluid (i.e. dark matter) during the radiation dominated era; 2) acoustic oscillations, when fluctuations do not grow due to pressure; 3) Silk damping, which consists in a damping on small scales due to diffusing photons; 4) free-streaming, which represents the damping on small scales due to non-zero velocity of dark matter; 5) radiation drag, which represents a stagnation that affects isothermal baryonic modes (i.e, modes that only involve matter density fluctuations, with the radiation field assumed to be uniform) prior to matter-radiation equality.

large number of different cosmological models. Such formulae exist both for the power spectrum (Takahashi et al., 2012) and for the bispectrum (Takahashi et al., 2019).

1.6.4 The galaxy 2-point and 3-point correlation functions

In the previous subsection we described the main statistical properties of the matter density field. The dark matter (which is the main constituent of the matter field), however, is not directly observable: what we can directly observe, with our telescopes, is the light emitted by galaxies. Galaxies naturally fall in the gravitational potential of dark matter halos, and are therefore considered (biased) "tracers" of the dark matter density field. We can follow the previous subsection and define a galaxy 2-point (3-point) correlation function and the relative galaxy power spectrum (bispectrum). This has to be interpreted as the probability over random to find a pair (or triplet) of galaxies at a given angular separation:

$$dP = \bar{n}^2 \left[1 + \xi_g(|\vec{x} - \vec{y}|)\right] dV_1 dV_2, \tag{1.77}$$

$$dP = \bar{n}^3 \left[1 + \xi_g(|\vec{x} - \vec{y}|) + \xi_g(|\vec{x} - \vec{z}|) + \xi_g(|\vec{z} - \vec{y}|) + \zeta_g(|\vec{x} - \vec{y}|, |\vec{y} - \vec{z}|)dV. \tag{1.78}$$

The galaxy N-point statistics are related to the matter N-point statistics through the so called "galaxy bias", which quantifies how a given population of galaxies trace the underlying matter distribution. The relation between galaxy and matter overdensities can be expressed as:

$$\delta_g = b\delta, \tag{1.79}$$

with $b(z)$ the galaxy bias, which can depend on the tracer population, on redshift and on the scale of the fluctuation considered. For a given tracer population and fixed redshift, at sufficiently large scales the bias becomes constant (i.e., we are in the "linear bias regime").

Assuming linear bias, we can express the galaxy 2-point correlation function as follow

$$\xi_g(|\vec{x} - \vec{y}|) = b^2 \xi(|\vec{x} - \vec{y}|), \tag{1.80}$$

$$\zeta_g(|\vec{x} - \vec{y}|, |\vec{y} - \vec{z}|) = b^3 \zeta(|\vec{x} - \vec{y}|, |\vec{y} - \vec{z}|). \tag{1.81}$$

In the case of galaxy photometric surveys, a large sample of galaxies is usually observed. Galaxies are located at different positions and redshift, but since the latter quantity is not known with high accuracy in photometric surveys, angular (i.e., projected) 2-point and 3-point correlation functions are usually considered.

Due to the spherical symmetry of the problem, it is easier to express the angular correlation functions by using a spherical harmonic transform. Note that in the following the vectors $\vec{x}$, $\vec{y}$ and $\vec{z}$ indicate the position on a sphere, we are not interested in the radial information. To avoid confusion with the notation above, we will add the subscript $_p$ to the vectors. For the 2-point correlation function, we can write, for two galaxy samples i and j:

$$\xi_g^{ij}(|\vec{x}_p - \vec{y}_p|) = \sum_\ell \frac{2\ell+1}{4\pi} P_\ell(\cos\theta)) C_\ell^{ij}, \tag{1.82}$$

with $P_\ell(x)$ the Legendre polynomial of order ℓ and:

$$C_\ell^{ij} = \left(\frac{8\pi}{c^2}\right)^2 \int \frac{k^2 dk}{2\pi^3} \int_0^\infty \frac{d\chi}{\chi} q_\delta^i(\chi) j_\ell(k\chi) \int_0^\infty \frac{d\chi'}{\chi'} q_\delta^j(\chi') j_\ell(k\chi') P(k,\chi,\chi'), \tag{1.83}$$

with j_ℓ the spherical Bessel function , $\ell = k\chi$ and

$$q_\delta^i = b^i(k, z(\chi)) \frac{n_g^i(z(\chi))}{\bar{n_g^i}} \frac{dz}{d\chi}. \tag{1.84}$$

with n_g^i the redshift distribution of the $i-th$ sample. For the 3-point correlation function the projected statistic will depend on the spatial configuration of the three projected points. Considering three galaxy samples i, j and m:

$$\zeta_g^{ijm}(|\vec{x}_p - \vec{y}_p|, |\vec{y}_p - \vec{z}_p|) = \sum_{\ell_1,\ell_2,\ell_3,m_1,m_2,m_3} B^{ijm}_{\ell_1,\ell_2,\ell_3,m_1,m_2,m_3} Y_{\ell_1 m_1}(\vec{x}_p) Y_{\ell_2 m_2}(\vec{y}_p) Y_{\ell_3 m_3}(\vec{z}_p), \tag{1.85}$$

with $Y_{\ell m}$ the spherical harmonics. By defining the Clebsch–Gordan coefficients $\begin{pmatrix} \ell_1 & \ell_2 & \ell_3 \\ m_1 & m_2 & m_3 \end{pmatrix}$, we can write:

$$B^{ijm}_{\ell_1,\ell_2,\ell_3,m_1,m_2,m_3} = \begin{pmatrix} \ell_1 & \ell_2 & \ell_3 \\ 0 & 0 & 0 \end{pmatrix} \begin{pmatrix} \ell_1 & \ell_2 & \ell_3 \\ m_1 & m_2 & m_3 \end{pmatrix} \times \frac{\sqrt{(2\ell_1+1)(2\ell_2+1)(2\ell_3+1)}}{4\pi} B^{ijm}_{\ell_1,\ell_2,\ell_3}, \tag{1.86}$$

$$B^{ijm}_{\ell_1,\ell_2,\ell_3} = \left(\frac{8\pi}{c^2}\right)^3 \int \frac{k^2 dk}{2\pi^3} \int_0^\infty \frac{d\chi}{\chi} q^i_\delta(\chi) j_{\ell_1}(k\chi) \int_0^\infty \frac{d\chi'}{\chi'} q^j_\delta(\chi') j_{\ell_2}(k\chi') \times \int_0^\infty \frac{d\chi''}{\chi''} q^m_\delta(\chi'') j_{\ell_3}(k\chi'') B(k,\chi,\chi',\chi''). \quad (1.87)$$

The above relations are usually simplified by means of the Limber approximation, which basically substitutes:

$$j_\ell(k\chi) \ \rightarrow \ \delta_D(\nu - k\chi), \quad (1.88)$$

with $\nu = \ell + 1/2$. This approximation is accurate if the rest of the integrand is slowly varying compared to the spherical Bessel function, which is generally the case at large ℓ (i.e., small scales). The approximation breaks down at large scales or for very narrow or barely overlapping redshift distributions.

Chapter 2

Weak Gravitational Lensing

Gravitational lensing generally refers to the phenomena of deflection of light trajectories due to the effect of gravitational fields. The idea that gravity could bend the trajectory of light rays was born before the advent of General relativity; under the dichotomic conception that light can be either considered as a wave or a particle, one could compute the bending of trajectory of massless light particles due to massive objects using standard Newtownian physics. However, as shown by Eddigton in 1919, the Newtownian prediction was incorrect by a factor of 2 compared to Einstein's theory. That very measurement corroborated the validity of General Relativity, which at the time was considered mostly as a speculation, paving the way to the theory of gravitational lensing as we know it today.

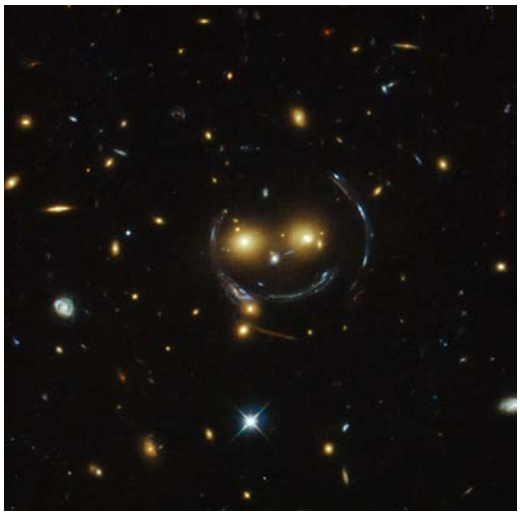

Figure 2.1: SDSS J1038+4849 galaxy cluster, from the NASA/ESA Hubble Space Telescope. Strong gravitational lensing effects are responsible for the Einstein's rings, which are the result of a strong deflection of the light emitted by two galaxies behind the cluster.

When the gravitational field responsible for the deflection is strong enough, it can generate evident patterns in the observed images. In this regime of strong gravitational lensing, one could observe multiple images of the same

objects, usually in the version of arcs or Einstein's rings (see Fig. 2.1). Magnification effects due to lensing can be as strong as to allow the detection of faint objects that could not be detected otherwise. Strong gravitational effects are usually confined to peculiar environments as, e.g., a dense cluster of galaxies.

In this thesis we focus on the regime were lensing effects are weak (weak gravitational lensing). This is the case of the light emitted by distant galaxies, which is deflected by the Large Scale Structure (LSS) of the Universe. Photons emitted by distant galaxies are subject to the gravitational fields of all the matter distribution of the Universe, and as a net result the images we detect are distorted. Contrary to the strong lensing regime, in the weak lensing regime the lensing effects are generally much smaller than the noise on a single galaxy basis and very large ensembles of galaxies (and statistical tools) are needed to detect them. This poses a number of observational challenges, making the detection (and interpretation) of the weak lensing signal not an easy task. Despite all the technical difficulties, the weak lensing signal has proven to be an extraordinary cosmological probe, due to its sensitivity to the LSS. In the following sections, we will lay out the formalism needed to describe the weak lensing observables used in this thesis.

2.1 Propagation of light in General Relativity

Let us consider the task of modelling the propagation of light rays in a general space-time. This can be achieved using Fermat's principle and minimising the light travel time for a generic trajectory followed by a light ray[1]. Let us consider the coordinate system of a flat Minkowski space time ξ^α and a generic coordinate transformation $\xi^\alpha = \xi^\alpha(x^\mu)$. Let $g_{\mu\nu} = \partial\xi^\alpha/\partial x^\mu \xi^\beta/\partial x^\nu \eta_{\alpha\beta}$ be the metric describing our new space-time, and $\eta_{\alpha\beta} = diag(-1, 1, 1, 1)$ the metric tensor of the flat, Minkowski space time. We can describe a generic path in space time as

$$x^\mu(s), \tag{2.1}$$

[1]In General Relativity, this approach is equivalent to solve the geodesic equation for massless particles.

where s is an arbitrary parameter describing the trajectory. The infinitesimal line element ds can be expressed as:

$$ds^2 = g_{\mu\nu} dx^\mu dx^\nu. \tag{2.2}$$

The element ds represents the infinitesimal space time interval between two events separated by dx^μ in a generic metric. Massless particles move along lines that minimise the space time interval, i.e., $ds^2 = 0$ (whereas massive particles are characterised by $ds^2 < 0$)[2]. One can further express the light travel time in a closed form if the metric is diagonal. E.g., we can consider the Minkowski metric perturbed by a lensing potential Φ: $g_{\mu\nu} = diag(-(1+2\Phi/c^2), 1-2\Phi/c^2, 1-2\Phi/c^2, 1-2\Phi/c^2)$ (note that here we do not consider the expansion of the Universe yet). The light travel time along a trajectory $x^\mu(s)$ between a point A and a point B reads:

$$T = \int_{t_A}^{t_B} dt = \int_{s_A}^{s_B} \frac{dt}{d\vec{x}} \frac{d\vec{x}}{ds} ds \approx \int_A^B \left(1 - \frac{2\Phi}{c^2}\right) \frac{d\vec{x}}{ds} ds, \tag{2.3}$$

where in the last approximation we expanded $\frac{dt}{d\vec{x}}$ at first order. This is analogous to geometrical optics, with the gravitational potential acting as a medium with variable refractive index $n = \left(1 - \frac{2\Phi}{c^2}\right)$ deflecting the path of light. To minimise the light path, we look for solutions of the equations $\delta T = 0$. This is is a standard variational problem[3] and Eq. 5.1 can be equivalently solved by:

$$\frac{d}{ds}\left[\left(1 - \frac{2\Phi}{c^2}\right)\vec{u}\right] - \vec{\nabla}\left(1 - \frac{2\Phi}{c^2}\right) = 0, \tag{2.4}$$

with $\vec{u} = \frac{d\vec{x}}{ds}$ the unit vector tangent to the path of the light. It follows:

$$\left(1 - \frac{2\Phi}{c^2}\right)\dot{\vec{u}} = \vec{\nabla}\left(1 - \frac{2\Phi}{c^2}\right) - \vec{u}\left[\vec{\nabla}\left(1 - \frac{2\Phi}{c^2}\right)\vec{u}\right], \tag{2.5}$$

[2] A 4-vector U^α can be either null ($U^\alpha U_\alpha = 0$), space-like ($U^\alpha U_\alpha > 0$), time-like ($U^\alpha U_\alpha < 0$). Massless particles follow geodesics whose 4-velocity is a null 4-vector, whereas the 4-velocity of massive particles is time-like. In Minkowski space time, it can be seen that a particle moving with 4-velocity $U^\alpha = dx^\alpha/d\tau$ will lay on the light-cone if $U^\alpha U_\alpha = -(dx^0/d\tau)^2 + (dx^1/d\tau)^2 + (dx^2/d\tau)^2 + (dx^3/d\tau)^2 = 0$ (for an observer centered at the origin of the reference system, the light cone is defined as $(dx^0/d\tau)^2 = (dx^1/d\tau)^2 - (dx^2/d\tau)^2 - (dx^3/d\tau)^2$). If the 4-velocity is such that $U^\alpha U_\alpha < 0$, the particle will only move inside the light-cone.

[3] Let us consider the functional $S(\vec{x}) = \int dt L(t, x(\vec{t}), \dot{\vec{x}}(t))$, with $\dot{x} = \frac{dx}{dt}$. Variational principles aim to find the function $\vec{x}(t)$ that minimises the functional $S(\vec{x}(t))$, i.e. $\delta S(\vec{x}) = 0$. This leads to solving the associated Euler–Lagrange equation $\frac{d}{dt}\frac{\partial L}{\partial \dot{x}^i} - \frac{\partial L}{\partial x^i} = 0$ for $i \in 0, .., n$.

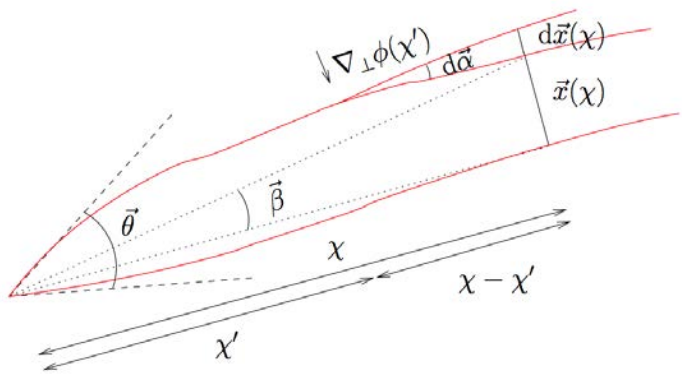

Figure 2.2: Sketch of propagation of light rays, from Kilbinger (2015). The quantity $\vec{\beta}$ represents the angular separation of two light rays in case of no gravitational perturbation, while the angular separation observed is $\vec{\theta}$.

$$\dot{\vec{u}} = \frac{d^2\vec{x}}{ds^2} = \vec{\nabla}_\perp \ln\left(1 - \frac{2\Phi}{c^2}\right) \approx -\frac{2}{c^2}\vec{\nabla}_\perp\Phi. \tag{2.6}$$

In the above equation, the gradient is meant to be taken perpendicular to the light paths. The left hand side of Eq. 2.6 represents the variation of the tangent unit vector along the path of light. By integrating along the whole trajectory, one can obtain the total deflection angle $\hat{\vec{\alpha}}$, defined as the deviation between the perturbed and unperturbed path:

$$\hat{\vec{\alpha}} \equiv \int_{s_A}^{s_B} \frac{d^2\vec{x}}{ds^2} = \frac{2}{c^2}\int_{s_A}^{s_B} \vec{\nabla}_\perp\Phi ds. \tag{2.7}$$

2.1.1 Propagation of light in an inhomogeneous Universe

Let us consider the deflection of light in an inhomogeneous Universe. We now consider the FLRW metric for a homogeneous Universe perturbed by a lensing potential Φ, adopting spherical coordinates for the spatial part of the metric $\xi^\mu = (ct, \chi, \theta, \phi)$. This metric was introduced in Eq. 1.54. It can be shown that the propagation equation (Eq. 2.6) can be re-written as the equation of a driven harmonic oscillator, with the gravitational potential playing the role of the external force:

$$\frac{d^2\vec{x}}{d\chi^2} + K\vec{x} = -\frac{2}{c^2}\vec{\nabla}_\perp\Phi, \tag{2.8}$$

which admits the general solution:

$$\vec{x}(\chi) = f_K(\chi)\vec{\theta} - \frac{2}{c^2}\int_0^\chi d\chi' f_K(\chi - \chi')\vec{\nabla}_\perp \Phi. \tag{2.9}$$

In eq. 2.9, $\vec{\theta}$ represents the angular separation of two light rays as seen by the observer (see Fig. 2.2). The quantity $\vec{\beta} \equiv f_k(\chi)\vec{\theta}$ (which, in case of flat curvature, reduces to the Euclidian $\vec{\beta} = \chi\vec{\theta}$), represents the angular separation of two light rays in case of no gravitational perturbation. We can write the deflection angle as:

$$\vec{\alpha} = \frac{f_K(\chi)\vec{\theta} - \vec{x}}{f_K(\chi)} = \frac{2}{c^2}\int_0^\chi d\chi' \frac{f_K(\chi - \chi')}{f_K(\chi)}\vec{\nabla}_\perp \Phi, \tag{2.10}$$

and define the lens equation, which relates the deflection angle $\vec{\alpha}$, the "unperturbed" angular separation $\vec{\beta}$ and the angular separation seen by the observer $\vec{\theta}$:

$$\vec{\beta} = \vec{\theta} - \vec{\alpha}. \tag{2.11}$$

Formally, the right-hand side of Eq. 2.10 must be evaluated along the perturbed path of the light ray, which is unpractical. The Born approximation is usually applied, and $\vec{\nabla}_\perp \Phi$ is evaluated along the unperturbed path of light. The approximation holds as long as the deflection angle is small (i.e. $\Phi/c^2 << 1$)[4], which usually holds in the weak lensing regime. Perturbative solutions to the propagation equation exist accounting for deviation from the Born approximation (e.g. Krause & Hirata 2010), but such corrections are usually neglected in current low redshift weak lensing surveys. Post-Born corrections become more important when modelling measurements involving CMB observables, due to the long path travelled by CMB photons, as in the case of the CMB lensing bispectrum (Pratten & Lewis, 2016) or CMB convergence cross-correlation with low redshift galaxy counts (Böhm et al., 2020).

2.2 Linearised lens mapping: shear and magnification

We now Taylor expand the lens equation (Eq. 2.11) at first order, considering the linear mapping between the infinitesimal lensed displacement $\delta\vec{\beta}$ and

[4]In galaxy clusters, e.g., $\Phi/c^2 << 10^{-5}$.

unlensed displacement $\delta\vec{\theta}$. We define the inverse amplification matrix $A = \partial\vec{\beta}/\partial\vec{\theta}$, whose elements read[5]:

$$A_{ij} = \frac{\partial\beta_i}{\partial\theta_j} = \delta_{ij} - \frac{\partial\alpha_i}{\partial\theta_j} = \delta_{ij} - \frac{2}{c^2}\int_0^\chi d\chi' \frac{f_K(\chi')f_K(\chi-\chi')}{f_K(\chi)}\frac{\partial^2}{\partial x_i \partial x_j}\Phi = \delta_{ij} - \frac{\partial^2}{\partial x_i \partial x_j}\psi(\vec{\theta},\chi), \quad (2.12)$$

where we introduced the lensing potential $\psi(\vec{\theta})$:

$$\psi(\vec{\theta},\chi) = \frac{2}{c^2}\int_0^\chi d\chi' \frac{f_K(\chi')f_K(\chi-\chi')}{f_K(\chi)}\Phi(f_K(\chi')\vec{\theta},\chi'). \quad (2.13)$$

The lensing potential is the lensing-efficiency-weighted integral of the gravitational potential; in case of a flat universe ($K = 0$), the lensing weight function $f_K(\chi')f_K(\chi-\chi')$ is a parabola peaking at $\chi/2$, meaning that lenses half-way between the observer and the sources maximise the contribution to the lensing potential. We also note that in absence of a lensing potential, the mapping between lensed and unlensed coordinates described by Eq. 2.12 reduces to the identity. The amplification matrix can be written in more compact form introducing the convergence κ and the shear field $\vec{\gamma} = \gamma_1 + i\gamma_2 = |\gamma|e^{2i\phi}$:

$$A_{ij} = \begin{pmatrix} 1-\kappa-\gamma_1 & -\gamma_2 \\ -\gamma_2 & 1-\kappa+\gamma_1 \end{pmatrix}. \quad (2.14)$$

where the convergence and the shear field are evaluated at a given position in the space time $(\vec{\theta},\chi)$ and are related to the lensing potential through the following equations:

$$\kappa \equiv \frac{1}{2}(\partial_i\partial_i + \partial_j\partial_j)\psi = \frac{1}{2}\nabla^2\psi; \quad (2.15)$$

$$\gamma_1 \equiv \frac{1}{2}(\partial_i\partial_i - \partial_j\partial_j)\psi; \quad (2.16)$$

$$\gamma_2 \equiv \partial_i\partial_j\psi. \quad (2.17)$$

The shear field is a spin-2 quantity; its amplitude describes the degree of distortion, whereas its phase[6] is related to the direction of distortion.

[5]We also used the fact that $\frac{\partial}{\partial\vec{x}} = \frac{1}{\chi}\frac{\partial}{\partial\vec{\theta}}$.

[6]Note that the phase is multiplied by a factor of "2", which reflects the fact that the shear field is a spin-2 quantity. Physically, it reflects the fact that ellipses transform into themselves after a rotation of 180 degrees.

The convergence field has also a very clear physical interpretation: it represents the integrated matter contrast along the line-of-sight (see § 2.3). It is customary to introduce the reduced shear field $\vec{g}$, defined as:

$$\vec{g}(\vec{\theta},\chi) = \frac{\vec{\gamma}(\vec{\theta},\chi)}{1-\kappa(\vec{\theta},\chi)}, \tag{2.18}$$

The reduced shear field has been introduced instead of the shear field as it is the quantity that can be directly accessed by observations. With this new notation, the amplification matrix assumes the form:

$$A_{ij} = (1-\kappa)\begin{pmatrix} 1-g_1 & -g_2 \\ -g_2 & 1+g_1 \end{pmatrix}. \tag{2.19}$$

The amplification matrix A_{ij} describes the mapping between the lensed coordinates $(\vec{\theta})$ sand the unlensed coordinates $(\vec{\beta})$; to obtain the opposite mapping, we simply invert the matrix:

$$d\vec{\theta} = A^{-1} d\vec{\beta}, \tag{2.20}$$

with

$$A^{-1}_{ij} = \frac{1-\kappa}{(1-\kappa^2)(1-|g|^2)}\begin{pmatrix} 1+g_1 & g_2 \\ g_2 & 1-g_1 \end{pmatrix}. \tag{2.21}$$

The fact we are considering the weak lensing regime, where κ and $|g|$ are expected to be small, guarantees the matrix to be invertible (i.e. $detA \neq 0$). The impact of the convergence and (reduced) shear field on a given image can be understood taking a circular image of radius R distorted by the matrix A^{-1}_{ij} as explanatory case. The distortion will map the circular image into an ellipse with semi-axes a, b corresponding to the eigen-values of the inverse amplification matrix A_{ij}:

$$a = \frac{R}{1-\kappa-|\gamma|} = \frac{R}{(1-\kappa)(1-|g|)}, \tag{2.22}$$

$$b = \frac{R}{1-\kappa+|\gamma|} = \frac{R}{(1-\kappa)(1+|g|)}. \tag{2.23}$$

and the major axis forms an angle ϕ with the θ_1 axis. In absence of shear, the convergence field act on the radius of the circle, without modifying its shape; on the other hand, the shear field will transform the circle into an

ellipse and rotate the image (see Fig. 2.3). The ellipticity of the image after the distortion will be:

$$\vec{\epsilon} \equiv \frac{a-b}{a+b} = \frac{\vec{\gamma}}{1-\kappa} = \vec{g}. \tag{2.24}$$

The ellipticity of the image is directly related to the reduced shear field, which is the direct observable, rather than the shear field. Moreover, real galaxies do not have a circular shape, but they have their own intrinsic ellipticity $\vec{\epsilon^s}$. The measured ellipticity $\vec{\epsilon}$ of a galaxy is thus a combination of the galaxy intrinsic ellipticity $\vec{\epsilon^s}$ and the value of the shear field $\vec{g}$ at the galaxy position:

$$\vec{\epsilon} = \frac{\vec{\epsilon^s} + \vec{g}}{1 + \vec{g}^* \vec{\epsilon^s}}, \tag{2.25}$$

where the asterisk denotes complex conjugation. In the weak lensing regime, the above equations can be approximated to :

$$\vec{\epsilon} \approx \vec{\epsilon^s} + \vec{\gamma}. \tag{2.26}$$

Assuming that the intrinsic ellipticities of galaxies are randomly oriented, the mean of the observed ellipticities is an unbiased estimator of the shear field, i.e, $\langle\vec{\epsilon}\rangle \approx \langle\vec{\gamma}\rangle$. In practice, this is not true for two reasons. The first reason is that galaxies are not randomly oriented because of an effect known as *intrinsic alignment*. Galaxies tend to have correlated orientations (and measured ellipticities), due to gravitational interactions. Intrinsic alignments add an excess of correlation between galaxy shapes, which has to be accounted for in any weak lensing cosmological analyses. The second reason is that measuring galaxies ellipticity is a complicated procedure and it is subject to a number of measurement biases. We will discuss in more depth in § 3.1 how to estimate the shear field from noisy data.

One can also compute the variation in the solid angle covered by the distorted image with respect to the source by defining the magnification factor μ[7] as:

$$\mu = \frac{\pi R^2}{\pi ab} = \frac{1}{(1-\kappa)^2 - |\gamma|^2} \approx 1 + 2\kappa. \tag{2.27}$$

Eq. 4.8 indicates that in the weak lensing regime, at first order, the change in the solid angle due to lensing effects is solely caused by the convergence field κ.

[7]The magnification coefficient is formally defined as $\mu \equiv \frac{1}{detA}$.

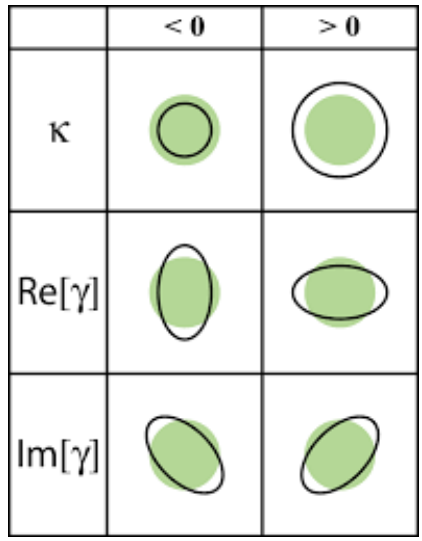

Figure 2.3: Effects of the convergence and shear field on a circular image. The green circle shows the unsheared, original image. Source: Wikipedia.

2.3 Lensing convergence as projected matter density

We anticipated in the previous section that the convergence field has a very clear physical interpretation: it represents the integrated matter contrast along the line-of-sight. This can be shown combining the Poisson equation for the perturbed density field (Eq.1.61, for matter only) with the definition of convergence (Eq. 2.15) and lensing potential (Eq. 2.13):

$$\kappa(\vec{\theta},\chi) = \frac{3H_0^2\Omega_m}{2c^2}\int_0^{\chi} d\chi' \frac{f_K(\chi')(f_K(\chi)-f_K(\chi'))}{f_K(\chi)}\frac{\delta(f_K(\chi')\vec{\theta},\chi')}{a(\chi')}, \quad (2.28)$$

where we used the definition of mean matter density:

$$\bar{\rho_m} = \frac{3H_0^2\Omega_m}{8\pi G a^3}. \quad (2.29)$$

Eq. 2.28 shows how the convergence field κ is related to the matter density contrast δ by an integration along the line-of-sight, weighted by a lensing kernel. For a given redshift distribution of sources $n(z(\chi))$, Eq. 2.28 becomes:

$$\kappa(\vec{\theta}) = \int_0^{\infty} d\chi n(z(\chi))\kappa(\vec{\theta},\chi) = \int_0^{\chi} d\chi g(\chi)\delta(f_K(\chi)\vec{\theta},\chi), \quad (2.30)$$

with

$$g(\chi) = \frac{3H_0^2\Omega_m}{2c^2}\frac{f_K(\chi)}{a(\chi)}\int_\chi^\infty d\chi' \frac{f_K(\chi'-\chi)}{f_K(\chi')}n(z(\chi')). \tag{2.31}$$

The quantity $g(\chi)$ represents the lensing strength of the source distribution at a given distance χ.

2.4 Shear 2-point and 3-point correlation functions

In analogy with the galaxy 2-point and 3-point correlation functions, one can define the shear 2-point and 3-point correlation functions, which specify the probability of having a pair or triplet of shear values at given angular separations. The main advantage is that, using the shear field, one can probe the underlying matter density field properties without the need of a galaxy bias model.

One starts by assuming spherical symmetry and define the spherical harmonic decomposition of the shear field:

$$\gamma(\vec{x_p}) = \sum_{\ell m}\gamma_{\ell m 2}Y_{\ell m}, \quad \gamma^*(\vec{x_p}) = \sum_{\ell m}\gamma_{\ell m -2}Y_{\ell m}, \tag{2.32}$$

with ${}_2Y_{\ell m}$, ${}_{-2}Y_{\ell m}$ spin-2 spherical harmonics (because the shear field is a spin-2 quantity). Given two galaxy samples i and j, we can define the usual shear two-point correlation functions ξ_+ and ξ_- as:

$$\xi_+^{ij}(|\vec{x}_p - \vec{y}_p|) \equiv \langle\gamma^*(\vec{x_p})\gamma(\vec{y_p})\rangle = \sum_\ell \frac{2\ell+1}{4\pi}d^\ell_{2,2}(\theta)C_\ell^{\epsilon\epsilon,ij}, \tag{2.33}$$

$$\xi_-^{ij}(|\vec{x}_p - \vec{y}_p|) \equiv \langle\gamma(\vec{x_p})\gamma(\vec{y_p})\rangle = \sum_\ell \frac{2\ell+1}{4\pi}d^\ell_{2,-2}(\theta)C_\ell^{\epsilon\epsilon,ij}, \tag{2.34}$$

with $d^\ell_{2,2}(\theta)$, $d^\ell_{2,-2}(\theta)$ the reduced Wigner D-matrices. The formalism is similar to the case of the galaxy 2-point correlation function (Eq. 1.82), but with the difference that the galaxy density field is a spin-0 quantity and we had to use $d^\ell_{0,0}(\theta) = P_\ell(cos(\theta))$. It is also common practice to adopt the flat-sky approximation, where the reduced D-matrices are approximated by ordinary Bessel functions:

$$d^\ell_{2,2}(\theta) \approx J_0(\ell\theta), \quad d^\ell_{2,-2}(\theta) \approx J_4(\ell\theta), \tag{2.35}$$

$$\xi_+^{ij}(|\vec{x}_p - \vec{y}_p|) = \frac{1}{2\pi}\int d\ell\ell J_0(\ell\theta) C_\ell^{\epsilon\epsilon,ij}, \tag{2.36}$$

$$\xi_-^{ij}(|\vec{x}_p - \vec{y}_p|) = \frac{1}{2\pi}\int d\ell\ell J_4(\ell\theta) C_\ell^{\epsilon\epsilon,ij}. \tag{2.37}$$

The quantity $C_\ell^{\epsilon\epsilon,ij}$ is the shear power spectrum. It is related to the convergence power spectrum via Eq. 2.15 (which becomes in spherical harmonics $C_\ell^{\epsilon\epsilon,ij} = \frac{1}{4}\left[[\ell(\ell+1)(\ell 1)(\ell+2)]\right] C_\ell^{\kappa\kappa,ij}$. The term $C_\ell^{\kappa\kappa,ij}$ is similar to Eq. 1.83, but once having replaced the redshift distributions with the quantity $g(\chi)$ (i.e., the lensing kernel weighted redshift distributions) defined above:

$$C_\ell^{\kappa\kappa,ij} = \left(\frac{8\pi}{c^2}\right)^2 \int \frac{k^2 dk}{2\pi^3} \int_0^\infty \frac{d\chi}{\chi} g^i(\chi) j_\ell(k\chi) \int_0^\infty \frac{d\chi'}{\chi'} g^j(\chi') j_\ell(k\chi') P(k,\chi,\chi'). \tag{2.38}$$

The shear 3-point correlation functions are definitely less used than their galaxy counterparts. In general, one can define 8 different combinations of shear 3-point correlation functions: $\langle\gamma(\vec{x_p})\gamma(\vec{y_p})\gamma(\vec{z_p})\rangle$, $\langle\gamma^*(\vec{x_p})\gamma(\vec{y_p})\gamma(\vec{z_p})\rangle$, $\langle\gamma(\vec{x_p})\gamma^*(\vec{y_p})\gamma(\vec{z_p})\rangle$, $\langle\gamma(\vec{x_p})\gamma(\vec{y_p})\gamma^*(\vec{z_p})\rangle$, $\langle\gamma^*(\vec{x_p})\gamma^*(\vec{y_p})\gamma(\vec{z_p})\rangle$, etc. The shear 3-point correlation functions can be written as

$$\langle\gamma^{(*)}(\vec{x_p})\gamma^{(*)}(\vec{y_p})\gamma^{(*)}(\vec{z_p})\rangle = \sum_{\ell_1,\ell_2,\ell_3 m_1,m_2,m_3} {}^{\epsilon\epsilon}B_{\ell_1,\ell_2,\ell_3}^{m_1,m_2,m_3} {}_{\pm2}Y_{\ell_1 m_1}(\vec{x}_p) {}_{\pm2}Y_{\ell_2 m_2}(\vec{y}_p) {}_{\pm2}Y_{\ell_3 m_3}(\vec{z}_p), \tag{2.39}$$

$${}^{\epsilon\epsilon\epsilon}B_{\ell_1,\ell_2,\ell_3}^{m_1,m_2,m_3} = \begin{pmatrix} \ell_1 & \ell_2 & \ell_3 \\ \pm2 & \mp2 & \mp2 \end{pmatrix} \begin{pmatrix} \ell_1 & \ell_2 & \ell_3 \\ m_1 & m_2 & m_3 \end{pmatrix} \times \frac{\sqrt{(2\ell_1+1)(2\ell_2+1)(2\ell_3+1)}}{4\pi} {}^{\epsilon\epsilon\epsilon}B_{\ell_1,\ell_2,\ell_3}. \tag{2.40}$$

The quantity ${}^{\epsilon\epsilon\epsilon}B_{\ell_1,\ell_2,\ell_3}$ relates to the convergence bispectrum as ${}^{\epsilon\epsilon\epsilon}B_{\ell_1,\ell_2,\ell_3} = \frac{1}{8}\left[[\ell(\ell+1)(\ell 1)(\ell+2)]\right]^{3/2} {}^{\kappa\kappa\kappa}B_{\ell_1,\ell_2,\ell_3}$. Similar to the case of the convergence power spectrum, the convergence bispectrum can be obtained from Eq. 1.87 substituting the redshift distributions with the quantity $g(\chi)$. As done in § 1.6.4, one can apply the Limber approximation to further simplify the above equations.

While the shear 2-point correlation function is widely used in current cosmological analysis, the same is not true for the shear 3-point correlation

functions. Usually other statistical tools are used to probe the higher-order information of the dark matter density using weak lensing observables e.g., convergence field moments, or aperture-mass statistics. In particular, in Chapter 7, we will show how to use the convergence fields second and third moments to infer cosmological parameters.

Chapter 3

The Dark Energy Survey

The Dark Energy Survey (DES) is designed to probe the origin of the accelerated expansion of the Universe and help understand the nature of dark energy. It is a huge collaborative effort, involving more than 400 scientists from over 25 institutions in the United States, Spain, the United Kingdom, Brazil, Germany, Switzerland and Australia (see Fig. 3.1). This international project built and used an extremely sensitive 570-Megapixel digital camera (DECam, Flaugher et al. 2015), installed at the prime focus of the 4-meter Blanco telescope at Cerro Tololo Inter-American Observatory (CTIO), in Chile (Fig.3.2). The camera consists of a set of 74 CCDs (charge-coupled devices) observing in 5 optical and near-infrared broadbands (*grizY*, see Fig. 3.3), with a nominal limiting magnitude of $i_{\rm AB} \sim 24$. DES had been conducting over the past 6 years (2013-2019) two nominal multi-band imaging surveys: a 5000 deg^2 wide-area survey in the *grizY* bands and a $\sim$27 deg^2 deep supernova survey observed in the *grizY* bands with a $\sim$7 days cadence. The wide-field survey adopted 10 passes with a $90s$ exposure time for the *griz* bands and a $45s$ exposure time for the Y band. During the period of observations, DECam detected and measured the position, shape and photometric redshift of $\sim$300 million galaxies, $\sim$3000 type Ia supernovae and tens of thousands of galaxy clusters.

To investigate the nature of dark energy (and to discriminate between different dark energy models), DES uses different probes, based on the data taken by DECam. Choosing probes that are sensitive to the geometry and the expansion rate of the Universe, as well as probes that are sensitive to the growth of structures is key, as we explained in Chapter 1. The four principal probes considered are:

- **type Ia supernovae**, which allow to test the expansion rate of the

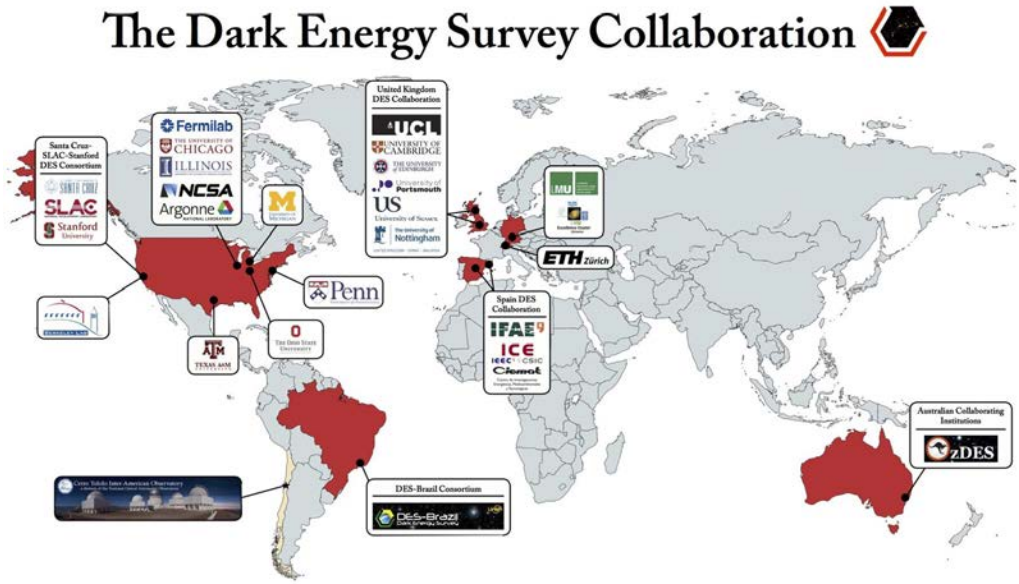

Figure 3.1: Map of the institutions involved in the Dark Energy Survey. Credit: Judit Prat.

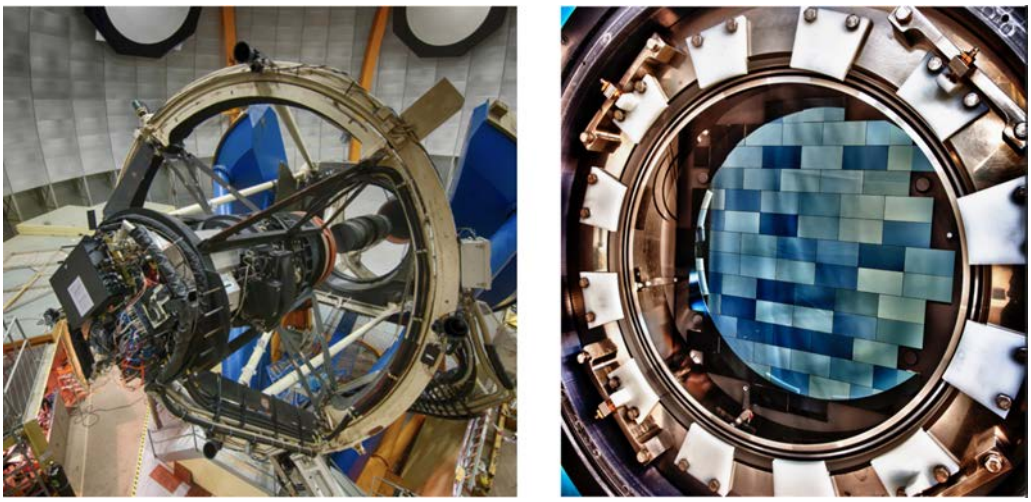

Figure 3.2: The 570-Megapixel digital camera DECam mounted at the Blanco Telescope at the Cerro Tololo Inter-American Observatory in Chile. 12 out of its 74 CCDs are used for guiding and focus, while the remaining 62 are used for imaging. Credit: Reidar/Hahn/Fermilab.

Universe. These objects are "standard candles", as their luminosity is known (after some calibration) when they reach their bright phase. This allows to measure their luminosity distance from their measured apparent magnitudes. A comparison between the redshift and the luminosity distance of a large number of supernovae allows to derive the history of the expansion of the Universe.

- **Baryonic Acoustic Oscillations (BAO)**, which are the fluctuations in the baryonic matter density field caused by acoustic density waves in the primordial photo-baryon plasma. These fluctuations in the early Universe have left an imprint in the large scale structure of the Universe at later stages, which can be observed and measured as an overdensity of galaxies at a very specific scale. This scale, which can be interpreted as the maximum travelling distance of the acoustic waves in the primordial plasma, can be computed from theoretical arguments and represents a "standard ruler". As its value depends on the cosmological model and on the values of the cosmological parameters, it can be used to constrain the properties of dark energy.

- Counting **galaxy clusters** is a sensitive probe of the history of growth and geometry of the Universe. The density and the formation of structures over cosmic time depends on the dark energy properties and the matter content of the Universe; therefore, the number density of galaxy cluster, as a function of cluster mass and redshift, is a sensible observable to constrain cosmological parameters values and more in general, to discriminate between different cosmological models.

- **Weak gravitational lensing** (Chapter 2): the deflection of light trajectories due to the effect of the gravitational fields generated by the large scale structure of the Universe. It allows to map the mass content of the Universe as a function of cosmic time, but it is also sensitive to the geometry of the Universe and, in turn, to the amount and the properties of dark energy.

While DES uses the four different probes to learn about dark energy, this thesis focuses on the last probe, the weak gravitational lensing. In particular, this thesis makes use of the data gathered over the first three years of observations (DES Y3) of DECam. The DES Y3 data represent a significant increase in total area compared to the Y1 data: the effective area reaches the nominal goal of $\sim$5000 deg^2, overtaking the $\sim$1800 deg^2 analysed in DES

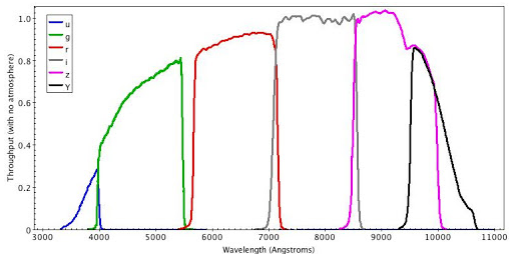

Figure 3.3: Standard bandpasses for the DECam g, r, i, z and Y filters. The bandpasses represent the total system throughput, including atmospheric transmission (airmass=1.2) and the average instrumental response across the science CCDs (Abbott et al., 2018)

.

Y1 (see Fig. 3.4). While the DES Y3 data are not as deep as we expect for the final DES sample, the number of shapes used for the weak lensing analysis in DES Y3 is already $\sim$ 120 million, making it the largest weak lensing survey up-to-date.

In the next two sections we will review two crucial techniques for DES (and for photometric surveys in general): the procedure to estimate the shear field from measured galaxy shapes and how to estimate the photometric redshift of galaxies. In particular, we will describe the procedures implemented in the DES Y3 analysis.

3.1 Shear estimation

Any weak lensing analysis relies on an estimate of the shear field across a part of the sky. The shear field is usually estimated from an ensemble of measured galaxy shapes. In order to beat down the contribution due to the intrinsic shape of galaxies (usually referred to as "shape noise"), a large number of faint galaxies is measured, which poses a number of observational and theoretical challenges. Briefly, we can divide the process of estimating the shear field from the observed images in two steps:

- Inferring galaxy shapes (and galaxy properties) from observed images. This involves implementing algorithms to detect sources, remove (i.e. deconvolve) the effects of the PSF, and measure the galaxy properties efficiently;

- inferring the shear field from the measured galaxy properties. This

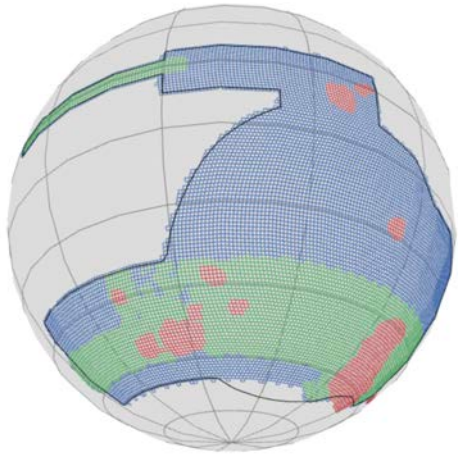

Figure 3.4: Footprint of the DES Y3 shear catalogue. The Y3 catalogue is shown in blue. For comparison the SV and Y1 footprints, which are nearly subsets of the Y3 are, are overplotted in red and green respectively.

.

includes a calibration phase through the use of image simulations in case the shear field estimator was biased (as in basically all the cases).

3.1.1 Detection

In the detection step objects are usually identified by detecting peaks above a given threshold (see, e.g., Source Extractor, Bertin & Arnouts 1996a). In DES, each patch of the sky is observed multiple times[1], and single-epoch images are co-added by a weighted average so that the global S/N is improved and the effect of transient imaging artifacts is mitigated. Sources are identified by imposing a threshold on a nonlinear combination of the r, i, and z co-added images[2]

[1]For DES Y3, the full footprint has been observed 6-7 times. Different exposures are slightly dithered (i.e., shifted) to reduce the impact of systematics related to the instrument response.

[2]In DES Y3, r, i, and z co-added images are combined using a variation of the combination method proposed by (Bertin, 2010), where the pixel value of a combined image is $\chi = \sqrt{(\sum w_i f_i^2)/n}$, with f_i the background-subtracted pixel value, w_i the weight of the pixel in a given co-added image, and n the number of inputs. Objects are detected by applying a 1.5 S/N threshold on the value of the pixels of the combined image.

The detection step can be affected by the problem of "blending", which refers to the case where the light of a brighter object influences a fainter neighbour. Not only does blending affect the inferred properties (e.g., their shapes) of a faint neighbour, but it can also prevent its detection, if the two objects are sufficiently close. This can result in shear biases (and photo-z biases, if the two objects are at different redshift). Blending is a very complicated problem; despite different strategies to mitigate blending effects, the DES Y3 analysis ultimately relies on sophisticated image simulations to quantify the bias induced by blends.

3.1.2 PSF

After detecting the objects, the image must be deconvolved with the point spread function (PSF). The PSF describes the response of an imaging system to a point source or point object. Any observed image will be the result of a convolution between the PSF and the incoming photons wave front. In order to recover the true image, an accurate modeling of the PSF is mandatory.

The PSF model is usually calibrated using point-like objects, i.e. stars. Different phenomena contribute to the total PSF, which further depends on the wavelength range of observations and on whether the telescope is observing from Earth or from space. In case of a Earth-based telescope, we can identify the following contributors to the total PSF:

- atmospheric PSF. This term includes all the effects responsible for the distortion of the image caused by the atmosphere. Incoming photons are scattered due to local differences in the refraction index of the atmosphere due to turbulence (seeing). The problem is exacerbated when the source of the photons is not monochromatic, due to the wavelength dependence of the seeing (e.g Meyers & Burchat 2015). Moreover, the refraction index n varies between the entrance in the atmosphere ($n \sim 1$) to the location of the telescope ($n > 1$), and this change depends on the zenith angle and on the wavelength of the incoming photons, generally causing a flattening of the image (the so called "differential chromatic refraction"). Seeing is the dominant contributor to the atmospheric PSF for DES, with chromatic effects being negligible. The process is stochastic, and can spatially vary over a large range of angular scales; chap

- detector pixel response. Ideally a top-hat function, it is convolved with the other PSF components. Detector non-idealities can cause prob-

lems that cannot be treated as a simple convolution. For instance, flux-dependent effects causing bright, saturated objects to have larger size (the so called "brighter-fatter effect", Antilogus et al. 2014). Electric fields transverse to the surface of the CCD can also displace the charges in the detector, causing features as rings or stripes near the detector edges (Plazas et al., 2014b,a) and potentially inducing spurious coherent patterns in the images.

DES uses an empirical method to estimate the PSF. Empirical methods usually choose a basis for the PSF model (with common choices being the Gaussian, Moffat or Kolmogorov functions for the radial profile) and fit the parameters of the model using a set of stars. For the DES Y3 analysis, a more flexible model is used involving a grid of pixels of 0.3 arcsec on a side, each with an independent amplitude at their centers. The amplitudes of the PSF between pixel centers are found using Lanczos interpolation. The interpolation between stars positions is then performed using a 3rd order polynomial basis. A different PSF model is estimated for each exposure (and therefore, for each band). Contrary to the strategy adopted in the DES Y1 analysis, the PSF is estimated in sky coordinates rather than in image coordinates. The PSF model is indeed smother in sky coordinates and this also allows to more easily correct for features like tree rings that would have needed otherwise to be included in the PSF modeling. An incorrect modeling of the PSF can cause both additive and multiplicative biases in the estimated shear signal (see §X).

3.1.3 DES: shear estimation and METACALIBRATION

To estimate the shear field, DES (as many other surveys) uses measured galaxy shapes as a proxy. This usually involves assigning a set of numbers to each galaxy describing the observed galaxy light profile, once having assumed a galaxy model. If the model is not adequate this procedure can induce biases (the so called "model bias", Voigt & Bridle 2010; Melchior et al. 2010). The presence of noise can also bias the galaxy parameters estimation when maximum-likelihood methods are used ("noise bias"[3], Melchior & Viola 2012a; Refregier et al. 2012a), with galaxies with low signal-to-noise ratio being particularly affected.

[3]Noise bias arises from the fact that ellipticity is not a linear function of pixel intensities in the presence of noise and PSF. This bias would vanish in case of a linear model, which is not the case of shape measurements.

In the case of DES Y3, a galaxy model is simultaneously fitted to all available epochs and bands for any detected object. The model is convolved by the local PSF in each single-epoch image, and a χ^2 sum is computed over all pixels and over multiple exposures/bands. A maximum-likelihood approach allows to find the best fit parameters of the galaxy model. During the fit, the light from neighbours is masked out (Jarvis et al., 2016).

Due to the aforementioned issues (the "model bias" and "noise bias"), the galaxy shapes inferred by the above procedure cannot be directly used as a proxy for the shear field, as it would represent a biased estimator. In the DES Y3 analysis we therefore used as a shear estimation algorithm the `METACALIBRATION` algorithm (Huff & Mandelbaum, 2017; Sheldon & Huff, 2017), which allows to self-calibrate the shear estimation process through a manipulation of real images.

`METACALIBRATION` assumes that we have a noisy and biased measurement of the shear field $\boldsymbol{e}$ that needs to be calibrated to obtain an unbiased measurement of the shear field $\boldsymbol{\gamma}$. In the weak lensing regime (i.e. small shears), we can write:

$$\begin{aligned} \boldsymbol{e} &= \boldsymbol{e}|_{\gamma=0} + \left.\frac{\partial \boldsymbol{e}}{\partial \boldsymbol{\gamma}}\right|_{\gamma=0} \boldsymbol{\gamma} + ... \\ &\equiv \boldsymbol{e}|_{\gamma=0} + \boldsymbol{R}_{\boldsymbol{\gamma}} \boldsymbol{\gamma} + ... \end{aligned} \tag{3.1}$$

where we have defined the *shear response matrix* $\boldsymbol{R}_{\boldsymbol{\gamma}}$. In what follows we will drop higher order terms[4], and assume the ellipticities in the absence of lensing $\boldsymbol{e}|_{\gamma=0}$ average to zero.

Given an ensemble of measurements $\{\boldsymbol{e}_i\}$ and responses $\{\boldsymbol{R}_{\boldsymbol{\gamma} i}\}$, we can form unbiased statistics of the shear $\boldsymbol{\gamma}$. For example, to measure an estimated mean shear $\boldsymbol{\gamma}^{\mathbf{est}}$ we can write

$$\langle \boldsymbol{\gamma}^{est} \rangle \approx \langle \boldsymbol{R}_{\boldsymbol{\gamma}} \rangle^{-1} \langle \boldsymbol{e} \rangle \tag{3.2}$$

where the averages for $\boldsymbol{e}$ and $\boldsymbol{R}_{\boldsymbol{\gamma}}$ are taken over the ensemble of measure-

[4]The next order term is $\propto \gamma^3$ (Sheldon & Huff, 2017); for large shears, such as in the case of tangential shear measurements near the centers of galaxy clusters (e.g., McClintock et al. (2019)), it can introduce a $\sim$ per cent bias, but it can be safely neglected here.

ments, e.g.

$$\langle \boldsymbol{e} \rangle = \frac{1}{N} \sum_i \boldsymbol{e}_i$$
$$\langle \boldsymbol{R}_{\boldsymbol{\gamma}} \rangle = \frac{1}{N} \sum_i \boldsymbol{R}_{\boldsymbol{\gamma}_i} \tag{3.3}$$

The shear estimate $\boldsymbol{\gamma}^{\mathbf{est}}$ is a *weighted* mean of true shear $\boldsymbol{\gamma}$, with weights $\boldsymbol{R}_{\boldsymbol{\gamma}}$. Responses can also be derived for other statistics of the shear (see Appendix B.1 for a generalisation of the formalism to the case of shear 2-point functions and in the case of intrinsic alignment).

For METACALIBRATION, the response matrix $\boldsymbol{R}_{\boldsymbol{\gamma}}$ is measured using finite difference derivatives. The derivative is calculated by producing versions of the image that have been sheared by small amounts $\pm\gamma \sim 0.01$, and repeating the measurement $\boldsymbol{e}$ on those sheared images. Central finite difference estimate is used:

$$R_{i,j} = \frac{e_i^+ - e_i^-}{\Delta\gamma_j}, \tag{3.4}$$

In order to perform this shearing, the image must be deconvolved by the PSF, sheared, and reconvolved by the PSF. Because the reconvolution results in a different PSFs, the basic ellipticity measurement used as the shear estimator must be performed on a similarly reconvolved but unsheared image. To optimise computational efficiency, the DES Y3 implementation of `METACALIBRATION` deconvolves the original image by the complete PSF solution, but then it uses a simplified single Gaussian model and Gaussian PSF to fit the detected objects in the sheared images. The `METACALIBRATION` has been shown to calibrate also for the biases introduced by this simplified model Sheldon & Huff (2017). Shear responses are of order $\boldsymbol{R}_{\boldsymbol{\gamma}} \approx 0.6$ for typical galaxies in DES, although the value depends on the details of the measurements such as object signal-to-noise ratio (S/N) and size relative to the PSF.

Usually, shear catalogues are defined applying additional ("selection") cuts on a catalogue of detected objects. For DES Y3, objectes are selected based on their signal-to-noise and size ratio (the ratio between the object size and the PSF size). On top of this, objects are assigned to different tomographic bins depending on their photometric redshift estimate. Any selection that - more or less implicitly - is based on the galaxies shape and or size can potentially introduce shear biases. If the details of the detection algorithm slightly prefer galaxies with a particular alignment with respect

to the shear field or to PSF anisotropies, the hypothesis that galaxy intrinsic shapes are randomly oriented will be violated, introducing biases. In this respect, METACALIBRATION can take into account most of the effects induced by selection cuts. As done for the DES Y1 shear catalogue, selection effects are taken into account by means of an ensemble selection response $\langle R_S \rangle$. This quantity is estimated by selecting the sample using sheared quantities (signal-to-noise, size ratio, and photometric redshift estimated from sheared fluxes, Huff & Mandelbaum 2017):

$$R_{S,i,j} = \frac{e_i^{s+} - e_j^{s-}}{\Delta\gamma_j}. \tag{3.5}$$

The total response is $R = R_\gamma + R_S$. The contribution of R_S to the total response is typically of few percent. Averages are then performed using the total response, which self-calibrate the shear estimator:

$$\langle \boldsymbol{\gamma}^{est} \rangle = \langle \boldsymbol{R} \rangle^{-1} \langle \boldsymbol{e} \rangle \tag{3.6}$$

As noted in Sheldon & Huff (2017), the total ensamble response matrix $\langle \boldsymbol{R} \rangle$ is, to good approximation, diagonal: as a consequence, the response correction reduces to element-wise division.

3.1.4 Remaining biases in the shear estimator

Shear catalogues are usually validated through a battery of null-tests or using sophisticated image simulations, to unveil remaining systematic and/or observational biases. This also applies to the DES Y3 METACALIBRATION shear catalogue; despite its self-calibration procedure, small multiplicative and additive biases are expected to persist, for a number of reasons. Following the standard notation introduced by Mandelbaum et al. (2014), we can write an estimate of the shear as:

$$\gamma_i^{\rm est} = m_i \gamma_i^{\rm true} + c_i \tag{3.7}$$

where m_i and c_i are the per-component multiplicative and additive biases, and $\gamma_i^{\rm est}$ is the value of the shear field estimated from the METACALIBRATION procedure. For instance, if the PSF is misestimated, both multiplicative and additive biases are expected (if the size of the PSF is misestimated, a multiplicative bias will occur; if the ellipticity of the PSF is misestimated, an additive bias will occur that is related to the PSF orientation). METACALIBRATION assumes a perfect knowledge of the PSF model, so any

PSF misestimation will clearly affect the performance of the algorithm. `METACALIBRATION`, in its DES Y3 implementation, do not self-calibrate blends (Sheldon et al., 2019), which induce a multiplicative bias of the order of 2-3 per cent (MacCrann et al., 2020), to be calibrated against simulations. In general, additive biases can be spotted by devising and performing null-tests on the catalogue itself (i.e, by measuring quantities whose dependence on the shear signal is expected to vanish). On the other hand, multiplicative biases are better estimated through the use of image simulations where the true shear signal is known, as it is hard to disentangle the effect of the shear field from potential multiplicative systematics in data. We will discuss in more depth the systematic null tests for the DES Y3 shear catalogue in Chapter 5, also providing an overview of the tests performed with the official DES Y3 image simulations.

3.2 Redshift estimation

Galaxy surveys like DES map the angular position of million of galaxies in the sky; the radial information along the line of sight is retrieved from a measure of the redshift of each single galaxy. Redshift (§ 1.4.1) is crucial to any cosmological analysis, as the redshift distribution of the sample of galaxies under study is usually needed to model the observables (like, e.g., cosmic shear or galaxy clustering).

There exist different ways to estimate the redshift of a galaxy (or a sample of galaxies):

- **spectroscopic redshift** (spec-z). The spectroscopic redshift is obtained by measuring the spectral energy distribution (SED) of a galaxy (i.e, the flux distribution in wavelength space) with a spectrograph. Features in the spectrum, as emission or absorption lines, need to be identified and their wavelengths need to be compared to the ones of a galaxy spectrum in the rest frame following Eq. 1.38. Measuring galaxy spectra is a time-consuming process, and spectroscopic surveys are limited to fewer, brighter objects compared to phomotetric surveys;

- **photometric redshift** (photo-z). In imaging surveys, redshift must be inferred from the SED integrated over a number of filter bands. This is a less accurate process, as 1) spectral features like emission

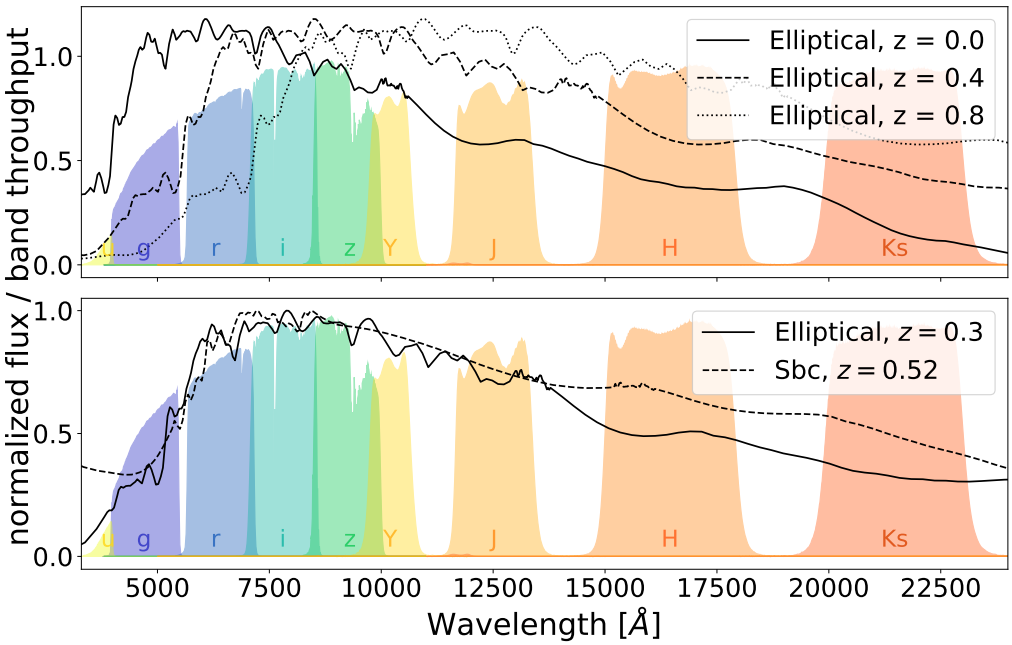

Figure 3.5: *Top*: rest-frame template of an elliptical galaxy redshifted at z = 0.4 and z = 0.8. These objects exhibit clearly different colours. *Bottom*: templates of an elliptical galaxy and a Sbc galaxy at different redshifts. In the *griz* bands those two objects are nearly indistinguishable, due to the degeneracy between galaxy type and redshift (Buchs et al., 2019)

or absorption liners cannot be detected anymore 2) two different rest-frame SEDs at two different redshifts can be indistinguishable, depending on the broadbands considered (see Fig. 3.5). Generally photo-z techniques fall into two categories: *template fitting* and *machine learning* techniques. In the template fitting methods, the measured broadband galaxy SED is compared to a library of redshifted galaxy template SEDs. In machine learning methods, a machine learning algorithm that infers redshift from a set of broadband fluxes is trained using a small (but representative when possible) spectroscopic sample, and then applied to the galaxy sample of interest.

- **clustering redshift** (WZ). Clustering-based redshift methods have met with success in the past years providing alternative ways to standard photo-z methods to infer redshift distributions. In short, clustering-based methods exploit the two-point correlation signal between a photometric sample and a "reference" sample of high-fidelty-redshift galaxies divided into thin bins to infer the redshift distributions of the photometric sample. One of the biggest advantage of clustering-based methods is that that the reference sample does not have to be a representative sample of the photometric sample.

In the DES Y3 analysis we use an hybrid approach to estimate redshift distributions which combine three different methods. In particular, we obtain a first estimate of the redshift distributions using a photometric method called "SOMPZ" (Buchs et al., 2019). The SOMPZ method uses spectroscopic information and data from a number of deep fields (DES collaboration, 2020b) where additional photometry in the infrared bands and u-band is available, besides the the standard 5-band ($grizY$) photometry available in the DES wide field. This additional information is used to break the degenerancies in the photo-z estimates of the DES wide field galaxies (which have fewer bands available). This is achieved by creating Self Organizing Maps (SOM, Kohonen, 1982) for the spectroscopic, deep and wide fields; a mapping of the spectroscopic redshifts to the deep SOM is first obtained and then it is followed by a mapping from the deep to the wide SOM. The SOMPZ methods provides a number of realisations of the redshift distributions, which should encompass the statistical and systematic uncertainties of the methods. We then filter those realisations using a clustering-based approach, selecting those that maximise a joint likelihood with clustering redshift estimates. This part of the analysis is explored in more details in Chapter 4. Finally, during the process of inferring cosmological parameters,

an extra constrain on the redshift distributions is provided by the "shear-ratio" test (Prat et al., 2018; DES collaboration, 2020d), which exploits the strong redshift dependence of ratios of galaxy-galaxy lensing signals that consider the same lens population but difference source samples.

Part II

Clustering-based Redshift Estimates

In this part we use simulations and data from the Dark Energy Survey to calibrate the fiducial DES Y3 photo-z redshift distributions using clustering-based techniques. The work presented in this Chapter is going to be published in Gatti & Giannini, et al. (DES collaboration) together with the DES Y3 cosmological release. The tools developed here represent the natural continuation of the DES Y1 clustering-redshift strategy, published in three papers but not discussed in this thesis (Gatti & Vielzeuf, et al, 2018; Davis, Gatti, et al. 2018; Cawthon, Davis, Gatti, et al. 2018).

Chapter 4

Calibrating DES Y3 redshift distributions with cross-correlations

4.1 Introduction

The DES Y3 Key Project (DES collaboration, 2020a) is planned to contrain cosmological parameters by combining three different measurements of two-point correlation functions: cosmic shear (Secco et al., 2020; Amon et al., 2020), galaxy-galaxy lensing (DES collaboration, 2020d), galaxy clustering (DES collaboration, 2020c). The cosmic shear measurement probes the angular correlation of more than 100,000,000 galaxy shapes from the weak lensing sample (Gatti et al., 2020), divided into four tomographic bins. The cross correlation of galaxy shapes and the positions of 1,000,000 red luminous galaxies identified by the *redMaGiC* algorithm (Rozo et al., 2016) are measured by galaxy-galaxy lensing. Lastly, galaxy clustering measures the auto correlation of the positions of *redMaGiC* galaxies.

The correct cosmological interpretation of these measurements relies on an accurate estimate of the redshift distributions of the samples, which can otherwise lead to biases in the inferred cosmological parameters (e.g. Huterer et al., 2006; Hildebrandt et al., 2012; Hoyle et al., 2018). Photometric surveys have been relying on different methodologies to derive redshift distributions (Hildebrandt et al., 2010; Sánchez et al., 2014), mostly based on galaxies' multi-band photometry (photo-z methods). However, these methods are plagued by a number of issues (ranging from the spectroscopic samples used for both training and calibration being incomplete, to SED

templates being inadequate; Lima et al. 2008; Newman et al. 2015; Bezanson et al. 2016; Masters et al. 2017) and are ultimately limited by the fact that any mapping from a set of photometric observables to redshift can be ambiguous. In this respect, systematics in the redshift distributions estimates have been recently called into play to explain the discrepancies among some recent weak lensing analyses (Joudaki et al., 2019; Asgari et al., 2019b; Wright et al., 2019).

Clustering-based redshift methods (Newman, 2008; Ménard et al., 2013; Davis et al., 2017; Morrison et al., 2017; Scottez et al., 2017; Johnson et al., 2017; Gatti et al., 2018) have met with success in the past years to provide an alternative way to infer redshift distributions with respect to standard photo-z methods. In short, clustering-based methods exploit the two-point correlation signal between a photometric "unknown" sample and a "reference" sample of high-fidelty redshift galaxies divided into thin bins, to infer the redshift distributions of the photometric sample. One of the biggest advantage of clustering-based methods is that that the reference sample does not have to be a representative sample of the photometric sample. Clustering-based methods (or clustering-z) have been in the past years successfully applied to both data (Hildebrandt et al., 2017; Johnson et al., 2017; Davis et al., 2017, 2018; Cawthon et al., 2018; Bates et al., 2019) and simulations (Schmidt et al., 2013; Scottez et al., 2017; Gatti et al., 2018), and they represent one credible alternative to standard photo-z methods for the new, upcoming generation of data sets (Scottez et al., 2017).

Depending on the particular application, cross-correlation methods have been used to provide an independent estimate of the redshift distributions or they have been used to calibrate other distributions inferred from photo-z methods. In the DES Y1 cosmological analysis we opted for the latter approach (Davis et al., 2017; Hoyle et al., 2018). In particular, we used high quality photometric redshifts provided by *redMaGiC* galaxies (Rozo et al., 2016) to measure the clustering-z signal with the weak lensing (WL) sample. The choice of using high quality photometric redshifts rather than spectroscopic redshifts was dictated by the higher statistical power of the *redMaGiC* sample, owing to the large number of *redMaGiC* galaxies ($650,000$ for DES Y1) in the DES footprint. Due to the limited redshift range of the *redMaGiC* sample, clustering-z estimates could not have been used on their own, but they have been used to calibrate the mean redshift of the distributions measured by other DES photo-z methods.

The calibration strategy of the DES Y3 weak lensing redshift distributions improves upon on the DES Y1 strategy outlined in Gatti et al. (2018)

on different aspects. We explore two different methods to calibrate redshift distributions from other photo-z codes using the clustering information: a method that mostly focuses on calibrating the mean redshift of the distributions (which is similar to what has been done in the DES Y1 analysis), and a second method that calibrates the full shape of the distributions. Furthermore, we improve the modelling of the clustering signal, accounting for the redshift evolution of the galaxy-matter bias of the reference sample and the clustering of the underlying dark matter density field, a fact that has been neglected in the DES Y1 analysis and accounted for only at the level of the systematic uncertainty of the method. In the second method that calibrates the shape of the redshift distributions, we also marginalise over magnification effects. Finally, we use a combination of two different reference samples: *redMaGiC* galaxies with high-quality photometric redshifts and a spectroscopic sample from the BOSS (Baryonic Oscillation Spectroscopic Survey, Dawson et al. 2013) and from the eBOSS (extended-Baryon Oscillation Spectroscopic Survey, Ahumada et al. 2019) surveys. We note that in the DES Y1 calibration strategy only *redMaGiC* galaxies have been used. ON one hand, *redMaGiC* galaxies span the full DES Y3 footprint and are characterised by a higher number density compared to BOSS and eBOSS galaxies, which only cover a small portion of the footprint; on the other hand, the latter sample spans a wider redshift range and have better redshift estimates, which makes the combination of the two samples desirable.

The fiducial photo-z estimates for the DES Y3 weak lensing sample are provided by a self-organizing maps based scheme (hereafter SOMPZ, Buchs et al. 2019; Myles et al. 2020). The SOMPZ method provides for each tomographic bin a number of posterior samples of the redshift distributions which encompass systematic and statistical uncertainties. These realisations are sampled over when estimating the cosmological parameters in the fiducial DES Y3 cosmological analysis. In this context, we use clustering redshift estimates to provide priors for the SOMPZ realisations.

We note that there exist other strategies to combine clustering-based and photo-z estimates. E.g., Sánchez & Bernstein (2019) and Alarcon et al. (2019) showed how to combine photo-z and clustering-based estimates in a principled way using a hierarchical Bayesian model (Leistedt et al., 2016). The application of this method to DES data is left to future works.

This Chapter is organised as follows. In § 4.2 we describe the methodology used in DES Y3 to calibrate photo-z posteriors using clustering-based redshift estimation. The simulations and the data sets used in this Chapter

are described and compared in § 4.3. In § 4.4 we perform extended tests in simulations assessing the systematic uncertainties of the methods. The clustering-based calibration of DES Y3 data is presented in § 4.5. Finally, in § 4.6 we discuss future prospects for clustering-z methods and present our conclusions.

4.2 Methodology

In the DES Y3 analysis we use clustering-based redshift estimates as a prior for the photo-z posterior distributions of a given science sample. We defer the description (and the choice of the binning) of the particular samples adopted in this work to § 4.3, while keeping the description of the methodology as general as possible. Here, "unknown" always refers to the photometric galaxy sample we wish to calibrate, whereas "reference" refers to the galaxy sample with known, highly accurate redshifts (be they spectroscopic or photometric).

4.2.1 First step: modelling the cross correlation signal and recovering the clustering-based redshift estimates

Clustering-based methods rely on the assumption that the cross-correlation between two samples of objects is non-zero only in case of 3D overlap. Let us consider two samples:

1. An *unknown* sample, whose redshift distribution $n_{\rm u}(z)$ has to be recovered.

2. A *reference* sample, whose redshift distribution $n_{\rm r}(z)$ is known (either from spectroscopic redshifts or from high-precision photometric redshifts). The reference sample is divided into narrow redshift bins.

To calibrate the redshift distribution of the unknown sample we bin the reference sample into narrow redshift bins, and then compute the angular cross-correlation signal $w_{\rm ur}$ between the unknown sample and each of these reference redshift bins. Under the assumption of linear biasing, we find

$$w_{\rm ur}(\theta) = \int dz' \; n_{\rm u}(z') n_{\rm r}(z') b_{\rm u}(z') b_{\rm r}(z') w_{\rm DM}(\theta, z') + M(\theta), \tag{4.1}$$

where $n_{\rm u}(z')$ and $n_{\rm r}(z')$ are the unknown and reference sample redshift distributions (normalised to unity over the full redshift interval), $b_{\rm u}(z')$ and $b_{\rm r}(z')$ are the biases of the two samples, and $w_{\rm DM}(\theta, z')$ is the dark matter 2-point correlation function. The term $M(\theta)$ refers to the contribution to the angular correlation function due to magnification effects.

In our methodology, we use a "1-point estimate" of the correlation function. In practice, the correlation function is measured as a function of angle and then it is averaged over angular scales via

$$\bar{w}_{\rm ur}(z) = \int_{\theta_{min}}^{\theta_{max}} d\theta \; W(\theta) w_{\rm ur}(\theta, z), \tag{4.2}$$

where $W(\theta) \propto \theta^{-\gamma}$ is a weighting function[1]. We assume $\gamma = 1$ to increase the S/N of the mesurements. The integration limits in the integral in Eq. 4.2 correspond to fixed physical scales. We use the Davis & Peebles (Davis & Peebles, 1983) estimator for the cross-correlation signal,

$$\bar{w}_{\rm ur}(r) = \frac{N_{Rr}}{N_{Dr}} \frac{D_{\rm u}D_{\rm r}(r)}{D_{\rm u}R_{\rm r}(r)} - 1, \tag{4.3}$$

where $D_{\rm u}D_{\rm r}(r)$ and $D_{\rm u}R_{\rm r}(r)$ are respectively data–data and data–random pairs. The pairs are properly normalised through N_{Dr} and N_{Rr}, corresponding to the total number of galaxies in the reference sample and in the reference random catalogues. As done in Gatti et al. (2018), we use the Davis & Peebles estimator rather than the Landy & Szalay estimator (Landy & Szalay, 1993) since the former involves using a catalogue of random points for just one of the two samples. This allows us to avoid creating high-fidelity random catalogues for the DES Y3 source galaxy sample whose selection function is very complex. For our analysis, we only rely on random points for the reference sample, whose selection function and mask are well understood (DES collaboration, 2020c).

Assuming the reference sample is divided into sufficiently narrow bins centered at z_i, we can approximate $n_{{\rm r},i}(z) \propto N_{\rm r}\delta_D(z - z_i)$ (with δ_D being Dirac's delta distribution, and $N_{\rm r}$ being the number of galaxies in the reference bin). Hence, Eq. 4.1 becomes:

$$\bar{w}_{\rm ur}(z_i) \approx n_{\rm u}(z_i) b_{\rm u}(z_i) b_{\rm r}(z_i) \bar{w}_{\rm DM}(z_i) + \bar{M}(z_i), \tag{4.4}$$

[1]In the DES Y1 analysis (Gatti et al., 2018) we used a slightly different estimator for the "1-point estimate" of the correlation function. In particular, rather than weighting the correlation function directly, we weighted the data-data and the data-random pairs counts of the correlation function estimator individually. This has been changed in the DES Y3 analysis, as this estimator is slightly faster to compute.

where barred quantities indicate they have been "averaged" over angular scales, reflecting the fact that we are using 1-angular bin estimates of the correlation function. In what follows, for simplicity, we will drop the barred notation. We note that in Eq. 4.4 we assumed the galaxy-matter biases to be described by a single number at all scales; this is true at large scales in the linear regime, but we do not expect this to necessary hold at the small scales used in this work[2]. The linear bias assumption is likely to introduce a small systematic uncertainty that needs to be quantified. If the quantities $b_{\rm r}(z_i)$, $b_{\rm u}(z_i)$, $w_{\rm DM}(z_i)$, $M(z_i)$ evolve with redshift, they need to be characterised to correctly recover the redshift distribution of the unknown sample. We turn now to how to model or estimate these terms.

- **The galaxy-matter bias evolution of the reference sample** $b_{\rm r}(z)$. As long as the redshifts of the reference sample are accurate enough, we can estimate $b_{\rm r}(z)$ by measuring the 1-point estimate of the autocorrelation function of the reference sample divided into thin redshift bins centered at z_i:

$$w_{rr}(z_i) = \int dz' \left[b_{\rm r}(z') n_{r,i}(z')\right]^2 w_{\rm DM}(z'). \tag{4.5}$$

  If the bins are sufficiently narrow so as to consider the biases and $w_{\rm DM}$ constant over the distributions, they can be pulled out of the above integrals.

$$w_{rr}(z_i) = b_{\rm r}^2(z_i) w_{\rm DM}(z_i) \int dz' n_{r,i}^2(z'), \tag{4.6}$$

  Knowledge of the redshift distributions of the narrow bins is then required to use Eq. 4.6 to estimate $b_{\rm r}(z_i)$. If the reference sample is binned into bins with equal widths, the integral over the reference bins distributions squared little change with redshift and can be considered constant. Last, we need to model $w_{\rm DM}(z)$ to correctly recover $b_{\rm r}(z)$.

- **The galaxy-matter bias evolution of the unknown sample** $b_{\rm u}(z)$. In principle, it could be estimated similarly to the bias of the reference sample. The limiting factor that prevents us from using the autocorrelation functions to estimate the galaxy–matter biases evolution for the unknown sample is the poor photo-z quality of the unknown sample. This is the only term we are not going to model in what follows.

[2]In the non linear regime, the fact that the terms inside the integral factorizes into $b_{\rm r}(z_i) b_{\rm u}(z_i) w_{\rm DM}(z_i)$ is not guaranteed and can introduce a small systematic uncertainty.

- **The dark matter 2-point correlation function** $w_{\rm DM}(z)$. This can be modeled assuming a given cosmology and a non linear power spectrum. At fixed z_i, this can be written as:

$$w_{\rm DM}(z_i) \;=\; \int d\theta W(\theta) \int \frac{dl\ l}{2\pi} J_0(l\theta) \frac{1}{\chi(z)^2 H(z)} P_{\rm NL}\left(\frac{l+1/2}{\chi}, z_i\right), \tag{4.7}$$

  where χ is the comoving distance, $H(z)$ is the Hubble expansion rate at redshift z, J_0 is the zeroth order Bessel function, and $P_{\rm NL}(k,\chi)$ is the 3D non linear matter power spectrum at wavenumber k (which, in the Limber approximation, is set equal to $(l+1/2)/\chi$) and at the cosmic time associated with redshift z_i. We found that the redshift evolution of $w_{\rm DM}(z_i)$ little depends on the particular value of cosmological parameters, so in the following we will compute this term at fixed cosmology (we assumed the *Planck* values, Planck Collaboration 2018).

- **Magnification effects** $M(z_i)$. Magnification (Narayan, 1989; Villumsen et al., 1997; Moessner & Jain, 1998) can lead to a change in the observed spatial density of galaxies: the enhancement in the flux of magnified galaxies can locally increase the number density, as more galaxies pass the selection cuts/detection threshold of the sample; at the same time, the same volume of space appears to cover a different solid angle on the sky, generally causing the observed number density to decrease. The net effect is driven by the slope of the luminosity function, and it has an impact on the measured clustering signal. Considering only the dominant terms, this can be written as:

$$M(z) = \int d\theta W(\theta) \int \frac{dl\ l}{2\pi} J_0(l\theta) \int \frac{d\chi}{\chi^2 H(z)} \times \left[b_{\rm r}\alpha_{\rm u} q_\delta^u q_\kappa^r + b_{\rm u}\alpha_{\rm r} q_\delta^u q_\kappa^r\right] P_{\rm NL}\left(\frac{l+1/2}{\chi}, z(\chi)\right), \tag{4.8}$$

  where the terms q_δ and q_κ read:

$$q_\delta(\chi) = \frac{n_(z(\chi'))}{n} \frac{dz}{d\chi'}, \tag{4.9}$$

$$q_\kappa(\chi) = \frac{3H_0^2\Omega_\mathrm{m}\chi}{c^2 a(\chi)} \int_\chi^{\chi(z=\infty)} d\chi' \frac{n(z(\chi'))}{n} \frac{dz}{d\chi'} \frac{\chi' - \chi}{\chi'}. \quad (4.10)$$

Under the approximation of thin bins, we can linearise Eq. 4.8 and write it using a discrete summation:

$$M(z_i) = b_\mathrm{r}(z_i)\alpha_\mathrm{u} \sum_{j>i} [D_{ij} n_\mathrm{u}(z_j)] + b_\mathrm{u}(z_i)\alpha_\mathrm{r}(z_i) n_\mathrm{u}(z_i) \sum_{j>i} D_{ij}, \quad (4.11)$$

with

$$D_{ij} = \frac{3H_0^2\Omega_\mathrm{m}}{c^2} w_\mathrm{DM}(z_i) \frac{\chi(z_i)}{a(z_i)} \frac{\chi(z_j) - \chi(z_i)}{\chi(z_j)}. \quad (4.12)$$

The term $\alpha \equiv 2.5s - 1$ is related to the slope s of the cumulative number counts evaluated at flux limit. The slope of the cumulative number counts is formally defined for a flux limited sample as

$$s = \frac{d log_{10} n(> m)}{dm}, \quad (4.13)$$

where $n(m)$ is the cumulative number counts as a function of magnitude m, and s is to be evaluated at the flux limit of the sample. For a sample which is not flux limited, evaluating the coefficient s is more complicated.

Under the assumption of thin reference bins, linear galaxy-matter bias, and using the linearised version of the equation describing magnification effects (Eq. 4.11) , Eq. 4.4 becomes a linear system of equations:

$$w_\mathrm{ur}(z_i) = n_\mathrm{u}(z_i) b_\mathrm{u}(z_i) b_\mathrm{r}(z_i) w_\mathrm{DM}(z_i) + b_\mathrm{r}(z_i)\alpha_\mathrm{u} \sum_{j>i} [D_{ij} n_\mathrm{u}(z_j)] + b_\mathrm{u}(z_i)\alpha_\mathrm{r}(z_i) n_\mathrm{u}(z_i) \sum_{j>i} D_{ij}. \quad (4.14)$$

If the values $b_\mathrm{r}(z_i)$, $b_\mathrm{u}(z_i)$, $w_\mathrm{DM}(z_i)$, $\alpha_\mathrm{r}(z_i)$, α_u are provided, it can be solved to obtain an estimate of $n_\mathrm{u}(z_i)$. This would be similar to standard clustering-based methods which use the cross correlation signal as a starting point to infer the redshift distributions of the unknown sample (Newman, 2008; Ménard et al., 2013; Schmidt et al., 2013; McQuinn & White, 2013).Alternatively, if an estimate of the $n_\mathrm{u}(z_i)$ is provided by, e.g., a photo-z method, it can be used to quickly evaluate the expected correlation signal $w_\mathrm{ur}(z_i)$ and compared to the one measured in data. This can be interpreted as a forward modelling approach (see e.g., Choi et al. 2016),

We note that in DES Y1 we did not model many of the terms described above. In particular, we assumed $b_{\rm r}(z_i)$, $b_{\rm u}(z_i)$, $w_{\rm DM}(z_i)$ to be constant as a function of redshift, and used simulations to estimate the systematic error induced by this assumption. We also did not model $M(z_i)$, but we decided to exclude the redshift range (i.e., the tails of the redshift distributions) where magnification effects are expected to have a non negligible impact.

4.2.2 Using the cross-correlation information

In DES Y3 we use the clustering information to provide a prior for the posterior distributions of a given photo-z code. In this Chapter, we consider two different approaches. Both approaches start assuming that a given photo-z code provides us a number k of $n_{\rm u}(z_i)$ estimates: $\{n_{\rm u}^{\rm pz,k}(z_i)\}$. E.g., in the DES Y1 analysis, such realisations were provided by a single $n_{\rm u}(z_i)$ estimate from the photo-z code BPZ (Benítez, 2000), shifted around their mean by a quantity Δz. The two approaches are described below.

- **Mean-matching method:** we select an interval around the mean of the redshift distribution such that we can neglect magnification effects. The exact definition of the interval is arbitrary; following what has been done in the DES Y1 analysis, we choose the interval $[\langle z\rangle_{\rm pz} - 2\sigma_{\rm pz}, \langle z\rangle_{\rm pz} + 2\sigma_{\rm pz}]$, where $\sigma_{\rm pz}$ is the root mean square of the redshift distribution $n(z)$ estimated from the photo-z code in the range where we have clustering estimates from the reference samples (see § 4.4.1 for more details). Starting from the cross correlation measurements $w_{\rm ur}(z_i)$, we estimate the redshift distribution using Eq. 4.14:

$$n_{\rm u}(z_i) = A\frac{w_{\rm ur}(z_i)}{b_{\rm r}(z_i)w_{\rm DM}(z_i)}, \tag{4.15}$$

  where A is a normalisation constant which has no relevant effect in this method. In the above equation the term $b_{\rm u}(z_i)$ does not appear as we cannot estimate it, and it must be compensated by an appropriate systematic uncertainty term. We then compare the mean of the clustering-based redshift distribution estimate with the mean of the distributions $\{n_{\rm u}^{\rm pz,k}(z_i)\}$ in the chosen interval. This is similar to what has been done in DES Y1, where we used clustering-based estimates to directly correct the mean of the posterior of a given photo-z code; the main difference is that now we further estimate the terms $b_{\rm r}(z_i)$ and $w_{\rm DM}(z_i)$ in the clustering-based redshift distributions.

Operationally, this method implies writing the following likelihood:

$$\mathcal{L}_{\langle \mathrm{z} \rangle} = -\frac{1}{2}\chi^2 \left(\langle z \rangle_{\mathrm{pz,k}};\ \langle z \rangle_{\mathrm{wz}};\ \hat{\Sigma}^{-1}_{\langle z \rangle_{\mathrm{wz}}} \right) + \mathrm{Prior}\left(\Delta_z\right). \tag{4.16}$$

In the above equation, $\langle z \rangle_{\mathrm{pz,k}}$ and $\langle z \rangle_{\mathrm{wz}}$ are the mean of the redshift distributions estimated by the k-th photo-z realisation and by the clustering-based method. The prior on the mean in Eq. 4.16 takes into account systematic uncertainties of the methods. The quantity $\hat{\Sigma}^{-1}_{\langle z \rangle_{\mathrm{wz}}}$ is the precision matrix of the clustering-based mean redshift measurement.

- **Shape-matching method:** we forward model the cross-correlation signal $\hat{w}_{\mathrm{ur}}(n^{\mathrm{pz,k}})$ using Eq. 4.14 and using as $n_{\mathrm{u}}(z_i)$ the k-th realisation provided by a given photo-z code. Then, we compute the likelihood with the measured cross-correlation signal $w_{\mathrm{ur}}(z_i)$ in data. In this case, the likelihood can be written as:

$$\mathcal{L}_{\mathrm{WZ}} = -\frac{1}{2}\chi^2 \left(w_{\mathrm{ur}};\ \mathrm{Sys}\left(z, \{s_i\}\right) \hat{w}_{\mathrm{ur}}(n^{\mathrm{pz,k}}, \{p_i\});\ \hat{\Sigma}^{-1}_{\mathrm{wz}} \right) + \mathrm{Prior}\left(\{p_i\}, \{s_i\}\right). \tag{4.17}$$

The model $\hat{w}_{\mathrm{ur}}$ is described by Eq. 4.14 multiplied by a function $\mathrm{Sys(z, \{s_i\})}$ that accounts for the systematic uncertainties of the method. The nuisance parameters $\{s_i\}$ are the parameters of the systematic functions; on the other hand, $\{p_i\}$ are the free parameters that appear in Eq. 4.14, i.e., the magnification parameters α_{u},α_{r}, and the bias of the unknown sample $b_{\mathrm{u}}(z)$. The systematic functions are quantified in § 4.4.2.

The quantity $\hat{\Sigma}$ for each of the likelihoods is the appropriate covariance matrix from the cross-correlation measurement. They are estimated from simulated data through a jackknife (JK) approach, using the following expression (Norberg et al., 2009):

$$\hat{\Sigma}(x_i, x_j) = \frac{(N_{\mathrm{JK}} - 1)}{N_{\mathrm{JK}}} \sum_{k=1}^{N_{\mathrm{JK}}} (x_i^k - \bar{x_i})(x_j^k - \bar{x_j}), \tag{4.18}$$

where the sample is divided into $N_{\mathrm{JK}} = 100$ sub-regions of roughly equal area, x_i is a measure of the statistic of interest in the i-th bin of the k-th sample, and $\bar{x_i}$ is the mean of our resamplings. The jackknife regions are safely larger than the maximum scale considered in our clustering analysis. The Hartlap correction (Hartlap et al., 2007) is used to compute the inverse covariance.

4.3 Simulations and data

4.3.1 DES Y3 Data

The Dark Energy Survey (DES) has been observing $\sim$ 5000 square degrees of the southern emisphere in 5 different broad phomotemtric bands ($grizY$) over the past six years. DES has been collecting images with the Dark Energy Camera (DECam, Flaugher et al. 2015), a 570-megapixel camera built by the collaboration and stationed at the Cerro Tololo Inter-American Observatory (CTIO) 4-meter Blanco telescope, and it is expected to infer the shapes of about 300 million galaxies up to redshift $z \sim 1.4$. In this Chapter we focus on the DES Year 3 (Y3) data, which comprises the analysis of the first three years of observations. DES Y3 data spans the full area of the survey ($\sim$4143 deg^2 after masking for foregrounds and problematic regions), representing a huge improvement over the DES Y1 area ($\sim$ 1321 deg^2 used in the Y1 cosmic shear analysis Troxel et al. 2018), but it does not reach yet the maximum depth. The total number of objects detected in this area is $\sim$ 333,246,422. Objects detection and measurements are described in (DES collaboration, 2020e).

4.3.2 Buzzard N-body simulation

We use one realisation of the DES Y3 Buzzard catalogue v2.0 (DeRose et al., 2019). Initial conditions were generated using 2LPTIC (Crocce et al., 2006) and the N-body run using L-GADGET2 (Springel, 2005). Cosmological parameters have been chosen to be $\Omega_{\rm m} = 0.286$, $\sigma_8 = 0.82$, $\Omega_b = 0.047$, $n_s = 0.96$, $h = 0.7$. Lightcones are generated on the fly starting from three boxes with different resolutions and size (1050^3, 2600^3 and 4000^3 Mpc^3h^{-3} boxes and 1400^3, 2048^3 and 2048^3 particles), to accommodate the need of larger box at high redshift. Halos are identified using the public code ROCKSTAR (Behroozi et al., 2013) and they are populated with galaxies using ADDGALS (DeRose et al., 2019). Galaxies are assigned magnitudes and positions based on the relation between redshift, r-band absolute magnitude and large-scale density found in a subhalo abundance matching model (Conroy et al., 2006; Lehmann et al., 2017) in higher resolution N-body simulations. SEDs are assigned to galaxies from the SDSS DR7 Value Added Galaxy Catalog (Blanton et al., 2005) by imposing the matching with the SED-luminosity-density relationship measured in the SDSS data. SEDs are k-corrected and integrated over the DES filter bands to generate DES $grizY$

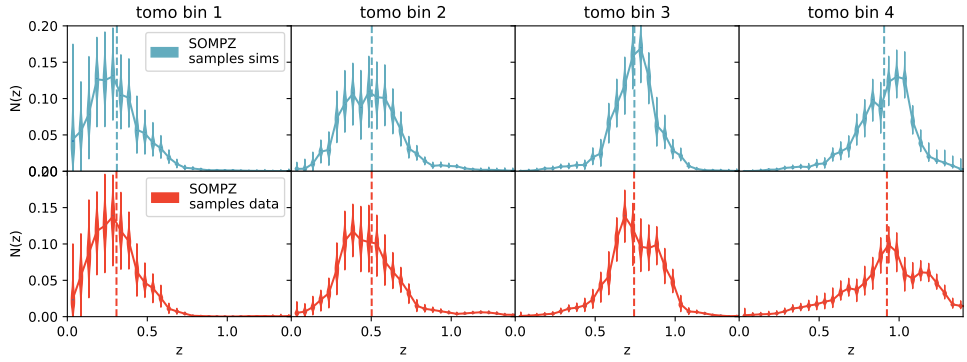

Figure 4.1: SOMPZ redshift distributions, as estimated in simulations (upper panels) and in data (lower panels), for the four tomographic bins considered in this analysis. The violin plots encompass the statistical and systematic uncertainties of the distributions, as estimated in Buchs et al. (2019). Vertical dashed lines indicate the mean redshifst of the distributions.

magnitudes.

Lensing effects are calculated using a multiple plane ray-tracing algorithm CALCLENS (Becker, 2013), which provides weak lensing shear, magnification and lensed galaxy positions for the lightcone outputs. CALCLENS is run onto the sphere using the HEALPix algorithm and is accurate to ~ 6.4 arcseconds. The WL galaxy sample in Buzzard is selected with the aim of reproducing the same selection applied in DES Y3 data in terms of size, signal-to-noise and colors. Shape noise has been added to the galaxies to match the measured shape noise of the DES Y3 WL sample.

4.3.3 Weak Lensing sample

The weak lensing sample in data is created using the METACALIBRATION pipeline, which is fully described in Gatti et al. (2020). After creating the DES Y3 'Gold' catalog (DES collaboration, 2020e), the METACALIBRATION pipeline measures the shapes of each detected object. The METACALIBRATION pipeline is able to self-calibrate the measured shapes against shear and selection biases by measuring the mean shear and selection response matrix of the sample $\langle \boldsymbol{R} \rangle = \langle \boldsymbol{R}_{\boldsymbol{\gamma}} \rangle + \langle \boldsymbol{R}_{\boldsymbol{s}} \rangle$. The current DES Y3 implementation of METACALIBRATION is able to correct for shear biases up to a multiplicative factor of 2-3 per cent, which is fully characterised using image simulations (MacCrann et al., 2020). Selection cuts for the sample are described in

(Gatti et al., 2020) and are determined based both on empirical tests and on tests on image simulations, and are designed to minimise systematic biases in the shear measurement. Galaxies are assigned an inverse variance weight, which increases the statistical power of the catalogue. The final sample comprises 100 million objects, for an effective number density of $n_{\rm eff} = 5.59$. Galaxies are further divided into 4 tomographic bins and redshift estimates for each of the tomographic bins are provided by the SOMPZ method (Buchs et al., 2019).

The preliminary (yet non-published) results on data have been obtained using the blinded version 3.30.20 of the DES Y3 catalogue. More details about the catalogue will be given in Chapter 5.

Photo-z estimates: SOMPZ and hyperrank

The SOMPZ method uses spectroscopic information and data from a number of deep fields (DES collaboration, 2020b) where additional photometry in the infrared bands and u-band is available, besides the the standard 5-band ($grizY$) photometry available in the DES wide field. This additional information is used to break the degenerancies in the photo-z estimates of the DES wide field galaxies (which have fewer bands available). This is achieved by creating Self Organizing Maps (SOM, Kohonen, 1982) for the spectroscopic, deep and wide fields; a mapping of the spectroscopic redshifts to the deep SOM is first obtained and then it is followed by a mapping from the deep to the wide SOM. The full procedure for the Y3 dataset is described in Buchs et al. (2019).

The weak lensing sample is reproduced with high fidelity in the Buzzard simulation by applying flux and size cuts to the simulated galaxies that mimic the DES Y3 source selection thresholds. Estimates of the N(z) are then provided using the same SOMPZ method applied to the simulations, showing a good agreement with the distributions obtained in the data (Fig. 4.1). The tomographic bins are selected such that they have equal number density.

4.3.4 Reference sample 1: *redMaGiC* galaxies

The first reference sample used in this analysis consists of DES *redMaGiC* galaxies. The *redMaGiC* algorithm selects red luminous galaxies with high quality photometric redshift estimates (Rozo et al., 2016). This is achieved by fitting each galaxy to a red sequence template; galaxies are then selected

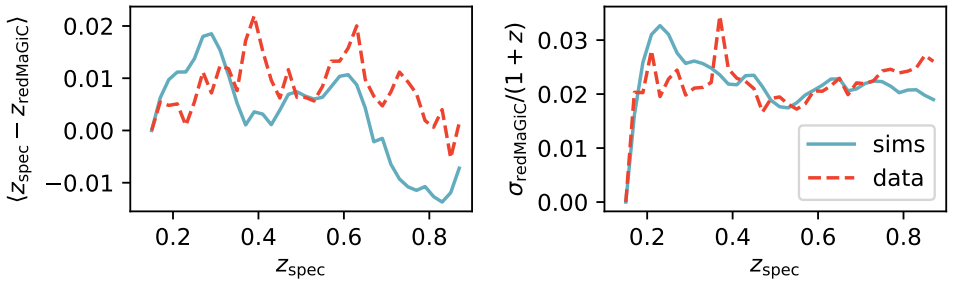

Figure 4.3: The scatter (right) and bias (left) of $z_{redMaGiC}$ for the simulated *redMaGiC* sample (solid lines) compared to the data (dashed lines).

only if they pass a goodness of fit and luminosity threshold. In DES, *redMaGiC*galaxies are used as lens sample in the galaxy-galaxy lensing analysis and in the clustering analysis (DES collaboration, 2020d,c). Three samples are selected with different number density by means of three distinct luminosity thresholds: a first sample called "high density" selected with a cut L/L* $>$ 0.5, a sample called "high luminosity" selected with a cut L/L* $>$ 1 and a sample called "higher luminosity", selected with L/L* $>$ 1.5. A combined sample is then obtained by joining these three samples, using the high density sample for redshifts $z < 0.65$, the high luminosity sample for the redshift range $0.65 < z < 0.8$, and the higher luminosity sample for higher redshifts.

In simulations, the *redMaGiC* sample is selected with the same algorithm used in the data. A comparison between the redshift distributions for the *redMaGiC* samples in data and in simulations is shown in Fig. 4.2, illustrating the good agreement between the two. Both in simulations and in data, the *redMaGiC* sample is divided into 60 thin bins spanning the redshift interval $0 < z < 1.2$.; then, only the bins in the range $0.14 < z < 0.90$ are considered, as no *redMaGiC* galaxies are avaliable outside this range[3]. The total number of *redMaGiC* galaxies is 3,041,935 on data, and 2,594,036 on simulations. This implies that the statistical uncertainties of the clustering redshift estimates obtained using the *redMaGiC* sample are overestimated in simulations compared to data. We do not expect this to be important, as we show in § 4.4.1 that the clustering-z methodology is dominated by

[3]We note that simulated *redMaGiC* sample sapans a slightly wider range in simulations; we nonetheless cut the redshift interval at z=0.90 to be consistent with the data.

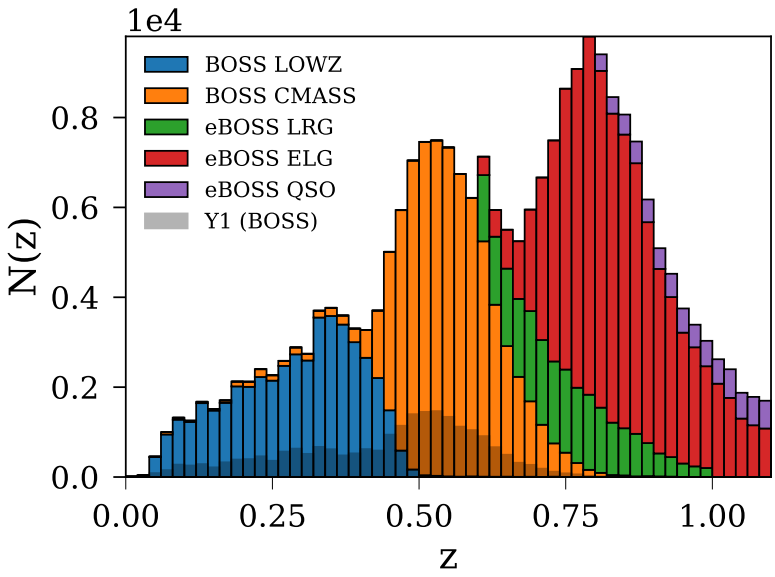

Figure 4.4: Redshift distributions of the various samples from BOSS and eBOSS overalapping with the DES Y3 footprint. For comparison purposes, we also show in shaded grey the overlap we had in the DES Y1 analysis.

systematic uncertainties, and the statistical uncertainties are negligible.

We further compare the typical *redMaGiC* photometric redshifts scatter and bias found in data and in simulations in Fig. 4.3. Since only a portion of the data sample has spec-z information, we re-weighted the magnitude distributions of the spectroscopic sample such that it matched the magnitude distributions of the *redMaGiC* galaxies before computing the statistics shown in Fig. 4.3. This re-weighting has been performed for each thin reference bin separately.

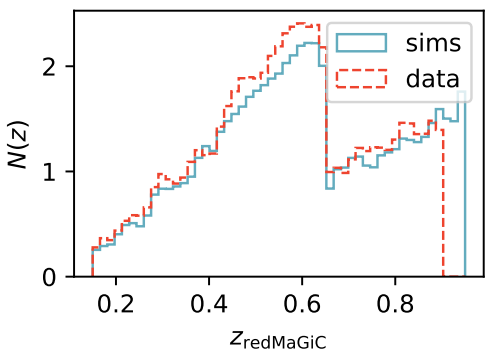

Figure 4.2: Redshift distributions of the *redMaGiC* samples, binned using the *redMaGiC* photo-z estimates, in data and in simulations.

A catalog of random points for *redMaGiC* galaxies is generated uniformly over the footprint. Both in data and in simulations, weights are

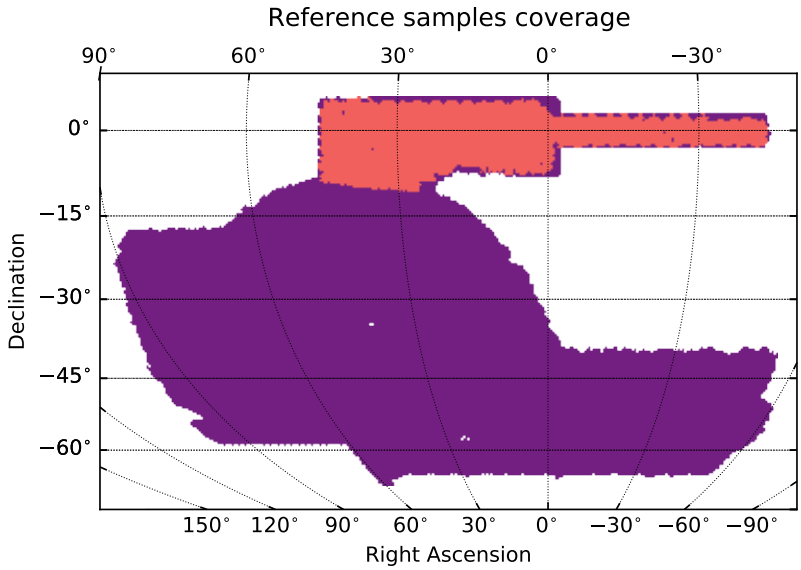

Figure 4.5: Spatial coverage of the two reference samples used in this work. Purple indicates the coverage by *redMaGiC* galaxies, pink indicates the coverage by BOSS and eBOSS galaxies.

assigned to *redMaGiC* galaxies such that spurious correlations with observational systematics are cancelled. The methodology used to assign weights is described in DES collaboration (2020c), and it is the same for data and simulations. The main difference between data and simulations is that the latter only models depth variations across the footprint, while data are subject to a larger number of systematics which are not modelled in simulations.

4.3.5 Reference sample 2: spectroscopic galaxies

The second reference sample used in this work is a spectroscopic sample obtained from the combination of SDSS galaxies from BOSS (Baryonic Oscillation Spectroscopic Survey, Dawson et al. 2013) and from eBOSS (extended-Baryon Oscillation Spectroscopic Survey, Ahumada et al. 2019). The BOSS sample includes the LOWZ and CMASS catalogs from the SDSS DR 12, fully described in Reid et al. (2016), while we included the large-scale structure catalogs from emission line galaxies (ELGs, see Raichoor et al. 2017 for the target selection description), luminous red galaxies (LRGs, target selection described in Prakash et al. 2016) and quasi stellar objects (QSOs)

Spectroscopic Samples			
Name	Redshifts	$N_{\rm gal}$	Area
LOWZ (BOSS)	$z \sim [0.0, 0.5]$	45671	~ 860 deg^2
CMASS (BOSS)	$z \sim [0.35, 0.8]$	74186	~ 860 deg^2
LRG (eBOSS)	$z \in [0.6, 1.0]$	24404	~ 700 deg^2
ELG (eBOSS)	$z \in [0.6, 1.1]$	89967	~ 620 deg^2
QSO (eBOSS)	$z \in [0.8, 1.1]$	7759	~ 700 deg^2

Table 4.1: List of the spectroscopic samples from BOSS/eBOSS overlapping with the DES Y3 footprint used as reference galaxies for clustering redshifts in this work.

(eBOSS in prep.) from eBOSS, which were provided to DES for clustering redshifts usage by agreement between DES and eBOSS. The redshift distributions of each samples are shown in Fig. 4.4 and the area coverage and number of objects of each sample is summarised in Table 4.1. The area coverage is smaller compared to *redMaGiC* galaxies, as it shown in Fig. 4.5. To replicate the spectroscopic sample in simulations, we selected bright galaxies with a similar area coverage and redshift distributions as the ones in data. We did not try to further match other properties of the sample. We note that even if the galaxy-matter bias of the BOSS/eBOSS sample selected in simulation might differ from the one measured in data, all the methods implemented in this Chapter will correct for it.

4.4 Results on simulations

In this section we present the results of our two calibration strategies performed in simulations. In particular, we aim to evaluate the systematic uncertainties of each method, and verify that the calibration procedure in simulations works as expected.

Before focusing on the details of the two calibration procedures, we show in Fig. 4.6 the redshift distributions estimates obtained using the clustering-based estimator (following Eqs. 4.14, 4.15) in simulations, compared to the true distributions. The angular scales considered in the clustering measurements have been chosen to span the physical interval between 1500 kpc and 5000 kpc[4]. We start from an idealised case: the distributions shown in

[4]We note that these scales are slightly larger than the ones adopted in the DES Y1 analysis (where we considered the range between 500 kpc and 1500 kpc). The main reason

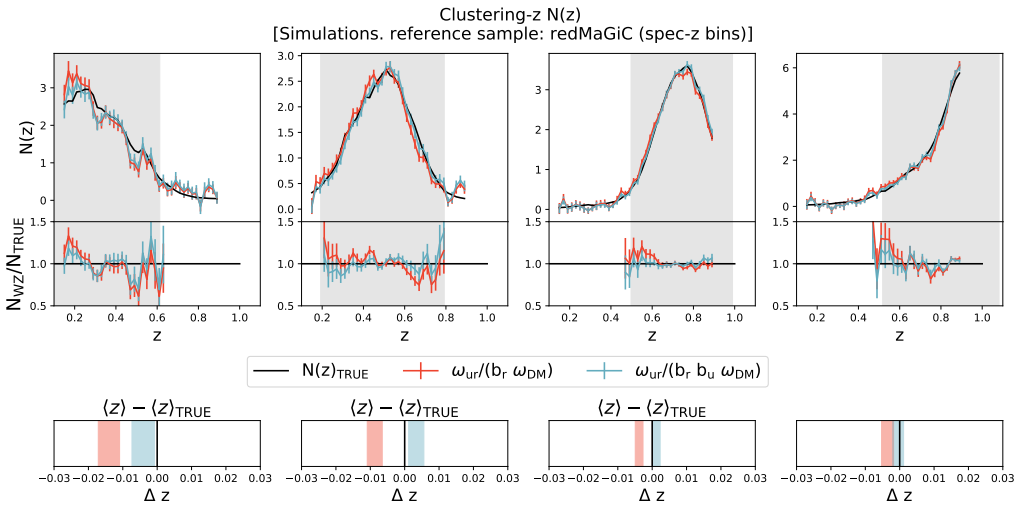

Figure 4.6: Redshift distributions estimated using clustering redshift in simulations, compared to the true (black lines). Top panels show the redshift distributions; middle panels show the ratio between the true $N(z)$ and the $N(z)$ estimated using clustering redshift; bottom panels show the mean of the redshift distributions. Red lines represent the clustering redshift estimates obtained using the estimator introduced by Eq. 4.15. Blue lines represent the clustering redshift estimated obtained further correcting for the term $b_u(z)$, which is only possible in simulations. The four different tomographic bins used in the DES Y3 cosmological analysis are shown. We used *redMaGiC* galaxies as the reference sample, binned using true redshifts. We also subtracted from the clustering redshift $N(z)$ estimates the expected magnification contribution in simulations. The redshift distributions are normalised over the same interval. Grey shaded regions indicate the interval considered for the mean matching method. The mean of the distributions showed in the bottom panels are computed only considering the grey intervals.

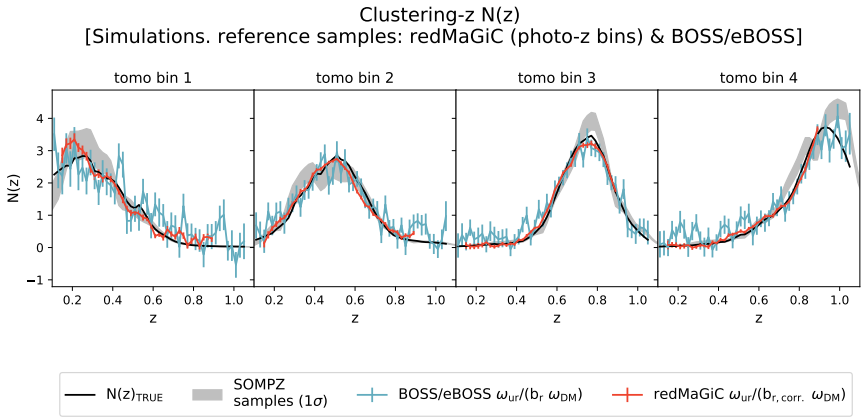

Figure 4.7: Redshift distributions estimated using clustering redshift in simulations, compared to the true (black lines). We both show the redshift distributions obtained using *redMaGiC* galaxies as a reference sample, binned using their *redMaGiC* photo-z estimates, and the ones obtained using BOSS/eBOSS galaxies as a reference sample. Magnification effects have not been subtracted here. The redshift distributions have been obtained using the estimator introduced by Eq. 4.15, without correcting for the bias of the unknown sample $b_{\rm u}$. The grey bands show, as a comparison, the 1 σ region encompassed by the SOMPZ realisations.

Fig. 4.6 are obtained using *redMaGiC* galaxies, but binned using true redshift. We have also subtracted magnification contributions to the clustering estimator, using the best estimates values for the magnification coefficients available in Buzzard. These have been estimated for *redMaGiC* galaxies comparing two samples in simulations selected using magnified and non-magnified fluxes, and ranges between $\alpha_{\rm r} = -2$ and $\alpha_{\rm r} = -2$ depending on the reference bin considered. For the unknown sample, we assumed $\alpha_{\rm u} = 0$ for all the four tomographic bins. In simulations we also dispose of an accurate estimate of $b_{\rm u}(z)$, obtained from the auto-correlations of each of the tomographic bins of the unknown sample. This is not possible in data since the precision of the photometric redshift is not sufficient to divide the sample in bins of the adequate width. Fig. 4.6 shows the impact on the estimated $n(z)$s of assuming we know $b_{\rm u}(z)$ with good accuracy, dividing Eq. 4.15 by $b_{\rm u}(z)$. We note that correcting for $b_{\rm u}(z)$ drives both the shape of the dis-

for choosing slightly larger scales was due to the fact that here we model/correct for the galaxy-matter bias evolution of the reference sample, and we preferred using slightly larger scales where the linear bias assumption is more valid. Nonetheless, these scales remain smaller than the ones used in the main cosmological analysis.

tributions and the mean value closer to the truth. As we do not estimate $b_u(z)$ in data, this introduces a systematic uncertainty in the method that has to be quantified.

Fig. 4.7 compares the $n(z)$ distributions obtained with *redMaGiC* and BOSS/eBOSS as reference samples. We produced Fig. 4.7 using a more realistic setup: *redMaGiC* galaxies have been binned into thin bins using the *redMaGiC* photo-z estimates rather than the true redshifts, we did not correct for the bias evolution of the unknown sample, we did not subtract the magnification contribution. This plot highlights the differences between the two samples, since *redMaGiC* has a smaller statistical uncertainty, but BOSS/eBOSS sample has a larger coverage in redshift that helps calibrating the redshift distributions at higher redshift. The distributions are compatible within errors. We note that in order to correct for the bias evolution of the reference sample when using *redMaGiC* galaxies as a reference, we had to apply a correction to the width of *redMaGiC* bins, as described by Eq. 4.2.1, to account for the broader distributions that realistic *redMaGiC* bins have compared to a top-hat bin. Such correction is shown in Fig. 4.8.

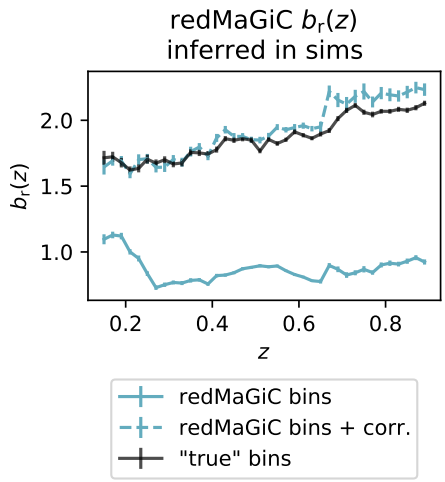

Figure 4.8: Redshift evolution of the galaxy-matter bias $b_r(z)$ of *redMaGiC* galaxies, estimated with different binning. In particular, the black line has been obtained binning *redMaGiC* galaxies using the true redshift, the solid light blue line has been obtained binning *redMaGiC* galaxies using *redMaGiC* photo-z. The lower amplitude is due due to the larger bin width of the *redMaGiC* bins due to the photometric uncertainties. The light blue dashed lines is the same as the light blue solid line, but after correcting for the larger width of the bins.

In the following subsections, we tested the accuracy of our calibration procedure using the two different approaches outlined in § 4.2: in a first case using the mean redshift of the recovered $n(z)$as metric, and in the second case using the whole shape of the redshift distributions.

Table 4.2: **Mean-matching method**, total systematic error budget for the two reference samples used in this work. We also report the contribution due to each single source of systematic, as a function of tomographic bin.

Systematic	**tomo bin 1**	**tomo bin 2**	**tomo bin 3**	**tomo bin 4**
method:	0.002 ±0.002	0.001 ±0.002	0.000 ±0.001	0.001 ±0.002
magnification:	0.004	0.005	0.003	0.004
WL bias syst:	0.013	0.013	0.013	0.013
redMaGiC syst:	0.000 (0.014)	0.001 (0.007)	0.002 (0.000)	0.005 (0.003)
total systematic *redMaGiC*:	0.014	0.014	0.014	0.015
statistical *redMaGiC*:	0.002	0.002	0.001	0.002
total systematic BOSS/eBOSS:	0.014	0.014	0.014	0.014
statistical BOSS/eBOSS:	0.007	0.006	0.004	0.006

4.4.1 Method 1 (mean-matching): systematic uncertainties estimation in N-body simulations

We test in this section the mean-matching clustering-based photo-z calibration method. The metric used here to assess the accuracy of our methodology is the difference between the mean of the recovered redshift distribution and the true mean, defined as follows:

$$\Delta\langle z\rangle \equiv |\langle z\rangle_{true} - \langle z\rangle_{WZ}|. \tag{4.19}$$

In order to heavily reduce the impact of magnification effects, we compute the mean over a restricted redshift interval of 2 standard deviations around the mean of the SOMPZ distributions, i.e. $\langle z\rangle_{\rm SOMPZ} - 2\sigma_{\rm SOMPZ} < z < \langle z\rangle_{\rm SOMPZ} + 2\sigma_{\rm SOMPZ}$. The extrema of the intervals considered throughout the Chapter are $[0.14, 0.62]$, $[0.18, 0.80]$, $[0.46, 0.94]$, $[0.48, 0.94]$ for *redMaGiC* and $[0.10, 0.62]$, $[0.18, 0.80]$, $[0.46, 0.98]$, $[0.48, 1.06]$ for BOSS/eBOSS. Given the similarities between the SOMPZ distributions in simulations and in data (Fig. 4.1), we also used the same intervals when applying our methodology to the data.

Systematic uncertainties

We quantify here the systematic uncertainties of the mean matching method. We remind that the absolute value of the terms in Eq. 4.15 are irrelevant for this method, as we are only interested in how they evolve with redshift. In principle, in absence of magnification, assuming perfect reference sample redshift accuracy (e.g., *redMaGiC* redshifts to be exact), assuming that we are able to successfully estimate all the terms in Eq. 4.15, and assuming that we know the galaxy-matter bias evolution of the unknown sample, we

should correctly recover the mean of the unknown redshift distributions. The above assumptions might not hold when applying this methodology in data, causing a systematic bias in the calibration, In particular, $\Delta\langle z\rangle$ can differ from zero because of the following reasons:

- 1) the approximations that allowed us to factorize the integral in Eq. 4.1 into $b_r(z)b_u(z)w_{DM}(z)$, might not hold (e.g., linear bias model, infinitesimally thin bins), leading to inaccuracies in the modelling at small scales. We will quote this effect as **methodology systematic**;

- 2) Magnification contribution. In the mean matching approach, we do not correct for magnification effects, as we cut the tails of the redshift distributions. This systematic quantifies how effective our cut is. We will refer to this has **magnification systematic**.

- 3) The clustering-based estimator ignores the redshift evolution of the galaxy-matter bias of the unknown sample (**weak lensing bias systematic**);

- 4) The reference sample is binned using photometric redshifts and not spectroscopic redshifts. This only applies to the *redMaGiC* case. We will refer to this as ***redMaGiC* systematic**.

We studied the performance of the estimator described in Eq. 4.15 for four cases, starting from an ideal environment free of the effects of systematics and introducing one uncertainty at the time, leading to a more complex, realistic case. This allows us to estimate separately the magnitude of each systematic independently. In the following tests, we will only use the *redMaGiC* galaxies as a reference sample to estimate the systematic uncertainties. Indeed, the BOSS/eBOSS sample should be affected by the same systematic uncertainties as the *redMaGiC* sample, except for the *redMaGiC* systematic.

We begin with the most ideal case possible, shown in Fig. 4.6, which we already described at the beginning of this section. We remind that for this case we used *redMaGiC* galaxies as a reference binned using true redshifts, we corrected for the bias evolution of the unknown and reference sample, we corrected for the redshift evolution of the clustering of dark matter, and we subtracted magnification effects assuming the fiducial values of $\alpha_{\rm r}$ and $\alpha_{\rm u}$. The $\Delta\langle z\rangle$ mean for this case provides an estimate of the methodology systematic, and it is reported in the first line of Table 7.1. This value is compatible with zero within statistical uncertainty, indicating that for the

scales considered in this work (1500 to 5000 kpc), the approximation of linear bias model and infinitesimally thin redshift bins are good enough for the purpose of calibrating the mean with clustering information.

We then proceed estimating the systematic uncertainty due to magnification effects. Since we have excluded the tails of the distributions, we do not expect this to be an important systematic. Indeed, when adding back the contribution due to magnification we subtracted in the precedent case, we obtain an increase of $\Delta\langle z\rangle \sim 0.002$. To be more conservative, we can try to estimate the impact on $\Delta\langle z\rangle$ if the data had different (and potentially larger) values of $\alpha_{\rm r}$ and $\alpha_{\rm u}$ than the ones estimated in simulations. We did this by computing the magnification term $M(\theta)$ assuming $\alpha_r \sim \mathcal{N}(0,2)$ and $\alpha_u \sim \mathcal{N}(0,2)$, and propagating the scatter to the relevant metric $\Delta\langle z\rangle$. We obtained a scatter on this metric of the order of $\Delta\langle z\rangle \sim (0.004, 0.005, 0.003, 0.004)$ for the four tomographic bins. We note that these values are up to a factor 10 smaller than what we would have obtained by including the tails of the redshift distributions, justifying the cut we introduced at the beginning of this section. To be conservative, we decided to consider the values of $\Delta\langle z\rangle \sim (0.004, 0.005, 0.003, 0.004)$ for the magnification systematic in Table 7.1, rather than a value of $\Delta\langle z\rangle \sim 0.002$ estimated for the realisation of Buzzard used here.

We then quantify the impact on the mean redshift of ignoring the redshift evolution of the galaxy-matter bias of the unknown sample $b_{\rm u}(z)$, as this cannot be measured in data. Building up from the precedent case, we estimate our redshift distributions without correcting for the bias evolution of the unknown sample, and look at the difference in the mean redshift compared to the previous case. The impact on $\Delta\langle z\rangle$ is quantified in Table 7.1, and reads, for the four tomographic bins, $\Delta\langle z\rangle = (0.010, 0.013, 0.006, 0.001)$. The effect on the mean and on the shape of the clustering redshift $n(z)$ can also be appreciated from Fig. 4.6, as the two clustering redshift $n(z)$ estimates only differ because of the $b_{\rm u}(z)$ term.

Also in this case we decide to take a more conservative approach, moved by the fact that the bias systematic is the dominant uncertainty of the method. We assume the bias systematic to be the same in each tomographic bin, and equal to largest value estimated in Buzzard, i.e., $\Delta\langle z\rangle = 0.013$ estimated for the second bin.

Finally, we estimate the systematic uncertainty due to the fact that *redMaGiC* galaxies are binned into thin bins using their photo-z estimates. This is done by comparing the mean of the clustering redshift $N(z)$ estimates obtained binning the *redMaGiC* galaxies using true redshifts (as in the

previous case) to the estimates obtained by binning using *redMaGiC* photo-z. The photo-z accuracy of *redMaGiC* galaxies is better than the one of the weak lensing sample, but it is not as good as the one of a spectroscopic sample. This can introduce some uncertainties in the recovered redshift distributions. E.g., if all *redMaGiC* photo-z estimates were biased towards lower redshift, we would expect the clustering redshift $N(z)$ to be similarly biased. Due to the non negligible scatter of *redMaGiC* photo-z, we also expect the clustering-z $N(z)$ to be smoother compared to the case where the true redshift is used to bin the reference sample, as we cannot capture fluctuations in the true $N(z)$ over scales smaller than the intrinsic *redMaGiC* photo-z uncertainty.

The values of the *redMaGiC* uncertainties are reported in Table 7.1. These values are relatively small, indicating that the main effect of *redMaGiC* uncertainties is to smooth the recovered redshift distributions (as it can be noticed by comparing Fig. 4.6 to Fig. 4.7), without strongly affecting the mean. We also report in parenthesis the values of the uncertainties we would have obtained if we had not included the correction factor (Eq. 4.2.1) when estimating the galaxy-matter bias of *redMaGiC* galaxies: this indicates that this correction constitutes an important factor that cannot be neglected when applying this methodology to data.

Before reporting the total error budget for the mean matching method, we further checked the assumption we made concerning assumming a fixed cosmology for the redshift evolution of the clustering of dark matter $w_{\rm DM}(z)$. We checked that assuming different values for the cosmological parameters ($\Omega_{\rm m} = 0.4$, $\sigma_8 = 0.7$) resulted in a shift of $\Delta\langle z\rangle < 10^{-3}$.

The systematic uncertainties evaluation performed in this section is key to understand which are the systematics clustering methods are most sensitive to. The total error budget is reported at the end of Table 7.1, and it is obtained following the procedure adopted in the DES Y1 analysis (Gatti et al., 2018; Davis et al., 2018) by adding in quadrature all the single source of errors, assuming they are independent. As we already mentioned, the dominant source of uncertainty is due to the potential redshift evolution of the galaxy-matter bias of the weak lensing sample, which we do not model in the current analysis.

Validation

We apply in this subsection the mean-matching method to calibrate the realisations of the redshift distributions from the SOMPZ method. We

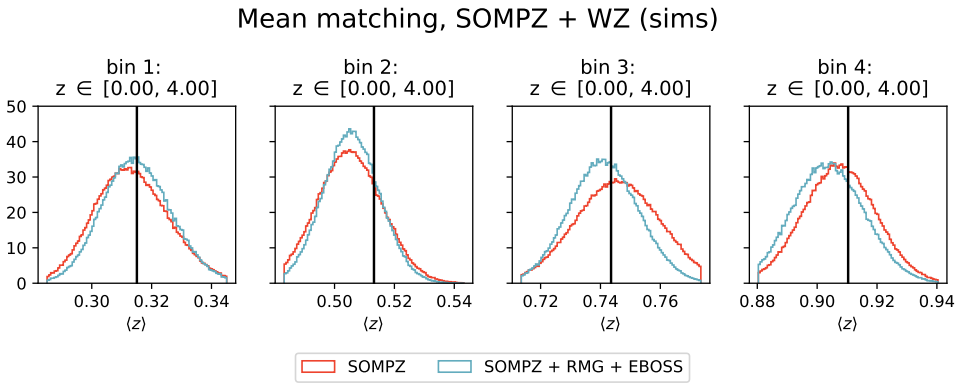

Figure 4.9: Mean redshift posteriors for the 4 tomographic bins obtained using the clustering information (WZ) through the mean matching method. Red histograms represent the distribution of the mean redshift of the SOMPZ realisations, whereas light-blue histograms show the mean redshift posteriors of the SOMPZ realisations using the clustering-redshift likelihood. The mean redshift of the SOMPZ realisations has been computed over a wide redshift interval ($0 < z < 4$), also including the redshift range where there is no clustering information.

recall that the SOMPZ method provides a number of realisations for the redshift posteriors; we assign a weight to each of them through the likelihood described by Eq. 4.16. As we have two reference samples, we combined the likelihood obtained using the *redMaGiC* and BOSS/eBOSS samples; we assumed the two likelihood were not completely independent, but that they shared the weak lensing bias systematic.

The distribution of the mean redshifts of the SOMPZ realisations, before and after having being weighted by the clustering-redshift likelihood, are shown in Fig. 4.9, compared to the true mean redshift. The mean redshift of the SOMPZ realisations are also reported in Table 4.4. The results obtained by weighting without combining the two reference samples are shown in Appendix A.2. It can be noted that the clustering information little improves the constraints from the SOMPZ realisation, owing to the better accuracy of the latter method. The constraints on the mean are reported in Table 4.4.

This means that given the DES Y3 analysis setup, the mean matching method can only be used as independent cross-check of the SOMPZ methodology, but it does not significantly improve the constraints on the mean of the redshift distributions.

Table 4.3: **Simulations**. The mean redshift estimates of the SOMPZ distributions with and without clustering-based information, in simulations.

case	tomo bin 1	tomo bin 2	tomo bin 3	tomo bin 4
True $\langle z \rangle$:	0.315	0.513	0.743	0.910
SOMPZ $\langle z \rangle$:	0.314 $\pm$0.013	0.505 $\pm$0.011	0.746 $\pm$0.014	0.907 $\pm$0.012
SOMPZ + WZ (mean matching) :	0.315 $\pm$0.012	0.506 $\pm$0.009	0.741 $\pm$0.012	0.904 $\pm$0.012
SOMPZ + WZ (shape matching) :	X	X	X	X

4.4.2 Method 2 (shape-matching): systematic uncertainties estimation in N-body simulations

We discuss here the second method investigated in this Chapter to combine the clustering information with the SOMPZ $N(z)$ realisations. This method involves forward modelling the full clustering signal across all the redshift range covered by the reference samplse (i.e., including the tails of the distributions). In practice, this allows to constrain the full shape of the redshift distributions, not only the mean.

Systematic uncertainty determination

First, we recall that in § 4.2 we described how the cross-correlation signal can be modelled starting from an estimate of the redshift distributions (provided by the $N(z)$ realisations of the SOMPZ photo-z code) and the values of the nuisance parameters of the model (the magnification parameters α_u, α_r, and the bias of the unknown sample b_u). The other ingredients of the model are either measured from data ($b_r(z)$) or estimated assuming a cosmological model (e.g., $w_{\rm DM}(z)$). Finally, we need to model the systematic uncertainty of the method. We define the systematic uncertainty of the method as the ratio between the measured correlation function $w_{\rm ur}(z_i)$ and the model $\hat{w}_{\rm ur}(z_i)$:

$$\text{Systematic uncertainty}(z_i) = \frac{w_{\rm ur}(z_i)}{\hat{w}_{\rm ur}(z_i)}. \tag{4.20}$$

We evaluated such ratio in an interval that excludes the tails of the $N(z)$, as the ratio can be very noisy and might assume very large values where $w_{\rm ur}(z_i)$ is supposed to be small. As for the measured $w_{\rm ur}(z_i)$, we used the measurement in the most realistic scenario (i.e., for the *redMaGiC* sample, this involves using *redMaGiC* photo-z to bin the reference sample). The systematic uncertainty of the method, as a function of redshift and tomographic bin, is shown in Fig. 4.10. The ratio deviates from unity due to systematic effects, which are the same effects considered in the previous section (i.e,

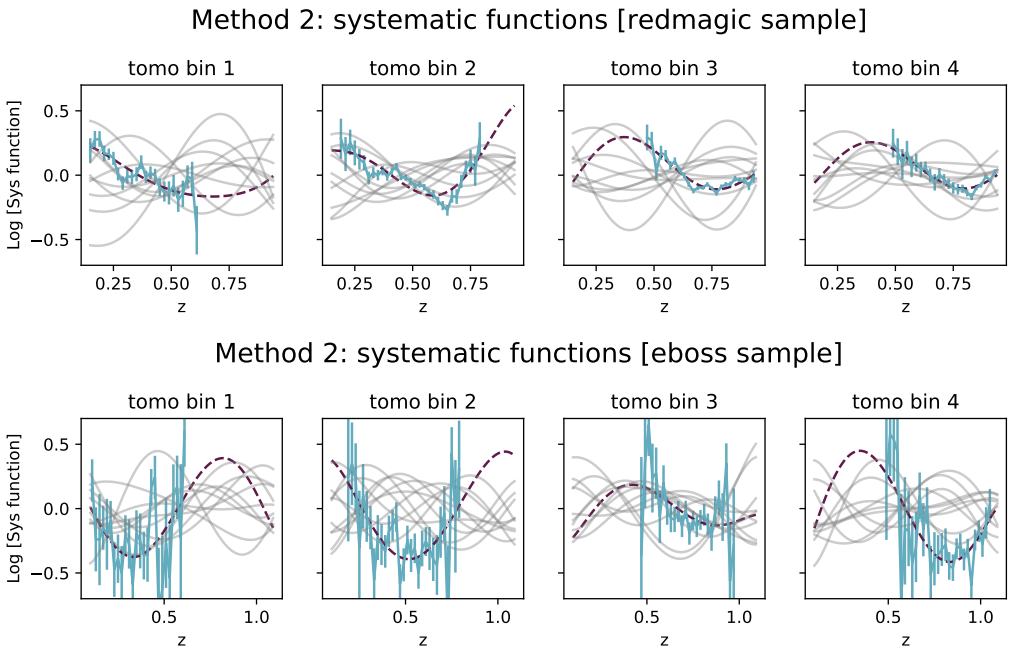

Figure 4.10: Systematic uncertainties of the shape-matching method as measured in simulations following Eq. 4.20, for the 4 tomographic bins and for the two reference samples considered (*redMaGiC* upper panels, BOSS/eBOSS, lower panels). The measured systematic uncertainties are represented by the light blue lines; the purple dashed lines represent the best fitting model. The grey lines represent 10 random realisations of the systematic uncertainty model assumed for the shape-matching method and described by Eq. 4.21.

method systematic, the redshift evolution of the galaxy-matter bias of the unknown sample, and uncertainties in the redshifts of the reference sample).

For this method, we assume we can model the systematic uncertainty shown in Fig. 4.10 by a function $\mathrm{Sys}\,(\mathrm{z_i}, \{\mathrm{s_k}\})$ that varies smoothly with redshift. Such function needs to have enough flexibility to fit properly the systematic uncertainty measured in Buzzard. Moreover, we assume that the overall root-mean-square (RMS) of the model $\mathrm{Sys}\,(\mathrm{z}, \{\mathrm{s_i}\})$ measured in Buzzard is similar to what can be expected in data. For both the *redMaGiC*and the BOSS/eBOSS samples, we found the RMS of the systematic function for different tomographic bins to be RMS $\sim 0.10 - 0.15$[5]. To be conservative, we imposed a Gaussian prior of RMS $\sim \mathcal{N}(\mu, 0.2)$ on the RMS of the family of systematic functions described by $\mathrm{Sys}\,(\mathrm{z_i}, \{\mathrm{s_k}\})$[6]. This also has the consequence that the model never diverges. We chose the $\mathrm{Sys}\,(\mathrm{z_i}, \{\mathrm{s_k}\})$ function to be given by:

$$log[\mathrm{Sys}\,(\mathrm{z_i}, \{\mathrm{s_k}\})] = \sum_{k<M} s_k P'_k(z_i), \tag{4.21}$$

with $P'_k(z_i)$ the k-th Legendre polynomial, after remapping the redshift argument into the interval (-1,1), and M the maximum order considered. The best fit model (obtained with the additional prior on the RMS of the systematic function) is shown in Fig. 4.10. The model is easily extrapolated beyond the range used for the fit, showing no sign of divergence. We set the maximum order of Legendre polynomials to be $M = 5$, as including higher order terms did not further improve the fit.

We note that compared to the mean matching method, in this case we did not try to characterise each individual source of systematic uncertainties as it would have increased unnecessarily the complexity of the modelling. On the other hand, the model for the systematic uncertainties is flexible enough to fully describe the systematic uncertainties found in the simulation. In Fig. 4.10 we also show few examples of systematic functions obtained random sampling $\mathrm{Sys}\,(\mathrm{z_i}, \{\mathrm{s_k}\})$ with the constrain on its RMS (in grey), alongside with the best fit found in simulation (in red). This illustrates the flexibility of our model for the systematic uncertainty, which is able to model a large variety of curves. The other important feature is that the

[5]In particular, we measured the RMS of the systematic uncertainties for the 4 tomographic bins to be (0.11,0.07,0.07,0.11) for *redMaGiC* and (0.18, 0.15, 0.10, 0.15) BOSS/eBOSS.

[6]In practice, this is achieved imposing a Gaussian prior on each of the parameters s_k.

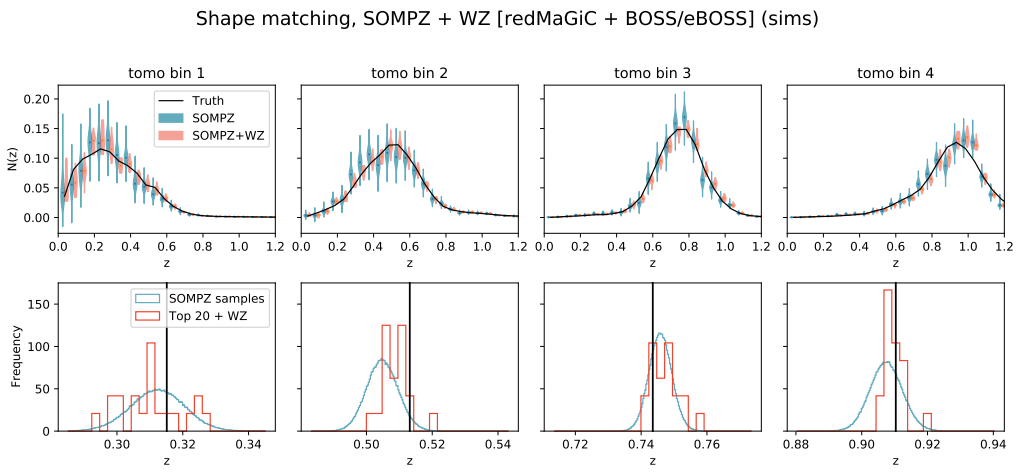

Figure 4.11: *Upper panels:* SOMPZ redshift distributions, as estimated in simulations, with and without clustering information (shape-matching method). The violin plots encompass the statistical and systematic uncertainties of the distributions. *Lower panels:* Mean redshift of the SOMPZ $N(z)$ realisations, with and without clustering information.

curves never diverge, and the logarithm of the curves is mostly confined in a horizontal band around zero.

We can compare this method with the mean matching method by looking at the impact that assuming different values of the systematic uncertainty model has on the mean of the $N(z)$ distributions. In particular, this can be done by drawing many (e.g., ~ 1000) realisations of Sys $(\mathrm{z_i}, \{\mathrm{s_k}\})$, considering the mean of the true distribution multiplied by a given realisation of the systematic function and looking at the Δz with respect to the true distribution. To facilitate the comparison with the previous section, we computed Δz in the same interval ($2\ \sigma$ around the mean) it was computed for the mean matching method. We obtained a typical $\Delta z \sim 0.010 - 0.015$ depending on the tomographic bin, in very good agreement with the systematic uncertainties estimated for the mean matching method.

Validation

Once our family of systematic functions is determined for the shape-matching method, we proceed computing the likelihood of the SOMPZ $\{n_u^{pz,k}(z_i)\}$ realisations in simulations. The likelihood obtained for the two reference samples is combined, and is always computed over the full range of redshifts available, i.e., including the tails of the distributions, when possible.

In order to compute the likelihood we need to evaluate the magnification parameters α_u, α_r. We analytically marginalise over α_u (see Appendix A.2 for more details). We cannot marginalise over the sets of α_r, as these parameters will be included in the cosmological analysis. We later verify in this section that the exact value of α_r little changes the outcome of the shape-matching method, so throughout the rest of this section we assumed the fiducial values of α_r as estimated for the Buzzard simulation.

The outcome of the shape-matching likelihood is shown in Fig. 4.11. As expected from the results of the mean matching method, the clustering information does not help tightening the scatter on the mean of the distributions (lower panels). On the other hand, the shape-matching likelihood does tighten the scatter on the shape of the SOMPZ distributions, as it can be noted from the upper panels. This is because the SOMPZ method suffers from sample variance, as the SOMPZ $N(z)$ realisations are estimated from relatively small deep fields, whereas the correlation functions are measured over the full DES Y3 footprint. Although the clustering signal is dominated by the weak lensing bias systematic uncertainty, such systematic is slowly varying as a function of redshift, and does not have "peaky" features typical of sample variance. This means that the weak lensing bias systematic maximally affects the mean of the distribution, but it affects less the higher moments of the redshift distributions.

Finally, we verify that the exact value of the the parameters α_r or the cosmology assumed to compute $w_{\rm DM}$ does not impact the methodology. We found that XXX.

4.5 Application to data

We present the clustering-based redshift estimates on data in Fig. 4.12. These have been estimated following Eqs. 4.14, 4.15. We show the distributions obtained with the two reference samples, and as a comparison, the 1 σ region encompassed by the SOMPZ realisations. Note that for the clustering redshift estimates obtained using *redMaGiC* galaxies we applied the correction to the galaxy-matter bias of the reference sample described by Eq. 4.2.1, using the fraction of the *redMaGiC* galaxies with a spec-z counterpart. As *redMaGiC* galaxies with spec-z counterparts tend to have brighter magnitudes compared to the full *redMaGiC* sample, we have applied a magnitude re-weighting to those galaxies before computing the correction, so as to have a representative *redMaGiC* subsample with spec-z information.

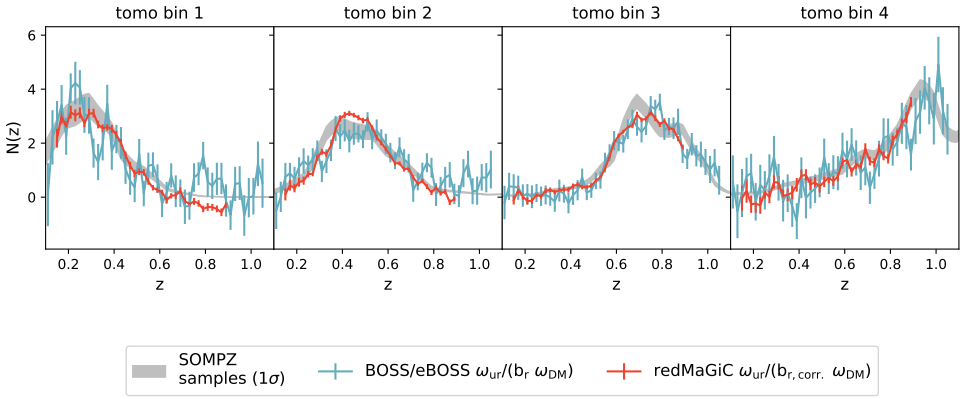

Figure 4.12: Redshift distributions estimated using clustering redshift in data. We both show the redshift distributions obtained using *redMaGiC* galaxies as a reference sample, binned using their *redMaGiC* photo-z estimates, and the ones obtained using BOSS/eBOSS galaxies as a reference sample. Magnification effects have not been subtracted here. The redshift distributions have been obtained using the estimator introduced by Eq. 4.15. The grey bands show, as a comparison, the 1 σ region encompassed by the SOMPZ realisations.

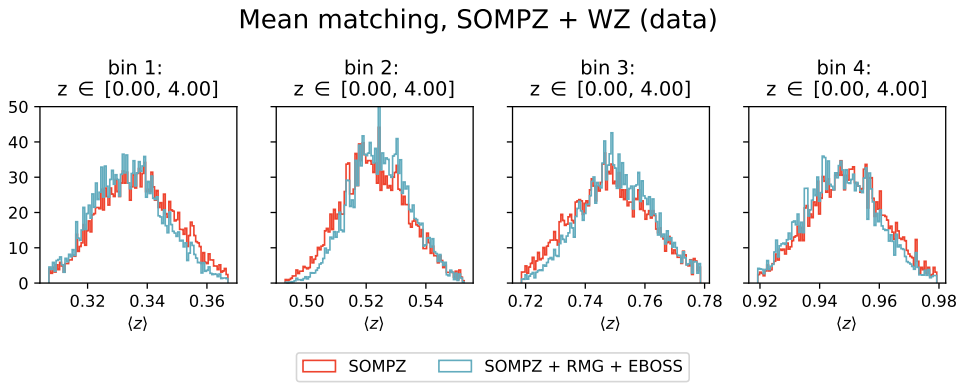

Figure 4.13: Mean redshift posteriors for the 4 tomographic bins obtained using the mean matching method. Red histograms represent the distribution of the mean redshift of the SOMPZ realisations, whereas light-blue histograms show the mean redshift posteriors of the SOMPZ realisations using the WZ likelihood. The mean redshift of the SOMPZ realisations has been computed over a wide redshift interval ($0 < z < 4$), also including the redshift range where there is no WZ information.

Table 4.4: **Data**. The mean redshift estimates of the SOMPZ distributions with and without clustering-based information, in simulations.

case	**tomo bin 1**	**tomo bin 2**	**tomo bin 3**	**tomo bin 4**
True $\langle z \rangle$:	0.315	0.513	0.743	0.910
SOMPZ $\langle z \rangle$:	0.314 $\pm$0.013	0.505 $\pm$0.011	0.746 $\pm$0.014	0.907 $\pm$0.012
SOMPZ + WZ (mean matching) :	0.315 $\pm$0.012	0.506 $\pm$0.009	0.741 $\pm$0.012	0.904 $\pm$0.012
SOMPZ + WZ (shape matching) :	X	X	X	X

We first checked that the *redMaGiC* and BOSS/eBOSS estimates were in agreement with each other within uncertainties. We computed the mean of the two clustering based redshift distributions in the redshift interval where the two samples overlap, also excluding the tails (as detailed at the beginning of § 4.4.1). We measured a mean redshift difference between the estimates obtained with *redMaGiC* galaxies and BOSS/eBOSS galaxies of $(-0.009 \pm 0.010, 0.006 \pm 0.009, 0.005 \pm 0.006, 0.022 \pm 0.014)$, for the four tomographic bins. The quoted uncertainties take into account the statistical and systematic uncertainties as reported in Table 7.1, except for the weak lensing bias systematic that is assumed to be shared by the two samples. We note that the statistical uncertainty for the last tomographic bin is roughly as twice as large in the data compared to the simulations, due to a broader $N(z)$. On the other hand, the other tomographic bins show more similar levels of statistical uncertainty.

We then show the results of the application of the mean-matching likelihood to data, in Fig. 4.13. We first checked that the mean redshifts of the clustering-based distributions obtained with the two reference samples were individually in agreement with the ones estimated from the SOMPZ realisations (this comparison is shown in Appendix A.2). Then we proceeded with the mean-matching likelihood. As expected from the tests on simulation, the clustering-based estimate little tighten the mean redshift distributions from the SOMPZ realisations.

mention: sensitivity to magnification parameters

mention: Sensitivity to weights

mention results from Gary's likelihood

4.5.1 Comparison with Shear ratio, and general redfshift strategy

4.6 Conclusions

We have presented the calibration of the Dark Energy Survey Year 3 (DES Y3) weak lensing source galaxy redshift distributions from clustering measurements. In particular, we cross-correlated the weak lensing source galaxies sample with *redMaGiC* galaxies (luminous red galaxies with secure photometric redshifts) and BOSS/eBOSS galaxies (with spec-z estimates) divided into thin redshift bins. We used the measured cross-correlations to inform the posterior of the redshift distributions from the fiducial DES Y3 photo-z code (SOMPZ). These is achieved using two methods: a method that focuses on the mean of the redshift distributions (mean-matching), and another method that forward model the full clustering signal (shape-matching), modeling the full shape of the redshift distributions.

We characterised the systematic uncertainties of each method in simulations. We found that both methodologies are limited by the lack of modelling of the redshift evolution of the galaxy-matter bias of the unknown sample, and that they are estimated to recover the mean redshift of the distributions with a redshift accuracy of ~ 0.015. We found that for the DES Y3 analysis, the clustering information does not help tightening the scatter on the mean of the SOMPZ distributions, given the superior constraining power of the latter. On the other hand, the shape-matching method does significantly tighten the scatter of the shape of the SOMPZ realisations. This is due to the fact that the SOMPZ realisations suffer from sample variance, as they are estimated from relatively small deep fields; as a consequence, SOMPZ realisations show the characteristic "peaky" features typical of sample variance, which are reduced by the combination with the clustering measurements.

We then presented the clustering-based calibration on data, finding consistent results with our simulation tests. We remind the reader that the final DES Y3 redshift calibration strategy includes an additional step, not addressed here: once the SOMPZ realisations have been informed by the clustering-based estimates, they are further constrained by the "shear-ratio" test during the cosmological inference process.

Despite the limits of the current clustering-redshift techniques, they still represent one of the most credible alternative to standard photo-z methods for the new, upcoming generation of data sets, which will be deeper than the

current data sets and therefore harder to calibrate using photo-z methods. In this respect, clustering techniques will not be particularly affected by the increased depth of the samples. One of the key aspect that requires additional work is the modelling of the evolution of the galaxy-matter bias of the unknown sample. In principle we believe we could be able to constrain it to some level by measuring the auto-correlation of the unknown sample in small deep fields with good photometry and redshift estimates. This possible improvement is left to a future work. We also note that for the final DES Y5 analysis we plan to combine the clustering-based and photo-z estimates in a more principled way, using the hierarchical Bayesian methodology developed by Sánchez & Bernstein (2019) and Alarcon et al. (2019).

Part III

Shape Catalogue

In this part we present the official DES Y3 shape catalogue used for the main DES Y3 cosmological analysis, along with a battery of systematic tests performed to assess the quality of the catalogue. The DES Y3 shape catalogue contains $\sim$ 100 million shapes, constituting the largest weak lensing shape catalogue up-to-date. The work presented in this Chapter is going to be published in Gatti & Sheldon, et al. (DES collaboration) together with the DES Y3 cosmological release.

Chapter 5

DES Y3 shape catalogue

5.1 Introduction

The measurement of weak gravitational lensing is an important component for constraining dark energy with current and planned imaging surveys (e.g. Kuijken et al., 2015; Takada, 2010; DES, 2005; Ivezic et al., 2008; Laureijs et al., 2011; Spergel et al., 2015). For the Dark Energy Survey (DES, 2005; Flaugher et al., 2015), weak lensing is one of four "key probes", the others being galaxy angular clustering, galaxy cluster abundances, and type IA supernovae distances. With these combined probes, DES will constrain cosmological parameters such as the dark energy equation of state parameter w with high precision. The goal of this work is to present empirical tests of the weak lensing measurements performed on the DES year 3 data set (DES Y3) in order to assess systematic errors that may degrade this precision.

Weak gravitational lensing is the deflection of light as it passes by mass concentrations in the universe (Schneider et al., 1992). The distant objects observed in our images appear in a different location than they would had their light passed through a homogeneous universe. This deflection can be inferred only in the rare cases that the unperturbed light path is known, for example in strong lens systems with multiple images of the source (Walsh et al., 1979). There is a higher order effect that can be inferred without such knowledge: the light deflections differ slightly across the face of a galaxy, resulting in a small distortion of the image. This distortion induces an ellipticity that is directly related to the mass concentrations that caused the deflections. This weaker "shear" effect results in a departure from isotropy in the orientations of galaxies that is spatially coherent: the ellipticities of galaxies become correlated on the sky (see, e.g. Bartelmann & Schneider,

2001, and references therein).

Because the shear is directly related to the lensing mass, the effect can be cleanly predicted given an accurate model of the mass concentrations. In turn, the distribution of matter in the universe inferred by modelling the shear signal depends sensitively on the cosmological parameters, such as the mass density Ω_m and the equation of state of the Dark Energy (Hoekstra & Jain, 2008).

In the past decades a large variety of methods to infer the value of the shear field have been developed. Many of them use galaxy ellipticies as a proxy of the shear field, which usually involves assigning a set of numbers to each galaxy describing the observed galaxy light profile, once having assumed a galaxy model. In order to infer the shear from measured ellipticities, one must therefore understand how the intrinsic ellipticities of galaxies are modified by gravitational shear, as well as other more mundane effects such as the point spread function of the atmosphere, telescope, and detector (Bernstein & Jarvis, 2002). In addition, there are often biases present in the determination of the shape itself due to noise rectification or model misspecification (Hirata et al., 2004; Refregier et al., 2012b; Melchior & Viola, 2012b; Bernstein, 2010). We note that there exist methods to infer the shear field that do not require a per-galaxy shape estimate, which allows to avoid model biases (e.g., Schneider et al. 2015, or the BFD algorithm proposed by Bernstein et al. 2016). None of these methods are considered in this work, but we are planning to implement BFD in future DES shape catalogues.

We can generally divide biases in the shear determination into two broad categories: additive and multiplicative biases. Following standard notation (Mandelbaum et al., 2014), we can write an estimate of the two-component shear as:

$$\boldsymbol{\gamma}^{\mathbf{est}} = m\boldsymbol{\gamma} + \boldsymbol{c}, \tag{5.1}$$

where $\boldsymbol{\gamma}^{\mathbf{est}}$ is a biased estimate of the true shear $\boldsymbol{\gamma}$. We call m the multiplicative and $\boldsymbol{c}$ the additive, or shear independent bias.

These biases can arise from a number of different causes. PSF-misestimation can contribute to both multiplicative and additive biases: if the size of the PSF is misestimated, a multiplicative bias will occur. If the ellipticity of the PSF is misestimated, an additive bias will occur that is related to the PSF orientation. Another cause of multiplicative bias is calibration errors in the shear estimation algorithm itself, the method for converting an ensemble of ellipticity measurements into an estimate of a shear signal. This can occur for a number of reasons, for example if the shear is not accurately inferred

from the observed shapes due to aforementioned modelling errors or noise effects, or if any applied empirical or simulation based corrections have limited accuracy. In addition, selection, and detection effects can contribute significant shear-dependent or PSF-dependent biases (Kaiser, 2000; Bernstein & Jarvis, 2002; Bernstein et al., 2016; Hoekstra et al., 2017; Sheldon & Huff, 2017).

In this Chapter we present the weak lensing shape catalogue measured in DES Year 3 (DES Y3) imaging data, and perform empirical tests of the catalogue in order to access potential biases. We focus on empirical tests of bias. Our primary tool is the "null test": we generate measurements that should yield zero signal in the absence of biases in the shape catalogue. For example, if our PSF modelling is accurate we should detect no correlation between object ellipticities and PSF ellipticities. Similarly, we should see no correlation between object ellipticities and unrelated quantities such as the location of an object's image within the focal plane and observing conditions.

The work presented in this Chapter is complemented by two papers in preparation. The first one describes in more depth the PSF modeling used in the DES Y3 analysis (Jarvis et al., 2020), and presents a number of diagnostic tests that are independent of the shape catalogue. The second work (MacCrann et al., 2020) describes the suite of image simulations used to provide the overall calibration of the catalogue. Indeed, some biases are difficult to test empirically due to the lack of an absolute calibration source for shear. In particular, noise and modelling biases, or biases that remain after applying an empirical calibration correction. For tests of the absolute calibration we therefore rely on simulations (MacCrann et al., 2020).

The specific method we employ for shear estimation in DES Y3 is METACALIBRATION[1] (Huff & Mandelbaum, 2017; Sheldon & Huff, 2017). This method is known to be unbiased for isolated galaxy images in the limit of weak shear. METACALIBRATION empirically corrects for noise, modelling, and selection biases (Sheldon & Huff, 2017). However, METACALIBRATION will suffer a bias due to some of the effects mentioned above, for example PSF misestimation, and we will test such biases in this work. The blending of galaxy images produces a calibration bias that is not addressed by the METACALIBRATION implementation used for DES Y3, and which is large

[1]In particular, we used the following packages:

- ngmix: v1.0.0, https://github.com/esheldon/ngmix
- ngmixer: v0.9.6, https://github.com/esheldon/ngmixer

enough that cannot be ignored for the DES Y3 analysis. In future releases we will apply empirical corrections using the METADETETCTION method presented in Sheldon et al. (2019). For DES Y3, we instead rely on the aforementioned simulations to derive a correction.

Contrary to the DES Y1 analysis where two different shape catalogues were produced with two different pipelines (Zuntz et al. 2018), we only rely on one shape catalogue in the DES Y3 analysis. Despite having two different catalogues in the DES Y1 analysis increased our confidence in the robustness of the catalogues calibration, the DES Y3 shape catalogue is backed up by a much more powerful and accurate suite of image simulations (MacCrann et al., 2020) compared to those used in the DES Y1 analysis. These image simulations replicate with high fidelity the features and properties of the DES Y3 shape catalogue, making us confident of the catalogue calibration.

The outline of the Chapter is as follows: in § 5.2 we outline the new observations used in the Y3 analysis, and present improvements compared to DES Y1 observations. Updates concerning PSF modelling and PSF estimation tests are presented in § 5.3. In §5.4 we discuss few technical aspects of the METACALIBRATION algorithm implemented in the DES Y3 analysis. In § 5.5 we discuss systematic tests associated to the PSF modelling, and in § 5.6 we present null tests of the shape catalogue, including shear variations in focal plane coordinates (§ 5.6.1), stellar contamination of the catalogue (§ 5.6.2), B-modes tests (§ 5.6.3), galaxy properties, and observing conditions tests (§ 5.6.4). in § 5.7 we summarise our results.

5.2 Data

5.2.1 New observations and footprint

The DES Y3 data represent a significant increase in total area compared to the Y1 data, with a similar depth. Slightly modified Data Management settings have lowered the threshold for detection (DES collaboration, 2020e), enabling an increase in the number of objects, more than expected from the increased area and depth alone. The effective area of the wide survey with observations in the *griz* bands, after masking for foregrounds and other problematic regions[2], is $\sim$4143 deg^2, compared to the $\sim$1321 deg^2 for the Y1 cosmic shear results (Troxel et al., 2018). The area coverage is shown in Fig. 5.1. Object selection additionally required that the object

[2] `FLAGS_FOREGROUND`=0 and `FLAGS_BADREGIONS`< 2

belonged to the Gold catalogue (DES collaboration, 2020e), that it was not marked as 'anomalous'[3] and that it was successfully measured and where necessary, deblended by the multi-object fitting code, which simultaneously fits blended groups or isolated objects in the full multi-epoch, multi-band dataset (DES collaboration, 2020e). This resulted in a final catalogue of 326,049,983 objects. For weak lensing, further cuts were performed using quantities measured as part of the METACALIBRATION procedure. For details see § 5.4.2.

The Y3 dataset includes other improvements, such as $\sim$ 0.003 magnitude photometric accuracy, better object flagging in the coadd catalogues, and a more complete array of survey property maps, see DES collaboration (2020e) for details.

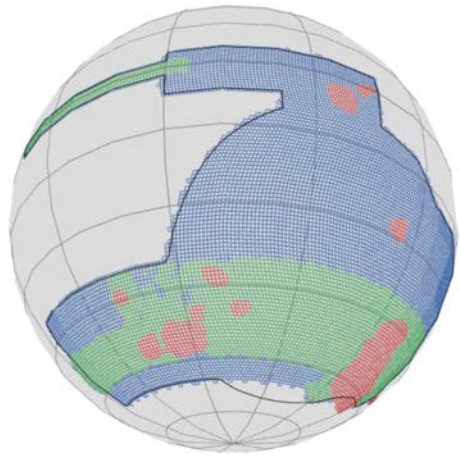

Figure 5.1: Footprint of the DES Y3 shear catalogue. The Y3 catalogue is shown in blue. For comparison the SV and Y1 footprints, which are nearly subsets of the Y3 are, are overplotted in red and green respectively.

5.2.2 Astrometry

Linearised astrometric solutions were derived for the pixels surrounding each Y3 target galaxy using methods similar to those of the Y1 reductions (DES collaboration, 2020e). Substantially improved solutions were, however, available for Y3 using the characterization of the DECam astrometric distortions derived in Bernstein et al. (2017). The new solutions incorporated small-scale distortions due to stray electric fields in the detectors, and were registered to the Gaia DR1 catalogue (Gaia Collaboration et al., 2016). The dominant sources of astrometric calibration error are the 5–10 milliarcsec distortions induced by atmospheric turbulence in a typical exposure, with a smaller contribution from proper motions of the reference stars during the $\approx$ 2-year span of the imaging. The improved astrometric solutions were applied to both the PSF determination

[3] `FLAGS_GOLD`< 8

and to the METACALIBRATION input postage stamps.

5.2.3 Blinding of the catalogue

A two-stage blinding procedure was adopted in the DES Y3 analysis to mitigate confirmation bias and avoid experimenters to (intentionally or unintentionally) tune the analysis to match expectations. A good blinding scheme must be capable of altering the output of the analysis without compromising the performance of systematic tests and pipeline validation. In particular, for the DES Y3 analysis we adopted a blinding scheme both at the shear catalogue level and at the summary statistics level.

The blinding of the shear catalogue was performed in a similar fashion to the DES Y1 analysis (Zuntz et al., 2018). The ellipticities $\mathbf{e}$ of the catalologue were transformed via $|\eta| \equiv 2\text{arctanh}|\mathbf{e}| \rightarrow \text{f}|\eta|$, with a hidden value $0.9 < f < 1.1$. This mapping preserved the confinement of the e values to the unit disc while rescaling all inferred shears.

The preliminary (yet non-published) results shown throughout this Chapter have been obtained using the blinded version 3.30.20 of the DES Y3 catalogue.

5.3 PSF modelling and estimation

5.3.1 PSF Measurement and Interpolation using PIFF

For modeling the point-spread function (PSF), a new software package, PIFF (PSFs In the Full FOV)[4] was used. The full details of this software are described in Jarvis et al. (2020), but here we give an overview of some salient features used in the DES Y3 analysis.

PIFF has a number of available models it can use to describe the PSF at any given location, as well as a number of possible interpolation schemes to calculate the coefficients of the model at different locations. For DES Y3, the `PixelGrid` model was used, which involves a grid of pixels, each with an independent amplitude at their centers. The amplitudes of the PSF between pixel centers were found using Lanczos interpolation (in particular, we used Lanczos interpolation kernels up to 3rd order). For DES Y3, we used for the model pixels of 0.3 arcsec on a side, slightly larger than the native image pixels (0.27 arcsec). It was found that this significantly increased

[4]Specifically, the PSF modeling used release version 0.2.2.

the stability of the fits and reduced the prevalence of noise artifacts in the solutions.

To interpolate the PSF model at other locations besides the locations of the stars, a 3rd order `BasisPolynomial` was used, which delayed the solution of the model coefficients for each star until also solving for the interpolation coefficients. This helped handle moderately degenerate solutions for some stars (e.g. stars with masks that cover one or more of the model pixels), as it allowed for all of the other stars help constrain the overall fit.

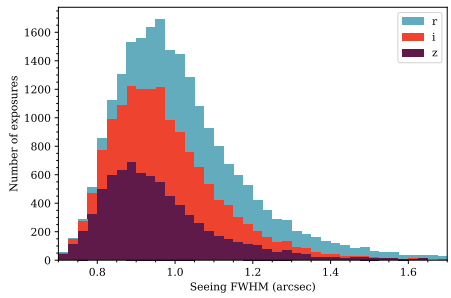

Figure 5.2: The distribution of the median seeing FWHM of the stars used to model the PSF in the riz-bands. The median seeing for the distributions shown is 1.05" in the r-band, 0.97" in the i-band and 0.93" in the z-band. The overall median seeing is 0.98".

Piff models the PSF in sky coordinates, rather than image coordinates. We used the `PIXMAPPY` [5] astrometric solutions to map from image coordinates to sky coordinates. This was a particularly important improvement over the Y1 PSF models, since the DES images have significant tree rings (Estrada et al., 2010; Plazas et al., 2014b,a), where the jacobian of the astrometric solution changes significantly across regions with only a few stars. When the modeling is done in sky coordinates, these variations can be removed using the highly accurate astrometric solutions, so these variations did not need to be included in the PSF interpolation.

5.3.2 Selection of PSF stars

Similar to Zuntz et al. (2018), the initial selection of candidate PSF stars used a size-magnitude diagram of all the objects detected per image. For the magnitude, we used the `SEXTRACTOR` (Bertin & Arnouts, 1996b) measurement `MAGAUTO`. For the size, we used the scale size as measured with `Ngmix` (Sheldon, 2015). The stars were easily identified in each exposure (and for different bands) at bright magnitudes as a locus of points with size nearly independent of magnitude. On the other hand, the galaxies have a

[5] https://github.com/gbernstein/pixmappy

range of sizes, all larger than the PSF size. The candidate PSF stars were taken to be this locus of objects from about $m \approx 16$, where the objects begin to saturate, down to $m \approx 22$, where the stellar locus merges with the locus of faint, small galaxies.

From the list of candidate stars, we removed objects that were not suitable to use as models of the PSF. In Y1, we removed all objects within 3 magnitudes of the faintest saturated star in the same CCD exposure. This was done to avoid the interaction of charges in CCDs with the already accumulated charge distribution, which can cause an increase of observed size with flux, an effect also known as the "brighter-fatter effect" (Antilogus et al. 2014; Guyonnet et al. 2015; Gruen et al. 2015; Coulton et al. 2018; Lage 2019; Astier et al. 2019; see § 5.5.1). For DES Y3 we exploited the correction described in Antilogus et al. and implemented for DECam/DES in Gruen et al. (2015) as part of the initial image processing (but see Coulton et al. 2018 for an alternative correction method). The correction has been applied after flat fielding and before the sky correction, which reduced the level of this effect seen on the images and allowed the selection of brighter stars. In particular, we imposed a lower magnitude limit which varies between CCD exposures and band considered, but typically of magnitude ~ 16.5 (to be compared to the Y1 cutoff at ~ 18.5). More details are provided in Jarvis et al. (2020). In the final star catalogue, each star has different entries for each exposure (and therefore band), as the DES Y3 PSF model is different for each exposure. Out of all the stars passing these selection cuts, we did not use $\sim 20\%$ of the stars to model PSF and used them for diagnostic tests (§ 5.5.3).

In Fig. 5.2, we show the distribution of the median measured full-width half-maximum (FWHM) for the PSF stars used in our study, restricted to the exposures used for shear measurements. The overall median seeing is 0.98".

5.4 The METACALIBRATION shape catalogue

In this section we discuss few more technical aspects of the METACALIBRATION algorithm implementation used for the DES Y3 analysis, as the algorithm has already been introduced in § 3.1.3.

5.4.1 Differences Between the Y3 and Y1 Catalogues

The METACALIBRATION shape catalogue differs from DES Y1 in the following ways:

- PIFF PSF solutions were used for the METACALIBRATION deconvolutions rather than the PSFEx solutions that were used for Y1 (See §5.3.1).
- The jacobian of the WCS transformation was taken from the PIXMAPPY astrometry solutions (see §5.2.2).
- We altered the weak-lensing selection criteria (see §5.4.2).
- We applied an inverse variance weight to galaxies (see §5.4.3).

In addition to these differences, we also applied a calibration correction (2-3%) to the catalogue based on simulations MacCrann et al. (2020). This correction mostly calibrates a *shear-dependent detection bias* which affects the shear estimates when objects are blended. We do not expect the aforementioned detection related biases to be addressed by the tests in this Chapter. The tests presented herein are mainly sensitive to additive shear biases. The multiplicative biases we can test empirically, e.g. those due to PSF measurement errors, are independent of the detection effects mentioned above. A short description of the absolute calibration corrections from image simulations is given in § 5.4.5, but we refer the reader to MacCrann et al. (2020) for a more detailed discussion.

5.4.2 Object Selection from the METACALIBRATION Catalogue

Here we discuss the weak lensing selection employed in all the DES Y3 shear analyses. Additional selections in analyses, such as tomographic binning, incur selection biases that must be accounted for with the selection response, $\boldsymbol{R_s}$.

We performed METACALIBRATION measurements on all objects detected by SExtractor in the DES coadds, using the *riz* bands. We excluded the *g* band measurements due to known issues in the estimation of the PSF (see Jarvis19 for a discussion). The Y3 detections are significantly different from those in Y1 due to changes to the SExtractor configuration that resulted in a more pure and complete catalogue (DES collaboration, 2020e).

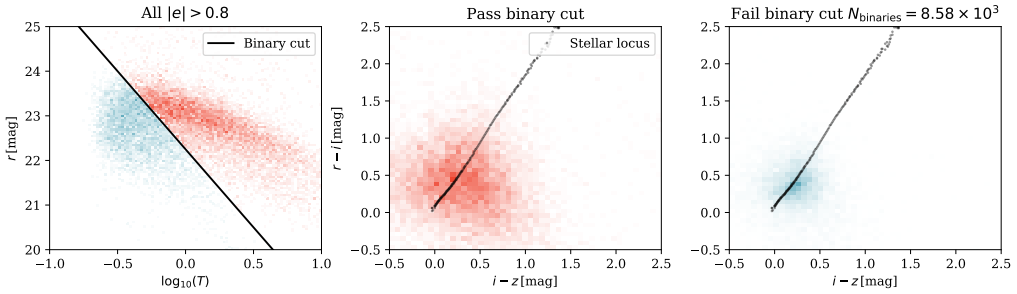

Figure 5.3: Shear bias from contamination by unresolved binary stars. *Left* shows the cut applied to isolate unresolved binaries from the population of objects in in our catalogue with measured $|e| > 0.8$, *centre* shows objects from above the cut, which have galaxy colors, and *right* shows objects below the cut, which have stellar colors.

A small subset of objects (less than a percent) were not measured due to lack of data in one or more bands, typically near the survey boundaries.

For objects processed with METACALIBRATION, we made the following further selections:

- The object measurements had to belong to the unmasked regions of the DES Y3 Gold catalogue after problematic regions have been removed and had not to be marked as 'anomalous' (DES collaboration, 2020e). These selections should be nearly shear independent.

- We selected objects with $10 <$ S/N< 1000, as determined by the Gaussian fit to the unsheared image. The S/N definition is the same as used in (Zuntz et al., 2018). The low cut limited faint objects impacted by detection biases. The high cut removed very bright objects, for which Poisson noise could create fluctuations larger than the typical background noise, erroneously flagging the detections as problematic[6].

- We selected the objects with galaxy to PSF size ratio as, $T/T_{\rm PSF} > 0.5$, as in DES Y1, to reduce the impact of PSF modeling errors. T is a measure of the size squared of the object before convolution by the PSF. T is defined the same way as in (Zuntz et al., 2018), as the trace of the covariance matrix fit to the unsheared image. The $T_{\rm PSF}$,

[6]In the implementation used for the DES Y3, matched pixels from different single epoch postage stamps were compared, and if some of the values were too far from the median, they were rejected.

determined by METACALIBRATION is the size squared of the PSF, also from a Gaussian fit.

- We imposed the selection $T < 10$, which removed the largest objects, where T is as previously defined. By visual inspection, many of these detections are not large objects, but their size estimate is affected by the light emitted by close, large neighbours.

- We excluded the objects characterised by $T > 2$ and S/N < 30 simultaneously. These relatively large, faint objects are mostly blends upon visual inspection, and their inclusion could potentially introduce large biases in the catalogue.

- We limited the objects to those for which the most reliable for photometric redshifts could be obtained: $18 < i < 23.5$, $15 < r, z < 26$ and fine-tuning against any outlier colours with $-1.5 < r, z - i < 4$.

- We imposed a selection to limit the binary star contamination of the galaxy catalogue. For high-ellipticity objects of the shape catalogue, unresolved binary stars could contribute significantly and are difficult to distinguish from galaxies. Following Hildebrandt et al. (2017), we cut our high ellipticity ($|e| > 0.8$) shape catalogue in r magnitude – size (T) space according to: $\log 10(T) < (22.5 - r)/2.5$ (see left panel of Fig. 5.3. Color-color plots of these objects more closely follow a stellar locus than the remainder of the catalogue (central and right hand panels of Fig. 5.3). We hence inferred that these were indeed unresolved binary stars and removed them from the shape catalogue. These objects constituted 20% of the $|e| > 0.8$ objects in the shape catalogue before their removal.

All the selections described here are combined using logical conjunction to obtain our final weak lensing selection. Except for the first selection, all the others are shear dependent and can induce a selection bias that can be corrected for using the selection response term $\boldsymbol{R_s}$. We recall that in the current implementation of METACALIBRATION detection effects are not corrected for by any selection response terms, and need to be calibrated for using image simulations. The selection discussed here constitutes a reliable weak lensing selection and is encompassed in a `SELECT` column, applied for all tests detailed in this Chapter, as well as further studies. The number of objects passing this selection is 100,202,538.

5.4.3 Inverse variance weight

An estimator of a shear signal is usually a linear combination of individual galaxy shapes. In that linear combination, one can assign equal weight to each galaxy or alternatively, a different weight w_i to each galaxy. A change of that weight with shear could introduce selection biases which, however, can be corrected by the METACALIBRATION formalism if the weight is determined from quantities also measured on artificially sheared versions of the galaxy image. For minimising the variance of the measured shear signal, it can be shown that the weight should be proportional to the inverse of the variance of the shear estimated from each galaxy.

The variance of mean shear estimated from a sample of galaxies as in Eq. 3.6 is

$$\sigma_\gamma^2 = \sigma_e^2 \langle \boldsymbol{R}_\gamma \rangle^{-2} \,, \tag{5.2}$$

where σ_e^2 is the variance of e[7], including intrinsic and measurement-related shape noise. While for any individual galaxy it is difficult to evaluate Eq. 5.2, e.g. due to the noise in $\boldsymbol{R}_\gamma$, for a large ensemble of galaxies it is straightforward to estimate both σ_e^2 and $\langle \boldsymbol{R}_\gamma \rangle^{-2}$.

We therefore chose to estimate σ_γ^2 and thus assigned a piecewise-constant $w_i = \sigma_\gamma^{-2}$ for ensembles of galaxies binned by the quantities S/N and $T/T_{\rm PSF}$ used in the object selection § 5.4.2. We used these two quantities because they are main proxies for measurement-related shape noise and variations of response.

Fig. 5.4 shows the counts, $\langle \boldsymbol{R}_\gamma \rangle$, and σ_e^2 of galaxies in 20×20 logarithmically scaled bins of S/N $= 10 \ldots 300$ and $T/T_{\rm PSF} = 0.5 \ldots 5$. The upper limit of each range is chosen such that more than 97.5% of the sample lies below it. Remaining galaxies with large S/N or $T/T_{\rm PSF}$ are subsumed to the respective last bin.

While shear response is a mostly monotonous function of S/N and a weak function of size, we found the scatter in measured ellipticity to have more complex behavior. Visual inspection of samples of galaxies with small and large size ratio at high S/N, and with small and large S/N at large size ratio indicated that this is a result of how galaxy morphology maps to this space of observed properties: the large scatter in ellipticity of galaxies with large S/N and size ratio results from the incidence of highly elliptical, nearly edge-on disk galaxies.

[7] We compute it as $\sigma_e^2 = \frac{1}{2}\left[\frac{\sum (e_{i,1})^2}{n_{\rm gal}^2} + \frac{\sum (e_{i,2})^2}{n_{\rm gal}^2}\right]$.

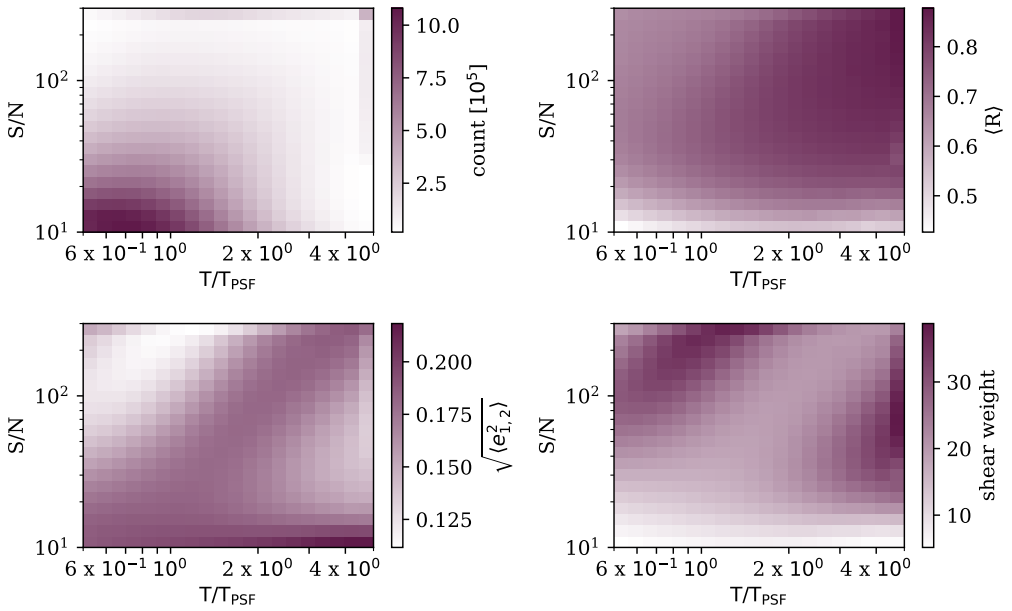

Figure 5.4: Properties of the Y3 METACALIBRATION catalog as a function of galaxy S/N and size ratio (defined as the ratio between galaxy size and PSF size). *Top left:* galaxy number counts; *top right:* METACALIBRATION response, as defined in § 5.4; *bottom left:* root-mean-square of components of galaxy ellipticity; *bottom right:* shear weights, as defined in § 5.4.3.

Table 5.1: Number density values and noise per component using the different definitions described in § 5.4.4. The last two columns,c_1 and c_2, indicate the per-component mean shear measured in the catalogue.

Definition	$n_{\rm eff}$	σ_e	c_1	c_2
			0.00036	0.00006
Chang+13	5.328	0.258		
Heymans+12	5.592	0.265		

The inverse-variance weighting significantly increases the statistical power of the METACALIBRATION catalog;without weighting of galaxies, the fiducial sample (S/N> 10) triples the statistical power of DES Y1. Inverse-variance weighting increases this further by $\approx 25\%$. The relative gain in statistical power is only a weak function of the S/N cut-off chosen. However, we note that for even lower S/N than the minimum of 10 usable here, the statistical power of the unweighted catalog has a maximum in the cut-off S/N due to the noise introduced by faint galaxies.

5.4.4 Number Density

After applying the appropriate selections, the effective number density, $n_{\rm eff}$, and shape variance, $\sigma_{\rm e}$, are computed and reported in Table 5.1, using the definitions from Chang et al. (2013) and Heymans et al. (2012). These quantities, together, typically quantify the overall constraining power of a shape catalogue as the variance of the estimated shear, $\sigma_\gamma^2 = \sigma_e^2/n_{\rm eff}$.

The definition for the effective number density is given by Chang et al. (2013) in terms of the area of the survey, A, as:

$$n_{\rm eff}^{\rm C13} = \frac{1}{A}\sum \frac{\sigma_{\rm sh}^2}{\sigma_{\rm sh}^2 + \sigma_{\rm m,i}^2}\,. \tag{5.3}$$

The shape noise variance, $\sigma_{\rm sh}$, is estimated from the high signal-to-noise objects, which have minimal measurement noise, accounting for the METACALIBRATION response. For METACALIBRATION the measurement noise term $\sigma_{\rm m,i}$ is estimated from the estimated measurement covariance matrix, accounting for the response term.

Alternatively, the definition by Heymans et al. (2012) is given in terms

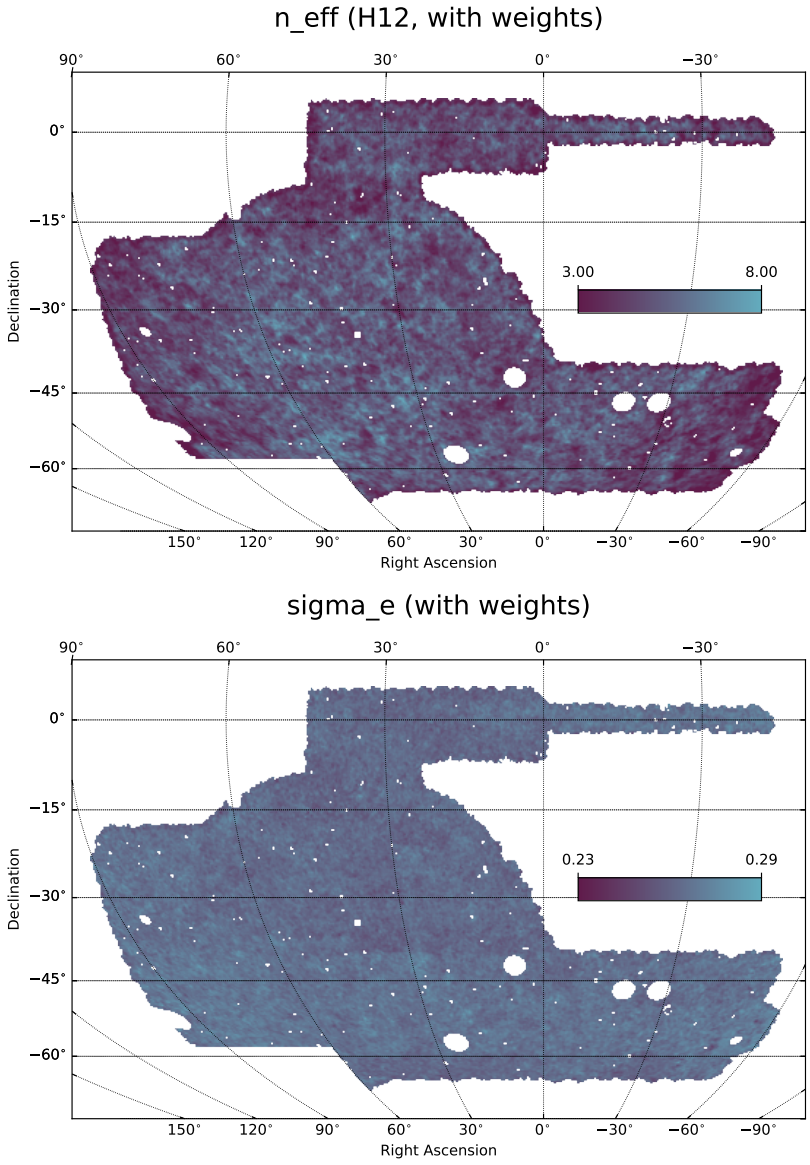

Figure 5.5: Weighted effective number density, $n_{\rm eff}$, and shape variance, σ_e, of sources in the weak lensing selection across the survey footprint.

of the shear weight, w_i, for each galaxy as:

$$n_{\rm eff}^{\rm H12} = \frac{1}{A}\frac{(\sum w_i)^2}{\sum w_i^2}\,. \tag{5.4}$$

The shape variance is given by,

$$\sigma_{\rm eff}^{\rm H12} = \frac{1}{2}\left[\frac{\sum(w_i e_{i,1})^2}{\sum(w_{i,1})^2} + \frac{\sum(w_i e_{i,2})^2}{\sum(w_i)^2}\right]\left[\frac{(\sum w_i)^2}{\sum w_i^2}\right]\,. \tag{5.5}$$

We use the H12 definition to compute the analytical covariances needed for the cosmic shear cosmological analysis (Amon et al., 2020; Secco et al., 2020). In Table 5.1 we further report the per component mean ellipticity measured in the catalogue. In particular, the mean shear measured for the first component is larger than the expected mean shear from cosmic variance ($\sim 0.5\ 10^{-5}$). The mean ellipticity needs to be subtracted before any science application. More details about the potential origin of such mean shear are provided in § 5.6.4.

Fig. 5.5 shows the spatial pattern of the weighted effective number density of the survey, as well as the shape variance.

5.4.5 Absolute calibration from image simulations

In the implementation adopted for the DES Y3 analysis, our shear measurement pipeline needs to be further calibrated against image simulations (MacCrann et al., 2020). The main reason is that the implementation of METACALIBRATION used in DES Y3 suffers from a shear-dependent detection bias of the order of 2-3 per cent, in case of blended galaxies. This bias also depends on redshift, as blending often occurs between galaxies along the same line-of-sight but located at different redshifts. We recall that empirical tests can hardly measure multiplicative shear biases, due to the lack of absolute calibration. The use of image simulations allows us to further test other aspects of the pipeline, isolating individual effects generating shear calibration biases by running variations of the fiducial simulations and quantifying their relative importance. At the moment of writing this thesis the tests on the DES Y3 image simulations are not completed, despite being already in an advanced stage; therefore, we can only report that the preliminary DES Y3 shear calibration is expected to calibrate up to a 2-3 per cent multiplicative shear bias with an accuracy of the order of 0.5 per cent.

5.5 PSF Diagnostics

In this section we detail the systematic effects that are connected to the DES Y3 PSF model and residuals. In particular, we discuss the tests we performed on:

- the impact of the brigher-fatter effect (§ 5.5.1) in the stars used for the PSF modeling;
- dependencies of the PSF model residuals on stars and galaxy colors (§ 5.5.2);
- additive biases due to PSF misestimation (§ 5.5.3) using ρ statistics (Rowe, 2010), both in real space and focal plane coordinates.

These tests aim at empirically detecting biases in the shape catalogue due to PSF modeling errors. Additional tests of the DES Y3 PSF modeling that are independent of the shape catalogue can be found in the DES Y3 PSF model paper (Jarvis et al., 2020).

5.5.1 Brighter-fatter effect

The interaction of charges in CCDs with the already accumulated charge distribution causes an increase of observed size with flux, also known as the brighter/fatter effect (Antilogus et al., 2014; Guyonnet et al., 2015; Gruen et al., 2015). In Fig. 5.6 we show size residuals (upper panel), fractional size residuals (second panel), and e_1 and e_2 shape residuals (lower panel) of the `PIFF` model for the reserved stars catalogue, relative to the actual PSF measurements, as a function of their magnitude. The impact of the brighter-fatter effect observed in DES Y1 was reduced by the exclusion of the bright stars from the PSF modeling procedure, with the cut-off varying between CCD exposures, but typically at magnitude ∼18.5. For DES Y3, we implemented a correction of the effect (Gruen et al., 2015; Morganson et al., 2018), which allowed for the utilisation of stars down to a magnitude brighter than ∼16.5. The gain of stars two magnitudes brighter than those considered in the Y1 analysis contributed to improving the PSF solutions for DES Y3. For stars brighter than ∼16.5, an upturn in the size residuals can still be seen, indicating that the correction implemented was not enough to remove the brighter-fatter effect for the brightest objects. On the other hand, for the stars passing the cut, the fractional size residuals are below 0.5 percent, and the trend with magnitude does not show the typical signature

of the brighter-fatter effect. Shape residuals show no significant trend with magnitude within the same magnitude range.

5.5.2 PSF residual with colour

We investigate the dependence of the PSF residuals on the colour of the stars, as compared to the colour of galaxies, in order to ensure that the PSF is well matched to the galaxies. In general, different effects cause the PSF to be wavelength-dependent (Plazas & Bernstein, 2012; Meyers & Burchat, 2015); no chromatic correction is included in the DES Y3 PSF model, so if the typical colors of the stars used to model the PSF are different from those of the galaxy sample, this can induce a bias. We anticipate that the DES Y6 PSF model will include a chromatic correction in the form of a single color parameter to be included during the PSF fit (see Jarvis et al. 2020 for more details), but this has not been included in the DES Y3 PSF model as it was deemed not necessary.

Fig. 5.7 shows the PSF size, the fractional PSF size and shape residuals as function of color. A noticeable dependence on color can be seen. It is possible that part of the mean shear trend can be explained by differential chromatic diffraction, while the PSF size trend is probably dominated by Kolmogorov seeing (Jarvis et al., 2020), but further investigation is needed to fully clarify the nature of these trends. In each panel, the median color of the DES Y3 galaxy sample is over-plotted, which corresponds to $(r-z) = 0.75$, as well as the 20th and 80th percentile color of the sample. This indicates that most of the sample is within $dT/T < 0.002$ and $\Delta e < 0.0001$, deemed acceptable as it would roughly correspond to an additive bias of the same order of magnitude of the expected cosmic variance on $\langle e \rangle$ ($\sim 0.510^{-4}$). Even if we do not directly correct for this, we stress that biases due to unaccounted chromatic effects should ultimately be captured by the ρ statistics test, described in the next section.

5.5.3 Additive biases from PSF Modeling: ρ statistics

In this section, the propagation of additive systematic errors due to PSF-misestimation to measurements of the ellipticity of galaxy images is quantified. It is assumed that the observed shape of a galaxy inherits additional contributions due to additive systematic errors and noise:

$$\boldsymbol{\gamma}^{\mathbf{est}} = \boldsymbol{\gamma} + \delta \boldsymbol{e}^{\mathrm{sys}}_{\mathrm{PSF}} + \delta \boldsymbol{e}^{\mathrm{noise}} \tag{5.6}$$

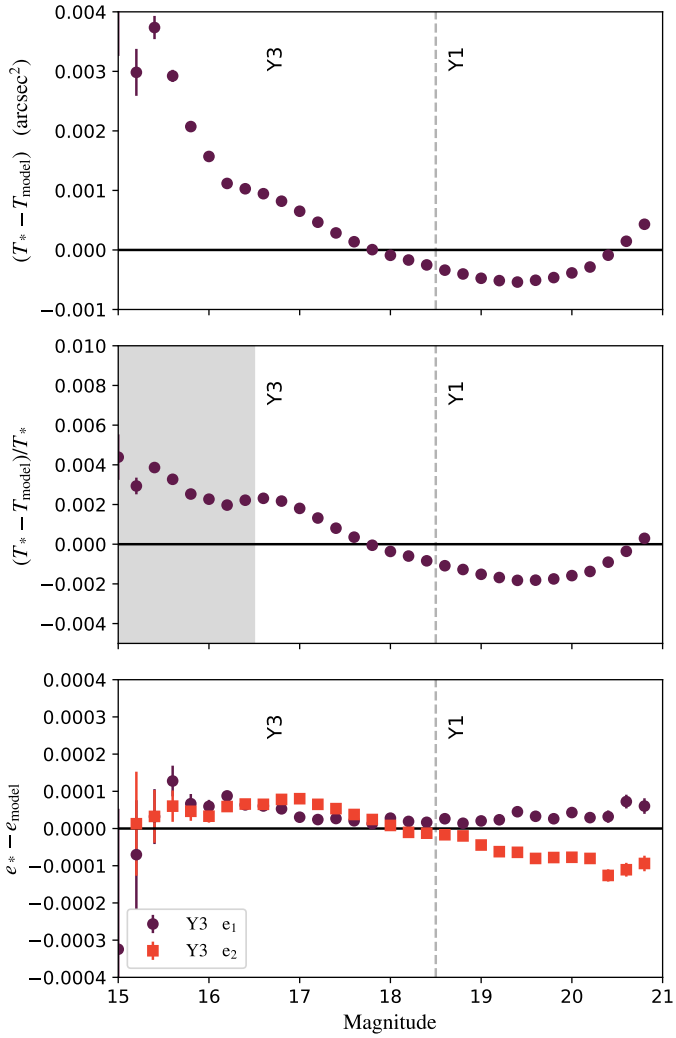

Figure 5.6: The PSF residual size (top), fractional size (middle) and shape (bottom) of stars as a function of their magnitude (relative to the band where the star has been detected). To reduce the impact of the brighter-fatter effect bright stars are excluded from our PSF models; the cut-off varies between CCD exposures but the shaded grey region shows a typical example.For comparison purposes, we also show as a vertical dashed line the cut-off implemented in DES Y1.

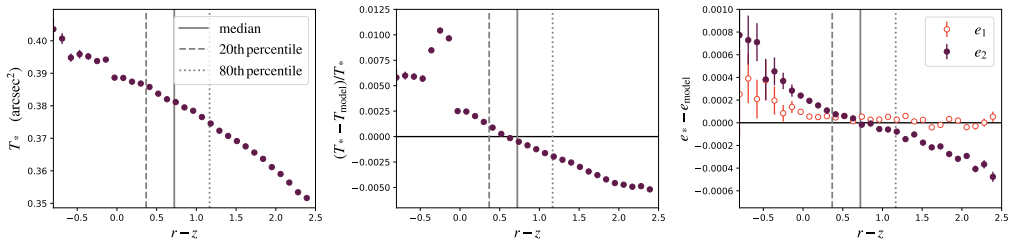

Figure 5.7: The PSF size (left), fractional size (middle) and shape (right) of stars as a function of their $r-z$ colour. For our galaxy sample, the median is $(r-z) = 0.75$ (vertical solid line). Most of the DES Y3 galaxy sample (the vertical dashed lines indicate the 20th and 80th percentiles) is within $dT/T < 0.002$ and $\Delta e < 0.0001$.

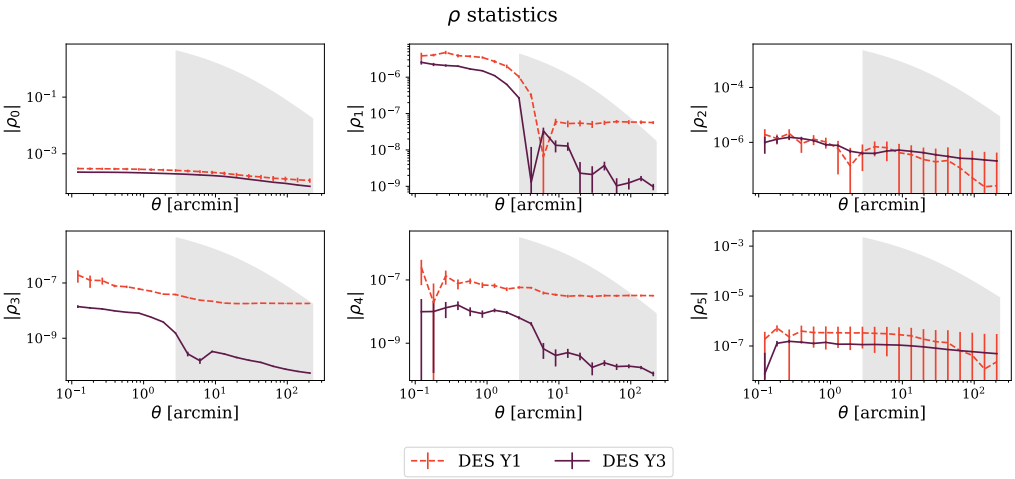

Figure 5.8: Rho statistics as measured for the catalogue of reserved stars. Only the ρ_+ components are shown. DES Y3 values are compared to DES Y1 values, showing a substantial improvement owing to a better PSF modeling. As a order of magnitude comparison, we show as grey region 10 per cent of the weakest expected cosmic shear ξ_- signal, which is from the lowest redshift tomographic bin. In order to effectively compare the cosmic shear signal to each single rho statistics, we divided it by (α^2, β^2, $2\beta\alpha$, η^2, $2\beta\eta$, $2\alpha\eta$), depending whether we compare to ρ_0, ρ_1, etc. We furthermore assumed the following realistic values: $\alpha = 0.001$,$\beta = 1$,$\eta = 1$. We recall this only serves as an order of magnitude comparison, the impact of PSF residuals on the cosmic shear analysis has been quantified in Amon et al. (2020) and deemed negligible.

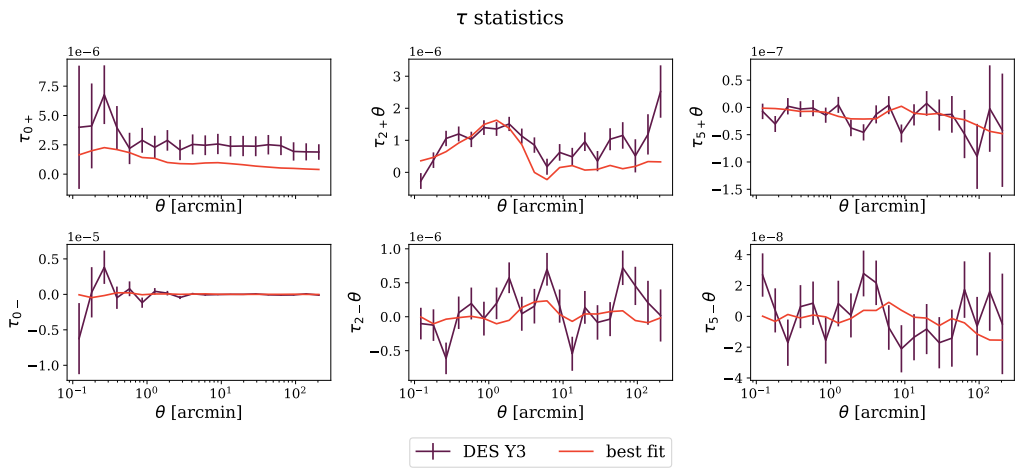

Figure 5.9: Measured τ_+ and τ_- together with the best fit models.

Specifically, $\delta \boldsymbol{e}^{\rm sys}_{\rm PSF}$ quantifies additive systematic biases from PSF modelling errors. Other sources of additive systematic biases are explored in § 5.6.4. Note that, in contrast to Eq. 5.1, Eq. 5.6 does not include any source of multiplicative biases, which are instead discussed in MacCrann et al. (2020) .

While we expect that $\langle \delta \boldsymbol{e}^{\rm noise} \rangle = 0$, detection of a signal for the PSF residual, $\langle \delta \boldsymbol{e}^{\rm sys}_{\rm PSF} \rangle$, would point to a problem. Following Paulin-Henriksson et al. (2008), we describe PSF modelling errors as:

$$\delta \boldsymbol{e}^{\rm sys}_{\rm model} = \alpha e_{\rm model} + \beta \left(e_* - e_{\rm model} \right) + \eta \left(e_* \frac{T_* - T_{\rm model}}{T_*} \right), \qquad (5.7)$$

where α, β, and η are the coefficients we must solve for, e_* is the PSF ellipticity measured directly from stars, $T_{\rm model}$ is the modeled PSF size and T_* is the PSF size measured from stars. The first term on the r.h.s is proportional to the PSF model ellipticity (sometimes this term is referred to as PSF leakage). Non-null α could arise from errors in the deconvolution of the PSF model from the galaxy image (see § 5.4). The second and third terms describe the impact of PSF model ellipticity and size errors. As PSF model errors produce an error in the shear estimate of similar order of magnitude (Paulin-Henriksson et al., 2008), the coefficients β and η are expected to be of the order of unity, although their exact value will depend on the detailed properties of both PSF and galaxy profiles.

For simplicity of notation, we rename the terms on Eq. 5.7 as $\boldsymbol{p} \equiv$

$e_{\rm model}$, $\boldsymbol{q} \equiv \boldsymbol{e}_* - \boldsymbol{e}_{\rm model}$, and $\boldsymbol{w} \equiv \boldsymbol{e}_* \left(T_* - T_{\rm model}\right)/T_*$, and rewrite it as

$$\delta \boldsymbol{e}_{\rm PSF}^{\rm model} = \alpha \boldsymbol{p} + \beta \boldsymbol{q} + \eta \boldsymbol{w}. \tag{5.8}$$

To solve for the three unknown coefficients α, β, and η, we correlated all the observed shears $\boldsymbol{\gamma}^{\rm est}$ (Eq. 5.6) in the METACALIBRATION catalogue with the quantities $\boldsymbol{p}$, $\boldsymbol{q}$, $\boldsymbol{w}$ measured for a catalogue of 'reserved' stars that have not been used to constrain the model of the PSF[8]. Assuming that the true shear signal $\boldsymbol{\gamma}$ does not correlate with PSF modeling errors, we obtain

$$\begin{aligned}
\langle \boldsymbol{\gamma}^{\rm est} \boldsymbol{p} \rangle &= \alpha \langle \boldsymbol{p}\boldsymbol{p} \rangle + \beta \langle \boldsymbol{q}\boldsymbol{p} \rangle + \eta \langle \boldsymbol{w}\boldsymbol{p} \rangle , & (5.9)\\
\langle \boldsymbol{\gamma}^{\rm est} \boldsymbol{q} \rangle &= \alpha \langle \boldsymbol{p}\boldsymbol{q} \rangle + \beta \langle \boldsymbol{q}\boldsymbol{q} \rangle + \eta \langle \boldsymbol{w}\boldsymbol{q} \rangle , & (5.10)\\
\langle \boldsymbol{\gamma}^{\rm est} \boldsymbol{w} \rangle &= \alpha \langle \boldsymbol{p}\boldsymbol{w} \rangle + \beta \langle \boldsymbol{q}\boldsymbol{w} \rangle + \eta \langle \boldsymbol{w}\boldsymbol{w} \rangle . & (5.11)
\end{aligned}$$

All quantities in the above equations are mean-subtracted. The resulting correlations can be re-written in terms of the ρ-statistics (Rowe, 2010; Jarvis et al., 2016; Zuntz et al., 2018): $\rho_0 = \langle \boldsymbol{p}\boldsymbol{p} \rangle$, $\rho_1 = \langle \boldsymbol{q}\boldsymbol{q} \rangle$, $\rho_2 = \langle \boldsymbol{q}\boldsymbol{p} \rangle$, $\rho_3 = \langle \boldsymbol{w}\boldsymbol{w} \rangle$, $\rho_4 = \langle \boldsymbol{q}\boldsymbol{w} \rangle$, and $\rho_5 = \langle \boldsymbol{p}\boldsymbol{w} \rangle$. To make notation even more compact we define: $\tau_0 = \langle \boldsymbol{\gamma}^{\rm est} \boldsymbol{p} \rangle$, $\tau_2 = \langle \boldsymbol{\gamma}^{\rm est} \boldsymbol{q} \rangle$, and $\tau_5 = \langle \boldsymbol{\gamma}^{\rm est} \boldsymbol{w} \rangle$:

$$\begin{aligned}
\tau_0 &= \alpha\rho_0 + \beta\rho_2 + \eta\rho_5, & (5.12)\\
\tau_2 &= \alpha\rho_2 + \beta\rho_1 + \eta\rho_4, & (5.13)\\
\tau_5 &= \alpha\rho_5 + \beta\rho_4 + \eta\rho_3. & (5.14)
\end{aligned}$$

Fig. 5.8 shows the ρ-statistics measured from the catalogue of reserved stars for DES Y3. For comparison purposes, we also show the DES Y1 ρ-statistics; due to better PSF modeling, the DES Y3 ρ-statistics have a substantially smaller amplitude compared to Y1. In DES Y1, some of the ρ-statistics were affected by large-scales constant contributions, which were partially responsible for a non-negligible mean shear measured at the catalog level. For DES Y3, no evident large-scale constant contribution is measured.

It is important to recall that the idea here is not to solve the system of equations in each scale, but instead to find the best scalar parameters α, β, and η that match the τ and ρ measurements within our model. To sample the posteriors of our parameters, we generated Monte Carlo Markov chain (MCMC) samples that map out the posterior space, leading to parameter constraints. To this end, we used the public software package `EMCEE` (Foreman-Mackey et al., 2013), which is an affine-invariant ensemble sampler

[8]The reserved stars constitute 20% of all the stars selected as explained in § 5.3.2.

for MCMC. The τ measurement covariance was estimated using multiple `FLASK` realisations (Xavier et al., 2016), but we also checked that estimating it from jackknife resampling did not change the results. We considered the angular range between 0.1 and 250 arcmin for all measurements. This range also includes scales smaller than the ones used in the main cosmological analysis. We nonetheless checked that including only small scales (< 10 arcmin) or only large scales (> 10 arcmin) did not significantly affect the constraints on the α, β, and η parameters. Finally, we note that before measuring ρ and τ from the catalogs, we assigned weights to stars to balance the ratio of the number densities of stars and galaxies across the footprint at large scales. In this test, we are using the PSF model and residual values of stars under the assumption that stars spatially sample PSF effects the same way galaxies do: therefore, large-scale differences in the number densities might alter the interpretation of the results. Nonetheless, we found these weights to have little impact on the best fitting values of α, β, and η.

The best fitting values for α, β, and η are reported in Table 5.2. The best fitting model to the measured τ is shown in Fig. 5.9. The reduced χ^2 of the best fitting values is $\chi^2 = 2.1$, for 111 d.o.f. We note that the coherent offset of the measured τ_{0+} with respect to the best fitting model is due to data points at scales larger than 1 arcmin being highly mutually correlated. We further checked that the best fitting values were robust against dropping the τ_- components from the system of equations described by Eqs. 5.12, 5.13, 5.14, or against dropping the PSF size residuals from the modelling (i.e., $\eta = 0$.).

We defer the assessment of the impact of PSF modelling uncertainties on our cosmological constraints to one of the DES Y3 cosmic shear papers (Amon et al., 2020). We note though that we expect a smaller impact compared to DES Y1. The α and β values have same order of magnitude of those measured in the DES Y1 analysis (Troxel et al., 2018), but the ρ statistics now have a substantially smaller amplitude, as may be expected from relatively minor updates to shape measurement, but more substantial improvements to PSF modeling since then (Jarvis et al., 2020).

ρ statistics from focal plane-averaged quantities

The values of α, β, and η estimated in the previous section can also be estimated from the correlation with reserved stars in focal plane coordinates. To proceed with this test, we first computed the mean $\boldsymbol{p}$, $\boldsymbol{q}$, and $\boldsymbol{w}$ in focal plane coordinates using the reserved stars catalogue; then, we assigned

Table 5.2: Values of the parameters α, β, and η as estimated from ρ statistics in real space coordinates (left column) and from focal-plane averaged PSF ellipticity, PSF ellipticity residuals and size residual (right column).

parameter	real space	parameter	focal plane
α	-0.001 ± 0.003	α_1	-0.017 ± 0.016
-	-	α_2	-0.046 ± 0.016
β	1.14 ± 0.06	β_1	0.93 ± 0.2
-	-	β_2	1.1 ± 0.2
η	-2.9 ± 0.7	η_1	-4 ± 6
-	-	η_2	-5 ± 6

the quantities $\boldsymbol{p}$, $\boldsymbol{q}$, and $\boldsymbol{w}$ to each galaxy based on the position in focal plane coordinates. Values from differing exposures were averaged. Last, we estimated α, β, and η coefficients performing a linear fit of the mean shear with respect to the focal plane-averaged $\boldsymbol{p}$, $\boldsymbol{q}$, and $\boldsymbol{w}$:

$$\frac{\partial \boldsymbol{\gamma}^{\mathbf{est}}}{\partial \boldsymbol{p}} = \alpha + \beta \frac{\partial \boldsymbol{q}}{\partial \boldsymbol{p}} + \eta \frac{\partial \boldsymbol{w}}{\partial \boldsymbol{q}}, \tag{5.15}$$

$$\frac{\partial \boldsymbol{\gamma}^{\mathbf{est}}}{\partial \boldsymbol{q}} = \alpha \frac{\partial \boldsymbol{p}}{\partial \boldsymbol{q}} + \beta + \eta \frac{\partial \boldsymbol{w}}{\partial \boldsymbol{q}}, \tag{5.16}$$

$$\frac{\partial \boldsymbol{\gamma}^{\mathbf{est}}}{\partial \boldsymbol{w}} = \alpha \frac{\partial \boldsymbol{p}}{\partial \boldsymbol{w}} + \beta \frac{\partial \boldsymbol{q}}{\partial \boldsymbol{w}} + \eta. \tag{5.17}$$

All the derivatives on the l.h.s of the above equations were also estimated from the data using a linear fit. This method provided two different estimates of the parameters α,β, η, one for each components of the shear, although our model for the PSF errors assumes there should be no difference between the two components. The values are shown in Table 5.2, showing a good agreement between the two components. We also note that the values of the α, β and η parameters estimated in such a way are generally compatible with the parameters estimated in the previous section. Only the parameter α_2 shows a mild tension compared to the value estimated from spatial coordinates, which is compatible with 0. This tension could be either due to a statistical fluke or could be a hint that our uncertainty budget for this method is slightly underestimated. We did not investigate this further, as no statistically significant trend of mean shear with respect to PSF model is measured in our catalog (see next subsection).

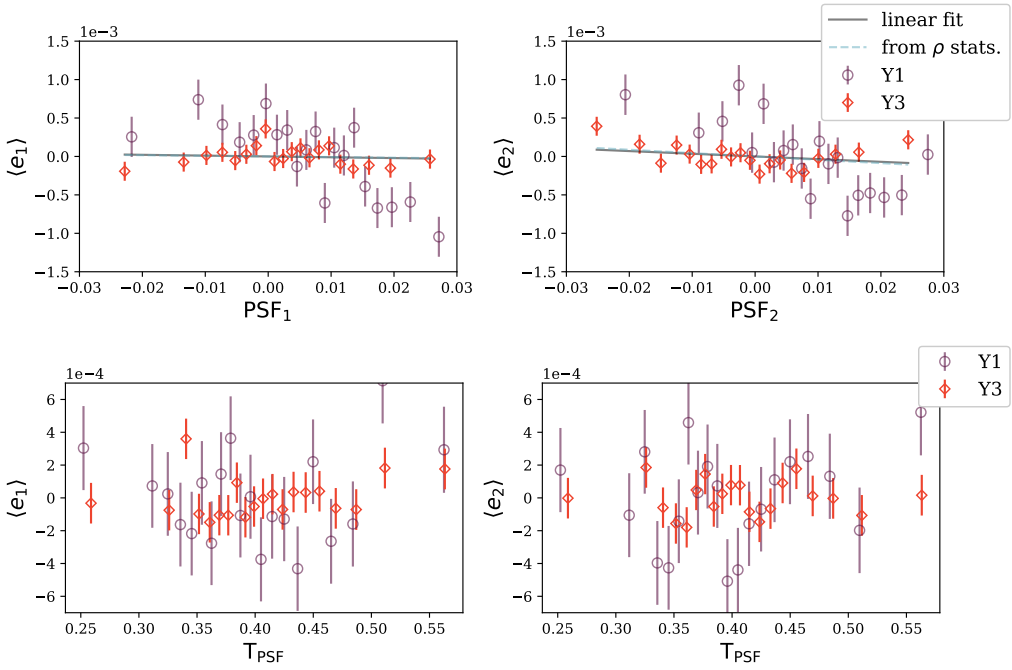

Figure 5.10: *Upper panels*: the mean shear $\langle e_i \rangle$ as a function of input PSF model ellipticity, for the two components. Solid lines are the linear best fit estimated using the PSF interpolated in real-space coordinates, dashed red lines are obtained using the α, β and η parameters estimated using focal-averaged quantities *Lower panels*: the mean shear $\langle e_i \rangle$ as a function of input PSF size.

Mean shear-PSF correlation

The DES Y1 catalogue (Zuntz et al., 2018) showed a linear dependence of the two components of mean shear $\langle e_i \rangle$ with the input PSF ellipticity at the galaxy position, caused mostly by PSF model ellipticity residuals. As shown in Fig. 5.10, for the DES Y3 catalogue this dependence vanished: the measured slopes for the two components are $\partial\gamma_1^{est}/\partial \mathrm{PSF}_1 = -0.001 \pm 0.002$, $\partial\gamma_2^{est}/\partial \mathrm{PSF}_2 = -0.003 \pm 0.002$. The measured slope (black solid line) is compared to that inferred from the ρ statistics obtained from focal-plane-averaged quantities (red dashed lines).

The lower panels of Fig. 5.10 show the correlation between the mean ellipticity and the PSF size. As for DES Y1 shape catalogue, no noticeable trend is observed.

5.6 Shape catalogue tests

Empirical tests lack an absolute calibration, therefore are more suited to test additive biases rather than multiplicative biases. They usually take the form of a 'null' test. Deviations from a null signal might indicate the presence of additive biases. The tests included in this section are the following:

- shear variations in focal plane coordinates (§ 5.6.1);
- tangential shear around field centers (§ 5.6.1);
- stellar contamination (§ 5.6.2): to test for potential biases due to the erroneous inclusion of stars in the DES Y3 shape catalogue;
- B-modes (§ 5.6.3): to detect potential systematic effects by measuring the catalogue B-mode signal using two different estimators;
- galaxy and survey properties (§ 5.6.4).

Note that unlike the other tests, the stellar contamination test is used to estimate a potential multiplicative shear bias.

5.6.1 Mean shear in focal plane coordinates

Fig. 5.11 shows the two components of the shear binned in focal plane coordinates. In particular, we computed the mean shear binned across all exposures and show the mean shear obtained stacking together all the CCDs in Fig. 5.12. It is possible for patterns to arise due to masking of bad columns in some of the CCDs, CCD pixels defects etc. In both Figs. 5.11 and 5.12, we observe no clear trends beyond variations due to shape noise and number count variations. This visual test is not stringent: given the bin size used to plot the two components of the shear, noise variations are much larger in amplitude than the mean shear measured at the catalogue level (§ 5.4.4). However, reducing the resolution of the plot did not show significant pattern.

Tangential shear around field center

We show in Fig. 5.13 the tangential shear binned by radius around field centres (the set of points where the centre of the focal plane is pointing over all exposures). A measurement of the tangential shear around a set of random points has been subtracted to the measurement. The measurement has been performed in sky coordinates; the field centers considered were

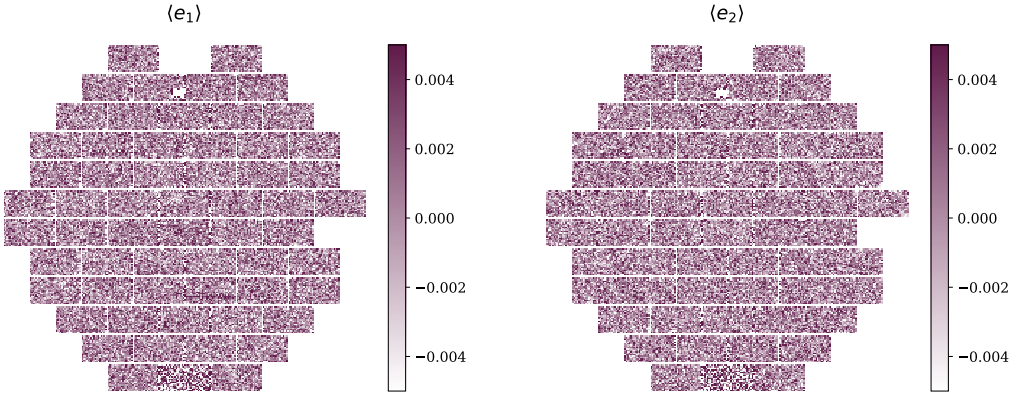

Figure 5.11: Mean shear in focal plane coordinates, for the two component of the shear.

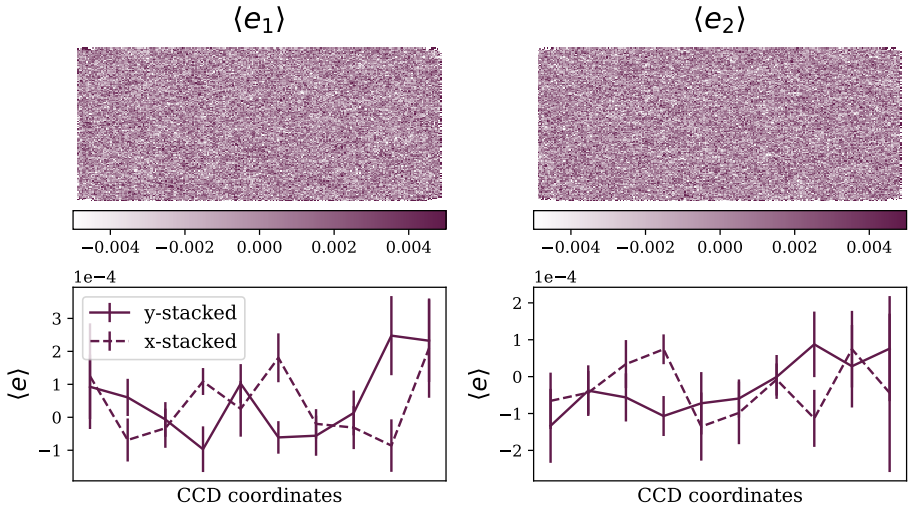

Figure 5.12: Mean shear in CCD coordinates, obtained stacking all the CCDs signal. *Upper panels*: the signal is stacked in a grid of 125 x 250 bins. Lower panels: the signal is further stacked in 10 bins along the x or y directions.

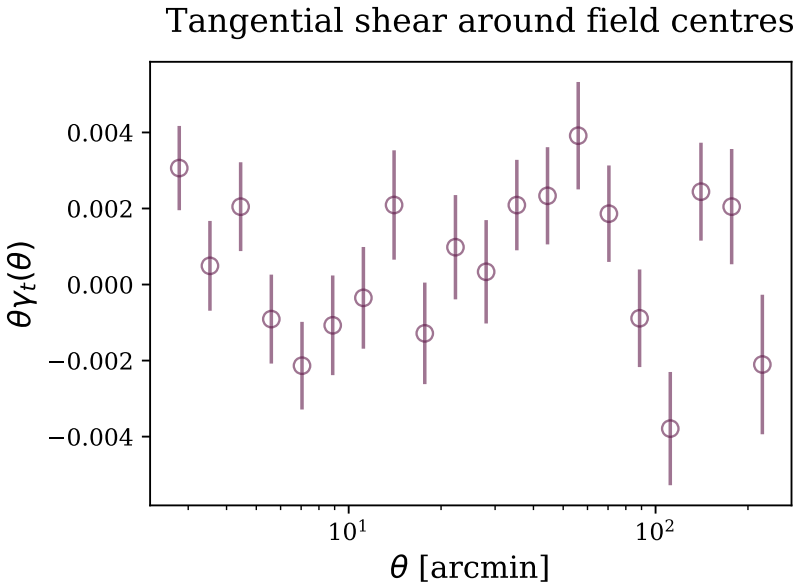

Figure 5.13: Tangential shear around field centers, as a function of angular distance. Field centers in the *riz* bands have been considered.

22331. A spurious signal might indicate residual systematics related to the position of the galaxies in the focal plane; however, no statistically significant signal has been measured.

5.6.2 Stellar Contamination Test

The shape catalogue should contain only distant galaxies from which a cosmic shear signal may be measured. However, stars within our own galaxy may be detected in the images and erroneously pass the galaxy selection. Separating stars and galaxies at faint magnitudes is known to be a difficult problem. It must be ensured that any stars which are mis-classified as galaxies and are included in the shape catalogue will not significantly dilute the measured shear.

Where stars are point-like and the PSF is accurately known, it is expected that their measured mean shear and response should be zero $\langle \boldsymbol{e} \rangle = \langle \boldsymbol{R} \rangle = 0$. This will not be the case, however, if stars are included in the sample preferentially when their size is overestimated due to noise. Also, a mean non-zero response can result from even a small bias in the estimated

PSF (see Fig. 11 of Zuntz et al., 2018).

Shear bias from stellar contamination

We assume the ellipticity distribution of the METACALIBRATION catalogue $P(\boldsymbol{e})$ is a weighted sum of galaxies and stars with ellipticity distributions $P_G(\boldsymbol{e})$ and $P_*(\boldsymbol{e})$ making up fractions f_G and f_* of the catalogue respectively:

$$P = f_G P_G + f_* P_*. \tag{5.18}$$

Assuming stars are not sheared, then the mean ellipticity of the METACALIBRATION catalogue is given by:

$$\langle \boldsymbol{e} \rangle = f_G \langle \boldsymbol{R}_G \boldsymbol{\gamma} \rangle. \tag{5.19}$$

Measuring the mean response for the full catalogue $\langle \boldsymbol{R} \rangle$ we can estimate the biased mean shear of the catalogue:

$$\langle \boldsymbol{\gamma}^{\rm est} \rangle = f_G \langle \boldsymbol{R} \rangle^{-1} \langle \boldsymbol{R}_G \boldsymbol{\gamma} \rangle. \tag{5.20}$$

The mean response of the METACALIBRATION catalogue is given by:

$$\langle \boldsymbol{R} \rangle = f_G \langle \boldsymbol{R}_G \rangle + f_* \langle \boldsymbol{R}_* \rangle. \tag{5.21}$$

We can approximate its reciprocal using a Taylor series given that there are many more galaxies than stars:

$$\langle \boldsymbol{R} \rangle^{-1} \approx \frac{1}{f_G} \left(1 - \frac{f_*}{f_G} \langle \boldsymbol{R}_* \rangle \langle \boldsymbol{R}_G \rangle^{-1} \right) \langle \boldsymbol{R}_G \rangle^{-1}. \tag{5.22}$$

Substituting Eq. 5.22 into Eq. 5.20 and using $\langle \boldsymbol{\gamma}^{\rm est} \rangle = \langle \boldsymbol{R} \rangle^{-1} \langle \boldsymbol{R} \boldsymbol{\gamma} \rangle$ for the mean shear gives:

$$\langle \boldsymbol{\gamma}^{\rm est} \rangle = \left(1 - \frac{f_*}{f_G} \langle \boldsymbol{R}_* \rangle \langle \boldsymbol{R}_G \rangle^{-1} \right) \langle \boldsymbol{\gamma} \rangle, \tag{5.23}$$

and as such we identify the multiplicative bias $\boldsymbol{m}$ as a result of stellar contamination to be:

$$\boldsymbol{m} = -\frac{f_*}{f_G} \langle \boldsymbol{R}_* \rangle \langle \boldsymbol{R}_G \rangle^{-1}. \tag{5.24}$$

In order to assess the level of contamination of the shape catalogue by stars $\frac{f_*}{f_G}$ and the stellar response $\langle \boldsymbol{R}_* \rangle$ we took advantage of the DES deep fields

(DES collaboration, 2020b) to construct a star-galaxy separation algorithm which is expected to work at the faint magnitudes relevant for objects in the shape catalogue (see Appendix B.2 for more details). Within the COSMOS field we matched DES deep fields objects to the HST-ACS catalogue of Leauthaud et al. (2007), which covers the full range of magnitudes for the DES deep field data and also includes the MU_CLASS morphological star-galaxy classification. Using the MU_CLASS as truth labels we trained a k-nearest neighbors (kNN) classifier in the available $ugrizJHK$ color space. We then applied this classifier in the other DES deep fields, which have both Y3 METACALIBRATION measurements and optical and near-infrared colors available, but not HST-ACS MU_CLASS. The METACALIBRATION responses for objects in the DES C3, X3, and E2 deep field classified in this way are shown in Fig. 5.14. The left panel shows responses for all DES deep objects in the field and shows the desired behaviour for stars as having shear response consistent with zero. The right panel shows shear responses for objects which pass the fiducial shape catalogue cuts described in Section 5.4.2 and shows the expected behaviour (the non-zero response caused by cosmic shear we are trying to measure) for galaxies. Objects which are classified as stars but also pass the fiducial METACALIBRATION cuts and make it into the shape catalogue are 0.5% of the shape catalogue, and have a response which peaks away from zero. Errors are jackknife resampling errors containing 66% of the distribution.

If we assume all of these objects are indeed contaminating stars and use their mean shear response $\langle \boldsymbol{R}_* \rangle$ then we may use Eq. 5.24 to find the resultant shear bias. Fig. 5.15 shows this measured bias for the objects across three deep fields regions, C3, X3, and E2. The median value for the inferred stellar contamination bias of $m = 0.004^{+0.001}_{-0.002}$. The potential for miss-classification by the kNN classifier (i.e. some of the supposedly 'contaminating' objects are likely to be galaxies in truth) and the low statistics means we regard this inferred bias from stellar contamination as an upper limit estimate from the data. As shown in Appendix B.2, the classifier's performance decreases at fainter magnitudes from $> 99\%$ stellar purity at i band magnitudes of ~ 24 to 60% stellar purity at i band magnitudes of ~ 25. We verified that repeating this test using the star-galaxy separation available from Data Release 1 of the Hyper Suprime-Cam Subaru Strategic Program (HSC DR1 Aihara et al., 2018) using the ICLASSIFICATION_EXTENDEDNESS parameter provided consistent results.

We note that we also performed this test on the DES Y3 image simulations (MacCrann et al., 2020) , which include a catalogue of stars from

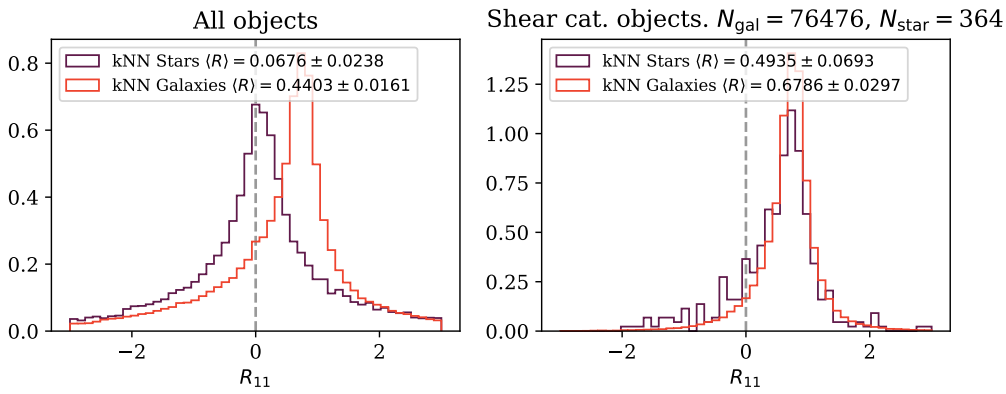

Figure 5.14: METACALIBRATION shear responses R_{11} for star and galaxy objects in the C3, X3, and E2 fields as classified by the kNN classifier. The non-zero response of the stars which make it into the METACALIBRATION shape catalogue (*right* panel) is the origin of the shear bias calculated in Eq. 5.24. The vertical dashed line represents zero on the x-axis.

the TRILEGAL (Pieres et al., 2019) model. In versions of the simulations where objects (both stars and galaxies) are placed randomly, the stellar contamination fraction of the shape catalogue, histogram of responses of stellar objects in the shape catalogue, and histogram of resulting stellar contamination shear bias were all reproduced to a high degree of accuracy. In simulations where the sources (both stars and galaxies) were instead placed on a grid, the stellar contamination of the shape catalogue reduced by 2/3, and the non-zero response of stellar objects in the shape catalogue disappeared, with the distribution peaking at zero. This indicates that the stellar contamination is an effect stemming from blending of star and galaxy sources, and one which is already included in the shear bias modelled by the image simulations. Due to the potential miss-classification issue and the low statistics affecting the data estimate, we decided not to use the upper limit estimated from data, but rather to resort to image simulations to model the shear bias induced by stellar contamination.

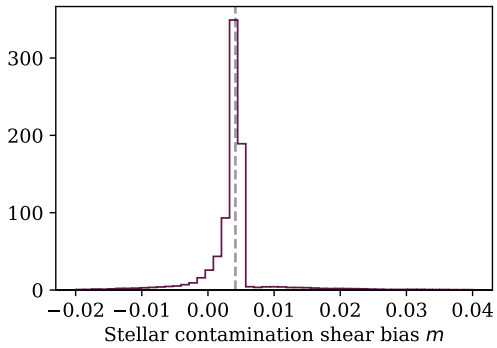

Figure 5.15: Shear bias from contamination by objects classified as stars by the kNN classifier in the C3, X3, and E2 deep fields regions, calculated using Eq. 5.24. Distributions over m are created by Monte Carlo sampling values of $\langle R_* \rangle$, $\langle R_* \rangle$, and f_*/f_G from the revelant distributions in Figure 5.14; and the vertical dashe lines represent the median of each distribution.

5.6.3 E/B-modes decomposition and null tests with systematics

In this section, we show the measured B-mode signals obtained using both the pseudo-C_ℓ (Hikage et al., 2011) and Complete Orthogonal Sets of E/B-Integrals (COSEBIs; Schneider et al., 2010) statistics. As the cosmic shear field to first-order predicts no B-modes, any detection in the shape catalog could indicate a contamination by systematic effects, in particular by the PSF generating an additive bias. Note that a small B-mode power spectrum can be sourced by higher-order physical effects, including intrinsic alignments, clustering of sources and higher order contribution to the shear signal. If detectable at significant levels, these contributions should be included when modelling the two-point correlation functions.

Pseudo-C_ℓ B-modes

We built two Healpix maps(Górski et al., 2005) (with resolution $n_{\rm side} = 1024$) of the cosmic shear signal by computing the weighted average of (response-corrected) ellipticities of galaxies within each pixel. We estimated the E- and B-mode power spectra of these maps with pseudo-C_ℓ using `NaMaster` (Alonso et al., 2019), an open-source code that deconvolves the effects of masked regions from the harmonic space coefficients. We used the inverse-variance weight masks, given by the weighted count maps. We measured

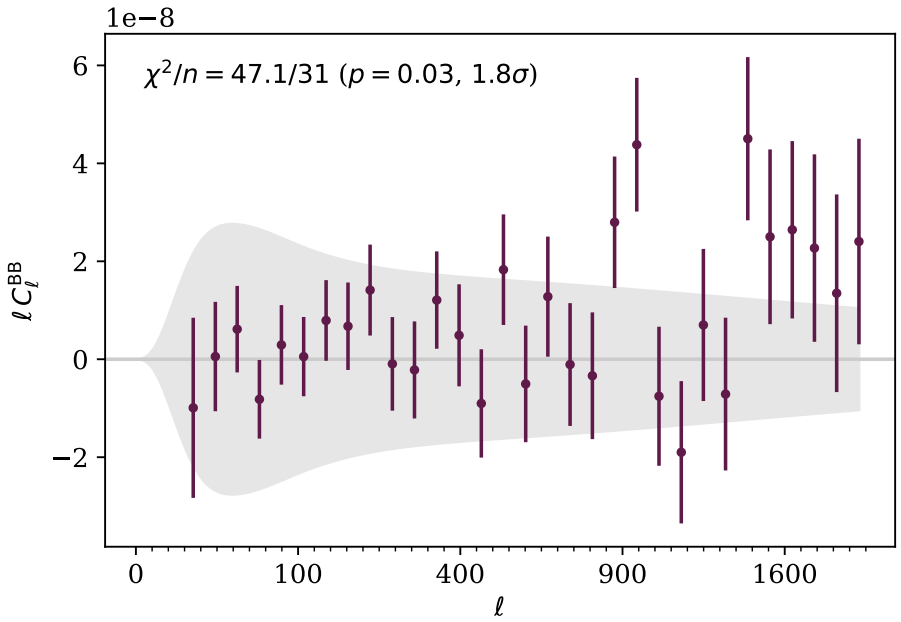

Figure 5.16: Pseudo-C_ℓ B-mode power spectra measured from the full DES Y3 shape catalog in the multipole range 8-2048. The noise power spectrum bias has been estimated from gaussian simulations (see text) and subtracted. As an order of magnitude comparison, we show as a grey shaded region 10 per cent of the expected E-mode power spectra of the weakest cosmic shear signal (the lowest redshift tomographic bin).

spectra for multipoles in the range $\ell = [2-2048]$ in 32 bins evenly separated on a square-root scale (spreading signal-to-noise more evenly than linear or logarithmic binning).

The measured power spectra receives an additive bias from the shape-noise power spectrum N_ℓ, which may diverge from the approximation $N_\ell = \sigma_e^2/n_{\rm eff}$ due to mask effects and properties of the pseudo-C_ℓ estimator. Moreover, the mask induces a leakage between E- and B-modes (especially at large scales) which increases the variance of affected multipole bins. Therefore, we generated 2000 mock catalogs to both obtain an accurate measurement of the noise power spectrum and the covariance matrix of the pseudo-C_ℓ B-modes[9].

The procedure to generate the mock catalogs is as follows. Given a fidu-

[9]We also applied the standard technique consisting in simply applying random rotations and obtained noise power spectra in agreement to better than 10^{-3}. The covariance matrix obtained with this method, however, failed at capturing the contribution due to E-mode leakage, which is particularly relevant at large scales.

cial E-mode power spectrum, we generated 2000 full-sky healpix maps of the cosmic shear field. The cosmic shear field is assumed to be Gaussian. For each galaxy in the catalog, we applied a random rotation to its measured ellipticity. Each rotated ellipticity is used as intrinsic ellipticity. We then sampled the shear field at the positions of galaxies and applied the shear addition formula (see, e.g, (Seitz & Schneider, 1997)) to the mock intrinsic ellipticity. This method preserves both geometric properties of the catalog and the ellipticity distribution over the DES Y3 footprint. We then applied the pseudo-C_ℓ estimator and obtained the noise power spectrum and an empirical covariance of the mock catalog B-mode spectra. Finally, we excluded the first multipole bin which includes scales larger than the survey footprint and showed mild E-mode leakage reproduced by simulations. Note, however, that compared to the DES Y1 analysis, we extended the measurement to smaller scales, $\ell_{\rm max} = 2048$, corresponding to angular scales of $\sim 5.3'$. The measurement is shown in Fig. 5.16. Overall, we found a $\chi^2/n = 47.1/31$ for multipole bins in the range $\ell = [8 - 2048]$, corresponding to a p-value of 0.03, or a 1.8σ deviation from the null hypothesis of no B-mode, suggesting that B-modes in the data are consistent with pure shape-noise. Although we do not consider the p-value of 0.03 particularly worrisome, we note that removing scales $\ell > 1500$ (roughly corresponding to scales smaller than $\theta \sim 7$ arcmin) improves the p-value to 0.06. We also note that the fiducial scale cut for the main cosmological analysis removes part of these scales, depending on the tomographic bin considered (Amon et al., 2020).

COSEBIs

We used Complete Orthogonal Sets of E/B-Integrals (COSEBIs; Schneider et al., 2010), which is an estimator designed to separate E- and B-modes and has been measured for previous releases of DES as well as for KiDS (Asgari et al., 2019a; Asgari & Heymans, 2019; Asgari et al., 2020). To calculate the B-mode, we first computed the real space shear-shear correlations, ξ_+ and ξ_- with TreeCorr (Jarvis, 2015) in 120000 linearly-spaced bins from $\theta_{\rm min} = 2.5'$ to $\theta_{\rm max} = 250'$ with a brute force calculation (`bin_slop`=0). These were converted to COSEBIs using filter functions that are described in Section 2 of Asgari et al. (2020) (see their Equation 7). We also calculated a noise-only covariance matrix following Appendix A of Asgari et al. (2020) (see their Equations A.5 and A.6). The resulting B-mode signal and corresponding square root of the diagonal of the covariance are plotted in Fig. 5.17.

The $\chi^2/n = 22.8/20 = 1.1$ corresponds to a p-value of 0.86, which indi-

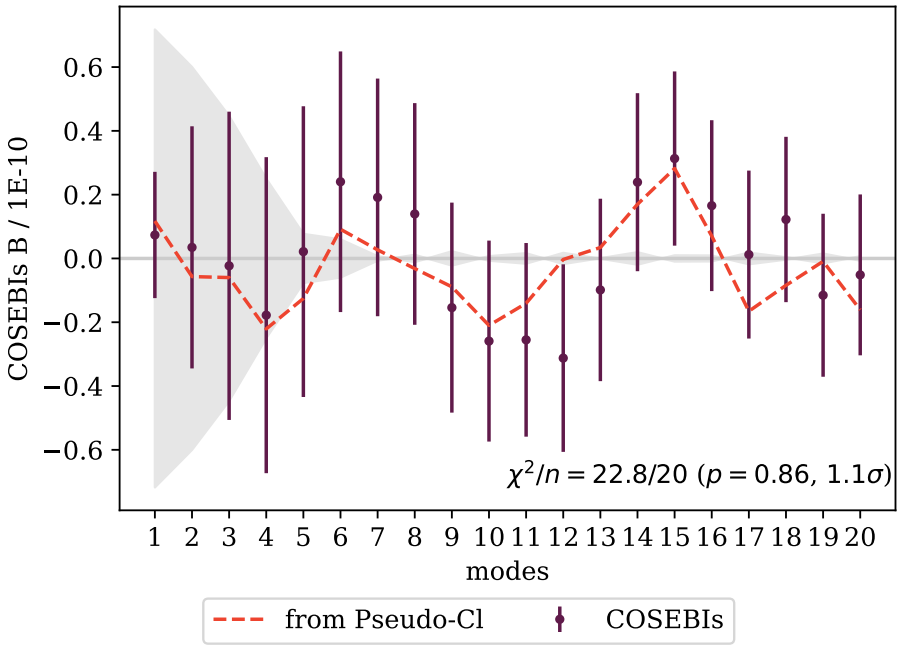

Figure 5.17: COSEBIs B-modes from the DES Y3 shape catalog are shown as data points with errors given by a noise-only analytical covariance matrix. The dashed line shows the pseudo-C_ℓ shown in Figure 5.16 converted to COSEBIs B-mode as described in the text. Note that the COSEBIs are always discrete measurements for individual modes, but the dashed line is connected for clarity. As an order of magnitude comparison, we show as a grey shaded region 10 per cent of the expected COSEBIs E-mode of the weakest cosmic shear signal (the lowest redshift tomographic bin)

cates that the null hypothesis fits the data, and the DES Y3 shear catalog is consistent with zero B-modes. This result can be qualitatively compared to the DES Y1 values (also consistent with zero for METACALIBRATION shape measurements, with a p-value of 0.325) shown in the right panel of Figure 1 from Asgari & Heymans (2019), although note that there is a different θ-ranges used. We also compared with the pseudo-C_ℓ shown in Figure 5.16 by converting those measurements to COSEBIs. We did this by approximating the pseudo-C_ℓ as a piece-wise constant function and integrating it with the Hankel transform of the COSEBIs filter functions (see Equation 8 of Asgari et al., 2020). This converted measurement is displayed as the dashed line in Figure 5.17, and we see that the two different B-mode estimations agree well.

5.6.4 Galaxy and survey properties tests

Our shear catalog is characterized by a non-null mean shear in one of the two components, whose origin is unknown. The values for the two components are respectively $\langle e_1 \rangle = 3.6\ 10^4$ and $\langle e_2 \rangle = 0.6\ 10^4$; for the first component, this value is larger than the expected cosmic variance ($\sim 0.5\ 10^4$, as estimated from `FLASK` log-normal mocks). The mean shear is measured and subtracted at the catalog level as it would have an impact on the measured cosmic shear signal. We further investigated the possibility that the mean shear could vary across the footprint, and that these variations could be non-cosmological but could be related to other galaxy or observing properties. To this aim, we assumed $\langle e_1 \rangle$, $\langle e_2 \rangle$ to depend linearly on a number of different galaxy and observational properties: depth, S/N, size ratio $T/T_{\rm PSF}$ (i.e., the ratio between galaxy size and PSF size), exposure time, brightness, and airmass. When applicable, these quantities were considered in the i band. We did not explicitly include PSF ellipticity, ellipticity or size residuals as this had already been investigated in § 5.5.3.

We then performed a linear fit for the two shear components as a function of the different properties across the footprint. In principle, this is a null test, as we do not expect *a priori* to detect any correlation. Any significant deviation from a null signal, however, could help shedding light on the origin of the mean shear signal measured in the catalogue. We show the measured coefficient for each of these systematic maps in Fig. 5.18; errors were estimated using 300 `FLASK` log-normal mocks. We also checked that using errors estimated jackknife resamples caused no significant difference

0.9

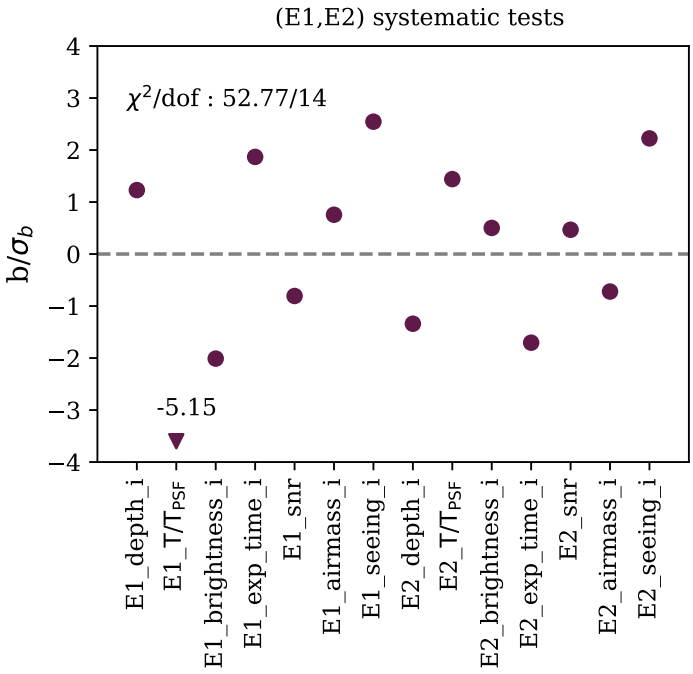

Figure 5.18: Best fit values for the coefficient of the relation $\langle e_i \rangle = b$ syst $+ c$ with syst a given systematic map. The values of the slopes are shown for different systematic maps, and the errors are estimated using log-normal `FLASK` simulations. The reported χ^2 takes into account correlations among different systematic maps.

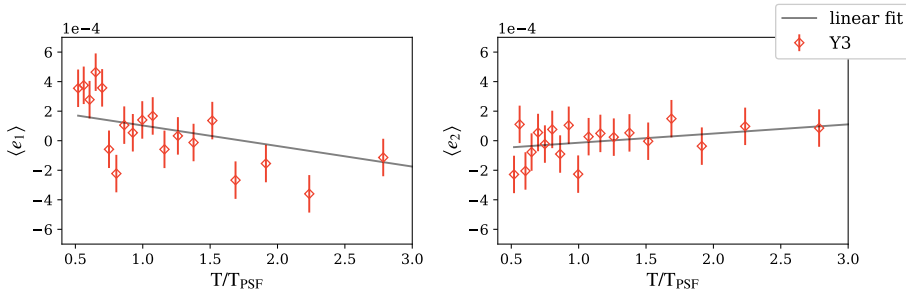

Figure 5.19: The mean shear $\langle e_i \rangle$ as a function of size ratio $T/T_{\rm PSF}$, defined as the ratio between galaxy size and PSF size. A statistically significant trend with $T/T_{\rm PSF}$ is measured for the first component of the mean shear, while for the second component we measure no significant dependence.

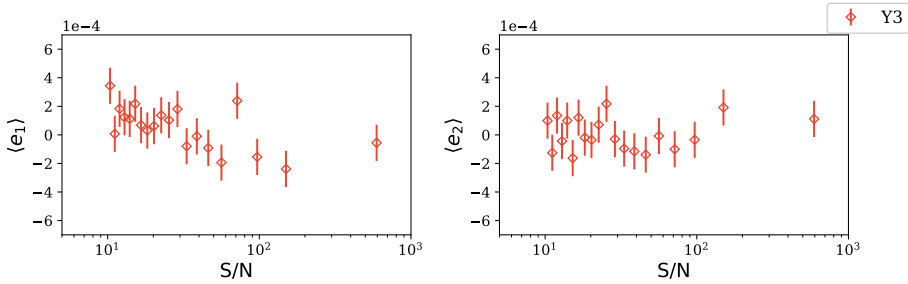

Figure 5.20: The mean shear $\langle e_i \rangle$ as a function of S/N. No statistically significant trend with S/N is measured, for both components.

in the results. We find a clear correlation between $\langle e_1 \rangle$ and the ratio between the galaxy size and the PSF size, while none of the other correlations are significant (removing the $\langle e_1 \rangle$−size ratio correlation from the analysis reduces the χ for the null hypothesis to 20 for 13 $d.o.f.$).

We plot the mean shear as a function of size ratio in Fig. 5.19. As we showed in Fig. 5.10 that the mean shear has no dependence on the $T_{\rm PSF}$, this test mostly highlights a dependence of the mean shear with respect to the galaxy size: this implies that smaller galaxies are associated with a positive, spurious, mean shear signal. The amplitude of the signal is compatible with the mean shear measured at the catalog level. The origin of this signal is unknown, but we checked that the scale-dependent part of this additive bias is sufficiently small to not bias the cosmological analysis.

We also show in Fig. 5.20 the measured mean shear as a function of S/N, as S/N is a relevant quantity used to select the DES Y3 weak lensing sample. No statistically significant trend is measured.

5.7 Summary

This Chapter presented the weak lensing shape catalogue from the DES Y3 imaging data, covering ~ 4143 deg^2 of the southern hemisphere and comprising ~ 100 million objects, resulting in a weighted source number density of $n_{\rm eff} = 5.59$. We described the shape measurement pipeline used for the DES Y3 analysis, METACALIBRATION which is based upon the pipeline used in the DES Y1 analysis (Zuntz et al., 2018), but with the following improvements:

- improved PSF solutions (PIFF, Jarvis et al. 2020) were used for the METACALIBRATION deconvolutions rather than the PSFEx solutions that were used for Y1;
- improved astrometric solutions, based on Bernstein et al. (2017);
- inverse variance weighting for the galaxies.

We further discussed the sample selection adopted for the DES Y3 analysis and the changes compared to DES Y1, which improved the reliability of the weak lensing sample. The METACALIBRATION pipeline is capable of self-calibrating biases in the shear estimation by correcting for the response of the shear estimator and selection biases. The current METACALIBRATION implementation, however, does not correct for a shear-dependent detection bias, which is calibrated using a dedicated suite of image simulations in (MacCrann et al., 2020). It is expected that the DES Y6 release will implement an updated version of METACALIBRATION (Sheldon et al., 2019), which accounts for the aforementioned effect. We note that we also expect to implement in the future a second shear measurement pipeline, following the BFD method outlined by (Bernstein et al., 2016), although more investigation is needed to see to what extent the BFD algorithm can cope with such shear-dependent detection bias.

In this Chapter we performed a variety of empirical null tests, mostly aimed at identifying additive biases in our shape catalogue. We tested potential systematic errors connected to PSF corrections, demonstrating that the improved PSF solutions reduced additive biases due to PSF misestimation to negligible levels for the current analysis. PSF tests have been performed both in real space and in focal plane coordinates, showing agreement. We also tested that PSF chromatic effects (which are currently not modelled) were negligible.

We further checked biases due to the erroneous inclusion of stars in the DES Y3 catalogue, estimating an upper limit for the stellar contamination bias, which we found to be in agreement with the results from image simulations. We looked at the signature of systematic effects by measuring the catalogue B-mode signals using both the COSEBIs and pseudo-C_ℓ estimators, which consistently revealed in a null detection. We checked the dependency of the two components of the shear with respect to a number of galaxy or survey properties, finding no significant correlations, except for a linear dependence between $\langle e_1 \rangle$ the ratio between the galaxy size. We found, however, that this trend has no relevant impact on the DES Y3 cosmic shear analysis. Finally, we tested in Appendix B.1 the validity of using the mean response to also calibrate shear two-point correlation functions, finding that a two-point response correction is not needed for the current DES Y3 analysis.

Part IV

Weak Lensing Mass Maps

In this part we present the official DES Y3 weak lensing mass maps, which are the largest weak lensing mass maps up-to-date. We discuss a variety of map-making methods, and compare their performance in simulations and data. We furthermore outline a potential application of the maps where we estimate cosmological parameters using the second and third moments of the convergence field. The work on the DES Y3 mass maps is going to be published in Jeffrey & Gatti, et al. (DES collaboration) together with the DES Y3 cosmological release. The work on the cosmology with mass map moments is published in Gatti et al. (DES collaboration) 2019.

Chapter 6

DES Y3 mass maps

6.1 Introduction

Weak (gravitational) lensing is one of the primary probes in recent galaxy surveys (See e.g. Bartelmann & Schneider, 2001, for a detailed review of weak lensing). By measuring the subtle distortions of galaxy shapes due to the mass distribution between the observed galaxies and us the observers, we are able to place tight constraints on the content of matter in the Universe (Ω_m) as well as the level at which they cluster (σ_8, defined to be the standard deviation of the linear overdensity fluctuations on a $8h^{-1}$ Mpc scale). So far, the main focus in weak lensing analyses has been on measuring two-point summary statistics such as correlation functions or power spectrum (Troxel et al., 2018; Hildebrandt et al., 2017; Hikage et al., 2019; Hamana et al., 2020). The two-point functions capture the Gaussian piece of information in the underlying matter field. The methodologies for measuring and modeling these two-point statistics are fairly mature – standard analysis of two-point statistics in weak lensing now include several non-trivial systematic effects that were not known a decade ago, for example, intrinsic alignment (IA), clustering of source galaxies, small-scale modeling of baryonic effects, and uncertainty in photometric redshift calibrations (a detailed review of recent developments in these areas can be found in Mandelbaum, 2017). As the analysis techniques for these two-point analyses become mature, it is natural to ask whether we could extract more information from the same data set simply by going to the next order of statistics, and whether we understand, at the same level as the two-point statistics, the non-trivial systematic effects in these higher-order statistics. Common higher-order statistics with weak lensing include shear peak statistics (Di-

etrich & Hartlap, 2010; Kratochvil et al., 2010; Liu et al., 2015; Kacprzak et al., 2016; Martinet et al., 2018; Peel et al., 2018; Shan et al., 2018), higher moments of the weak lensing convergence (Van Waerbeke et al., 2013; Petri et al., 2015; Vicinanza et al., 2016; Chang et al., 2018; Vicinanza et al., 2018; Peel et al., 2018; Gatti et al., 2019), three-point correlation functions or bispectra (Takada & Jain, 2003, 2004; Semboloni et al., 2011; Fu et al., 2014), Minkowski functionals (Kratochvil et al., 2012; Petri et al., 2015; Vicinanza et al., 2019; Parroni et al., 2020), machine-learning methods (Fluri et al., 2018, 2019; Jeffrey et al., 2020). Many of these have recently been applied to data, performing well in terms of cosmological constraints (Liu et al., 2015; Kacprzak et al., 2016; Martinet et al., 2018; Fluri et al., 2019). This Chapter will focus on the key element for many of the methods described above: a weak lensing convergence map, often referred to as a "mass map[1]" The two crucial features that make a convergence map appealing for extracting higher-order statistics are that 1) the map preserves the *phase* information of the mass distribution and 2) the convergence is a scalar field, which can be easier to manipulate/model than a shear field (which is closer to what we observe, as explained in sec:theory). Over the years, many methods for generating these convergence maps have been proposed. The foundation of most of these methods is the direct inversion algorithm developed in Kaiser & Squires (1993a, hereafter KS), which is a purely analytic solution for converting between shear (the observable) and convergence. A large number of papers are based on the KS method, including cosmological analyses (Van Waerbeke et al., 2013; Vikram et al., 2015; Chang et al., 2015, 2018; Oguri et al., 2018). The main issues associated with the method is the treatment of the noise and mask effects. To deal with these issues, more sophisticated methods were developed, mostly imposing certain priors and implementing a Bayesian framework around the KS method. These include applying general Wiener filters and more specific sparsity priors. All methods show success in some aspects of reconstructing the convergence maps. However, it is not clear how to compare the results between these methods and how to interpret the differences. Fundamentally, the issue lies in the fact that there is a wide range of science these maps could potentially be used for – with different applications different optimization choices can be made.

The goal of this Chapter is to present an objective and systematic comparison between several map reconstruction methods using the same set of

[1]The convergence quantifies the integrated total mass along the line of sight, weighted by the lensing efficiency, which roughly peaks half-way between the source and the observer.

simulations and data. In particular, we will study this in the context of the DES Y3 shear catalogue. Our results will make clear what is the expected differences in the maps constructed via the different algorithms and highlight the advantages and disadvantages for using the maps in different science cases. We present a comprehensive framework under which most of the convergence map-making methods described previously can be connected and compared. We particularly focus on four methods that span the range of the most popular methods: KS, No B-mode prior, Wiener and GLIMPSE. The methods are applied first to a set of DES Y3-like mock galaxy catalogs to demonstrate the performance of each method when the true underlying convergence field is known. Next, we apply the four methods to the DES Y3 data, where we perform additional tests for observational systematic effects. We also present a number of cross-correlation analyses to showcase the usage of the maps. One or more DES papers will follow using the maps generated here for cosmology analyses.

The structure of the Chapter is as follows: In §6.2 we provide high-level theoretical background for weak lensing and the theory framework that connects convergence with observable quantities in a galaxy survey. In §6.3 we present a mathematical framework where the four different mass mapping methods of interest (KS, No B-mode prior, Wiener, GLIMPSE) are different only by the priors that they choose to adopt. The data product as well as the simulations used in this work are described in §6.4. In §6.5 we carry out a series of tests on mass maps generated from the four methods and systematically compare them. We then apply the four methods to the DES Y3 data in §6.6 and present tests for additional systematic residuals from observational effects. We conclude in §6.7.

6.2 Weak gravitational lensing on the sphere

We begin with the gravitational potential Φ and the matter overdensity field $\delta \equiv \delta\rho/\bar{\rho}$; these real scalar fields on spacetime are related by the Poisson equation

$$\nabla_r^2 \Phi(\boldsymbol{x}) = \frac{3\Omega_m H_0^2}{2a(t)} \delta(\boldsymbol{x}) \ . \tag{6.1}$$

Here $\boldsymbol{x} = (t, \boldsymbol{r})$ (with t time and $\boldsymbol{r}$ a comoving spatial coordinate), Ω_m is the total matter density today, H_0 is the Hubble constant today, and $a \equiv 1/(1+z)$ is the scale factor.

Weak gravitational lensing is the small distortion of the shapes of distant galaxies caused by the gravitational warping of spacetime (and hence the distortion of light paths) by mass located between the galaxies and an observer; see Bartelmann & Schneider (2001) for a comprehensive introduction.

We will parametrize the observer's past lightcone as (χ, θ, φ) with χ the comoving radial distance from the observer and θ, φ a point on the observer's celestial sphere. The effect of weak lensing can be encapsulated in the *lensing potential*, denoted ϕ, a real scalar field on the lightcone; its value is related to the gravitational potential Φ projected along the line of sight:

$$\phi(\chi, \theta, \varphi) = \frac{2}{c^2} \int_0^\chi d\chi' \frac{f_K(\chi - \chi')}{f_K(\chi) f_K(\chi')} \Phi(\chi', \theta, \varphi). \tag{6.2}$$

This equation assumes the Born approximation (the path of integration is not perturbed by the intervening mass). Here the angular distance factor f_K is sin, the identity, or sinh depending on whether the curvature K is positive, zero, or negative.

The radial dependence of ϕ in 6.2 would allow a three-dimensional analysis; however, instead of this, we integrate away the radial dependence using as a weight function the normalised redshift distribution $n(z)$ of source galaxies, obtaining

$$\phi(\theta, \varphi) = \int d\chi \; n(z(\chi)) \; \phi(\chi, \theta, \varphi), \tag{6.3}$$

a real scalar field on the celestial sphere.

To handle ϕ as well as derived quantities we use the formalism of spin-weight functions on the sphere as described in Castro et al. (2005). Let ${}_sY_{lm}(\theta, \varphi)$ denote the spin-weight s spherical harmonic basis functions. Recall that the covariant derivative $\eth$ increments the spin-weight s while its adjoint $\bar{\eth}$ decrements it; these operators act in a straightforward fashion on the basis functions.

Now the convergence $\kappa = \kappa_E + i\kappa_B$ (of spin-weight 0 i.e. a scalar) and shear $\gamma = \gamma^1 + i\gamma^2$ (of spin-weight 2) are related to the lensing potential via:

$$\kappa = \frac{1}{4}(\eth\bar{\eth} + \bar{\eth}\eth)\phi, \tag{6.4}$$

$$\gamma = \frac{1}{2}\eth\eth\phi. \tag{6.5}$$

We now move to harmonic space, obtaining harmonic coefficients $\hat{\phi}_{\ell m}$, $\hat{\kappa}_{\ell m}$ and $\hat{\gamma}_{\ell m}$ for ϕ, κ and γ respectively. Here for example:

$$\gamma = \sum_{\ell m} \hat{\gamma}_{\ell m}\, {}_2Y_{\ell m} \tag{6.6}$$

with

$$\hat{\gamma}_{\ell m} = \int d\Omega\ \gamma(\theta, \varphi)\, {}_2Y^*_{\ell m}(\theta, \varphi). \tag{6.7}$$

We can decompose the harmonic coefficients into real and imaginary parts: $\hat{\kappa}_{\ell m} = \hat{\kappa}_{E,\ell m} + i\hat{\kappa}_{B,\ell m}$ and $\hat{\gamma}_{\ell m} = \hat{\gamma}_{E,\ell m} + i\hat{\gamma}_{B,\ell m}$. In harmonic space equations 6.4 and 6.5 become:

$$\hat{\kappa}_{\ell m} = -\frac{1}{2}\ell(\ell+1)\hat{\phi}_{\ell m} \tag{6.8}$$

and

$$\hat{\gamma}_{lm} = \frac{1}{2}\sqrt{(\ell-1)\ell(\ell+1)(\ell+2)}\hat{\phi}_{\ell m}. \tag{6.9}$$

Thus

$$\hat{\gamma}_{lm} = -\sqrt{\frac{(\ell-1)(\ell+2)}{\ell(\ell+1)}}\hat{\kappa}_{\ell m}. \tag{6.10}$$

6.3 Mass map inference

The formalism in the previous section relates the ideal shear field defined on the full celestial sphere γ to the convergence κ field for a given source redshift distribution. Inferring the unknown convergence field from ellipticity measurements of a finite set of source galaxies in the presence of survey masks and galaxy "shape noise" is the challenge of mass mapping.

The real and imaginary parts of the shear γ represent a chosen two dimensional coordinate system. In weak lensing, the observed ellipticity of a galaxy ϵ_{obs} is related to the reduced shear g plus the intrinsic ellipticity of the source galaxy ϵ_s through

$$\begin{aligned} \epsilon_{obs} &\approx g + \epsilon_s \\ \text{where}\quad g &= \frac{\gamma}{1-\kappa}\ . \end{aligned} \tag{6.11}$$

The reduced shear is approximately the true shear, $g \approx \gamma$, in the weak lensing limit. This allows a standard definition of observed shear, $\gamma_{obs} = \epsilon_{obs}$, where the measurements are degraded by "shape noise", caused by the ϵ_s values of the observed galaxies:

$$\gamma_{obs} \approx \gamma + \epsilon_s \ . \tag{6.12}$$

The shape noise due to the intrinsic unlensed shapes of the source galaxies, ϵ_s, is of order a factor $\mathcal{O}(100)$ larger than the lensing signal per galaxy. It it therefore a dominant source of noise.

In a Bayesian framework we consider the posterior distribution of the convergence κ conditional on the observed shear γ and on model $\mathcal{M}$:

$$P(\kappa|\gamma, \mathcal{M}) = \frac{P(\gamma|\kappa, \mathcal{M})\ P(\kappa|\mathcal{M})}{P(\gamma|\mathcal{M})} \quad , \tag{6.13}$$

where $P(\gamma|\kappa, \mathcal{M})$ is the likelihood (encoding our noise model), $P(\kappa|\mathcal{M})$ is the prior and $P(\gamma|\mathcal{M})$ is the Bayesian evidence.

We formulate all reconstructed convergence κ maps as the most probable map, given our observed data and assumptions, which is the *maximum a posterior* (MAP) estimate. From the posterior distribution $P(\kappa|\gamma, \mathcal{M})$ the MAP estimate is given by

$$\hat{\boldsymbol{\kappa}} = \arg\max_{\boldsymbol{\kappa}} \ \log P(\boldsymbol{\gamma}|\boldsymbol{\kappa}, \mathcal{M}) + \log P(\boldsymbol{\kappa}|\mathcal{M}) \ , \tag{6.14}$$

where $\mathcal{M}$ is prior information about the model. Here, the vector $\boldsymbol{\kappa}$ are elements of a pixelised convergence map and elements of $\boldsymbol{\gamma}$ are the pixelised observed shear field.

We can express the linear data model in matrix notation,

$$\boldsymbol{\gamma} = \mathbf{A}\boldsymbol{\kappa} + \mathbf{n} \quad , \tag{6.15}$$

where the matrix operation $\mathbf{A}$ corresponds to the linear transformation from the ideal (noise-free and full-sky) shear field to convergence (equation 6.10). The noise term $\mathbf{n}$ is the vector of noise contributions per pixel (equation 6.12)

We can begin by assuming that the average shape noise per angular pixel on the celestial sphere (e.g. per pixel) is Gaussian, so that the likelihood (dropping $\mathcal{M}$ for brevity) is given by

$$P(\boldsymbol{\gamma}|\boldsymbol{\kappa}) = \frac{1}{\sqrt{(\det 2\pi \mathbf{N})}} \exp\Big[-\frac{1}{2}(\boldsymbol{\gamma} - \mathbf{A}\boldsymbol{\kappa})^\dagger \ \mathbf{N}^{-1}(\boldsymbol{\gamma} - \mathbf{A}\boldsymbol{\kappa})\Big] \tag{6.16}$$

where it is assumed that the noise covariance $\mathbf{N} = \langle \mathbf{n}\mathbf{n}^\dagger \rangle$ is known and the average noise per pixel is both Gaussian and uncorrelated (so that $\mathbf{N}$ is diagonal). With this likelihood, the masked (unobserved) pixels have infinite variance.

6.3.1 Prior probability distribution

This work considers four forms for the prior probability distribution $P(\boldsymbol{\kappa}|\mathcal{M})$, the second term in equation 6.14. This prior probability is intrinsic to the method and cannot be "ignored". One may choose to assume a uniform distribution[2] for $P(\boldsymbol{\kappa}|\mathcal{M})$, but this is nevertheless an active choice, which assigns equal prior probability to all possible convergence κ maps.

The various prior probability distributions used in this work correspond to various mass mapping methods, with each prior arising from a different physically-motivated constraint. They are:

1. Direct Kaiser-Squires inversion, which in the absence of smoothing corresponds to a *maximum a posterior* estimate with a uniform prior:

$$P(\boldsymbol{\kappa}) \propto 1 \quad . \tag{6.17}$$

   Usually the Kaiser-Squires inversion is followed by a smoothing of small angular scales, where it is expected that noise dominates over signal. The corresponds to a lower bound on the prior with respect to angular scale.

2. No B-modes prior – as is discussed further in Sec. 6.3.3, this prior includes our knowledge that weak gravitation lensing produces negligible B-mode contributions.

   This corresponds to the following log-prior:

$$-\log P(\boldsymbol{\kappa}) = i_{Im(\kappa)=0} \; + \; \text{constant} \quad , \tag{6.18}$$

   where the indicator function $i_{Im(\kappa)=0}$ is discussed in Sec. 6.3.3.

[2]Perhaps bounded within some reasonable κ range, to allow the prior to be a true (proper) probability distribution.

3. Gaussian random field prior with an assumed E-mode power spectrum (i.e. Wiener filtering) and with zero B-mode power. The prior distribution,

$$P(\boldsymbol{\kappa}) = \frac{1}{\sqrt{(\det 2\pi \mathbf{S}_\kappa)}} \exp\Big[-\frac{1}{2} \boldsymbol{\kappa}^\dagger \, \mathbf{S}_\kappa^{-1} \boldsymbol{\kappa} \Big] \, . \tag{6.19}$$

   with the power spectrum contributing to the signal covariance matrix $\mathbf{S}_\kappa$, which will be discussed in Sec. 6.3.4.

4. Sparsity-enforced wavelet "halo" prior with no B-modes. In the late Universe it is expected that quasi-spherical halo structures form. A wavelet basis whose elements have this quasi-spherical structure in direct (angular pixel) space should be a sparse representation of the convergence κ signal. This is included in the log-prior distribution

$$-\log \, P(\boldsymbol{\kappa}) = \lambda ||\boldsymbol{\phi}^\dagger \boldsymbol{\kappa}||_1 + i_{Im(\kappa)=0} \quad , \tag{6.20}$$

   where the l_1 norm of the wavelet transformed convergence $\boldsymbol{\phi}^\dagger \boldsymbol{\kappa}$ is small when the convergence field contains quasi-spherical halo structures, for a suitable choice of wavelet transform. Unlike the Gaussian prior where the lack of B-modes can be included in the power spectrum, here the second term is added to enforce that the signal is only E-mode. This is discussed in Sec. 6.3.5.

In the rest of this section we will explain the physical motivation for these choices and show how they are implemented.

6.3.2 Kaiser-Squires on the sphere

In the flat sky limit, for relatively small sky coverage, the $\eth$ operators on the sphere may be approximated as partial derivatives ∂ with respect to θ and ϕ. In this regime the relationship between shear γ and convergence κ (equations 6.4 and 6.5) is reduced to

$$\tilde{\gamma}(\mathbf{k}) = \frac{k_1^2 - k_2^2 + 2ik_1k_2}{k_1^2 + k_2^2} \tilde{\kappa}(\mathbf{k}) \quad , \tag{6.21}$$

where k_1 and k_2 are the components of $\mathbf{k}$, defined in terms of the Fourier transform

$$\tilde{\kappa}(\mathbf{k}) = \int_{R^2} \mathrm{d}\boldsymbol{\theta}\ \kappa(\boldsymbol{\theta})\ \ \exp\big[i\boldsymbol{\theta}\cdot\mathbf{k}\big]\ \ , \tag{6.22}$$

where $\boldsymbol{\theta}$ has components θ and φ. The well-known Kaiser-Squires (KS) method estimates the convergence by directly inverting equation 6.21.

For the DES Y3 sky-coverage, the flat sky approximation cannot be used without introducing substantial errors (Wallis et al., 2017). As in the Y1 mass map analysis (Chang et al., 2018) we require a curved-sky treatment. KS on the sphere corresponds to a decomposition a spin-2 field (γ) into a curl-free E-mode component and a divergence-free B-mode component, as described in Sec. 6.2.

With these components $\gamma_{E,\ell m}$ and $\gamma_{B,\ell m}$ we use equation 6.10 to recover $\kappa_{E,\ell m}$ and $\kappa_{B,\ell m}$, which are transformed as scalars using a spin-0 spherical harmonic transform to recover $\kappa(\theta,\varphi) = \kappa_E(\theta,\varphi) + i\ \kappa_B(\theta,\varphi)$.

The spherical harmonic operations described above are entirely analogous with CMB linear polarization, where the Q and U Stokes parameters correspond to the γ_1 and γ_2. As such, all spherical harmonic transformations use either the scalar or "polarization" transforms of the `HEALPY` package. All maps presented in this work use an `NSIDE`= 1024 and all relevant spherical harmonic transforms use an $\ell_{max} = 2048$.

As with flat-sky KS, this generalization of KS to the celestial sphere corresponds to an inverse of the linear operation $\mathbf{A}$ in equation 6.15 and, as such, corresponds to a maximum likelihood estimate (c.f. equation 6.16) of the convergence field κ. Direct KS inversion therefore corresponds to a *maximum a posterior* estimate with a uniform prior $P(\boldsymbol{\kappa}) \propto 1$.

As is standard practice the KS inversion is followed by a smoothing of small angular scales, corresponding to a lower bound on the prior with respect to angular scale. We treat the choice of the angular smoothing scale as a free parameter, the effects of which we investigate using simulated data.

6.3.3 No B-modes prior

We can decompose a convergence map into a real E-mode and imaginary B-mode component

$$\kappa = \kappa_E + i\ \kappa_B\ \ , \tag{6.23}$$

where the shear representation of the E-mode κ_E is curl-free and the B-mode κ_B is divergence-free.

Through the Born-approximation weak lensing derivation of Sec. 6.2, it is clear that weak gravitational lensing generates no B-mode component. Higher order contributions can contribute to non-zero B-modes (e.g., Krause & Hirata 2010), though these effects are generally much smaller than the leading E-mode contribution. Additionally, intrinsic alignments of galaxies can induce a non-zero B-mode contribution (Blazek et al., 2017; Samuroff et al., 2019), though intrinsic alignment effects are not included in this map reconstruction analysis. We also note that systematic effects, as shear measurement systematics of PSF residuals, can also generate spurious B-modes (e.g., Asgari et al. 2019b), but no significant B-modes have been measured in the DES Y3 shape catalogue (Gatti et al. 2020, Chapter 5).

The standard Kaiser-Squires reconstruction generates spurious B-modes due to shape noise and masks. It is therefore a well-motivated to have a prior probability distribution for convergence κ that gives no probability to κ_B and the Kaiser-Squires uniform prior to κ_E only, giving the following log-prior,

$$-\log P(\boldsymbol{\kappa}) = i_{Im(\kappa)=0} \; + \; \text{constant} \quad , \tag{6.24}$$

where the indicator indicator function of a set $\mathcal{C}$ is defined as

$$i_{\mathcal{C}}(x) = \begin{cases} 0 & \text{if } x \in \mathcal{C} \\ +\infty & \text{otherwise} \end{cases} \quad , \tag{6.25}$$

which in our case gives zero prior probability to convergence κ maps with an imaginary component (corresponding to B-modes). The MAP estimate with this prior and Gaussian likelihood is given by the following optimisation problem:

$$\hat{\boldsymbol{\kappa}} = \arg\min_{\kappa} \; (\boldsymbol{\gamma} - \mathbf{A}\boldsymbol{\kappa})^{\dagger} \; \mathbf{N}^{-1} (\boldsymbol{\gamma} - \mathbf{A}\boldsymbol{\kappa}) + i_{Im(\kappa)=0} \; . \tag{6.26}$$

This formulation allows us to maximize the log posterior (equation 6.14) using Forward-Backward Splitting, with a proximity operator corresponding to an orthogonal projector onto the set $\mathcal{C}$. This is implemented with the following iterative method

$$\boldsymbol{\kappa}^{(n+1)} = \mathrm{Re}\Big[\boldsymbol{\kappa}^{(n)} + \mu \mathbf{A}^{\dagger} \mathbf{N}^{-1} \big(\boldsymbol{\gamma} - \mathbf{A}\boldsymbol{\kappa}^{(n)}\big)\Big] \quad , \tag{6.27}$$

where μ controls the gradient steps and is free to be chosen.

On the sphere we use the combined harmonic transformation (as described in § 6.3.2) incorporating an upsampling of resolution to avoid the cumulative effects of non-orthogonal `HEALPIX` spherical harmonic transforms.

6.3.4 Gaussian prior (Wiener filter)

This prior on the convergence is that of a Gaussian random field, which is applicable for the density field on large scales at late times,

$$P(\boldsymbol{\kappa}|\mathbf{S}_\kappa) = \frac{1}{\sqrt{(\det 2\pi \mathbf{S}_\kappa)}} \exp\Big[-\frac{1}{2} \boldsymbol{\kappa}^\dagger \, \mathbf{S}_\kappa^{-1} \boldsymbol{\kappa} \Big] \, . \tag{6.28}$$

The MAP estimate with this prior and Gaussian likelihood is given by the following optimisation problem:

$$\hat{\boldsymbol{\kappa}} = \arg\min_{\kappa} \, (\boldsymbol{\gamma} - \mathbf{A}\boldsymbol{\kappa})^\dagger \, \mathbf{N}^{-1} (\boldsymbol{\gamma} - \mathbf{A}\boldsymbol{\kappa}) + \boldsymbol{\kappa}^\dagger \, \mathbf{S}_\kappa^{-1} \boldsymbol{\kappa} \, . \tag{6.29}$$

The solution for this is the Wiener filter:

$$\begin{aligned} \hat{\kappa}_W &= \mathbf{W}\gamma \\ \mathbf{W} &= \mathbf{S}_\kappa \mathbf{A}^\dagger \big[\mathbf{A} \mathbf{S}_\kappa \mathbf{A}^\dagger + \mathbf{N} \big]^{-1} \, . \end{aligned} \tag{6.30}$$

Here $\mathbf{S}_\kappa$ and $\mathbf{N}$ are the signal and noise covariance matrices respectively, which are $\langle \kappa \kappa^\dagger \rangle$ and $\langle \mathbf{n}\mathbf{n}^\dagger \rangle$ for this problem.

Direct evaluation of the matrix $\mathbf{W}$, which has at least 10^{12} elements and is sparse in neither pixel space nor harmonic space, would be extremely computationally expensive. We therefore make use of a class of methods that use additional *messenger fields* (introduced by Elsner & Wandelt 2012) to iteratively transform between pixel space, where $\mathbf{N}$ is diagonal, and harmonic space, where $\mathbf{S}_\kappa$ is diagonal.

For a Wiener filter messenger field implementation on the sphere we use the software DANTE (DuAl messeNger filTEr), presented in Ramanah et al. (2019). The signal covariance matrix in harmonic space is diagonal, with elements given by an assumed fiducial power spectrum. Our fiducial E-mode power spectrum matches that of the simulate (noise-free) Buzzard convergence κ maps. We explicitly provide a B-mode power spectrum set to zero, thus simultaneously achieving the no B-modes prior equivalent to Sec. 6.3.3.

6.3.5 Sparsity prior

The optimisation problem solved by the GLIMPSE algorithm using a sparsity prior is

$$\hat{\kappa} = \arg\min_{\kappa} \; (\gamma - \mathbf{A}\kappa)^{\dagger} \; \mathbf{N}^{-1}(\gamma - \mathbf{A}\kappa) + \lambda||\omega\mathbf{\Phi}^{\dagger}\kappa||_1 + i_{\mathrm{Im}(\kappa)=0} \; , \qquad (6.31)$$

where ω is a diagonal matrix of weights, and $\mathbf{\Phi}^{\dagger}$ is the inverse wavelet transform. The indicator function $i_{\mathrm{Im}(\cdot)=0}$ in the final term imposes realness on the reconstruction (no B-modes). The use of NDFT (non-uniform discrete Fourier transform) allows the first term to perform a forward-fitted Kaiser-Squires-like step without binning the shear data, allowing the smaller scales to be retained in the reconstruction. The full algorithm, including the calculation of the weights, is described in Sec. 3.2 in Lanusse et al. (2016).

GLIMPSE operates on a small patch of the sky, which it treats as flat. Input shape data is transferred from the celestial sphere to the tangent plane (i.e. the plane tangent to the sphere at the patch centre); the 'shape to convergence' calculation is done on the tangent plane (where the flatness simplifies the analysis); the results (which are reported at a lattice of points - call this an 'output lattice') are then mapped back to the sphere. The mapping between sphere and tangent plane is the orthographic projection. To analyse the large DES footprint we run GLIMPSE on multiple (overlapping) small patches and paste the results together. We set each of our patches to be 256 square degrees (a compromise: larger would stress the flat-sky approximation while smaller would suppress large-scale modes). The density of such patches is one per 13 square degrees. The output lattices were set to have 330×330 points. Each pixel in our final convergence map (`NSIDE` of 2048) is obtained from a weighted average of the convergences at all the output lattice points, from all the patches, that happen to fall in that pixel. The weights are chosen to be unity in the centre of each patch but to fall away to zero (sharply but smoothly) away from the central one-ninth of each output patch. As a last step the output convergence map is downsampled to an `NSIDE` of 1024.

The choice of dictionary depends on the structures contained in the signal. Theory predicts the formation of quasi-spherical halos of bound matter. It is standard practice to represent the spatial distribution of matter in halos with spherically symmetric Navarro-Frenk-White (Navarro et al., 1996) or Singular Isothermal Sphere profiles. Coefficients of Isotropic Undecimated

Wavelets (Starck et al., 2006) in two dimensions are well suited to the observed convergence of a dark matter halo. The wavelet transform used in the GLIMPSE algorithm is the starlet (Starck et al., 2007), which can represent positive, isotropic objects. This prior in the starlet basis represents a physical model that the matter field is a superposition of spherically symmetric dark matter halos.

6.4 Data and simulations

In this work we use data products from the third year (Y3) of the Dark Energy Survey (DES Flaugher, 2005), and mock galaxy catalogs reproducing the properties of the DES data. In particular, we used the version 1.8 of the Buzzard simulation introduced in § 4.3.2. The preliminary (yet non-published) results on data have been obtained using the blinded version 3.30.20 of the DES Y3 catalogue, as presented in Chapter 5. Below we give a description of the redMaPPer clusters used in the results section of this Chpater.

6.4.1 redMaPPer Clusters

In this work we also consider the DES Y3 redMapper cluster catalogue (based on the homonym algorithm Rykoff et al. 2015) to compute correlations with the reconstructed convergence maps. The algorithm optically selects clusters and estimate cluster's richness $\lambda_{\rm RM}$. The richness is a proxy of the number of galaxies belonging to the cluster; it is formally defined as the membership probability over all galaxies within a scale radius. The radius is chosen such that it minimises the scatter in the mass-richness relation. The redMaPPer catalogue comes with excellent redshift accuracy ($\sigma_z/(1+z) \sim 0.01$), as the clusters members are mostly well modelled red galaxies.

6.5 Simulation tests

In this section we discuss and compare the different mass map methods outlined in § 6.3. To this aim, we use simulated convergence maps and a number of different statistics to test the quality of the reconstruction with respect to the input convergence map available in simulations. All the maps considered had been converted to `HEALPIX` (Górski et al., 2005) maps with

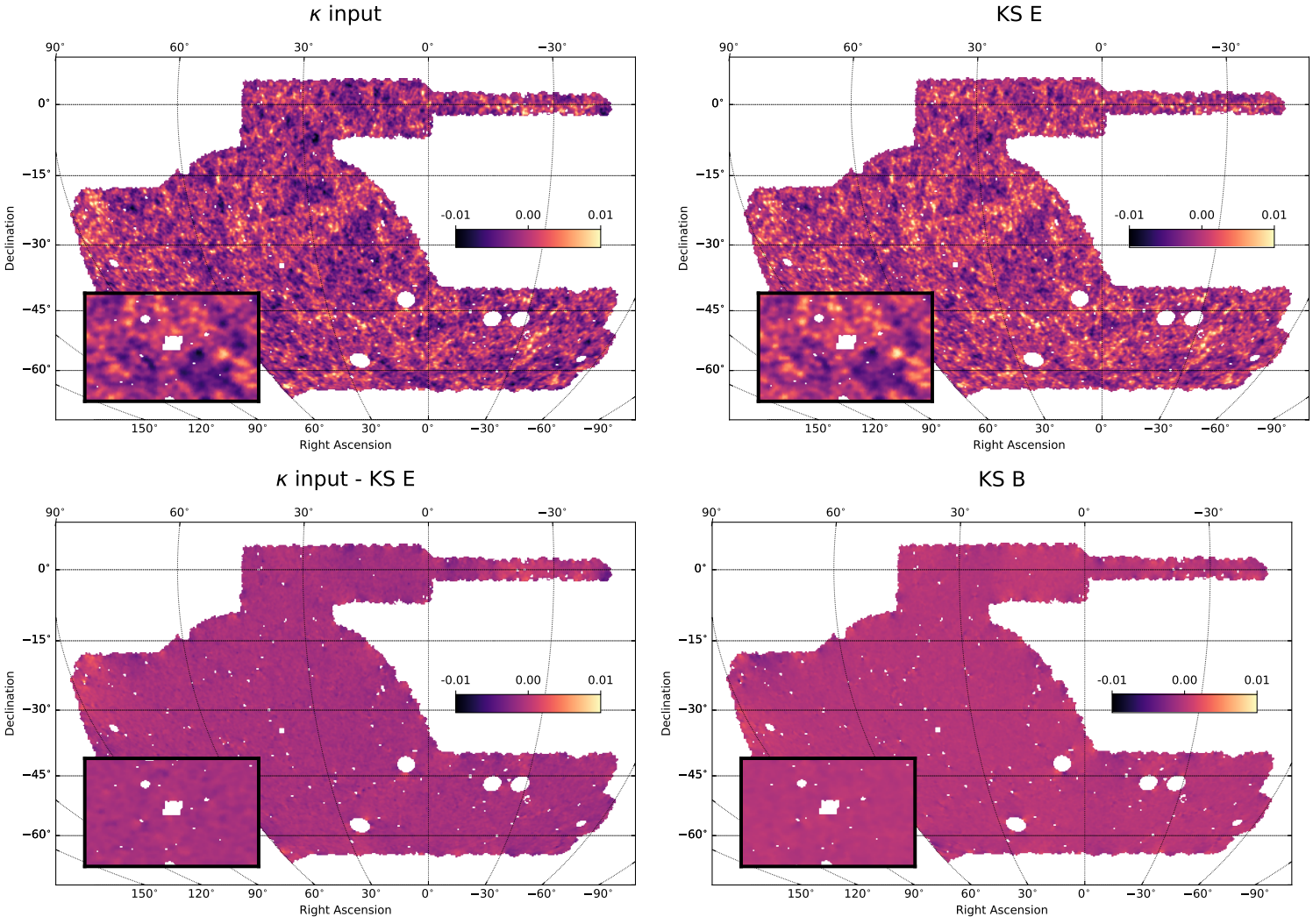

Figure 6.1: Simulated DES Y3 weak lensing mass maps. *Top left panel*: the original input convergence field map. *Top right panel*: the convergence field map (E-mode) obtained using the spherical KS algorithm from a noiseless realisation of the shear field. *Bottom left panel*: residual map of the input convergence field and the KS map. *Bottom right panel*: KS B-mode map. Maps have been smoothed at 10 arcminutes for visualisation purposes.

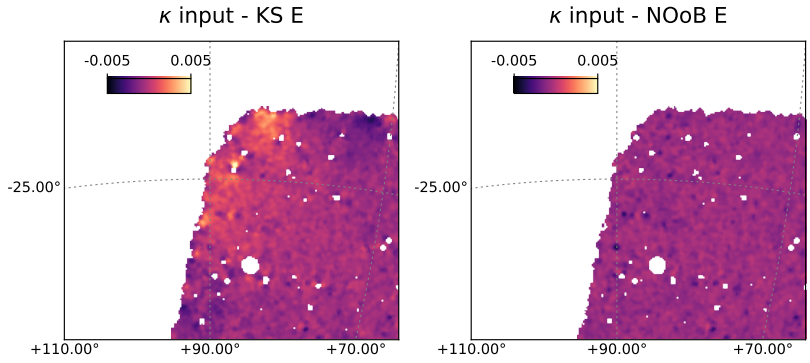

Figure 6.2: Zoomed in version of the residual maps for the KS (left) and No B-mode prior methods (right). The maps have been zoomed close to the edge of the footprint. The No B-mode prior method is characterised by a lower amplitude of the residual map, owing to a better handling of the mask effects.

`NSIDE` 1024, for an easier comparison. The pixel size corresponding to such resolution is of 3.2 arcminutes and it has been chosen based on the expected DES Y3 galaxy number density.

Figs. 6.1, 6.3 show a number of simulated maps. For visualisation purposes, the KS, the No-B-modes prior and the original convergence maps have been smoothed at 10 arcminutes. For the Glimpse map we imposed a sparsity prior of $\lambda = 3$. No smoothing has been applied to the Wiener map.

In particular, Fig. 6.1 shows the input convergence map, the KS E-mode and KS B-mode maps[3] and the KS residual map (defined as the difference between the true map and the recovered E-mode map), obtained from a noiseless realisation of the shear field. In this idealised case with no shape noise, the KS method is able to recover most of the features of the input convergence map, except for the part of the map close to the edges of the footprint. The KS method is susceptible to mask effects in the case of partial sky coverage, resulting in a non-zero residual map and spurious B-modes due to E-modes leakage.

Fig. 6.3 shows the E-mode maps for the four methods obtained from a noisy realisation of the shear field. The KS E-mode map is now noisier: despite the most significant features of the input convergence field can still be spotted by eye, a number of noise-induced small-scale peaks dominate the reconstructed map. The impact of noise is reduced in the case of the other

[3]Note that, KS method excluded, all the methods set the B-mode maps to 0.

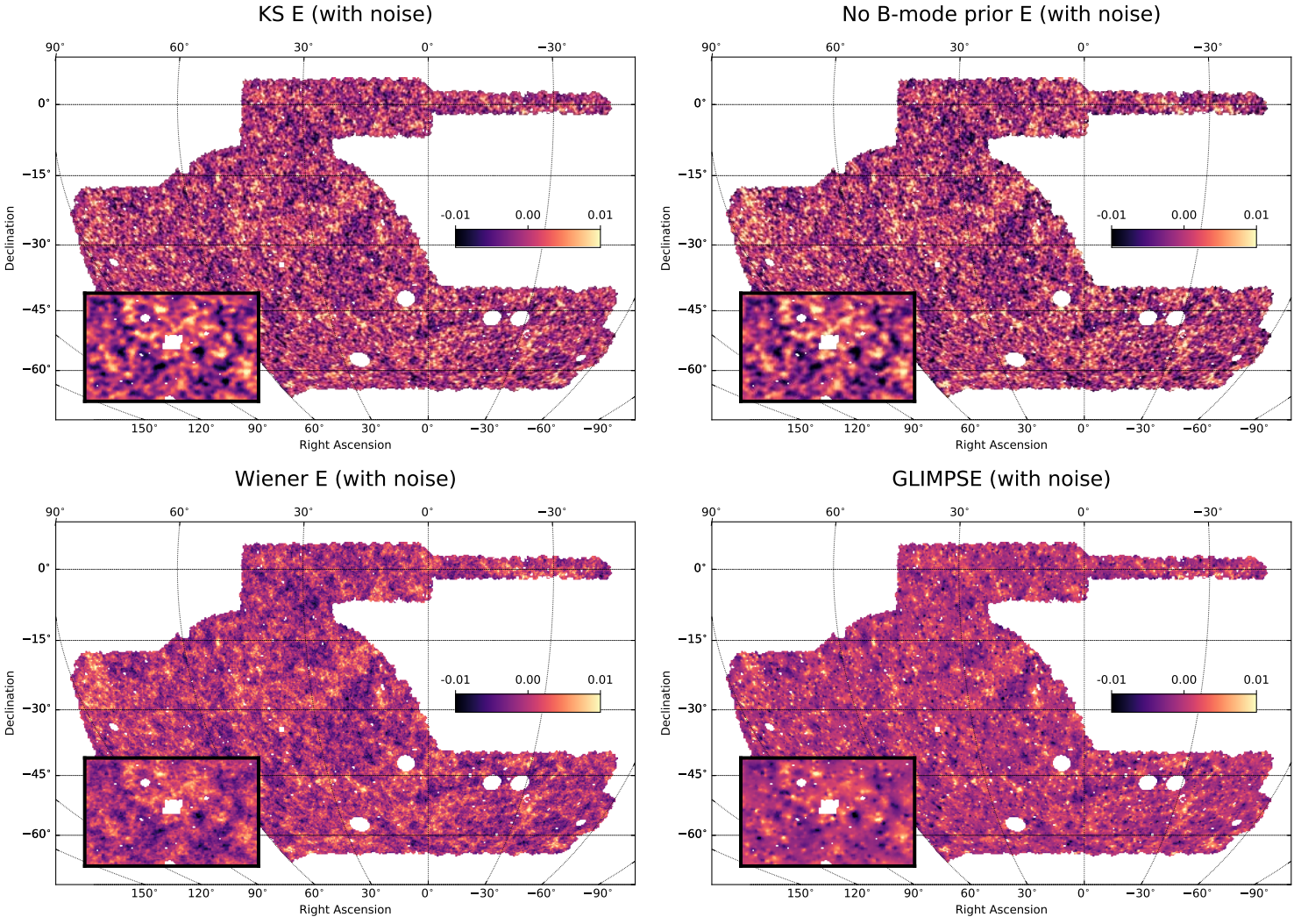

Figure 6.3: Simulated DES Y3 weak lensing mass maps, obtained from a noisy realisation of the shear field, with different map making methods. *Top left panel*: noisy KS E-mode map *Top right panel*: E-mode map obtained with the no B-mode prior method. *Bottom left panel*: E-mode Wiener filter map. *Bottom right panel*: E-mode GLIMPSE map. The maps in the top panels have been smoothed at 10 arcminutes; no further smoothing is applied to the maps showed in the lower panels.

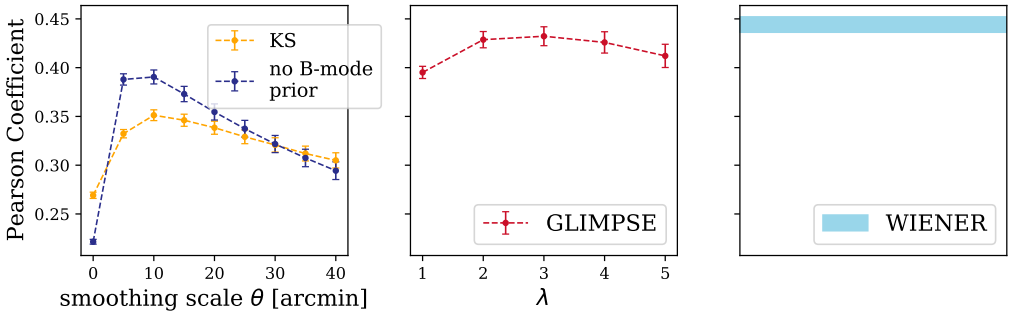

Figure 6.4: Pearson coefficient between the reconstructed map and the true, noiseless convergence map, for the four different mass map methods. When possible, we varied the tuning parameters of the methods. Errors are estimated from jackknife resampling.

methods, due to the additional priors included in the map making process. In particular, the sparsity prior adopted by the GLIMPSE method suppresses the noise enhancing peaky features, which are assumed to be the result of a superposition of spherically symmetric dark matter halos (a feature that can be noted in the zoomed-in portion of the GLIMPSE map). The noise is also suppressed in the case of the Wiener method, despite the map shows less peaky features compared to the GLIMPSE map. The Wiener method assumes the convergence field to be Gaussian, therefore is better suited to recover the large scale signal of the map. In the case of the No-B-modes prior, the map looks similar to the KS E mode map, but with structures enhanced due to noise suppression.

In the following subsections, we proceed to a more quantitative comparison between the different map-making methods, discussing a number of tests we performed on maps. Whenever possible, we varied the parameters of the method (i.e., smoothing scale θ of the smoothing function for KS and No-N-mode prior methods, sparsity parameter λ GLIMPSE). In particular, we discuss in § 6.5.1 a test involving the Pearson coefficient between the true, simulated convergence map and the reconstructed map; in § 6.5.2 we show the root-mean-square error of the residual maps; we discuss the power spectrum recovered by different methods and the power spectrum of the residual maps in § 6.5.3; we show the 1-point distribution function of the reconstructed map in § 6.5.4.

6.5.1 Pearson coefficient

The first statistic we examined is the Pearson coefficient. The Pearson correlation coefficient, defined for two convergence fields κ_1 and κ_2, is:

$$\text{Pearson} = \frac{\langle \kappa_1 \kappa_2 \rangle}{\sqrt{\langle \kappa_1^2 \rangle} \sqrt{\langle \kappa_2^2 \rangle}} \tag{6.32}$$

In this case, we computed the Pearson coefficient between the true, simulated convergence map and the reconstructed map. In this test, we only considered E-mode maps and maps recovered from noisy estimates of the shear field. The results are show in Fig. 6.4. In general, the closer to unity the Pearson coefficient value, the better the reconstruction. For KS and the No-B-modes prior methods we varied the smoothing scale, while for GLIMPSE we varied the sparsity prior. The No-B-modes prior method, GLIMPSE and Wiener perform better (i.e, the Pearson coefficient is closer to unity) than standard KS for some value of their tuning parameters. The effect of the tuning parameter for the No-B-modes prior method is similar to KS: basically, smoothing helps improving the Pearson coefficient. This is due to the fact that small scales are shape noise dominated, with 10 arcminutes corresponding to the scale where the amplitude of shape noise is comparable to the amplitude of the signal. This means that smoothing up to 10 arcminutes removes more small-scale noise-induced peaks than "true" peaks. A different amount of shape noise would change this scale; in the limit of no shape noise, the optimal scale would be the smallest scale allowed by the pixellisation scheme. As for GLIMPSE ,the level of suppression of the shape noise is controlled by the sparsity coefficient λ, for which we found $\lambda = 3$ to be the optimal parameter. The Wiener filter map does not have any tuning parameter, but has the highest Pearson coefficient among all the methods. We note that in the case of Glimpse and Wiener maps, further smoothing the maps would not improve the Pearson coefficient, as the noise is suppressed by the sparsity and Gaussian priors to a level such that the amplitude of the shape noise is smaller than the amplitude of the signal.

6.5.2 RMSE

The second statistic we examine is the root-mean-square error (RMSE) of the residuals, defined as:

$$\text{RMSE}(\kappa^{\text{truth}}, \kappa^{\text{recon}}) \equiv \sqrt{\frac{1}{n} \sum_{i=1}^{n} \Delta\kappa_i^2}, \tag{6.33}$$

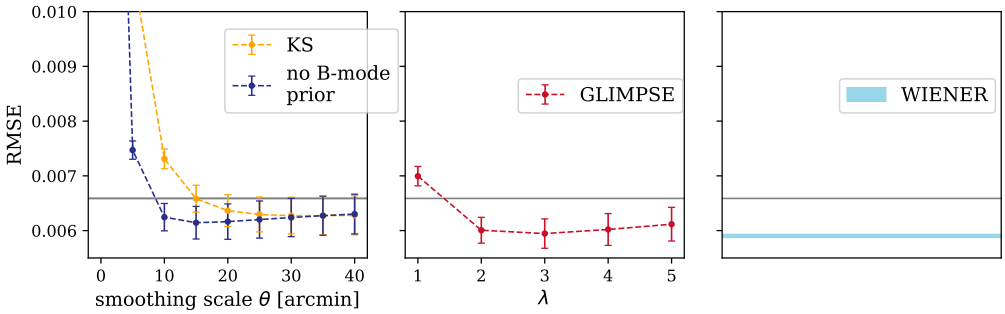

Figure 6.5: Root-mean-square error (RMSE, see § 6.5.2 for a definition) for the four different mass map methods. When possible, we varied the tuning parameters of the methods. Errors are estimated from jackknife resampling.

with $\Delta\kappa_i$ being the difference between the reconstructed map and the true map in a given pixel i. In this test, we only consider E-mode maps and maps recovered from noisy estimates of the shear field. The results are shown in Fig.6.5. In general, the closer to zero the RMSE, the better the reconstruction. In the plots, the blacked dashed lines refer to the RMSE of the original convergence field. The results from this test are in line with the results from the Pearson coefficient test: the No-B-modes prior method, GLIMPSE and Wiener perform better (i.e, the RMSE is closer to zero) than standard KS for some value of their tuning parameters, which are similar to the ones determined from the Pearson coefficient test.

For KS and the No-B-modes prior methods the RMSE is reduced strongly with smoothing, indicating that the variance at small scales is completely dominated by shape noise, reaching a minimum after smoothing the reconstructed maps at 10∼20 arcminutes. We note that the minimum of the RMSE signal and the maximum of the Pearson coefficient for these two maps are at a similar smoothing scale (even though the value does not need to be exactly the same). For these two methods, the RMSE should converge at very large scales (larger than those showed here) to the RMSE of the original field, as the reconstructed map signal would be washed out by the smoothing.

As concerns the GLIMPSE method, it is characterised by a smaller RMSE compared to KS. This indicates how the sparsity prior successfully deal with shape noise, reducing it. The minimum is reached for a sparsity parameter $\lambda = 3$, the same value that maximise the Pearson coefficient. The Wiener map does not have any tuning parameter to vary, but shows a smaller RMSE

compared to the KS method. As in the case of the Pearson coefficient, further smoothing the maps obtained from GLIMPSE or the Wiener method would not improve the RMSE.

6.5.3 Power Spectrum of the signal and of the residuals

We now study the power spectrum of the reconstructed maps, along with the power spectrum of the residual maps. Results are shown in Fig. 6.6.

We first consider the power spectrum of the reconstructed maps; this is shown in the upper left panel of Fig. 6.6 for the maps obtained from the noiseless estimate of the shear field, and in the upper right panel for the maps obtained considering shape noise. The power spectrum is binned in 10 bins between $\ell = 0$ and $\ell = 2048$. We do not show higher multipoles as KS and the No B-modes methods have a hard cut at $\ell = 2048$. From the upper left plot it can be noted that the standard KS method underestimates the power at large scales ($\ell < 200$), due to the lack of priors that account for mask effects. The missing power is leaked into B-modes. The No B-modes method, on the other hand, better recovers the large scale fluctuations. The same behaviour for the KS and No B-modes method can be noted in the upper right panel, when the reconstruction from a noisy realisation of the shear field is considered (although the recovered power spectrum is of course noisier). In this case, the power spectrum obtained from a noise-only map is subtracted. The Wiener and GLIMPSE maps are characterised by a power spectrum with a much smaller amplitude compared to the true power spectrum. This is expected, as the sparsity prior is not meant to preserve the correct amplitude of the moments of the input field. The exact effect of the prior on the amplitude of the power spectrum is however hard to predict analytically: this suggests that cosmological information can be extracted from Wiener and GLIMPSE maps only in a forward modelling fashion.

The lower panels of Fig. 6.6 show the power spectrum of the residual field. The lower left panel, in particular, shows again the effect of the mask on the standard KS method (the first bin at low ℓ), and that for both methods the power of the residuals increase at small scales. This effect is exacerbated by the presence of shape noise for KS and the No B-modes methods (lower right panel). Wiener and GLIMPSE maps, on the other hand, show a lower amplitude of the power spectrum of the residuals.

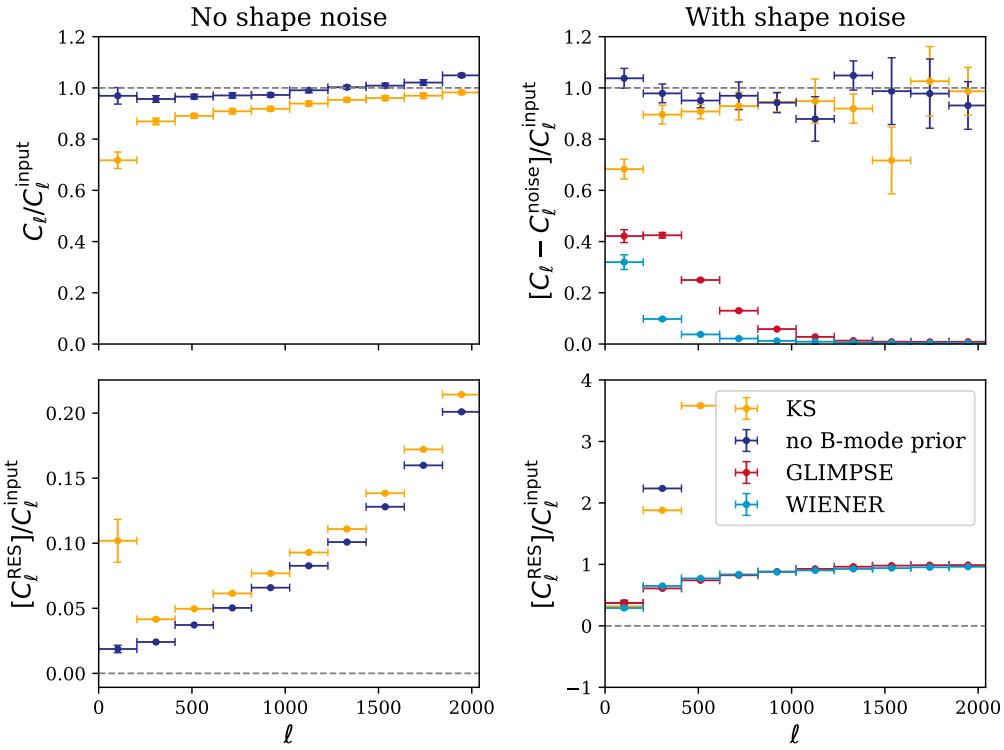

Figure 6.6: *Upper left*: power spectrum of the reconstructed maps obtained from a noiseless realisation of the shear field with respect to the expected theory power spectra for the simulation. *Upper right*: same as upper left, but with the maps obtained from the noisy realisation of the shear field, and with the power spectrum of the noise subtracted. *Lower left*: power spectrum of the residuals (defined as the difference between the reconstructed map and the input map) with respect the the input map power spectra. The reconstructed maps are obtained from a noiseless realisation of the shear field*Lower right*: same as lower left, but with the maps obtained from the noisy realisation of the shear field.

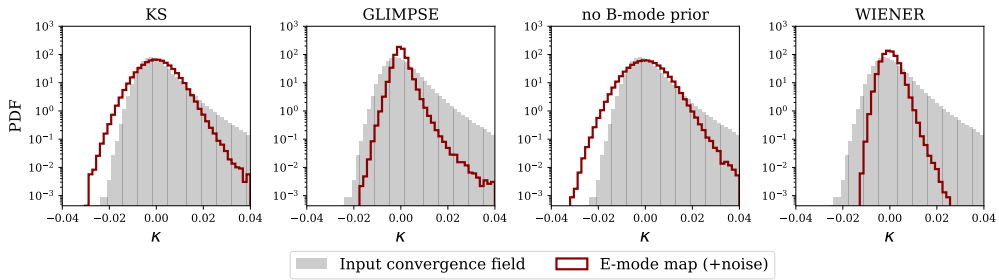

Figure 6.7: PDF (1-point distributions) for the different map reconstruction methods, obtained from a simulated, noisy realisation of the shear field. The grey shaded histogram in each panel represents the PDF of the true, input convergence field.

6.5.4 Convergence PDF

We next show in Fig. 6.7 the 1-point distribution function (PDF) of the convergence field. For KS and the No B-modes methods, we considered the maps with 10 arcminutes smoothing. The PDF of the reconstructed map, while showing an asymmetric distribution, fall short in reproducing the correct input PDF, due to the effect of smoothing and the presence of noise. The asymmetric distribution is a sign that the recovered map is not dominated by noise, whose PDF is completely Gaussian. The PDF of the Wiener and the GLIMPSE maps also falls short in reproducing the true PDF - despite noise has a smaller impact.

6.5.5 Summary of the tests on simulations

The tests we performed in this section clearly suggest that using priors to recover the converge field from a noisy realisation of the shear field improves the reconstruction according to a number of metrics. All methods, for some value of their tuning parameters, performed better than the raw, non-smoothed KS method in terms of the Pearson coefficient with the true convergence map. This means that the priors effectively make the maps more similar to the "true" convergence field. In particular, the Wiener and GLIMPSE methods generally delivered larger values of the Pearson coefficient and smaller values of the RMSE among the four methods. We furthermore showed that assuming B-modes to be null reduces mask effects (we remind the reader that this prior is assumed by all methods except for the KS method). As a downside, we also showed how the choice of the prior can

make the comparison of certain statistics with theoretical predictions particularly hard. E.g., we showed that the priors assumed by the Wiener and Glimpse map methods can severely dampen the amplitude of the measured power spectrum, making a direct comparison with the standard theoretical predictions meaningless.

The choice of the method clearly depends on the goals and details of the science application. For instance, cosmological analyses using Wiener and Glimpse map methods necessarily need to forward model the desired statistics and data vectors with N-body simulations, due to the difficulties in theoretically modelling the effects of their priors. On the other hand, science applications that are more interested in preserving the variance of the maps might prefer to use the KS or No B-mode methods.

In the next section we present the four different maps obtained using the DES Y3 data, along with a number of systematic tests. Any extensive science application of the maps is left to future work.

6.6 Application to data

We present in this section the DES Y3 weak lensing mass maps on data. Fig. 6.8 shows the four maps obtained with the KS, No B-mode prior, Wiener and Glimpse methods, obtained from the `METACALIBRATION` catalogue. We recall that these maps have been obtained applying the `METACALIBRATION` response correction and the inverse variance weights, as explained in § 5.4.3. The maps obtained with the different methods visually show the same differences as the ones obtained in simulations (Fig. 6.3), with the Weiner and Glimpse maps particularly suppressing the noise thanks to their prior.

We then perform a number of tests on the recovered maps. We first test if there exists any spurious correlation between our maps and quantities that are not expected to correlate with the convergence maps. The shape catalogue used to produce the mass maps have been largely tested in Chapter 5, but the potential correlation between convergence maps and systematics has not been investigated there. We therefore consider a number of catalogue and observational properties as potential systematics, in a similar fashion to what has been done in Chapter 5. In particular, we consider the two components of the PSF ellipticity at the galaxy position (PSF_1, PSF_2), their E and B-modes maps (PSF_E, PSF_B); and the size of the PSF (T_{PSF}). As observing condition properties, we consider the mean i-band airmass, the mean i-band brightness, the mean i-band magnitude

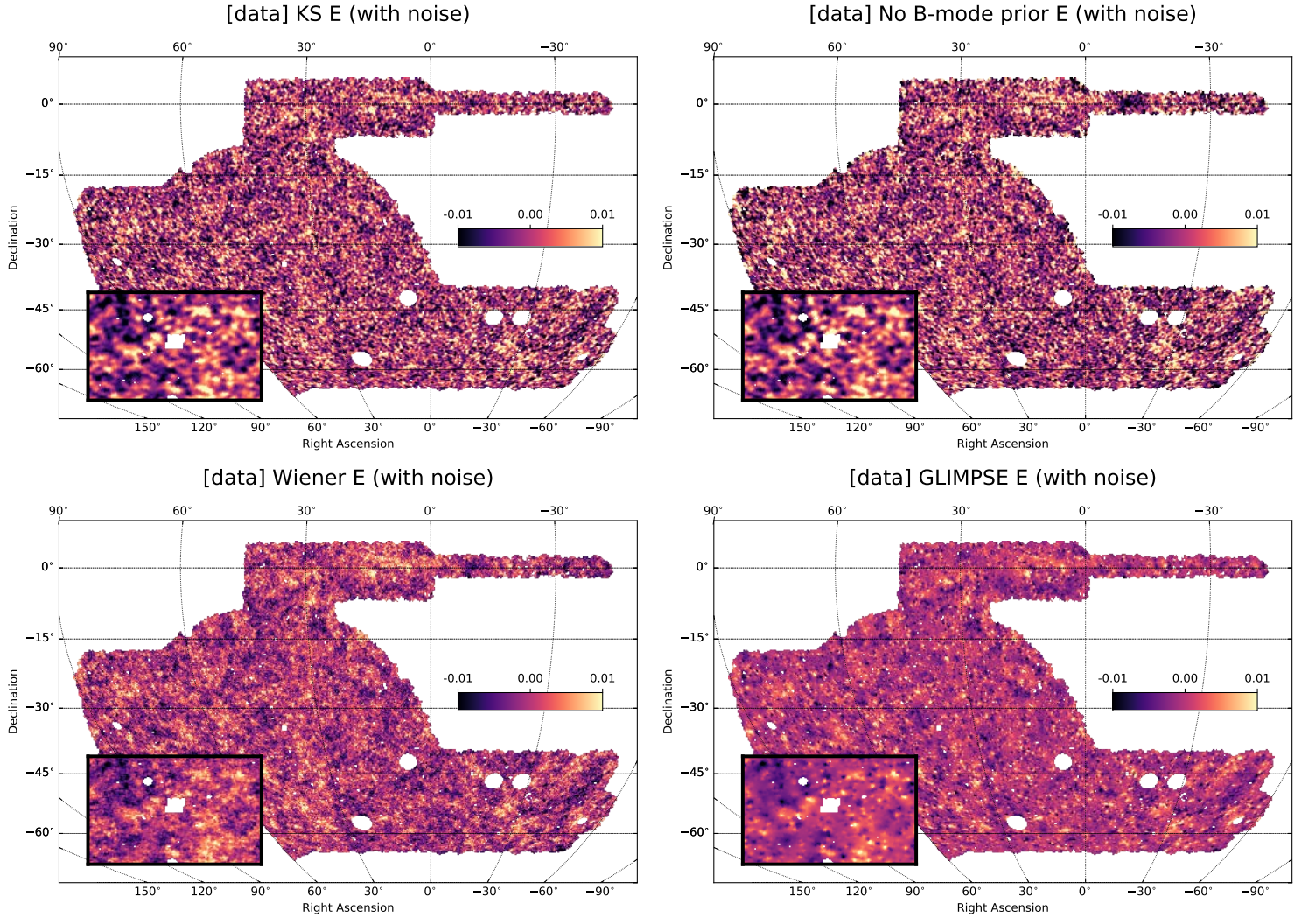

Figure 6.8: METACALIBRATION DES Y3 weak lensing mass maps, obtained from the official DES Y3 shape catalogue, with different map making methods. *Top left panel*: noisy KS E-mode map *Top right panel*: E-mode map obtained with the No B-mode prior method. *Bottom left panel*: E-mode Wiener filter map. *Bottom right panel*: E-mode GLIMPSE map. The maps in the top panels have been smoothed at 10 arcminutes; no further smoothing is applied to the maps showed in the lower panels.

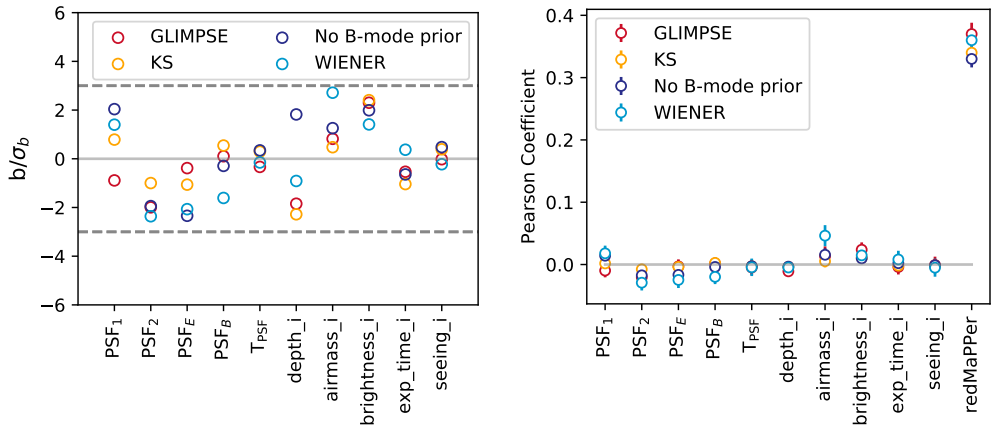

Figure 6.9: Left panel: Best fit values for the coefficient of the relation $\langle\kappa\rangle = b\text{syst}+c$ with syst a given systematic map. The values of the slopes are shown for different systematic maps and the errors are estimated using log-normal `FLASK` simulations. *Right panel:* Pearson coefficient of the convergence maps and a number of systematic maps. Errors are estimated using log-normal `FLASK` simulations. We also show the Pearson coefficient with the redMaPPer clusters effective richness $\lambda_{\text{eff,RM}}$.

limit (depth), the mean i-band exposure time, and the mean i-band seeing. There are a few maps that we considered in the shape catalogue tests and that we exclude here. For instance, we do not include the signal-to-noise ratio maps among the systematic maps, as we actually expect to measure a signal: indeed, over-dense regions of the sky should be populated by red ellipticals with high signal-to-noise. Similarly, we expect (and measure) a high significance correlation between galaxy colors and our mass maps.

We follow Chang et al. (2018) and create a systematic map M^{S} for each of the systematics using the mean-subtracted values. We first assume a linear dependence between the convergence maps and the systematics maps, such as:

$$\kappa_{\text{E}} = bM^{\text{S}} \tag{6.34}$$

We fit all the pixel values of the convergence maps assuming such a linear relationship with the systematic maps. We show the measured coefficient for each of these systematic maps in the left panel of Fig. 6.9. Errors are estimated using 300 `FLASK` log-normal mocks, but we verified that using jackknife errors substantially caused no difference in the results. We do not find any particularly significant correlation; individually, the coefficients are measured with a significance smaller than 3σ. The overall χ^2 of

the null hypothesis (considering the correlations among the 10 systematic maps considered here) is 5,20,23,15 for KS, No B-mode prior, Wiener and GLIMPSE respectively. We also compute the Pearson coefficient between the convergence maps and the systematic maps; results are shown in the right panel of Fig. 6.9. The main difference with the linear fit is that the Pearson coefficient does not assume *a priori* any relation between the convergence maps and systematic maps. Again, we do not find any strong evidence of systematic contamination, with the χ^2 of the null hypothesis being 14,16,20 and 23 for KS, No B-mode prior, Wiener and GLIMPSE respectively.

For obvious reasons the true convergence map is not available in data; we can nonetheless check that the reconstructed mass maps probe the foreground matter density field by correlating them with a sample of other tracers. We therefore proceed computing the Pearson coefficient of the reconstructed maps with redMaPPer cluster richness. Groups and clusters of galaxies are expected to trace the highest density regions in the foreground; as a consequence, we do expect to detect a high correlation with the mass maps. We only consider here the biggest clusters in the redMaPPer catalogue with richness $\lambda_{RM} > 20$, as smaller clusters are generally associated with larger detection uncertainties. Furthermore, we only consider clusters at redshift $z < 0.7$.

In order to take into account the fact that our mass maps are proxies of the mass distribution effectively weighted by a lensing kernel, we compute the Pearson coefficient with an effective cluster richness. Following Jeffrey et al. (2018), we define the effective cluster richness as:

$$\lambda_{\rm eff,RM} = \frac{p(z)\chi(z)}{a(z)} \times \lambda_{\rm RM}, \tag{6.35}$$

where $p(z)$ is the lensing efficiency at the location of the cluster, $\chi(z)$ is the comoving distance to the cluster and $a(z)$ the scale factor.

We measure at high significance the Pearson coefficient between the maps and the redMaPPer effective cluster richness, obtaining values of 0.34 ± 0.02, 0.33 ± 0.02, 0.36 ± 0.02, 0.37 ± 0.02 for KS, No B-mode prior, Wiener and GLIMPSE respectively. The amplitude of the signal is definitely larger than the any of the signal measured between the convergence and the systematic maps. The Wiener and GLIMPSE maps have slightly higher Pearson coefficients with respect to the KS and No B-mode prior maps, although with the given uncertainties the difference is not particularly significant. For visualisation purposes, we show in Fig. 6.10 the GLIMPSE map with a few redMaPPer clusters super-imposed. From the Figure it can be noted how

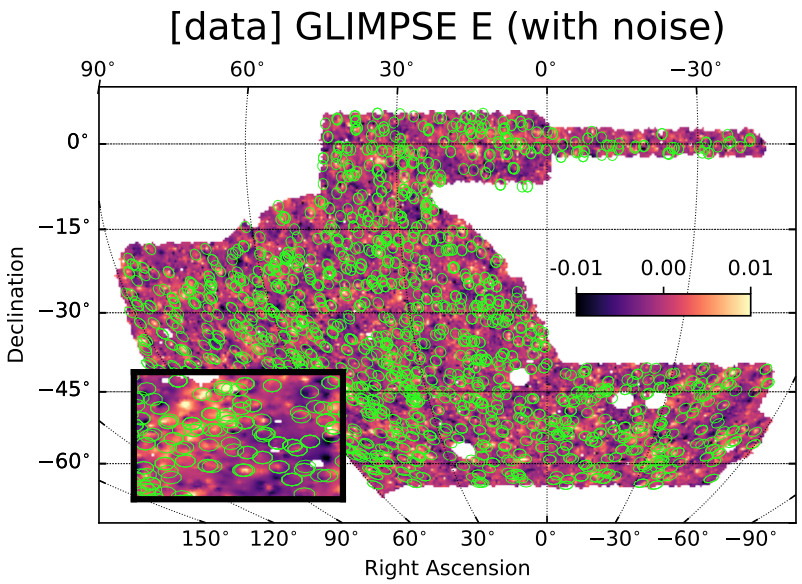

Figure 6.10: `METACALIBRATION` DES Y3 weak lensing mass maps, obtained with the GLIMPSE method, with redMaPPer clusters (green circles) super-imposed. In the wide field, we randomly selected a sub-sample of the clusters with richness $\lambda_{\rm RM} > 70$; for the small inset, we randomly selected a few clusters with $20 < \lambda_{\rm RM} < 30$. The circles are centered in the cluster center, but the circle size is not representative of the cluster size and it has been fixed to 100 arcminutes for visualisation purposes.

clusters tend to populate most overdense regions of the convegence map, avoiding the regions with negative signal.

6.7 Summary

In this Chapter we constructed weak lensing convergence maps ("mass maps") from the DES Y3 dataset using four reconstruction methods. The first method considered is the direct inversion of the shear field, also known as the Kaiser-Squires method, followed by a smoothing of small angular scales. The second method adds a prior on the B-modes of the map, imposing the reconstructed convergence field to be purely an E-mode map (No B-mode prior). Also this method has been followed by a smoothing at small scales. The third method, the Wiener filter method, assumes a Gaussian prior on the recovered mass map. Last, the GLIMPSE method implements a sparsity prior which can be interpreted as a physical model where the

matter field is considered as a superposition of spherically symmetric dark matter halos.

All methods are implemented on the sphere to accommodate the large sky coverage of the DES Y3 footprint. We compared the different methods using simulations that are closely matched to the DES Y3 data. We quantified the performance of the methods at the map level using a number of different summary statistics: the Pearson coefficient with the "true" simulated convergence map, the root-mean-square error (RMSE) of the residual maps, the power spectrum of the mass maps and residual maps, and the 1-point distribution function (PDF) of the mass maps.

The tests performed suggested that using priors to recover the converge field from a noisy realisation of the shear field generally improves the reconstruction, i.e., the recovered maps are more similar to the true convergence field. In particular, the Wiener and GLIMPSE methods generally delivered larger values of the Pearson coefficient and smaller values of the RMSE among the four methods. We furthermore showed that assuming B-modes to be null reduces the effect due to masked areas and missing data. As a downside, we also showed how the choice of the prior can make the comparison of certain statistics with theoretical predictions particularly complex. E.g., we showed that the priors assumed by the Wiener and GLIMPSE map methods can severely dampen the amplitude of the measured power spectrum, making a direct comparison with the standard theoretical predictions meaningless.

We then presented the official DES Y3 mass maps, obtained with the four different methods, and assessed their robustness against a number of systematic maps representing catalogue properties and observing conditions. We furthermore correlated the maps with redMaPPer clusters, showing that the clusters sit on top of the most overdense regions identified by the mass maps.

We stress that the choice of the particular mass map method depends on the goals and details of the science application. For instance, cosmological analyses using Wiener and GLIMPSE map methods necessarily need to forward model the desired statistics and data vectors with N-body simulations, due to the difficulties in theoretically modelling the effects of their priors. On the other hand, science applications that are more interested in preserving the variance of the maps might prefer the use of the KS or No B-mode methods.

In the next Chapter we focus on one particular science application of the mass map: we use the second and third moments or the mass maps to

constrain cosmological parameters.

Chapter 7

Cosmology with mass map moments

7.1 Introduction

A map of the mass distribution of the Universe, or the large-scale structure (LSS), contains a vast amount of cosmological information. A given cosmological model predicts the spatial statistics of the mass distribution as well as its evolution over time. One of the cleanest ways to probe the mass distribution in the Universe is through weak (gravitational) lensing. Gravitational lensing refers to the phenomenon that light rays from distant galaxies bend as they travel through space-time, causing distortion of the observed galaxy images. This is because the space-time is perturbed by mass distribution between the galaxy and the observer according to General Relativity (Einstein, 1936). Weak lensing is the regime where this perturbation is small; its effect is usually much smaller than the noise on a single galaxy basis, and the signal is extracted statistically using a very large ensembles of galaxies. As lensing is a purely gravitational effect, it is directly sensitive to the total mass distribution compared to other cosmological probes that use galaxies as tracers of the mass density field, such as galaxy clustering (for a review of weak gravitational lensing see e.g., Bartelmann & Schneider, 2001).

A key element of a weak lensing analysis is to have a large number of galaxies with well-measured shapes. This means that we need 1) cosmological surveys that collect photons from as many galaxies as possible, and 2) well-controlled systematic errors in the shape measurement of these galaxies. Motivated by the potential cosmological power of weak lensing, photometric galaxy surveys targeted at weak lensing science have been operating over

the past two decades. Today, unprecedented large galaxy surveys such as the Dark Energy Survey (DES, Flaugher, 2005), the Hyper Suprime-Cam (HSC) Subaru Strategic Program (Aihara et al., 2018), the Kilo-Degree Survey (KiDS, de Jong et al., 2013) are all pushing the limits of weak lensing measurements.

Most of the current weak lensing analyses have focussed on tomographic 2-point correlation measurements (e.g. Troxel et al., 2018; Hildebrandt et al., 2017; Hikage et al., 2019). With the past two decades of work, the theoretical modelling of the shear 2-point correlation function has matured significantly. Although there is still active research on, for example, the modelling of the small scales and of non-linear lensing corrections,the baseline theory of shear 2-point correlation function is reasonably robust. State-of-the-art datasets from the first year (Y1) of the DES currently give the tightest constraints from cosmic shear surveys on the Universe's clustering amplitude under a ΛCDM cosmology, $S_8 \equiv \sigma_8\sqrt{\Omega_\mathrm{m}/0.3} = 0.782^{+0.027}_{-0.027}$ (Troxel et al., 2018). The parameter S_8, which is a combination of σ_8 (the amplitude of structure in the present day Universe, parameterised as the standard deviation of the linear overdensity fluctuations on a $8h^{-1}$ Mpc scale) and Ω_m (the density of the total matter today) is designed to be approximately the parameter most constrained by weak lensing observations. We note that these constraints are at a level similar to those provided by the cosmic microwave background (CMB) from the *Planck* satellite $S_8 = 0.841^{+0.027}_{-0.025}$, when marginalising over neutrino mass and considering the same parameter space as DES (see Troxel et al. 2018, table III).

However, there is much more information stored in the matter fields beyond what can be captured by 2-point statistics. Two-point correlation functions only capture the Gaussian information stored in the field, while it is well known that the probability distribution function (PDF) of the galaxy density contrast in the late Universe has a 1-point distribution that is approximated better as log-normal than Gaussian (Hubble, 1934; Coles & Jones, 1991; Wild et al., 2005). Over the years, efforts have been made to explore statistics beyond 2-point for cosmology. These include 3-point correlation functions and bi-spectrum (Takada & Jain, 2003, 2004; Semboloni et al., 2011; Fu et al., 2014), weak lensing peak statistics (Dietrich & Hartlap, 2010; Kratochvil et al., 2010; Liu et al., 2015; Kacprzak et al., 2016; Martinet et al., 2018; Peel et al., 2018; Shan et al., 2018), higher moments of the weak lensing convergence field (Van Waerbeke et al., 2013; Petri et al., 2015; Vicinanza et al., 2016; Chang et al., 2018; Vicinanza et al., 2018; Peel et al., 2018), the PDF of the weak lensing convergence field (Patton et al.,

2016), density-split statistics (Friedrich et al., 2018; Gruen et al., 2018), Minkowski functionals (Kratochvil et al., 2012; Petri et al., 2015; Vicinanza et al., 2019; Parroni et al., 2020) and the Minimum Spanning Tree (MST, Naidoo et al. 2019). For some of these summary statistics (peak statistics, Minkowski functionals), one major challenge is that no analytic theoretical prediction of the target statistics exist and cosmological constraints must come from a large number of numerical simulations that span a range of cosmological parameters. In addition, these simulations also need to be closely matched to data and it is not clear what the requirements are for the matching between simulation and data (though there exist some work in systematically addressing this question, e.g. Bruderer et al., 2016; Kacprzak et al., 2019). With the increasingly large datasets, the demand on simulations for these statistics become increasingly hard to meet. For the other statistics where analytical forms exist (3-point function, higher moments, PDF, density split statistics), most of the exploration work has been carried out with idealised simulations that in many respects do not represent the survey data. One of the reasons for this is that once one moves beyond 2-point statistics, the computation of the statistic estimator and the theoretical modelling of the signal becomes more complicated. This means that the noise and systematic effects propagate non-trivially.

In this Chapter we focus on using the second and third moments of the weak lensing convergence field to constrain cosmology using the third year (Y3) of DES data. The modelling of second and third moments is based on theoretical predictions, rather than relying on large suites of N-body simulations. The goal of this Chapter is to describe and validate the methodology using simulations, determining the lower bounds on scales where systematic or modelling uncertainties are not expected to affect the cosmological analysis.

First studied in Jain & Seljak (1997), the moments of the weak lensing convergence field is one of the simpler high-order statistics both in terms of the measurement and in terms of the theoretical modelling. Several papers (e.g., Gaztanaga & Bernardeau 1998; Fosalba et al. 2008; Van Waerbeke et al. 2013; Pujol et al. 2016; Chang et al. 2018) have performed various moments measurements on simulations and/or data and compared the results with theoretical predictions, although this information was not then used to place constraints on cosmological parameters. In Vafaei et al. (2010), the authors studied the tradeoff between different survey strategies in CFHTLenS for combined two and three-point statistics using simulations. They concluded that combining two and three-point statistics of the convergence field

could increase the cosmological constraints by 10-20 per cent, in the case of CFHTLens data. In Petri et al. (2015), the authors used a set of simulations with different cosmological parameters to study how the moments of the convergence field can help constrain cosmology. They included up to the fourth moments and showed that the constraints improve by up to 20-30 per cent compared to the power spectrum-only constraints.

We build on the previous work and make several improvements. First, we use an analytic framework to incorporate the effect of masking, adapting a well-tested pseudo angular power spectrum estimation formalism (pseudo-C_ℓ in the following). Second, we include several systematic effects that are commonly accounted for in shear 2-point correlation function measurements and are key to obtaining unbiased cosmological constraints: namely, shear calibration bias, photometric redshift calibration uncertainty and intrinsic alignment. Third, we test how robust our statistics are to small-scales, higher order lensing corrections such as reduced shear and source clustering, and to the effect of small-scales baryonic physics. Finally, we test our framework with two different sets of simulations (simple log-normal simulations and full N-body simulations that match the characteristics of the dataset of interest), each suited for specific purposes. Although the simulations and analysis choices here are specific to the DES Y3 data, we note that the general approach in this Chapter can be easily transferred to a different dataset.

This Chapter is organised as follows. In § 7.2 we describe how we generate the weak lensing convergence maps from a shape catalog using a generalisation of the Kaiser & Squires (1993b) algorithm. In the same section, we further show how the second and third moments of this convergence map can be modelled, taking into account the effect of the mask as well as other systematics. In § 7.3 we describe the characteristics and purpose of the two set of simulations used in this work. We test the validity of our modelling with simulations in § 7.4 and determine the regime where our model can correctly predict the second and third moments. In § 7.5 we derive the final components needed for a cosmology analysis: the covariance matrix, the scale cuts, and the likelihood. We describe also a fast emulator for evaluating the theory prediction for the cosmology inference. In § 7.6 we determine the final fiducial scale cuts by examining how the cosmological constraints are biased as a function of scale cuts, and we forecast the cosmological constraints for DES Y3 and Y5 data. We summarise our findings in § 7.7.

7.2 Map making and theoretical modelling

In order to extract cosmological information from weak lensing convergence maps, we need to first construct the convergence map κ from the observed weak lensing shear γ. The theoretical modelling of the moments measured from the convergence map depends on the particular procedure one took to construct the map. As for the map making procedure, we rely on the full-sky Kaiser-Squires method outlined in § 6.3. The full-sky Kaiser-Squires method we implemented in this Chapter does not assume any prior knowledge of the convergence field to be reconstructed. We are not considering here the other methods explored in Chapter 6, as our goal is to model the convergence moments from theory. Indeed, including the additional effects of the priors assumed during the map-making process on the maps moments would be difficult. On the other hand, these alternative methods are valuable when N-body simulations are used to model the observables (e.g., Petri et al. 2015; Fluri et al. 2018).

7.2.1 Theoretical modelling of convergence moments

We adopt the theoretical model for second and third moments (variance and skewness) of the convergence field using a non-linear extension of cosmological perturbation theory (Van Waerbeke et al., 2001; Scoccimarro & Couchman, 2001; Bernardeau et al., 2002).

As we are interested in highlighting the features of our convergence field at different angular scales, we smooth our recovered convergence fields using a top-hat filter at different angular scales. We chose a top-hat filter to facilitate the analytical evaluation of third moments, but different filters with different properties can be chosen (e.g., Van Waerbeke et al. 2013 used a Gaussian filter). A top-hat filter W in harmonic space of smoothing length θ_0 is defined as:

$$W_\ell(\theta_0) = \frac{P_{\ell-1}(cos(\theta_0)) - P_{\ell+1}(cos(\theta_0))}{(2\ell+1)(\ell - cos(\theta_0))}, \tag{7.1}$$

where P_ℓ are Legendre polynomials of order l. The variance of matter contrast δ smoothed by such a filter at a given comoving distance χ is:

$$\langle \delta^2_{\theta_0,\mathrm{NL}} \rangle(\chi) = \sum_\ell \frac{2\ell+1}{4\pi} P_{\mathrm{NL}}(\ell/\chi, \chi) F_\ell^2 W_\ell(\theta_0)^2, \tag{7.2}$$

where F_ℓ is the pixel window function (modelled using the pixel window function provided by `HEALPIX`) and $P_{\rm NL}(\ell/\chi, \chi)$ the non linear power spectrum. For the latter we used `HALOFIT` as detailed in Takahashi et al. (2014) and assumed in the fiducial DES Y3 analysis.

For the smoothed version of the third moment (or skewness) of the matter contrast, at leading order in perturbation theory it reads:

$$\langle \delta^3_{\theta_0,\rm NL}\rangle(\chi) = S_3[\langle \delta^2_{\theta_0,\rm NL}\rangle(\chi)]^2, \tag{7.3}$$

where S_3 is the reduced skewness parameter. The analytical derivation of the reduced skewness parameter is performed to leading order, which is linear in the power spectrum, but as such predictions perform well even in the mildly non-linear regime ($k \approx 0.1h^{-1}$ Mpc Bernardeau et al. 2002), we assume their validity when a non-linear power spectrum (the `HALOFIT` from Takahashi et al. 2014) is used to compute the variance. We also implement a refinement (in the form of analytical fitting formulae) of the treatment of the skewness at small scales based on N-body, cold dark matter only simulations. In this Chapter we focus on the analytical fitting formulae presented in Scoccimarro & Couchman 2001 (hereafter SC01) and Gil-Marín et al. 2012 (hereafter GM12), but we note that there are alternative formulae such as that recently presented in Takahashi et al. (2019) . The SC01 and GM12 analytical refinements come with a modelling uncertainty (Van Waerbeke et al., 2001; Semboloni et al., 2011; Harnois-Déraps et al., 2016; Simon et al., 2015), which ultimately depends on the resolution of the N-body simulations that have been used to perform the fit and on the flexibility of the formulae to model all the configurations (e.g., equilateral, flattened, squeezed) of the measured bispectrum. In this Chapter we implement the analytical fitting formulae from SC01, as they provide a better fit to the N-body simulations used in this Chapter to validate the methodology. The analytical expression of the reduced skewness parameter is provided in Appendix C.1.

The analytical expression of the second and third moments of the convergence field for a given redshift distribution are provided under the Limber approximation (Limber, 1953). The Limber approximation allows to relate the 3D spatial clustering properties of the density field to 2D projected quantities. The approximation usually breaks down at small scales and for narrow redshift distributions. Under such approximation, the second and third moments read:

$$\langle \kappa^2_{\theta_0}\rangle^{i,j} = \int d\chi \frac{q^i(\chi) q^j(\chi)}{\chi^2} \langle \delta^2_{\theta_0}\rangle(\chi), \tag{7.4}$$

$$\langle \kappa^3_{\theta_0} \rangle^{i,j,k} = \int d\chi \frac{q^i(\chi) q^j(\chi) q^k(\chi)}{\chi^4} \langle \delta^3_{\theta_0} \rangle(\chi). \tag{7.5}$$

The superscripts i, j, k refers to different tomographic bins. We have dropped the subscript $_{\rm NL}$ for brevity. The term q^i represents the lensing kernel and reads:

$$q^i(\chi) = \frac{3H_0^2 \Omega_{\rm m}}{2c^2} \frac{\chi}{a(\chi)} \int_\chi^{\chi_h} d\chi' n^i(z(\chi')) dz/d\chi' \frac{\chi' - \chi}{\chi}, \tag{7.6}$$

where H_0 is the Hubble constant at present time, c the speed of light, $n^i(z)$ the normalised redshift distribution of a given tomographic bin, and $a(\chi)$ the scale factor.

We note that the variance and skewness of the convergence field have differing dependencies on the parameters $\Omega_{\rm m}$ and σ_8 (Seljak & Zaldarriaga, 1996; Bernardeau et al., 1997).

Effects of masking

One of the problems in estimating the convergence field from the observed shapes is that we observe only a portion of the sky. This means that the reconstruction will suffer edge effects, due to the convolution with a window function representing the survey footprint. Some methods deal with mask effects at the level of map making (Pires et al., 2009; Mawdsley et al., 2019), whereas in this work, we will account for the mask effects in our theoretical predictions using a pseudo-C_ℓ formalism (Brown et al., 2005; Hikage et al., 2011).

The pseudo-C_ℓ formalism correctly recovers the shear power spectrum estimated from the shear field in the case of partial sky coverage. It also predicts mode mixing (that is, part of the E-modes leaks into B-modes and vice-versa). In particular, if we define:

$$C_\ell^{EE} = \frac{1}{2\ell + 1} \sum_m |\hat{\gamma}_{E,\ell m}|^2, \tag{7.7}$$

$$C_\ell^{EB} = \frac{1}{2\ell + 1} \sum_m \hat{\gamma}_{E,\ell m} \hat{\gamma}^*_{B,\ell m}, \tag{7.8}$$

$$C_\ell^{BB} = \frac{1}{2\ell + 1} \sum_m |\hat{\gamma}_{B,\ell m}|^2, \tag{7.9}$$

one can write the masked (pseudo) spectra as the convolution of the true spectra with a mode-coupling matrix:

$$\hat{\mathbf{C}}_\ell = \sum_{\ell'} \mathbf{M}_{\ell\ell'} \mathbf{C}_{\ell'}, \tag{7.10}$$

where have we introduced the vector $\mathbf{C}_\ell \equiv (C_\ell^{EE}, C_\ell^{EB}, C_\ell^{BB})$. The mode-mode coupling matrix $\mathbf{M}$ is expressed in terms of $M_{\ell\ell'}^{EE,EE}$, $M_{\ell\ell'}^{BB,BB}$, $M_{\ell\ell'}^{EB,EB}$, $M_{\ell\ell'}^{EE,BB}$. The mode-coupling matrices contain information about the survey geometry; analytical expressions for the mode-coupling matrices in terms of the window function can be found in Hikage et al. (2011) and in Appendix C.2. The pseudo-C_ℓ formalism can be incorporated in Eq. 7.4 as:

$$\langle \kappa_{\theta_0}^2 \rangle^{i,j,EE/BB} = \int d\chi \frac{q^i(\chi) q^j(\chi)}{\chi^2} \times \sum_\ell \frac{2\ell+1}{4\pi} f_\ell^{-1} W_\ell(\theta_0)^2 \sum_{\ell'} M_{\ell\ell'}^{EE/BB,EE} P_{\rm NL}(\ell'/\chi, \chi) F_{\ell'}^2 f_{\ell'}. \tag{7.11}$$

In the above equations, the factor $f_\ell = [(\ell+2)(\ell-1)]/[\ell(\ell+1)]$ accounts for the fact that the mode-coupling matrix is applied to the shear field rather than to the convergence field directly. Depending on the mode-coupling matrix used ($M_{\ell\ell'}^{EE,EE}$ or $M_{\ell\ell'}^{BB,EE}$), with Eq. 7.11 we can predict the variance of both E and B modes of the recovered convergence field. As for the third moments, if we neglect the contribution of the masking due to the reduced skewness parameter S_3, we can write:

$$\langle \kappa_{\theta_0}^3 \rangle^{i,j,k,EE/BB} = \int d\chi \frac{q^i(\chi) q^j(\chi) q^k(\chi)}{\chi^3} S_3 [\langle \delta_{\theta_0,NL}^2 \rangle^{EE/BB}(\chi)]^2. \tag{7.12}$$

We note that neglecting the effects of masking on S_3 do not imply we are neglecting the effects on masking on the third moment $\langle \kappa_{\theta_0}^3 \rangle$ but rather we assume that most of the effect of the mask is included in the term $[\langle \delta_{\theta_0,\rm NL}^2(\chi)]^2$. We note that Gil-Marín et al. (2015) made a similar assumption when modelling mask effects in the bispectrum predictions of SDSS DR11 BOSS galaxies, demonstrating its validity for modes smaller than the size of the footprint. We show in § 7.4 that Eq. 7.12 captures the mask effects on the third moment well for the scales considered in this analysis.

Systematic effects

Astrophysical and measurement systematic effects are modelled through nuisance parameters. We marginalise over all the nuisance parameters when

Table 7.1: Cosmological, systematic and astrophysical parameters. The cosmological parameters considered are $\Omega_{\rm m}$, σ_8, $\Omega_{\rm b}$ (the baryonic density in units of the critical density), n_s (the spectral index of primordial density fluctuations) and h (the dimensionless Hubble parameter). The nuisance parameters are the multiplicative shear biases m_i and the photometric uncertainties in the mean of the WL samples Δz_i. The astrophysical parameters $A_{\rm IA,0}$ and $\alpha_{\rm IA}$ describe the IA model. We report the boundaries for both Flat and Gaussian priors. For Gaussian priors we also report the mean and the 1 σ in the prior column. Priors are described in § 7.2.1.

Parameter	**Range**	**Prior**
$\Omega_{\rm m}$	0.1...0.9	Flat
σ_8	0.4...1.3	Flat
h_{100}	55...90	Flat
$n_{\rm s}$	0.87...1.07	Flat
$\Omega_{\rm b}$	0.03...0.07	Flat
$\rm m_1$-$\rm m_4 \times 10^2$	$-10.0...10.0$	0.0 ± 2.3
$\Delta z_1 \times 10^2$	$-10.0...10.0$	0.0 ± 1.6
$\Delta z_2 \times 10^2$	$-10.0...10.0$	0.0 ± 1.3
$\Delta z_3 \times 10^2$	$-10.0...10.0$	0.0 ± 1.1
$\Delta z_4 \times 10^2$	$-10.0...10.0$	0.0 ± 2.2
$A_{\rm IA,0}$	$-5.0...5.0$	Flat
$\alpha_{\rm IA}$	$-5.0...5.0$	Flat

estimating the cosmological parameters. Values and priors are summarised in Table 7.1.

Photometric redshift uncertainties. Photometric redshift uncertainties are parametrized through a shift Δz in the mean of the redshift distribution:

$$n^i(z) = \hat{n}^i(z + \Delta z), \tag{7.13}$$

where $\hat{n}^i$ is the original estimate of the redshift distribution coming from photometric redshift code. We assume DES Y1 priors for the shift parameters.

Multiplicative shear biases. Biases coming from the shear measurement pipeline are modelled through an average multiplicative parameter $1+m^i$ for each tomographic bin. Such parameter affects our moments in the following way:

$$\langle \kappa^2_{\theta_0} \rangle^{i,j} \rightarrow (1 + m^i)(1 + m^j)\langle \kappa^2_{\theta_0} \rangle^{i,j}, \tag{7.14}$$

$$\langle \kappa^3_{\theta_0} \rangle^{i,j,k} \rightarrow (1 + m^i)(1 + m^j)(1 + m^k)\langle \kappa^3_{\theta_0} \rangle^{i,j,k}. \tag{7.15}$$

Gaussian priors are assumed for each of the m^i.

Intrinsic galaxy alignments (IA). IA is modelled according to the non-linear alignment (NLA) model (Hirata & Seljak, 2004; Bridle & King, 2007). It can be incorporated in the modelling by modifying the lensing kernel:

$$q^i(\chi) \to q^i(\chi) - A(z(\chi))\frac{n^i(z(\chi))}{\langle n^i \rangle}\frac{dz}{d\chi}. \tag{7.16}$$

The NLA model is usually used in the context of 2-point correlation statistics, but the above equation generalises it to the third moments case as well. The amplitude of the IA contribution can be written as a power-law:

$$A(z) = A_{\rm IA,0}\left(\frac{1+z}{1+z_0}\right)^{\alpha_{\rm IA}}\frac{c_1\rho_{m,0}}{D(z)}, \tag{7.17}$$

with $z_0 = 0.62$, $c_1\rho_{m,0} = 0.0134$ (Bridle & King 2007, Krause et al. 2017) and $D(z)$ the linear growth factor. We marginalise over $A_{\rm IA,0}$ and $\alpha_{\rm IA}$ assuming flat priors.

Moments estimator

To estimate the moments of a smoothed map, we use a simple estimator:

$$\langle \hat{\kappa^2_{\theta_0}} \rangle^{i,j} = \frac{1}{N_{\rm tot}}\sum_{\rm pix}^{N_{tot}} \kappa^i_{\theta_0,{\rm pix}}\kappa^j_{\theta_0,{\rm pix}}, \tag{7.18}$$

$$\langle \hat{\kappa^3_{\theta_0}} \rangle^{i,j,k} = \frac{1}{N_{\rm tot}}\sum_{\rm pix}^{N_{tot}} \kappa^i_{\theta_0,{\rm pix}}\kappa^j_{\theta_0,{\rm pix}}\kappa^k_{\theta_0,{\rm pix}}, \tag{7.19}$$

where i, j, k refers to different tomographic bins. The sum runs over all the pixel of the sky, also outside the footprint: the transformation from the shear field to the convergence field is non-local and some of the power is transferred outside the footprint, despite most of it remaining confined to the footprint. The lack of power outside of the footprint (due to the fact the shear field is not defined there) is taken into account by the mode-coupling matrices (Eqs. 7.11, 7.12).

Due to the presence of shape noise, the measurement of galaxy shapes will be a noisy estimate of the shear field γ. This means also that our estimate of the convergence field will be noisy:

$$\kappa_{E,{\rm obs}} = \kappa_{E,{\rm true}} + \kappa_{E,{\rm noise}}, \tag{7.20}$$

$$\kappa_{B,{\rm obs}} = \kappa_{B,{\rm true}} + \kappa_{B,{\rm noise}}. \tag{7.21}$$

In the above equations, we omitted the smoothing angle θ_0. The contribution of the noise to the convergence field can be estimated by randomly rotating the shape of the galaxies and applying the full-sky spherical harmonics approach to obtain the convergence (Van Waerbeke et al., 2013; Chang et al., 2018). As the random rotation should completely erase the cosmological contribution, the resulting convergence signal will just contain noise and should average to 0 (but with a non-negligible variance).

It follows that when estimating second and third moments from noisy convergence maps it is necessary to properly de-noise the measured moments. Following Van Waerbeke et al. (2013):

$$\langle\hat{\kappa}^2\rangle^{i,j} = \langle\kappa^2\rangle^{i,j} - \langle\kappa\kappa_{\rm rand}\rangle^{i,j} - \langle\kappa_{\rm rand}\kappa\rangle^{i,j} - \langle\kappa^2_{\rm rand}\rangle^{i,j}, \quad (7.22)$$

$$\langle\hat{\kappa}^3\rangle^{i,j,k} = \langle\kappa^3\rangle^{i,j,k} - \langle\kappa^3_{\rm rand}\rangle^{i,j,k} - \left[\langle\kappa^2_{\rm rand}\kappa\rangle^{i,j,k} - \langle\kappa_{\rm rand}\kappa^2\rangle^{i,j,k} + \text{cycl.}\right], \quad (7.23)$$

where cycl. refers to the cyclic permutation of the indexes i, j, k for the terms in parenthesis. In the above equations, the term $\langle\kappa^2_{\rm rand}\rangle^{i,j}$ is the noise-only contribution to the second moment of the tomographic bins i, j; for $i \neq j$ it vanishes. The map $\kappa_{\rm rand}$ represents the estimate of the shape noise contribution to the convergence map; it is estimated by randomly rotating the galaxy shapes. The intrinsic ellipticity distribution of observed galaxies is not expected to be perfectly Gaussian, but by the central limit theorem, it would be the correct distribution in the limit of large numbers of galaxies averaged in the pixels of the convergence map (Jeffrey et al., 2018). If this holds, also the term $\langle\kappa^3_{\rm rand}\rangle^{i,j,k}$ (which is the noise-only contribution to the third moment of the tomographic bin i, j, k) would vanish. Additional checks will need to be performed on DES Y3 data, as we do not include potential sources of noise inhomogeneities (e.g. astrophysical or observational systematics) in this work. Finally, we note that if the convergence field and the shape noise term in a given map pixel are uncorrelated, mixed terms should be consistent with zero.

7.3 Simulations

Two different sets of simulations are used to validate our theoretical approach. These simulations differ in the complexity of the physics included, and are used to validate different parts of our methodology. In particular, we make use of:

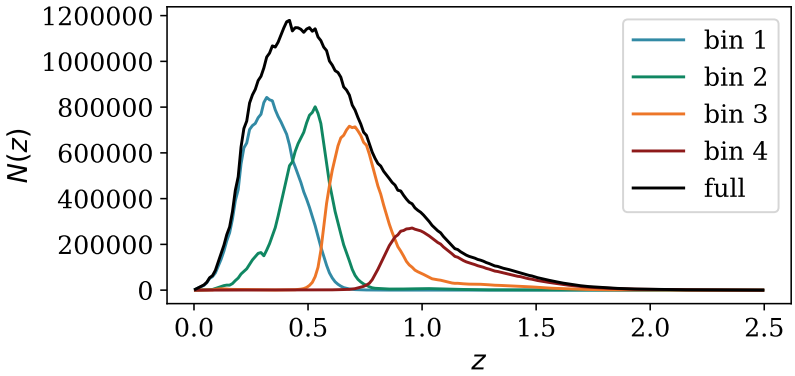

Figure 7.1: Redshift distributions of the 4 tomographic WL bins (and the full sample), from a fiducial DES simulated sample (DeRose et al., 2019). A bin width of $\Delta_z = 0.01$ has been used for the histograms.

- `FLASK` simulations (Xavier et al., 2016). These are log-normal realisations, and are used to produce a large number of realisations (of the order of 1000) of the shear and convergence fields. They require input power spectra at the redshift of the observation for their predictions, so they cannot be used to test the modelling of the second and the third moments, as they are key ingredients to run the simulations. We use them to model the covariance matrices of our measurements and to test the modelling of mask effects.
- Takahashi et al. (2017, hereafter T17) mocks. We use 100 full-sky gravitational lensing convergence and shear maps obtained from full N-body simulations and a ray-tracing algorithm described in T17. We use these to validate the theoretical modelling of second and third moments over a large number of simulations. We also use them to check the effect of non-linear lensing corrections in our modelling.

Below we provide a more in-depth descriptions of each of the simulations.

7.3.1 `FLASK` simulations

The `FLASK` software (Xavier et al., 2016) allows one to rapidly generate full-sky, log-normal realisations of a given field (in our case, the convergence field). In particular, `FLASK` assumes the convergence field to be described by a zero-mean shifted log-normal distribution, where the parameters of

the log-normal probability distribution function (PDF) are chosen to match the variance and skewness of the input. The lognormal approximation is usually adopted for the density field (Hubble, 1934; Coles & Jones, 1991; Wild et al., 2005) and is not expected to exactly hold for the convergence field, as it is a weighted projection of the mass density field along the line of sight. Tests on numerical simulations showed a lognormal PDF to be a reasonable model (e.g Taruya et al. 2002; Hilbert et al. 2011), although generalised lognormal PDFs have been shown to improve the fit at the tails of the distribution (Das & Ostriker, 2006; Takahashi et al., 2011; Joachimi et al., 2011). Observational evidences from DES SV (Clerkin et al., 2017) finds that at intermediate scales between 10 and 20 arcmin, the convergence distributions are more lognormal than Gaussian (at larger scales noise dominates). We show in § 7.6.1 that relying on the lognormal approximation to build our covariance matrix does not bias the recovery of the cosmological parameters.

The software requires as inputs a set of auto and cross power spectra and a log-normal shift parameter. This latter parameter is a combination of the variance and skewness (Xavier et al., 2016) and it is computed from theory and fixed to the value at no smoothing. Formally, this means that the third moment computed in `FLASK` should match theoretical predictions only at no smoothing. Slight variations can occur with a non zero smoothing as the convergence field is not perfectly log-normal. The second moment should agree at every smoothing scale as the full power spectrum is provided. We generated theoretical predictions for the power spectra of the convergence field for four tomographic bins of our WL source sample. We used the true redshift distributions of the WL sample as measured in a fiducial DES simulated sample (DeRose et al. 2019). Redshift distributions are shown in Fig. 7.1. We fixed the cosmology of our input power spectra to be $\Omega_{\rm m} = 0.286$, $\sigma_8 = 0.82$, $\Omega_b = 0.047$, $n_s = 0.96$, $h_{100} = 0.7$[1]. We generated 1000 realisations of the convergence fields in the form of `HEALPIX` maps with NSIDE = 1024. This resolution is chosen based on the expected number density of the DES Y3 WL sample. For each of the realisations, we cut out a DES Y3 footprint using a mask that is close to what will be used for DES Y3 weak lensing. We assign shape noise to each pixel $\epsilon_{\rm int}$ of the shear fields based on the expected per-component shape noise of the full DES

[1]The values of the cosmological parameters used to compute the covariance are slightly different than the ones of the mocks used to validate the modelling of second and third moments. These values have been chosen to facilitate the comparison with other simulated cosmological analysis for DES Y3.

Y3 WL sample (σ_ϵ) and the galaxy number density predicted by FLASK in each pixel ($n_{\rm g,pix}$), so as $\epsilon_{\rm int,pix} = \sigma_\epsilon/[n_{\rm g,pix}]$. The average number density over the full footprint of each bin are respectively 1.38, 1.36, 1.35, 0.86 gal/arcmin^2, while the σ_ϵ (the standard deviation of the two components for the measured galaxy shapes) are 0.29, 0.29, 0.29, 0.30. We use such FLASK mocks to validate our modelling of the mask effects and to generate covariance matricies for our measurements. In future sections, to quantify the offset between the third moments generated by FLASK and the theory predictions, we use the offset function defined as follows:

$$\text{offset}(\theta_0) \equiv \frac{\langle\kappa^3_{\theta_0}\rangle_{\rm FLASK,full-sky} - \langle\kappa^3_{\theta_0}\rangle_{\rm theory,full-sky}}{\langle\kappa^3_{\theta_0}\rangle_{\rm theory,full-sky}}, \tag{7.24}$$

such that $\langle\kappa^3_{\theta_0}\rangle_{\rm theory,full-sky}(1 + \text{offset}(\theta_0)) = \langle\kappa^3_{\theta_0}\rangle_{\rm FLASK,full-sky}$. The offset function is 0 at no smoothing (since the shift parameter provided to FLASK as input is only valid at no smoothing), and reaches values up to ~ 40 per cent for $\theta_0 \sim 200$ arcmin.

7.3.2 T17 N-body simulation

The simulations are a set of 108 full-sky lensing convergence and shear maps obtained for a range of redshifts between z = 0.05 and 5.3 at intervals of 150 h^{-1} Mpc comoving distance.

Initial conditions were generated using 2LPTIC (Crocce et al., 2006) and the N-body run using L-GADGET2 (Springel, 2005), consistent with WMAP 9 year results (Hinshaw et al., 2013): $\Omega_{\rm m} = 0.279$, $\sigma_8 = 0.82$, $\Omega_b = 0.046$, $n_s = 0.97$, $h = 0.7$.

The simulations begin with 14 boxes with side lengths L = 450, 900, 1350, ..., 6300 h^{-1} Mpc in steps of 450 h^{-1} Mpc, with six independent copies at each box size and 2048^3 particles per box. Snapshots are taken at the redshift corresponding to the lens planes at intervals of 150 h^{-1} Mpc comoving distance. The authors checked that the agreement of the average matter power spectra with the revised HALOFIT (Takahashi et al., 2012) was within 5 per cent for $k < 1\ h$ Mpc^{-1} at $z < 1$, for $k < 0.8\ h$ Mpc^{-1} at $z < 3$, and for $k < 0.5\ h$ Mpc^{-1} at $z < 7$. Weak lensing quantities were estimated using the multiple plane ray-tracing algorithm GRayTrix (Hamana et al., 2015), and shear and convergence HEALPIX maps with resolution NSIDE = 4096 are provided. Halos are identified in the simulation using the public code ROCKSTAR (Behroozi et al., 2013). The simulations do not come with a galaxy catalogue. For each of the 108 realisations, we produced convergence

maps for the 4 WL tomographic bins by stacking the convergence snapshots taking into account the redshift distributions of the bins. We used the same redshift distribution as that used in the FLASK simulations.

7.4 Model Validation with Simulations

In this section we present a series of validation tests with simulations to show that our model presented in § 7.2.1 does indeed model the second and third moments of the convergence maps. We first validate our model for the effect of masking (i.e. the mode-coupling matrix approach) in § 7.4.1, then validate the remaining components of the modelling of the second and third moments in § 7.4.2. In §7.4.3 we estimate the potential impact of baryonic feedback at smal scales; finally, in §7.4.4, we assess the impact of higher-order lensing corrections (such as reduced shear or source crowding) not included in our modelling.

7.4.1 Testing mask effects

We first considered the case of no shape noise. We used 1000 FLASK realisations of the DES Y3 footprint, and measured the convergence field starting from the shear field using the full-sky Kaiser-Squires method. This has been done for the four tomographic bins and the non-tomographic sample. We then smoothed the map with a top hat filter at different smoothing scales. We choose as an interval $\theta_0 \in [3.2, 220]$ arcmin, and we used 10 equally (logarithmic) spaced scales (even though we expect scales close to the pixels size, which is ≈ 3.4 arcmin, to not contain much information).

The (smoothed) second moments, both for the E and B modes, are shown in the top and middle panels of Fig. 7.2 and compared with theoretical predictions. In the figure, we just show auto-moments (i.e., moments obtained from maps of the same tomographic bin). We also show the average of the 1000 partial-sky FLASK realisations, which agrees to better than 0.5 per cent with the theoretical modelling. Without the mode-coupling matrices, we would have not been able to predict any B-modes. Moreover, our theoretical predictions for the E-modes would have been biased high, as no leakage of E-modes into B-modes would have occurred. We note that in Fig. 7.2 we do not show uncertainties for the average measurements, as they are negligibly small; on the other hand, the amplitude of the measurement uncertainty from a *single* realisation is represented by the shaded region.

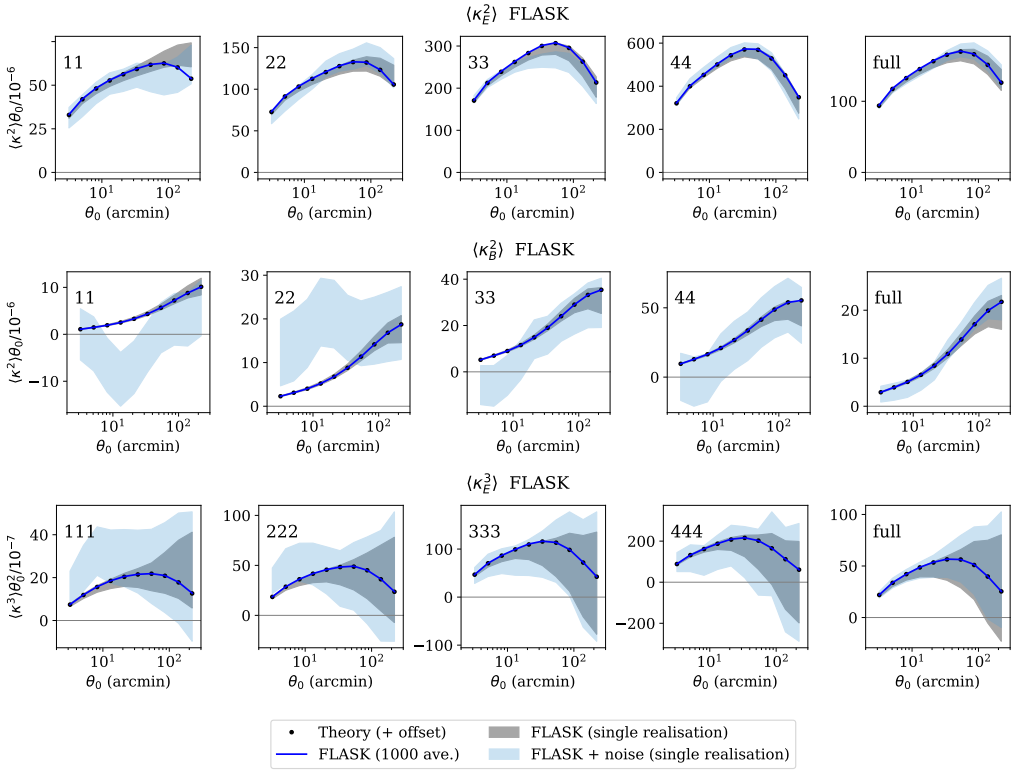

Figure 7.2: Second moments (E and B modes) and third moments (E only) measured in FLASK simulations from partial-sky coverage realisations of the DES Y3 footprint. The convergence maps are obtained from the realisations of the FLASK shear fields configured as explained in §7.3.1. Mask effects are included in the theory modelling (black dots, Eqs. 7.11, 7.12). The "offset" term refers to the function that accounts for the differences between theory predictions and the average of FLASK moments in the full-sky case (see text for more details). It is non null only for third moments (FLASK is not expected to produce the correct third moments for a given input cosmology). Grey bands represent the measurement from one (taken at random) noiseless FLASK realisation, together with its uncertainty (measurements uncertainties are estimated in § 7.5.1). Light blue bands also include shape noise. The average of the measurement over 1000 FLASK realisations are shown by the blue lines (error bars are omitted). The numbers 11, 22, 33 etc. in each plot refers to the combination of tomographic bins considered to compute the moments, while "full" refers to the non-tomographic case. Only auto-correlations are shown. *Upper panels:* second moments, E-mode of the convergence maps. *Middle panels:* second moments, B-mode of the convergence maps. B-modes are much smaller than E-modes and are due to mask effects. *Lower panels:* third moments, E-mode of the convergence maps. Third moments measured in FLASK simulations are not expected to match the input theory perfectly (see text for more details); here, the theoretical predictions for the third moments are replaced by the average measurement of third moments in many full-sky FLASK realisations.

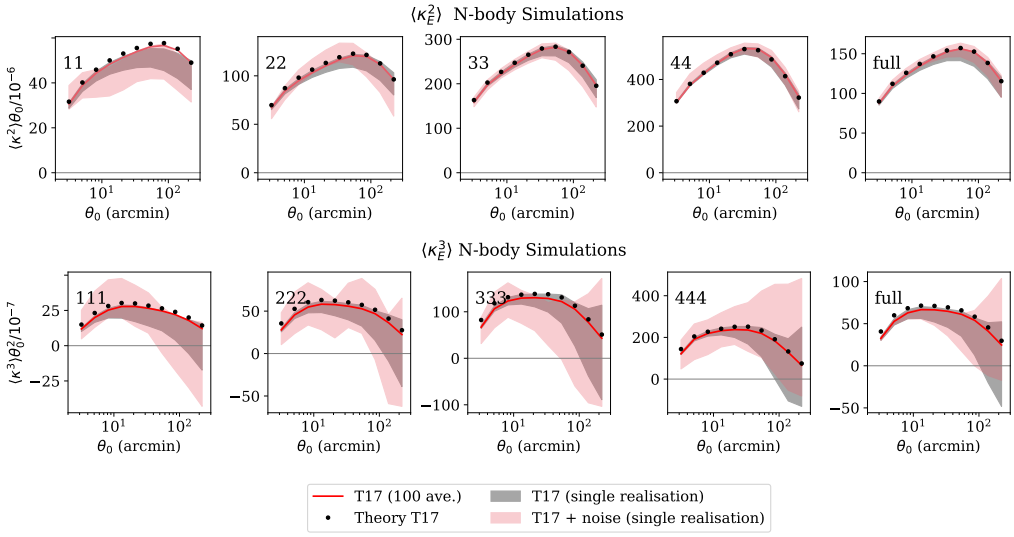

Figure 7.3: Second moments and third moments (E-modes) measured in the T17 simulations from partial-sky coverage realisations of the DES Y3 footprint. The convergence maps have been obtained starting from a realisation of the DES Y3 shear field. Mask effects are included in the theory modelling (black dots, Eqs. 7.11, 7.12). The label of the theory modelling points specifies "theory T17" to differentiate it from the `FLASK` theory lines, since the two sets of simulations have a slightly different cosmology. Grey bands represent the measurement from one (taken at random) noiseless T17 realisation, together with its uncertainty (measurements uncertainties are estimated in §7.5.1). Red bands also include shape noise. The average of the measurement over 100 T17 realisations are shown by the red lines (error bars are omitted). The numbers 11, 22, 33 etc. in each plot refers to the combination of tomographic bins considered to compute the moments, while "full" refers to the non-tomographic case. Only auto-correlations are shown. *Upper panels:* second moments, E-modes of the convergence maps. *Lower panels:* third moments, E-modes of the convergence maps

The third moments are shown in the lower panel of Fig. 7.2. We just show E-modes as B-modes are not measured at any statistical significance. We cannot directly compare third moments measured from partial-sky FLASK mocks to masked theory predictions: as explained in § 7.3.1, FLASK simulations are expected to recover the input third moments only at no smoothing; for larger smoothing scales, we expect (and measure) an offset with respect to theoretical predictions such that $\langle\kappa^3_{\theta_0}\rangle_{\rm FLASK,full-sky} \sim \langle\kappa^3_{\theta_0}\rangle_{\rm theory,full-sky}[1+{\rm offset}(\theta_0)]$. To check that we correctly model third moments mask effects in the partial-sky predictions, we need then to verify that the third moments computed from partial-sky FLASK realisations follows $\langle\kappa^3_{\theta_0}\rangle_{\rm FLASK,partial-sky} \sim \langle\kappa^3_{\theta_0}\rangle_{\rm theory,partial-sky}[1+{\rm offset}(\theta_0)]$. This is shown in the lower panel of Fig. 7.2 . The FLASK third moments theory lines include the offset function. These agree with the average of 1000 DES Y3 (partial-sky) FLASK realisations within 3 per cent, which is much smaller than the observational uncertainties. We conclude that our mode-coupling matricies deal efficiently with mask effects also for the third moments.

We next consider a more realistic scenario in which shape noise is included. In this case we need to perform the de-noising procedure (Eqs. 7.22, 7.23), which subtracts the shape-noise contributions from the measured moments. For the second moments we first checked that the mixed terms ($\langle\kappa_{\rm rand}\kappa\rangle^{i,j}$ and $\langle\kappa_{\rm rand}\kappa\rangle^{j,i}$) averaged to zero, while the terms $\langle\kappa^2_{\rm rand}\rangle^{i,i}$ (corresponding to the noise-only second moments) did not and needed to be subtracted. As for the third moments, we found out that mixed terms of the form $\langle\kappa\kappa^2_{\rm rand}\rangle^{i,j,k}$ did not vanish for some choice of indices and needed to be subtracted. This is due to source galaxy density – convergence field correlations that do not vanish at the third order. All the other terms, including $\langle\kappa^3_{\theta_0,{\rm rand}}\rangle^{i,i,i}$, averaged to zero and did not need to be subtracted.

The de-noised measurements are shown again in Fig. 7.2 (light blue shaded regions). The measurements are clearly noisier than the previous case, but we verified that when the averages over the 1000 FLASK realizations are considered, the match with the theory shows the same level of agreement as the noiseless case.

7.4.2 Testing second and third moments modelling

To validate our modelling of the second and third moments we need a full N-body simulation. In particular, we need to validate the E-modes, as they will be used in the cosmological analysis (B-modes have a low signal-to-noise, and they will be mainly used as a diagnostic). To do this, we

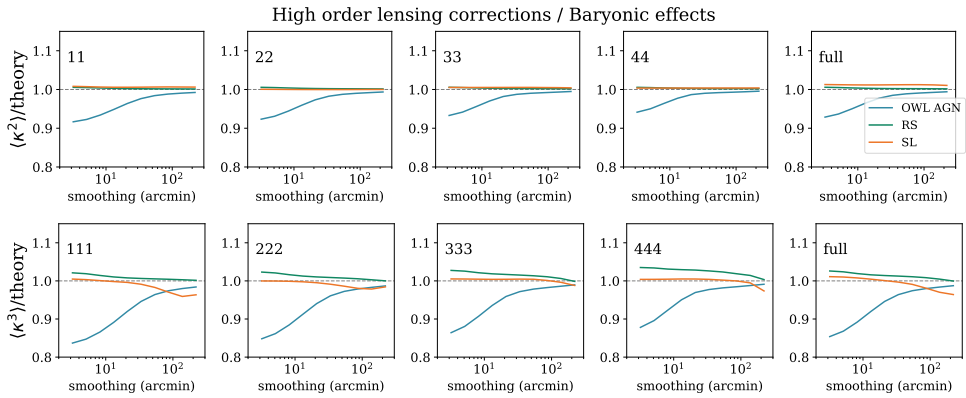

Figure 7.4: Impact of baryonic effects (from OWLS simulations) and two non-linear lensing corrections to (E-modes) moments. The blue line (OWL) refers to the rescaled predicted moments including baryonic contributions from AGN feedback. The orange line (label RS) shows the contribution to reduced shear correction, as measured in simulations. The green line refers to source-lens clustering (label SL), as measured in simulations. The grey shaded regions represent the angular scales cut out from the analysis (see § 7.6.1; as the scales cut is determined only for the tomographic version of the data vector, we do not show any shaded region for the non-tomographic case).

use 100 realisations of the shear field obtained using the T17 simulations. The comparison with the theory (second and third moments, E-modes) is shown in Fig. 7.3. In the same figure, we also show the average of the 100 realizations of the DES Y3 footprint. For the second moments, the match with the theory is better than 1 per cent at large scales (comparable with the uncertainties in the modelling of mask effects) and it is at the level of 2-3 per cent at small scales (comparable with the accuracy of the simulations at low redshift). The good match at large scales also justify the use of the Limber approximation in our modelling.

For the third moments, the theory matches the measurement to better than 10 per cent at all scales. The modelling at small scales is obtained including the SC01 analytical refinement based on N-body, cold dark matter only simulations. We note that without the SC01 formulae, the predictions of the third moments from perturbation theory only would start departing from the T17 measurement at $\sim 30 - 40$ arcmin, reaching a disagreement of 80 per cent at 5 arcmin in the first tomographic bin.

7.4.3 Baryonic effects

We discuss in this and in the next subsection the impact of a number of effects not included in our fiducial modelling. Ultimately, the impact of these effects (together with the comparison with T17 sims from the previous section) will directly determine the scales to be used in the cosmological analysis.

We consider here the possible contamination of our data vector by baryonic feedback effects at small scales. Including baryonic feedback models in the theoretical modelling is an on-going issue in current cosmic shear analyses, due to the uncertainties in current baryonic feedback models. The strategy adopted by DES (in the Y1 and Y3 analyses) is to not model baryonic feedback effects, but to exclude the scales of the data vector possibly contaminated by baryonic feedback.

To this aim we contaminate a data vector by the effects of baryonic feedback as estimated from the OWLS "AGN" simulations (Schaye et al., 2010; van Daalen et al., 2011). We note that the OWLS suite is not the only set of simulations including baryonic effects (see, e.g. EAGLE simulation, Hellwing et al. 2016, IllustrisTNG simulations, Springel et al. 2018, Horizon simulations, Chisari et al. 2018). The impact of baryons on the dark matter power spectrum in the OWLS simulations is large compared to other simulations, though more extreme models exist. We use the OWLS predictions to contaminate our data vector and use it as an upper limit on the magnitude of baryonic effects.

To contaminate the data vector, we proceed in similar fashion to what has been done in the DES Y1 cosmic shear analysis (Troxel et al., 2018). We rescale the power spectrum so as to include contribution from the OWLS "AGN" sub-grid prescriptions:

$$P_{\rm NL}(k,z) \rightarrow \frac{P_{\rm DM+baryons}}{P_{\rm DM}} P_{\rm NL}(k,z), \tag{7.25}$$

where $P_{\rm DM}$ is the OWLS power spectrum due to dark matter, and $P_{\rm DM+baryons}$ is the OWLS power spectrum including the "AGN" feedback prescription. Applying such contamination procedure to the power spectrum should account for most of the baryonic effects on the third moments as well (Foreman et al. 2019 shows that baryonic contributions to the bispectrum goes as $P^2_{\rm DM+baryons}/P^2_{\rm DM}$, at least for the scales under study here).

The effects of contaminating a theoretical data vector with baryonic feedback are shown in Fig. 7.4, where we show the ratio between a contaminated, theoretical data vector and one that is not contaminated. The OWLS

power spectrum dampens the measured moments at small smoothing scales, whereas the effect is almost negligible at larger scales. This implies that a range of small scales needs to be excluded from the cosmological analysis: including such scales could introduce biases in the cosmological inference. The angular scales cut that safeguards against possible baryonic effects is shown in Fig. 7.4 (grey shaded regions) and it is quantitatively determined with a simulated likelihood analysis in § 7.6.1.

Last, we note that from Fig. 7.4 it is not straightforward to compare the smoothing scales at which the OWLS power spectrum starts affecting the moments with the angular scales used in the DES Y1 cosmic shear analysis (Troxel et al., 2018), as the two probes get contributions from the high multipoles in harmonic space differently.

7.4.4 Higher-order lensing corrections

We next verify the impact of a number of higher-order lensing corrections to our theoretical modelling (Schneider et al., 1998, 2002; Schmidt et al., 2009; Krause & Hirata, 2010). As we have not implemented theoretical modelling of the following effects, we resort to simulations to asses their impact on the data vector. We look at three different effects: reduced shear, source-lens clustering and magnification bias. The first is due to the fact that we cannot directly observe the shear field, but rather we observe the reduced shear. Source-lens clustering is due to the correlation between source galaxies and lensing potentials along the line-of-sight. The convergence field traces the integrated density contrast up to the position where the sources are detected. Since we estimate the convergence field from an ensemble of sources at different redshifts, and the source galaxies are not uniformly distributed along the line-of-sight, this affects the estimated convergence values. The effect is enhanced in case of broad redshift distributions. We note that fluctuations in the density field are also caused by magnification effects (magnification bias).

The simulation setup of the tests shown in § 7.4.2 did not include such high order effects. In order to include the reduced shear contribution, we start from Eq. 6.11 and note that in the weak lensing limit $1/(1-\kappa) \sim 1+\kappa$. It follows that the observed shear has an additional contribution that can be modelled as:

$$\gamma_{\rm obs} \rightarrow \gamma(1+\kappa). \tag{7.26}$$

Source-lens clustering and magnification effects can be modelled by accounting for the effect of the density fluctuations along the line-of-sight when

estimating the shear field:

$$\gamma_{\rm obs} \rightarrow \gamma(1+\delta_{\rm obs}), \tag{7.27}$$

where the $\delta_{\rm obs} \equiv 1 - N_{\rm obs}/\langle N \rangle$ is the estimated density contrast ($N_{\rm obs}$ is the number of galaxies along the line-of-sight and $\langle N \rangle$ is the average number of galaxies). The fluctuations in the density field are due source galaxies overdensities and lensing magnification effects. Lensing magnification enhances the flux of galaxies and this can locally increase the number density, as more galaxies pass the selection cuts/detection threshold of the sample; at the same time, the same volume of space appears to cover a different solid angle on the sky, causing the observed number density to decrease. At first order, the impact of source galaxies overdensities and lensing magnification effects can be modelled as:

$$\delta_{\rm obs} = \delta_{\rm gal} + q\kappa, \tag{7.28}$$

with q expected to be the order of unity (see Schmidt et al. 2009 for an approximate description of the term q). Summing up Eqs. 7.26 and 7.27:

$$\gamma_{\rm obs} = \gamma[1 + \delta_{\rm gal} + (1+q)\kappa]. \tag{7.29}$$

Reduced shear contributes as $\approx 1+\kappa$, magnification effects as $\approx 1+q\kappa$, lens-source clustering as $\approx 1+\delta_{\rm gal}$. To test the impact of these effects, we used the T17 simulations. Using the full-sky spherical Kaiser-Squires approach, we generated for every redshift layer of the simulations: 1) shear field γ distributions starting from the convergence maps κ; 2) shear field distributions with $1+\kappa$ and $1+\delta_{\rm gal}$ contributions (Eqs. 7.26 and 7.27); 3) density contrast field distributions $1+\delta_{\rm obs}$. We then stacked the redshift layers together according to the redshift distributions of the WL tomographic bins, and generated the following maps:

$$\langle\gamma\rangle_{{\rm pix}(\theta)} \approx \frac{\int dz n(z)\gamma(z,\theta)}{\int dz n(z)}, \tag{7.30}$$

$$\langle\gamma\rangle^{\rm RS}_{{\rm pix}(\theta)} \approx \frac{\int dz n(z)(1+\kappa(z,\theta))\gamma(z,\theta)}{\int dz n(z)}, \tag{7.31}$$

$$\langle\gamma\rangle^{\rm SL}_{{\rm pix}(\theta)} \approx \frac{\int dz n(z)(1+\delta(z,\theta))\gamma(z,\theta)}{\int dz n(z)(1+\delta(z,\theta))}. \tag{7.32}$$

Eqs. 7.30, 7.31 and 7.32 are, respectively, the shear fields with no non-linear lensing corrections, with reduced-shear contributions and source-lens clustering. As for the latter, we divided by the integrated density field to mimic the map making process, where each pixel contains the average of the shear field along the line of sight.

The impact of such corrections on E modes are shown in Fig. 7.4. We estimated the moments from a full-sky, noise-free realisation of the simulation. For the reduced shear and source-lens clustering we considered as a "theory" the moments estimated from the same realisation of the simulations using Eq. 7.30 to estimate the shear field. We do not show error bars for the moments measurement as we expect them to be much smaller than DES Y3 uncertainties[2]. We also do not show magnification effects as they are of the same order as the reduced-shear correction (assuming q of the order of unity). We find that these non-linear lensing corrections are much smaller then DES Y3 uncertainties and sub-dominant with respect to baryonic effects. We checked that the small bias due to source-lens clustering at very large scales of the third moments does not affect the cosmological analysis (at very large scales, the signal-to-noise for the third moments is much smaller than 1. Thus, a 5 per cent bias on the signal does not bias the cosmological constraints).

7.5 Covariance and Likelihood

7.5.1 Covariance estimation

To correctly infer cosmological parameters from our data, we need an accurate estimate of the measurement uncertainty. We estimate the covariance from 1000 independent realisations of the `FLASK` simulation. For each `FLASK` realisation, we measure the second and third moments of the smoothed convergence field as explained in § 7.4.1. We then build our covariance matrix as:

$$\hat{C} = \frac{1}{\nu}\sum_{i=1}^{\mathrm{N_s}}(\hat{d}_i - \hat{d})(\hat{d}_i - \hat{d})^T, \tag{7.33}$$

[2]First, since we are considering the full sky, we expect the covariance of the moments measurement to be roughly ≈ 8 times smaller. Second, as we are using the moments of the same realisation with no non-linear lensing corrections as the "theory", we can expect the measurements to be highly correlated, and the uncertainties in their ratio should be very small as cosmic variance would cancel

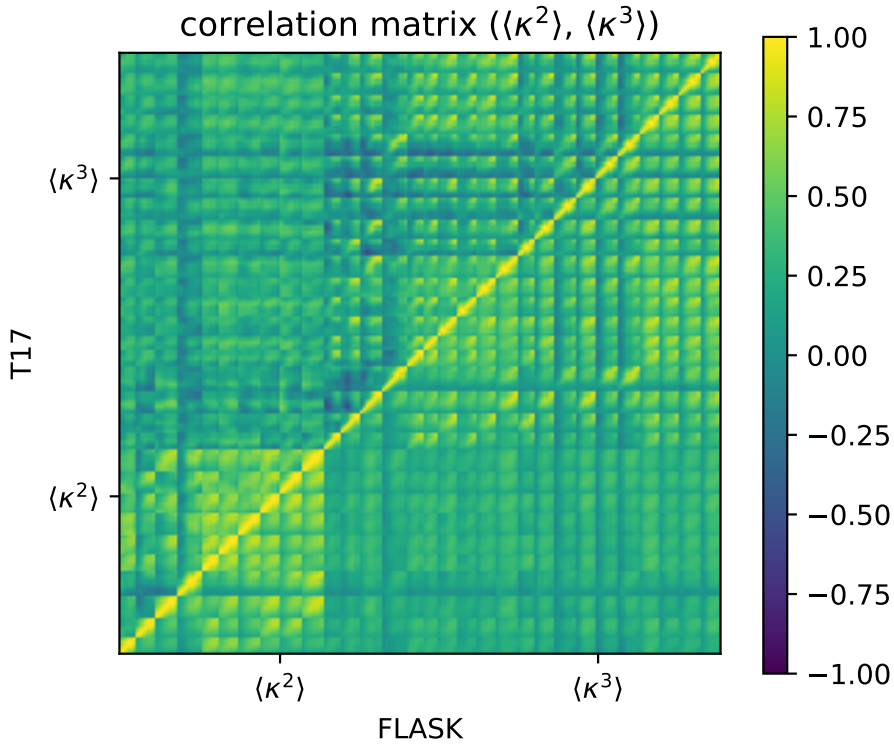

Figure 7.5: Measured correlation matrix of second and third moments from 1000 `FLASK` simulations (lower right corner) and from 100 T17 simulations (upper left corner). A $24h^{-1}$ Mpc scale cut has been applied.

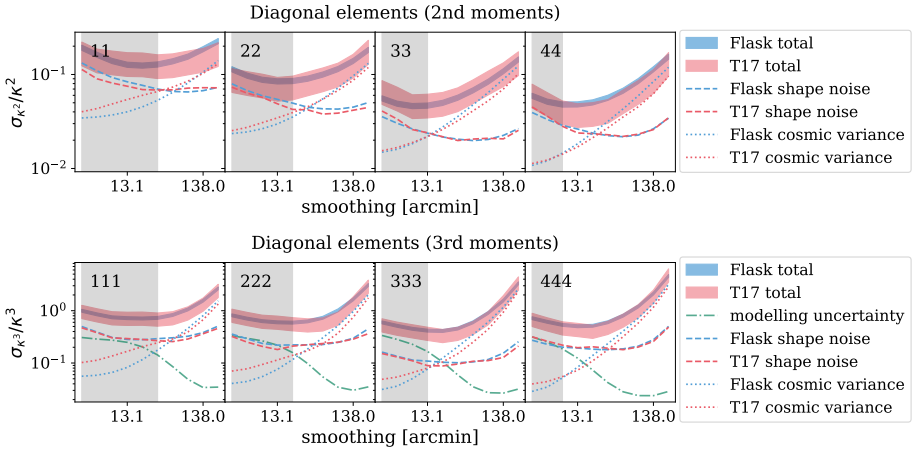

Figure 7.6: Diagonal elements of the covariance of the second and third moments estimated from FLASK simulations. The x-axis shows the corresponding data vector entries. We show separate contributions due to shape noise and cosmic variance. For the third moments, we also show the modelling uncertainties related to the small scales analytical fitting formulae. For comparison, we also show the covariance estimated from the T17 simulations. For the total covariance, we show uncertainty due to the finite number of simulation realisations. The shaded regions represent the scales excluded in the cosmological analysis (a $24h^{-1}$ Mpc scale cut has been applied).

where $\nu = \mathrm{N_s} - 1$ with $\mathrm{N_s}$ the number of realisations, $\hat{d}_i$ the data vector measured in the i-th simulation and $\hat{d}$ the sample mean. The data vector is made of a combination of second and third moments as measured at different smoothing scales.

Within single realisations, variations in the measured moments among different simulations are mostly due to two different contributions: 1) a combination of galaxy intrinsic shape and measurement noise, or "shape noise", and 2) the cosmic density field inside the DES Y3 footprint is a random realisation of the underlying cosmology, or "cosmic variance". For third moments, we also include in our covariance a "modelling uncertainty" related to the analytical fitting formulae describing the third moments at small scales. To this aim, we add to the diagonal part of the covariance the the difference between SC01 and GM12 squared (this approach is similar to the one adopted by Simon et al. 2015, who included a 20 per cent r.m.s in the covariance to take into account small-scale modelling uncertainties in the bispectrum). We note that for the scale cuts used in this analysis, the contribution of such modelling uncertainty to the error budget is small (see Fig. 7.6 and Appendix C.1).

The measured correlation matrix is shown in Fig. 7.5. The matrix obtained using Eq. 7.33 and selecting the data vector elements passing a $24h^{-1}$ Mpc scale cut (we selected the scales θ_0 such that $\theta_0 > R_0/\chi(\langle z \rangle)$, where $\chi(\langle z \rangle)$ is the comoving distance of the mean redshift of a given tomographic bin and $R_0 = 24h^{-1}$ Mpc.) Values at different smoothing scales but for the same moment are highly correlated. Fig. 7.5 also shows that second and third moments are not very correlated. This is mostly due to shape noise and third moment modelling uncertainties at small scales that wash out existing correlations.

The values of the diagonal elements of the covariance matrix, relative to values of their data vector entries, are shown in Fig. 7.6, for both `FLASK` and T17 simulations. We also show the errors due to the finite number of simulation realisations. One can see that for both second and third moments the intermediate scales are the ones with better signal-to-noise, and that in general second moments have a much better signal-to-noise than third moments.

The sample variance part of the covariance is cosmology-dependent and dominates at large scales. We do not expect this cosmological dependence to significantly impact the recovery of cosmological parameters (see discussion in § 7.6.1). We also note here that the lognormal approximation assumed by `FLASK` needs to be checked for the sample variance part of the covariance

for third moments. However, the scales dominated by sample variance have a smaller signal-to-noise for the third moments; moreover, despite FLASK limitations, Fig. 7.6 shows that the FLASK and T17 covariances agree within uncertainties. In Appendix C.3 we provide further evidence that the uncertainties in the modelling of the third moments covariance have little effect on the cosmological inference.

We therefore decided to rely on FLASK simulations to build our fiducial covariance because the cosmological parameters can be easily changed and we can produce a large number of simulations. The T17 simulations have a fixed cosmology, and, above all, are limited in numbers, causing the inverse of the covariance matrix to be extremely noisy (and biased, see, e.g., Hartlap et al. (2007)). However, in the next section we show an implementation of a data-compression algorithm that greatly reduces the size of the data vector (and the noise in the covariance due to the paucity of simulations). The data compression algorithm is implemented in our fiducial analysis and in principle allows us to run our cosmological pipeline also using the T17 covariance (although it will be still noisier than the FLASK covariance). While we still use FLASK as our fiducial covariance, we show in Appendix C.3 that the differences in the recovered cosmological parameters between using the T17 covariance (in combination with the data compression algorithm) or FLASK covariance are small.

7.5.2 Data-compression

To reduce the noise in our covariance matrix estimated from FLASK mocks, we implement the MOPED data-compression algorithm (Tegmark et al., 1997; Heavens et al., 2000; Gualdi et al., 2018). We follow Heavens et al. (2000) and include a data-compression scheme based on the Karhuned-Loève algorithm. The algorithm works by assigning weights to each element of the data vector that are proportional to the sensitivity of the element to the variation of a given model parameter. In such a way, it is possible to reduce the dimension of the data-vector to the number of model parameters considered. The compressed data vector can be written as:

$$d_i^{\rm compr} = \langle d \rangle_{,i}^T \hat{C}^{-1} d \equiv b_i d, \tag{7.34}$$

where x is the full-length data vector, $\hat{C}$ is the measurement covariance and $d_i^{\rm compr}$ is the i-th element of the compressed data vector. The index i refers to the i-th model parameter p considered, and $\langle d \rangle_{,i}^T$ is the derivative of the model data vector with respect that parameter.

The above equation assumes that the dependence of the covariance on cosmological parameters is mild ($\partial \ln C / \partial \ln p_i \ll 1$). While being reasonable, we do not explicitly prove the latter assumption as it would require producing many covariance matricies, which is computationally expensive. We also note that for the compression algorithm to be lossless, the likelihood of the non-compressed data vector must be Gaussian. We check this in Appendix C.3, and we show that the uncompressed data vector shows only mild deviations from Gaussianity. We note, however, that we expect the compressed data vector to have a more Gaussian distribution, due to the central limit theorem (Heavens et al., 2017). We show this in § 7.6.1.

In general, if one or more assumptions underlying the data-compression algorithm are violated, we can expect the compression to be not optimal. In this case the credible regions would be larger than they could be (Heavens et al., 2017; Alsing et al., 2018), but the parameter inference would still be valid.

To implement the algorithm described in Eq. 7.34, we use the `FLASK` covariance, and we estimate the derivative of the data vector using a 5-point stencil derivative centred on the true value of the simulation parameters. As the model parameters we use the five cosmological parameters and all the nuisance parameters as described in § 7.2.1. The compressed covariance can be easily obtained as:

$$\hat{C}_{ij}^{\rm compr} = b_i^T \hat{C} b_j. \tag{7.35}$$

We defer the validation of the compression algorithm to Appendix C.3, where we compare the posterior distributions obtained with and without the data-compression algorithm. In general, we find smaller contours for the chains run with the compressed data vector, as expected by the lower noise in the covariance (we explain how we deal with the noise in the covariance in the next section).

7.5.3 Data vector and likelihood

The final data vector includes all the "auto" moments of different tomographic bins (e.g., $[1,1]$, $[1,1,1]$, $[2,2]$, $[2,2,2]$) and the "cross" moments (e.g., $[1,2]$, $[1,1,2]$, $[1,2,2]$), for a total of 10 combinations for second moments and 20 combinations for third moments. The full data vector is shown in Appendix C.4. The scale cuts are discussed in the next section.

We evaluate the posterior of the parameters conditional on the data by

assuming a Gaussian likelihood for the data, i.e.

$$-2\ln\mathcal{L} = f_2 f_1[\hat{d} - M(p)]\hat{C}^{-1}[\hat{d} - M(p)]^T \tag{7.36}$$

(see § 7.6.1 for an investigation of this assumption). Here $M(p)$ is our theoretical model, $\hat{d}$ is the data vector, and $\hat{C}^{-1}$ is the inverse of our covariance estimate. The posterior is then the product of the likelihood and the priors. Note that the quantities $M(p)$, $\hat{d}$ and $\hat{C}^{-1}$ in Eq. 7.36 are to be considered compressed quantities, and we have dropped the superscript "compr" for brevity. The terms f_1 and f_2 account for noise introduced when the covariance matrix is estimated from random realisations of the data. Even if a covariance estimate $\hat{C}$ from N_{sims} random realisations is an unbiased estimate of the true covariance of the data, its inverse $\hat{C}^{-1}$ is only a biased estimate of the true precision matrix C^{-1} (Hartlap et al., 2007). This bias can be corrected with the multiplicative factor

$$f_1 = \frac{N_{\rm sims} - N_{\rm data} - 2}{N_{\rm sims} - 1}, \tag{7.37}$$

where in our case the number of independent realisations used to estimate the covariance is $N_{\rm sims} = 1000$, and $N_{\rm data}$ is the length of the data vector. Note that this is just an approximate treatment of the noise in the covariance matrix, since the data likelihood depends on the precision matrix in a non-linear way. Sellentin & Heavens (2016) have devised a more accurate treatment, taking into account the impact of the covariance estimation noise on the entire likelihood. We investigate their alternative likelihood in Appendix C.3 and find that after our data compression it has a negligible effect.

There is a second - and often more severe - problem in estimating the likelihood of data from a finite number of random realisations that is not solved by the likelihood of Sellentin & Heavens (2016). This problem is that the noise in a covariance estimate does not just change the width of parameter contours but also their location (Dodelson & Schneider 2013, see also Fig. 1 in Friedrich & Eifler 2018 for a simple demonstration of the effect). An approximate way to take this into account is to multiply our log-likelihood by

$$f_2 = \left[1 + \frac{(N_{\rm data} - N_{\rm par})(N_{\rm sims} - N_{\rm data} - 2)}{(N_{\rm sims} - N_{\rm data} - 1)(N_{\rm sims} - N_{\rm data} - 4)}\right]^{-1} . \tag{7.38}$$

This correction (dubbed Dodelson-Schneider-factor by Friedrich & Eifler 2018) assumes the model to be linear in all the parameters and widens

the contours to encompass the additional noise inhibited by the maximum likelihood parameter estimates due to the noise in the parameters (Dodelson & Schneider, 2013). We note that as the data-compression greatly reduces the length of the data vectors, f_1 and f_2 become close to 1.

To sample the posteriors of our parameters, we generate Monte Carlo Markov chain (MCMC) samples that map out the posterior space leading to parameter constraints. To this aim, we use the public software package `EMCEE` (Foreman-Mackey et al., 2013), which is an affine-invariant ensemble sampler for MCMC. To test the convergence of our MCMC chains we adopted the Gelman & Rubin (1992) test.

For the cosmological parameters, we assume a flat ΛCDM cosmology and vary five parameters: $\Omega_{\rm m}$, σ_8, $\Omega_{\rm b}$ (the baryonic density in units of the critical density), n_s (the spectral index of primordial density fluctuations) and h (the dimensionless Hubble parameter). We assume wide flat priors on Ω_m and σ_8 and adopt the informative priors in h, n_s and Ω_b that have been used the DES Y1 2-point function analysis (see Table 7.1). When constraining cosmological parameters, we marginalise over nuisance parameters describing photo-z uncertainties, shear biases and IA effects in our measurements. The modelling of our nuisance parameters is described in § 7.2.1. As at the time of finishing this work, the DES Y3 priors were not finalised yet, so we again assume DES Y1 priors for all the nuisance parameters (priors are summarised in Table 7.1). Photo-z uncertainties are parametrised by a shift in the mean of the distribution (one for each tomographic bin). Priors for the shifts come from redshift distributions of a matched sample of galaxies in the COSMOS survey and angular cross correlation with *redMaGiC* galaxies (Hoyle et al., 2018). Multiplicative shear bias priors are described in Zuntz et al. (2018). We also assume wide flat priors for intrinsic alignment.

Due to the fact that the theory predictions described in § 7.2.1 can be quite time-consuming to compute due to the large number of cross-correlations and integrations involved, we further implemented an emulator (Heitmann et al., 2006; Habib et al., 2007) to speed up the calculations. In our implementation, the emulator provides fast theoretical predictions by interpolating over a number of predictions computed at some training points spanning the parameter space of interest. The speedup stems from the fact that the time-consuming part of the calculation is substituted by an interpolation over few training points. The speedup achieved by using the emulator is of two orders of magnitudes, with a negligible impact on the accuracy of the theoretical predictions. We note that emulators are often implemented when N-body simulations are used to model the data vector

(e.g., Knabenhans et al. 2019) due to the impracticability of producing a simulation for every point of the parameter space. In our case, even if we do not directly use any N-body simulation to model the data vector, we take advantage of the computational speed up provided by the emulation of our own theoretical model. More details are provided in Appendix C.5.

7.6 Cosmological constraints from mass map moments

7.6.1 Fiducial scale cuts

The last analysis choice to make before presenting the final cosmological constraints of the second and third moments of the convergence field is which scales are to be used for the analysis. The scale cuts we use are determined based on two tests. First we check that our theoretical modelling is adequate to describe the data vectors as obtained from the average of many N-body simulations from T17. Second, we check that the impact of baryons on our data vector is not significant. We recall that we adopt a strategy to mitigate baryonic effects which aims at excluding the scales potentially affected by baryonic feedback, without trying to model such effects. For both tests we run MCMC chains for different combinations of scale cuts. For the former test, we use a data vector from T17 simulations; for the latter, we use a baryons-contaminated data vector (obtained using the outputs of the OWLS simulation, as explained in § 7.4.3), which should represent a reasonable upper limit to the magnitude of baryonic feedback effects in real data. We vary the scales under study and we require the resulting constraints on cosmological parameters not to be biased against the truth, to check our modelling is adequate for the range of scales considered.

For a combination of scales to be acceptable, we require the mean of the marginalised 1-D posterior of Ω_m, $S_8 = \sigma_8(\Omega_\mathrm{m}/0.3)^{0.5}$ to be within 0.3 σ of the values obtained with a "theory" data vector. As we partially constrain n_s, we also require the posterior of n_s to be within 0.5 σ of the baseline value.

We also adopt a second criterion on the χ^2 of the best-fit cosmology. When analysing the data, the best-fit χ^2 is used for hypothesis testing and as a proxy of the adequacy of the data vector modelling. A bad best-fit χ^2 implies that either our covariance or the parametrisation of the data vector is not adequate to describe the measurement. Since we do not model baryonic

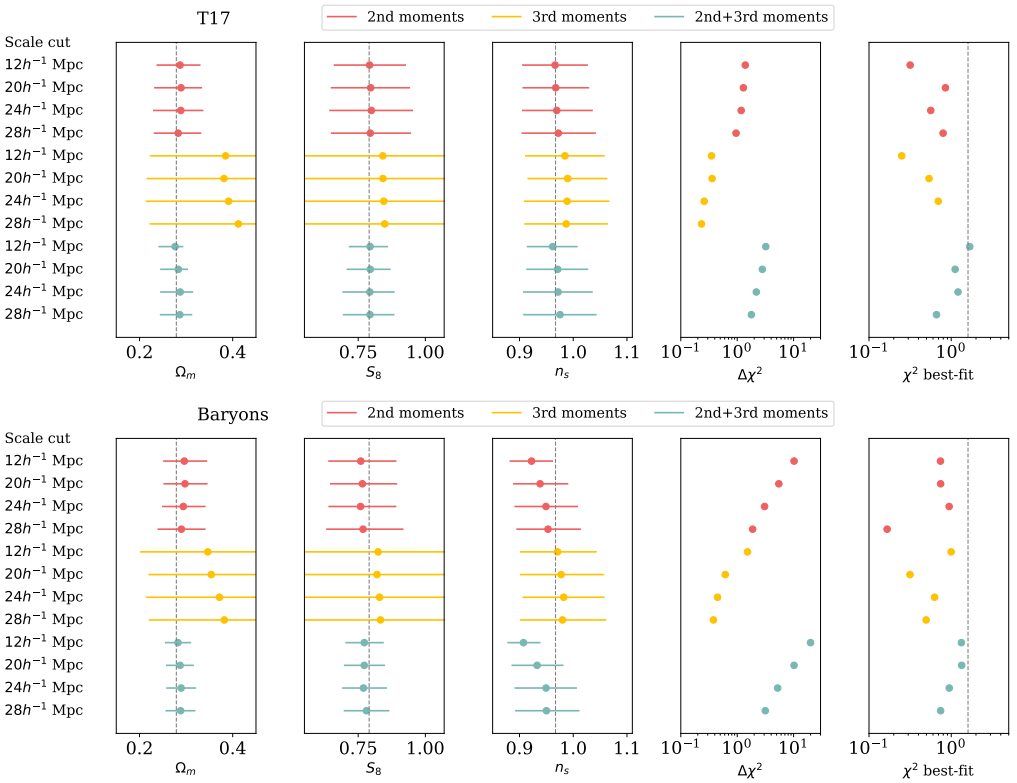

Figure 7.7: The 1-σ marginalised constraints on cosmological parameters for a number of different scale cuts. In the upper plot, the average of 100 T17 simulations have been used as the data vector. In the lower plot, the constraints are obtained by using a theory data vector contaminated with the OWLS AGN power spectrum. Data points represents the mean of the 1-D marginalised posterior, while for the confidence interval we show the two-tail symmetric intervals. The vertical dashed lines in the first three columns represent the input values input cosmological parameters. The column $\Delta\chi^2$ represents the χ^2 of the data vector contaminated with baryonic effects or from the average of T17 sims with respect to a theory data vector. The χ^2 best-fit column represents the χ^2 of the best-fitting cosmology from the MCMC chain. The vertical line in the last column marks the $\Delta\chi^2 = 1.6$ boundary.

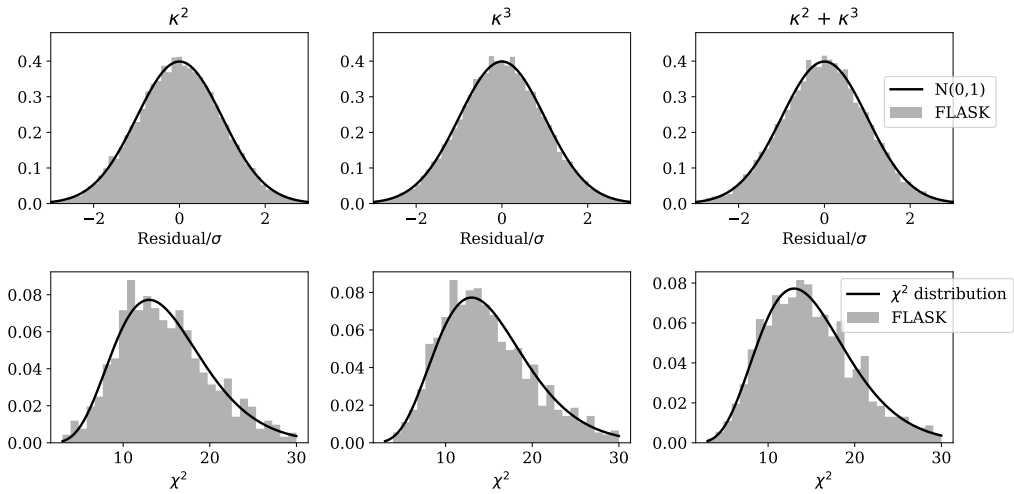

Figure 7.8: *Top panels*: residuals (i.e., the difference between the measurement signal in a `FLASK` simulation and the simulations mean value) of individual data points in units of their expected standard deviation for a compressed data vector. We compare to a Gaussian with zero mean and unit standard deviation. *Bottom panels*: Distribution of the χ^2 of each realisation of the FLASK simulations, compared to a theoretical χ^2 distribution.

effects or the small discrepancies between our theoretical predictions and the data vector from T17 simulations, we should expect the best-fit χ^2 from the data to be biased. By adopting a criteria on the χ^2 of the best-fit cosmology of the contaminated data vector we make sure the biases from these two effects are small. In particular, we require the χ^2 of the best-fit cosmology obtained from a contaminated data vector to be within 0.3 of the expected spread of the χ^2 distribution. Therefore, since the length of the compressed data vector is 15, we require the best-fit $\chi^2 < 1.6$. Ideally, for negligible contamination we expect a best-fit $\chi^2 = 0$, as we are using a theory data vector as a baseline (whereas using a noisy data vector would give, on average, $\chi^2 \sim$ d.o.f.).

In this section, scale cuts are expressed in terms of a specific comoving scale R_0; the relation with the smoothing scale θ_0 is given by $\theta_0 = R_0/\chi(\langle z \rangle)$, where $\chi(\langle z \rangle)$ is the comoving distance of the mean redshift of a given tomographic bin. In the case of moments from different tomographic bins, we took the average of the $\langle z \rangle$ of the bins.

The tests run on the data vectors obtained from the average of the T17 simulations are shown in the upper plot of Fig. 7.7. As we estimated the bias

in the cosmological parameters induced by the emulator in Appendix C.5, we re-scaled the measured data vector by the ratio between an emulated theory data vector and a non-approximated one predicted at the T17 cosmology. This assumes the emulator uncertainties propagate linearly to the data vector; this is justified as at the T17 cosmology the emulator accuracy is below the per cent level.

There are different known reasons why the data-vector from the average of T17 might differ from our theoretical predictions: inaccuracies of the simulations or in the modelling of the third moments at small scales (§ 7.3 and § 7.4.2), inaccuracies in accounting for mask effects (§ 7.4.1), inaccuracies in the covariance modelling (§ 7.5.1), etc. In the past sections we showed (or discussed) these differences to be small at the level of the data vector, but here we want to assess the impact on the cosmological parameters posteriors.

The plots show the marginalised 1-D posterior for three out of five cosmological parameters under study. We do not show constraints for Ω_b and h_{100} because the posteriors are heavily prior dominated. For each parameter, we show the mean of the posterior and the symmetric 1-σ confidence interval. We note that n_s is mildly constrained and its posterior is partially dominated by the prior (which is assumed to be flat with $n_s \in [0.87, 1.07]$; see Table 7.1). The constraints from second moments and from the combination of second and third moments are close to the input cosmology, and pass our 0.3σ criteria at all scales. We note that the values of Ω_m from the third moments are biased. This is due to the fact that the posterior is strongly asymmetric. We checked that the posterior of a theory data vector shows the same level of shifts in the mean value of Ω_m for the third moments, and the difference with respect to the results from the T17 data vector are much smaller than 0.3σ.

In Fig. 7.7 we show both the difference $\Delta\chi^2$ of the T17 data vector and the theory data vector, and the χ^2 of the best-fit cosmology. The former quantity gives a rough idea of the discrepancy of the data vector with respect to the truth: a variation of $\Delta\chi^2 = 1$ could, in the worst case possible, cause a 1-σ shift in the marginalised 1-D posterior of one of the parameters probed. Usually the difference is absorbed and shared across all the parameters probed (and this is the case). The values of best fit χ^2 for the T17 data vectors also pass our 0.3σ criteria, being always $\chi^2 < 1.6$.

We next test the impact of baryonic effects, by contaminating a theory data vector with the effects from the OWLS AGN simulation, as described in § 7.4.3. The results are shown in the lower panel of Fig. 7.7. The impact on the data vector from baryons is more pronounced than from the T17

data vector, as shown by the larger $\Delta\chi^2$ values, and it is more important at small scales. This translates in a bias in n_s at small scales. Second moments pass our scale cuts criteria starting from $20h^{-1}$ Mpc, while the combination of second and third moments from $24h^{-1}$ Mpc. As for the third moments, they pass our criteria at all the scales probed here (similarly to the T17 data vector test, the values of the mean of the $\Omega_{\rm m}$ posteriors show a negligible shift with respect to the values obtained using a theory data vector). At all scales and for the the combinations of second and third moments, our criteria on the best-fit χ^2 is passed.

We note that we performed these tests adopting a FLASK covariance, which has a slightly different cosmology with respect to the T17 data vector. This, however, did not significantly bias our posteriors, as shown in the upper panel of Fig. 7.7.

Based on these tests, we adopt the following fiducial scale cuts: $20h^{-1}$ Mpc as a minimum smoothing scale for second moments, $12h^{-1}$ Mpc for third moments, and $24h^{-1}$ Mpc when second and third moments are combined. We note that the scale $24h^{-1}$ Mpc translates into a cut at ≈ 33 (8) arcmin for the first (fourth) tomographic bin, while $12h^{-1}$ Mpc translates into a cut at ≈ 16 (4) arcmin for the first (fourth) tomographic bin. As there is no significant information below twice the pixel size (i.e., < 7 arcmin) and most of the constraining power comes from the two high redshift tomographic bins, we have not considered scales smaller than $12h^{-1}$ Mpc in the above tests.

With the final scale cuts determined, we perform extra checks on the covariance and data vector. We checked that the mean χ^2 of the 1000 FLASK realisations agreed within errors with the number of degree of freedom of our data vector. The distributions of the measured χ^2 are shown in the bottom panels of Fig. 7.8. We also verified that the distribution of the residuals (i.e., the difference between the measurement signal in a `FLASK` simulation and the simulations mean value) for each entry of our data vector followed a Gaussian distribution. This is shown in the top panels of Fig. 7.8. We note that the data-compression algorithm surely helps in giving the compressed data a more Gaussian distribution, due to the central limit theorem (Heavens et al., 2017).

7.6.2 Simulated likelihood analysis

We simulate a DES Y3 likelihood analysis and show the expected constraints for DES Y3 in Fig.7.9, for 5 cosmological parameters. All the tests shown in

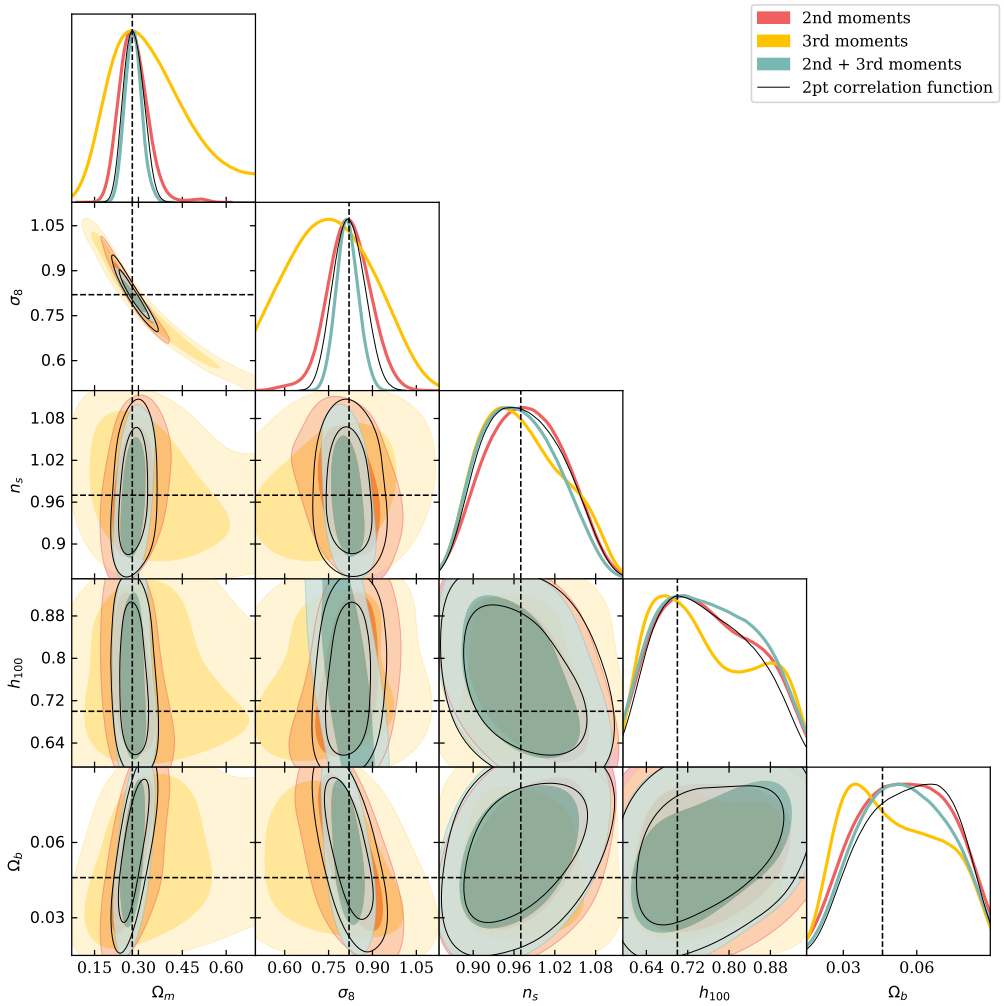

Figure 7.9: Cosmological parameters posterior obtained from the simulated likelihood analysis. We marginalise over nuisance parameters as explained in §7.5.3. We show constraints from second moments, third moments and second and third moments combined, along with constraints from a shear 2-point correlation function analysis.

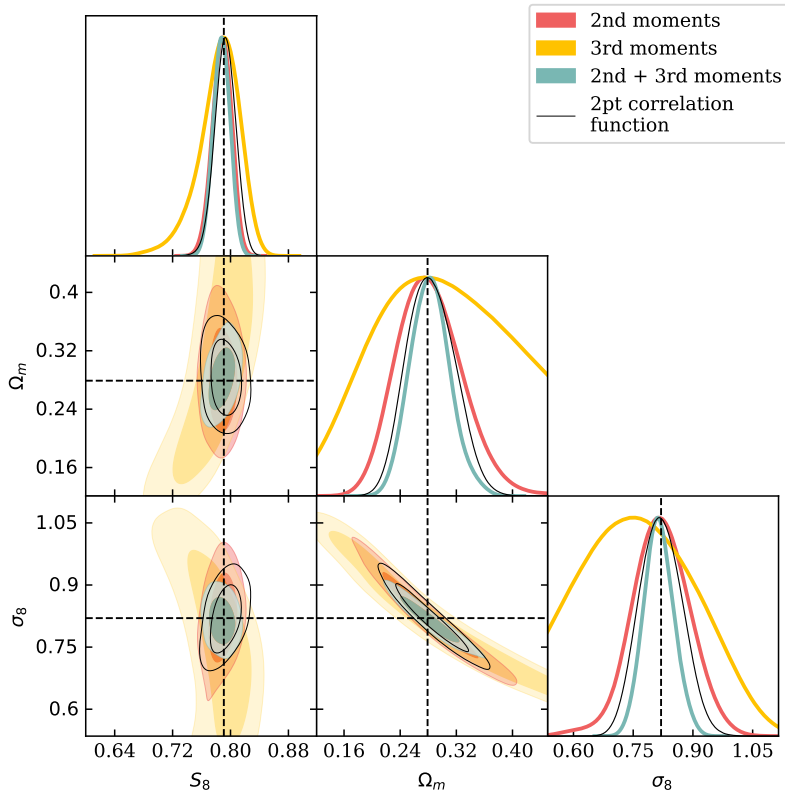

Figure 7.10: Same as Fig. 7.9, but now a zoomed in version of the $S_8 - \sigma_8 - \Omega_\mathrm{m}$ plane.

Table 7.2: DES Y3/Y5 simulated likelihood analysis comparison. Fractional accuracy (1-σ marginalised posterior confidence intervals over input value) for Ω_m, S_8 and n_s. DES Y5 constraints are obtained with the expected DES Y5 number density and DES Y3 scale cuts and tomographic binning.

	Ω_m	S_8	n_s
2 moments (Y3)	17 %	1.8 %	6.9 %
3 moments (Y3)	66 %	3.6 %	7.9 %
2 + 3 moments (Y3)	10 %	1.5 %	6.5 %
2pt function (Y3)	12 %	1.8 %	6.4 %
2 moments (Y5)	14 %	1.5 %	6.0 %
3 moments (Y5)	48 %	2.8%	7.9 %
2 + 3 moments (Y5)	8 %	1.4 %	5.7 %

Table 7.3: DES Y3/Y5 simulated likelihood analysis comparison. We show the ratio between the 1-σ marginalised posterior confidence intervals for Ω_m, S_8 and n_s for a number of cases (a value of < 1 indicates improvement). DES Y5 contraints are obtained with the expected DES Y5 number density and the same DES Y3 scale cuts and tomographic binning.

	$\Omega_{\rm m}$ (ratio)	S_8 (ratio)	$n_{\rm s}$ (ratio)
2 (Y3) $\rightarrow$ 2 + 3 (Y3)	0.57	0.79	0.97
2 (Y5) $\rightarrow$ 2 + 3 (Y5)	0.58	0.89	1.01
2 (Y3) $\rightarrow$ 2 (Y5)	0.85	0.86	0.83
3 (Y3) $\rightarrow$ 3 (Y5)	0.78	0.80	0.99
2 + 3 (Y3) $\rightarrow$ 2 + 3 (Y5)	0.87	0.97	0.89

this section use a theory data vector that includes all the "auto" moments of different tomographic bins (e.g.,[1,1],[1,1,1],[2,2],[2,2,2]) and the "cross" moments (e.g.,[1,2],[1,1,2],[1,2,2]), for a total of 10 combinations for second moments and 20 combinations for third moments. The fiducial scale cuts determined in the previous section has been adopted ($20h^{-1}$ Mpc for second moments, $12h^{-1}$ Mpc for third moments, and $24h^{-1}$ Mpc when second and third moments are combined). For the data vector, a fiducial T17 cosmology is assumed, with nuisance and astrophysical parameters (photo-z biases, multiplicative shear biases, intrinsic alignment IA) assumed to be null, and no baryonic contamination. We adopted the `FLASK` covariance described in § 7.5.1, and compressed our data vector following § 7.5.2. When estimating parameters posterior, we further marginalise over nuisance parameters as explained in § 7.2.1.

As we commented in the previous section, second and third moments mostly constrain $\Omega_{\rm m}$ and σ_8, while n_s is partially affected by the prior and h_{100} and $\Omega_{\rm b}$ are prior dominated. In general, third moments are less constraining than second moments; however, they contain additional non-Gaussian information and they have a slightly different degeneration axis in the $\Omega_{\rm m} - \sigma_8$ plane compared to second moments. This helps breaking the degeneracy when the two are combined, delivering tighter constraints. This is also shown in Fig.7.10, where we show results in the $\Omega_{\rm m} - S_8$ plane.

We report in Table 7.2 the constraining power of moments for $\Omega_{\rm m}$, S_8 and n_s; the level of improvement when the moments are combined (quantified as the ratio between predicted confidence intervals) is reported in Table 7.3. Second, third moments and their combination constrain $\Omega_{\rm m}$ to 17 per cent, 66 per cent and 10 per cent respectively, and S_8 to 1.8 per cent, 3.6 per cent and 1.5 per cent respectively. These particular values are obtained specifically for DES Y3 and depends on the particular scales and the noise

properties of sample considered.

We also show in Table 7.3 how much we expect to improve our constraints when moving to the final DES release, which will include all the data from the five years (Y5) of observations. This is quantified in terms of the ratio between predicted confidence intervals. The values have been obtained by assuming the expected DES Y5 number density (which should roughly double DES Y3 one) and the same DES Y3 scale cuts and tomographic binning. We did not take into account the possibility of having more than four tomographic bins, which would be possible having a deeper sample. In general, we can expect to further improve our constraints by $10 - 20$ per cent with respect to DES Y3.

We overlay in Figs. 7.9, 7.10 the expected posteriors from the DES Y3 shear 2-point correlation function analysis. Scale cuts for the 2pt correlation function analysis have been chosen by contaminating a shear 2-point data vector with the effect of baryons and looking at the bias in the parameters' posteriors, in a fashion similar to what has been done in § 7.6.1. The measurement covariance has been obtained using jackknife resampling and a fiducial DES Y3 simulation (DeRose et al., 2019). The shear 2-point analysis delivers slightly tighter posteriors than second moments alone, but is less constraining than the combination of second and third moments. Indeed, we find it to constrain $\Omega_{\rm m}$ and S_8 at the level of 12 per cent and 1.8 per cent; the combined second and third moments result is 20 per cent more constraining. Without measuring the cross-covariance between moments and shear 2-point correlation function, it is hard to quantitatively explain why the latter is more constraining than second moments alone. One reason could be that they have access to the same information (the power spectrum), but they probe scales differently (the 2pt correlation function is more localised in harmonic space, whereas moments get contributions from a broader range of multipoles, being prone to baryonic effects at all smoothing scales). A different sensitivity to the effects that drive the scale selection can limit the constraining power of a probe compared to others (see, e.g., Asgari et al. 2019b). More in general, a different sensitivity to angular scales might cause different observables to be only weakly correlated, even if they belong to the same category of 2-point statistics (see, e.g. Hamana et al. 2019). Future works will investigate further the correlation between 2pt correlation function and second and third moments.

One relevant feature that can be observed from Fig. 7.9 and Fig. 7.10, is that shear 2-point correlation function has a similar degeneracy direction compared to second moments only. Combining shear 2-point correlation

function with any other probes sensitive to the bispectrum (such as the third moments) is likely to significantly improve the constraints due to the different degeneracy direction of their constraints.

7.7 Summary

In this Chapter, we have presented a simulated cosmology analysis using the second and third moments of the weak lensing mass (convergence) maps. We targeted the analysis at the third year (Y3) data from the Dark Energy Survey (DES), but the methods developed here are general and can be applied to other datasets. The goal of this Chapter was to describe and validate the methodology using simulations, determining the lower bounds on scales where systematic or modelling uncertainties are not expected to affect the cosmological analysis. A future analysis, applying the methodology to DES Y3 data, together with observational systematic checks (e.g. potential systematic effects such as modelling errors in the point spread function, inhomogeneities in the noise, and spurious dependencies of shear with observing conditions) and consistency checks with the results from other DES Y3 probes and external datasets, will follow.

The second moment of the convergence as a function of smoothing scale contains similar information as the standard two-point shear correlations. The third moment, or the skewness, contains additional non-Gaussian information of the field. We described how the convergence maps are constructed starting from the shear catalogue using a full-sky Kaiser-Squires (Kaiser & Squires, 1993a; Chang et al., 2018) formalism. We obtain analytical predictions for the second and third moments using perturbation theory. We included the effects of partial sky coverage in the theoretical modelling of the moments using the pseudo-C_ℓ formalism. We validated the modelling of the convergence moments using a large suite of simulations, including the effects of the survey mask and non-linear lensing corrections (such as reduced-shear and source crowding). We used the same simulations to estimate the covariance. We furthermore showed how the computation of theoretical predictions can be sped up without introducing biases in the cosmological analysis by implementing a 5-parameter emulator.

We tested our pipeline through simulated likelihood analyses varying five cosmological parameters (Ω_m, σ_8, n_s, Ω_b, h_{100}) and 10 nuisance parameters (modelling redshift uncertainties, shear biases, and intrinsic alignments). We determined the scale cuts based on the impact of baryonic physics and

modelling inaccuracies of the third moments at small scales.

We then simulated the constraints achievable with a DES Y3 analysis. We found that second moments, third moments, and their combination constrain $\Omega_{\rm m}$ to 17 per cent, 66 per cent and 10 per cent respectively, and S_8 to 1.8 per cent, 3.6 per cent and 1.5 per cent respectively. The combination of second and third moments provides improved constraints with respect to second moments due to the extra non-Gaussian information probed by the third moments and the different inclination of the degeneracy axis in the $\sigma_8 - \Omega_{\rm m}$ plane of the two probes. For DES Y5, where we expect to have a data set with higher galaxy density, we forecast a further improvement in the constraining power at the level of $10 - 20$ per cent.

We also compared with a simulated shear 2-point analysis for DES Y3, which yields constraints at the level of 12 per cent and 1.8 per cent for $\Omega_{\rm m}$ and S_8. The combined second and third moments result is about 20 per cent more constraining. This analysis shows the importance of including in the analysis probes of higher order statistics to improve on the cosmological constraints.

Summary and conclusions

In this thesis we have addressed some key aspects of gravitational weak lensing in the context of photometric surveys. In particular, we used simulations and data taken during the first three years of observations of the Dark Energy Survey (DES Y3). DES is scheduled to release their main DES Y3 cosmological analysis later this year, and this thesis covers some parts of the analysis.

In Part II of this thesis, we have focused on the "clustering-redshift" technique and its role in the main DES Y3 redshift calibration strategy. Clustering-redshift is a method to obtain (or calibrate) redshift distributions which is based on cross-correlations with small samples with secure redshifts. Two different variants of the technique have been presented, where the clustering information is used to calibrate the redshift distributions from the DES Y3 fiducial photo$-z$ method (SOMPZ). The methodology has been completely characterised in simulations, and then applied to DES Y3 data. We found that the current implementation of clustering-redshift is limited by the lack of modelling of the redshift evolution of the galaxy-matter bias of the DES Y3 weak lensing sample. We found that for DES Y3 the clustering information does not help tightening the uncertainty on the mean of the redshift distributions, but it does significantly tighten the scatter on the shape. We further discussed future perspectives of the methodology at the end of Chapter 4.

Part III was devoted to the testing of the official DES Y3 shape catalogue, covering ~ 4143 deg^2 of the southern hemisphere and comprising ~ 100 million objects, which effectively makes it the largest shape catalogue ever created. We gave an overview of the shape measurement pipeline, describing the improvements with respect to previous versions, and discussed the sample selection adopted for the DES Y3 cosmological analysis. We then performed a variety of empirical null tests, mostly aimed at identifying additive biases in our shape catalogue. Among all, we tested potential

systematic errors connected to PSF corrections and to PSF chromatic effects, we checked whether we detected spurious B-mode signals, and looked at dependencies of the mean shear with respect to a number of galaxy or survey properties. In the majority of the null tests we did not detect any statistically significant signal, and in the cases were we did, we checked they were not significantly affecting our cosmic shear analysis. In the last part of the thesis (Chapter 6 & 7), we presented the official DES Y3 weak lensing mass maps, and discussed a potential cosmological application of the maps. In particular, we introduced in Chapter 6 four different mass map reconstruction techniques, each of those assuming different priors on the recovered convergence field. The different methods have been compared in simulations using a number of different summary statistics. The tests performed suggested that using priors to recover the converge field from a noisy realisation of the shear field generally improves the reconstruction, i.e., the recovered maps are more similar to the true convergence field. As a downside, we also showed how the choice of the prior can make the comparison of certain statistics with theoretical predictions particularly complex, and gave recommendations on how to choose the mass map method depending on the particular science application. We then presented the official DES Y3 mass maps, obtained with the four different methods, and assessed their robustness against a number of systematic maps representing catalogue properties and observing conditions.

Chapter 7 presented a simulated cosmology analysis using the second and third moments of the weak lensing mass maps, targeted at the DES Y3 data. The second moment of the convergence as a function of smoothing scale contains similar information as the standard two-point shear correlations whereas the third moment, or the skewness, contains additional non-Gaussian information of the field. We showed how to obtain analytical predictions for the second and third moments using perturbation theory. We tested our pipeline through a simulated likelihood analyses varying 5 cosmological parameters and 10 nuisance parameters and we identified the scales where systematic or modelling uncertainties are not expected to affect the cosmological analysis. Our simulated likelihood analysis showed that the combination of second and third moments provides a 1.5 percent constraint on $S_8 \equiv \sigma_8(\Omega_\mathrm{m}/0.3)^{0.5}$ for DES Y3 data, 20 percent better than an analysis using a simulated DES Y3 shear 2-point statistics, owing to the non-Gaussian information captured by the inclusion of higher-order statistics. Subsequent works will apply the methodology developed in this part of the thesis to the DES Y3 data.

Appendix A

A.1 Individual mean-matching likelihoods

We show in this Appendix the posteriors of the mean of the SOMPZ realisation obtained with the mean matching method when using the two reference samples individually. We both show the results obtained in simulations and in data.

In particular, Fig. A.1 shows the mean redshift posteriors of the SOMPZ realisation obtained in simulations. To facilitate the comparison with the clustering only prior, we computed the mean in the 2 σ interval of the reference sample used. The first thing that can be noted is that the clustering prior is consistent - within uncertainties - with the mean of the SOMPZ realisations before combining the two pieces of information. The other thing that can be noted is that the histograms clearly show that the clustering prior is much wider than the scatter of the SOMPZ realisations, especially for the low redshift tomographic bins, which explain why the mean matching clustering likelihood little helps tightening the posterior. Last, we note that the final scatter on the mean of the SOMPZ realisations is larger than what shown in Fig. A.1, as it gets contributions from the redshift range where there is no WZ information.

Fig. A.2 shows the mean redshift posteriors of the SOMPZ realisation obtained on data, along with the WZ prior. The results are qualitatively and quantitatively very similar to what has been obtained in simulations: the clustering prior and SOMPZ realisations are consistent within errors before combining, and the mean matching clustering likelihood little tightens the mean redshift posterior of the SOMPZ realisations.

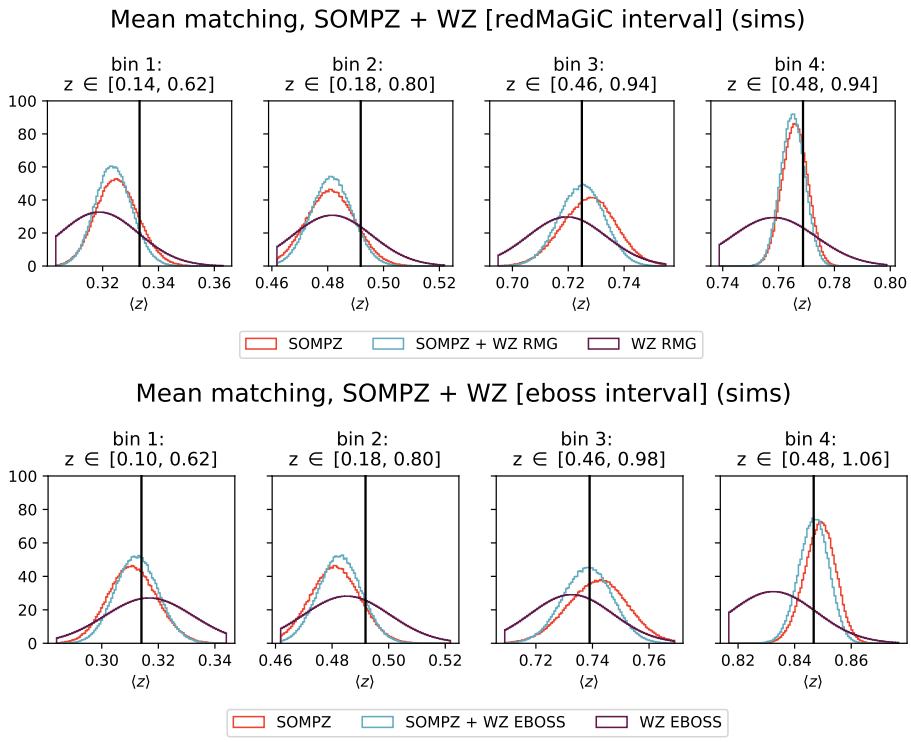

Figure A.1: Mean redshift posteriors for the 4 tomographic bins obtained using the mean matching method. The top panels show the results obtained using the *redMaGiC* sample only, the lower panels show the results obtained using the eboss sample only. Red histograms represent the distribution of the mean redshift of the SOMPZ realisations, while the purple histograms represent the clusttering only prior. Light-blue histograms show the mean redshift posteriors of the SOMPZ realisations using the clustering likelihood. To facilitate the comparison with the clustering prior, the mean redshift has been computed in the fiducial 2 σ interval, i.e., excluding the tails of the redshift distributions. The black vertical lines represent the true mean redshift as computed in simulations.

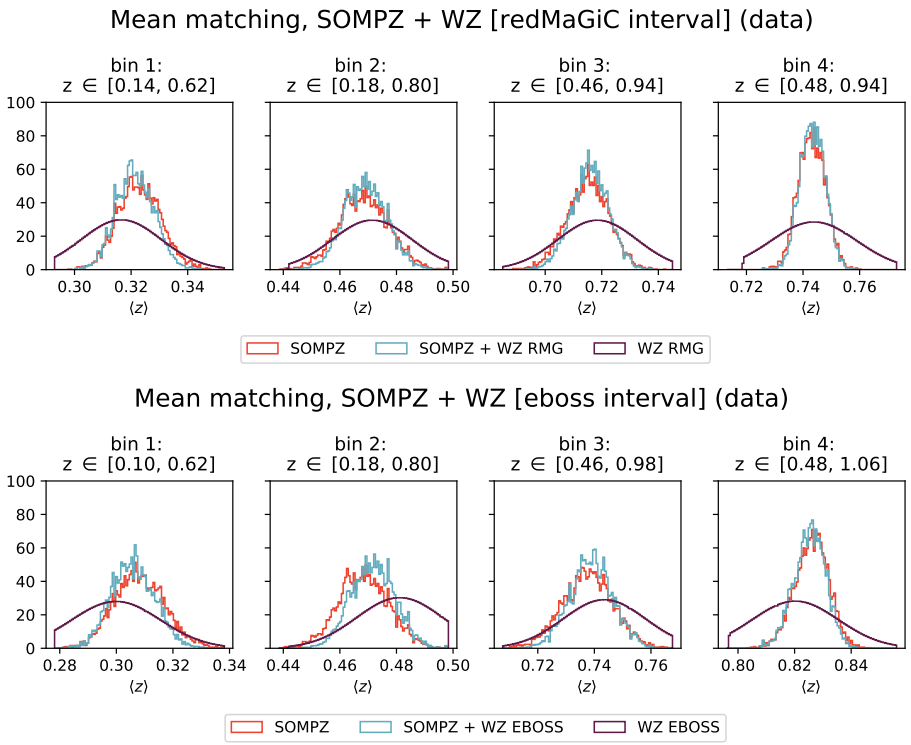

Figure A.2: Same as Fig. A.1, but now on data.

A.2 Full $\hat{w}_{ur}$ model and analytical marginalisation

We provide here more details about the implementation of the shape-matching method. The method uses the cross-correlation information to constrain the redshift distributions $\{n_u^{\mathrm{pz,k}}(z_i)\}$ provided by a given photo-z code (in this case, these are a number of realisations provided by SOMPZ). The method evaluates the likelihood that the data $w_{ur}(z_i)$ arose from any proposed $\{n_u^{\mathrm{pz,k}}(z_i)\}$, along with a slew of other relevant parameters. As for the model, we extend the model described by Eq. 4.14 so as to incorporate systematic uncertainties:

$$w_{ur}(z_i) = \mathrm{Sys}\,(\mathrm{z_i}, \{\mathrm{s_k}\}) n_u(z_i) b_r(z_i) w_{\mathrm{DM}}(z_i) + b_r(z_i)\alpha_u(z_i) \sum_{j>i} [D_{ij} n_u(z_j)] + \bar{b}_u \alpha_r(z_i) n_u(z_i) \sum_{j>i} D_{ij}. \quad \text{(A.1)}$$

The function $\mathrm{Sys}\,(\mathrm{z}, \{\mathrm{s_i}\})$ varies smoothly with redshift and accounts for the three systematics described in § 4.4.2 (method systematic, bias evolution of the weak lensing sample, uncertainties in the redshifts of the reference sample). Since the systematic functions model the redshift evolution of the bias of the unknown sample, we removed the term $b_u(z_i)$ from the clustering term. Nonetheless, we kept a redshift averaged nuisance parameter $\bar{b}_u$ in the magnification term. We note that we did not multiply the magnification terms by the systematic function: despite the magnification terms are not immune to the above systematics, we assumed that it was necessary further modelling those, as the α_r, $\alpha_r u$ and $\bar{b}_u$ parameters provide enough flexibility to the model. The $\mathrm{Sys}\,(\mathrm{z_i}, \{\mathrm{s_k}\})$ function is given by:

$$log[\mathrm{Sys}\,(\mathrm{z_i}, \{\mathrm{s_k}\})] = \sum_{k<M} s_k P'_k(z_i), \quad \text{(A.2)}$$

with $P'_k(z_i)$ the kth Legendre polynomial, after remapping the redshift argument into the interval (-1,1), and M the maximum order considered. We found that $M = 6$ describes with good accuracy the systematics in Buzzard. We then proceed to linearise the the systematic function, Taylor expanding it:

$$\mathrm{Sys}\,(\mathrm{z_i}, \{\mathrm{s_k}\}) \approx \mathrm{Sys}\,(\mathrm{z_i}, \{\mathrm{s_{k,0}}\}) + \left.\frac{\partial Sys\,(z_i, \{s_k\})}{\partial \{s_k\}}\right|_{\{s_{k,0}\}} (\{s_k\} - \{s_{k,0}\}) \quad \text{(A.3)}$$

We can then write:

$$w_{ur}(z_i) - \hat{w}_{ur}(z_i) = \Delta w_{ur}(z_i) - A(z_i)\mathbf{x}. \tag{A.4}$$

In the above equation, $\mathbf{x}$ is a vector made of all the nuisance parameters we wish to marginalise over ($\{s_\natural k$, α_r, $\alpha_r u$ and $\bar{b}_u$), $A(z_i)$ is the local gradient from the $\mathbf{x}$ parameters to the model $\Delta w_u r(z_i)$, and $\Delta w_u r(z_i)$ is the difference between the observed cross-correlations and the model evaluated for some fiducial value of the nuisance parameters.

$$\begin{aligned}\Delta w_u r(z_i) \equiv w_{ur}(z_i) - \\ \left[\mathrm{Sys}\left(z_i, \{s_{k,0}\}\right) + \left.\frac{\partial \mathrm{Sys}\left(z_i, \{s_k\}\right)}{\partial\{s_k\}}\right|_{\{s_{k,0}\}} \{s_{k,0}\}\right] \times \\ n_u(z_i) b_r(z_i) w_{\mathrm{DM}}(z_i) + \\ b_r(z_i)\alpha_{u,0}(z_i)\sum_{j>i}\left[D_{ij} n_u(z_j)\right] + \bar{b}_{u,0}\alpha_{r,0}(z_i) n_{u,0}(z_i)\sum_{j>i} D_{ij}.\end{aligned} \tag{A.5}$$

If we assume the nuisance parameters we want to marginalise over to have a Gaussian prior $\mathbf{x} \sim \mathcal{N}(\mu, C_x)$, we can write the full likelihood as follows:

$$\begin{aligned}\mathcal{L}_{\mathrm{WZ}} = |2\pi\hat{\Sigma}_{\mathrm{wz}}|^{-1/2}|2\pi\hat{\Sigma}_x|^{-1/2} \times \\ \int d\mathbf{x} \exp\left[-\frac{1}{2}(\Delta w_{ur} - A\mathbf{x})^T \hat{\Sigma}_{\mathrm{wz}}^{-1}(\Delta w_{ur} - A\mathbf{x})\right] \times \\ \exp\left[-\frac{1}{2}(\mathbf{x} - \mu_{\mathbf{x}})^T \hat{\Sigma}_x^{-1} + (\mathbf{x} - \mu_{\mathbf{x}})\right],\end{aligned} \tag{A.6}$$

$$\begin{aligned}\mathcal{L}_{\mathrm{WZ}} \propto \left[A^T \hat{\Sigma}_{\mathrm{wz}}^{-1} A + \hat{\Sigma}_x^{-1}\right] \times \\ \exp\left[\frac{1}{2}(\Delta w_{ur} - A\mathbf{x})^T (\hat{\Sigma}_{\mathrm{wz}} + A\hat{\Sigma}_x A^T)^{-1}(\Delta w_{ur} - A\mathbf{x})\right]\end{aligned} \tag{A.7}$$

In practice, we note that we cannot marginalise over the parameters α_r, as they are marginalised over in the main cosmological analysis. Instead, we fix them to some fiducial values, and we show the impact on the likelihood of varying them by a reasonable amount $\Delta\alpha_r$ (§ 4.4.2).

Appendix B

B.1 The shear two-point METACALIBRATION Response

We derive in this Appendix the response for the shear two-point correlation function, following Sheldon & Huff 2017. We can write the two-point correlation function as follows

$$\xi = \int d\boldsymbol{e_\alpha} d\boldsymbol{e_\beta} S_\alpha S_\beta P(\boldsymbol{e_\alpha}, \boldsymbol{e_\beta}) \boldsymbol{e_\alpha} \boldsymbol{e_\beta} \tag{B.1}$$

where S_α and S_β are selection functions, and $P(\boldsymbol{e_\alpha}, \boldsymbol{e_\beta})$ the joint probability distribution of $\boldsymbol{e_\alpha}$ and $\boldsymbol{e_\beta}$. In the DES Y1 analysis, we assumed that the shapes of galaxies are not correlated in the absence of lensing, i.e. $P(\boldsymbol{e_\alpha}, \boldsymbol{e_\beta})|_{\gamma=0} = P(\boldsymbol{e_\alpha})|_{\gamma=0}\, P(\boldsymbol{e_\beta})|_{\gamma=0}$. Under this hypothesis, the response of the shear two point function is equal to the mean response squared: $\langle \boldsymbol{R^{2pt}} \rangle \approx \langle \boldsymbol{R} \rangle^2$. In what follows we drop this assumption. The response at leading order can be written as:

$$\langle \boldsymbol{R^{2pt}} \rangle = \int d\boldsymbol{e_\alpha} d\boldsymbol{e_\beta} \frac{\partial^2 S_\alpha S_\beta P(\boldsymbol{e_\alpha}, \boldsymbol{e_\beta}) \boldsymbol{e_\alpha} \boldsymbol{e_\beta}}{\partial \gamma_\alpha \partial \gamma_\beta} \tag{B.2}$$

$$\langle \boldsymbol{R^{2pt}} \rangle = \int d\boldsymbol{e_\alpha} d\boldsymbol{e_\beta} \frac{\partial}{\partial \gamma_\alpha} S_\alpha \times \left[P(\boldsymbol{e_\alpha}, \boldsymbol{e_\beta}) \boldsymbol{e_\alpha} \boldsymbol{e_\beta} \frac{\partial S_\beta}{\partial \gamma_\beta} + S_\beta \boldsymbol{e_\alpha} \frac{\partial (P(\boldsymbol{e_\alpha}, \boldsymbol{e_\beta}) \boldsymbol{e_\beta})}{\partial \gamma_\beta} \right] \tag{B.3}$$

$$\langle \boldsymbol{R}^{\mathbf{2pt}} \rangle = \int d\boldsymbol{e_\alpha} d\boldsymbol{e_\beta} \left[P(\boldsymbol{e_\alpha}, \boldsymbol{e_\beta}) \boldsymbol{e_\alpha} \boldsymbol{e_\beta} \frac{\partial S_\alpha}{\partial \gamma_\alpha} \frac{\partial S_\beta}{\partial \gamma_\beta} \right] + \int d\boldsymbol{e_\alpha} d\boldsymbol{e_\beta} \left[S_\alpha \boldsymbol{e_\beta} \frac{\partial (P(\boldsymbol{e_\alpha}, \boldsymbol{e_\beta}) \boldsymbol{e_\alpha})}{\partial \gamma_\alpha} \frac{\partial S_\beta}{\partial \gamma_\beta} \right] + \int d\boldsymbol{e_\alpha} d\boldsymbol{e_\beta} \left[S_\beta \boldsymbol{e_\alpha} \frac{\partial (P(\boldsymbol{e_\alpha}, \boldsymbol{e_\beta}) \boldsymbol{e_\beta})}{\partial \gamma_\beta} \frac{\partial S_\alpha}{\partial \gamma_\alpha} \right] + \int d\boldsymbol{e_\alpha} d\boldsymbol{e_\beta} \left\{ S_\alpha S_\beta \frac{\partial}{\delta \gamma_\alpha} \left[\boldsymbol{e_\alpha} \frac{\partial (P(\boldsymbol{e_\alpha}, \boldsymbol{e_\beta}) \boldsymbol{e_\beta})}{\partial \gamma_\beta} \right] \right\} \quad \text{(B.4)}$$

For the first term of Eq. B.4:

$$\int d\boldsymbol{e_\alpha} d\boldsymbol{e_\beta} \left[P(\boldsymbol{e_\alpha}, \boldsymbol{e_\beta}) \boldsymbol{e_\alpha} \boldsymbol{e_\beta} \frac{(S_\alpha^+ - S_\alpha^-)}{\Delta\gamma} \frac{\left(S_\beta^+ - S_\beta^-\right)}{\Delta\gamma} \right] = \frac{1}{(\Delta\gamma)^2} \left[\xi^{++}(\alpha, \beta) - \xi^{-+}(\alpha, \beta) - \xi^{+-}(\alpha, \beta) + \xi^{--}(\alpha, \beta) \right] \quad \text{(B.5)}$$

where derivatives have been approximated using finite differences. The notation $\xi^{-+}(\alpha, \beta)$ indicates that the shear two-point correlation function has been computed applying the negatively sheared selection on the sample α and the positively shared selection on the sample β.

The second term of Eq. B.4 reads:

$$\int d\boldsymbol{e_\alpha} d\boldsymbol{e_\beta} \left[S_\alpha \boldsymbol{e_\beta} \frac{(P(\boldsymbol{e_\alpha}^+, \boldsymbol{e_\beta}) \boldsymbol{e_\alpha}^+ - P(\boldsymbol{e_\alpha}^-, \boldsymbol{e_\beta}) \boldsymbol{e_\alpha}^-)}{\Delta\gamma} \frac{\left(S_\beta^+ - S_\beta^-\right)}{\Delta\gamma} \right] = \frac{1}{(\Delta\gamma)^2} \left[\xi^{0+}(\alpha^+, \beta) - \xi^{0-}(\alpha^+, \beta) - \xi^{0+}(\alpha^-, \beta) + \xi^{0-}(\alpha^-, \beta) \right] \quad \text{(B.6)}$$

where the notation $\xi^{0-}(\alpha^+, \beta)$ indicates that the shear two-point correlation function has been computed applying the normal selection to the positively shared sample α, and applying the negatively shared selection to the sample β.

The third term of Eq. B.4 reads:

$$\int d\boldsymbol{e_\alpha} d\boldsymbol{e_\beta} \left[S_\beta \boldsymbol{e_\alpha} \frac{(P(\boldsymbol{e_\alpha}, \boldsymbol{e_\beta}^+)\boldsymbol{e_\beta}^+ - P(\boldsymbol{e_\alpha}, \boldsymbol{e_\beta}^-)\boldsymbol{e_\beta}^-)}{\Delta\gamma} \frac{(S_\alpha^+ - S_\alpha^-)}{\Delta\gamma} \right] = \frac{1}{(\Delta\gamma)^2} \left[\xi^{+0}(\alpha, \beta^+) - \xi^{-0}(\alpha, \beta^+) - \xi^{+0}(\alpha, \beta^-) + \xi^{-0}(\alpha, \beta^-) \right] \quad \text{(B.7)}$$

Lastly, the fourth term of Eq. B.4:

$$\int d\boldsymbol{e_\alpha} d\boldsymbol{e_\beta} \left\{ S_\beta S_\alpha \frac{\partial}{\partial \gamma_\alpha} \left[\boldsymbol{e_\alpha} \frac{(P(\boldsymbol{e_\alpha}, \boldsymbol{e_\beta}^+)\boldsymbol{e_\beta}^+ - P(\boldsymbol{e_\alpha}, \boldsymbol{e_\beta}^-)\boldsymbol{e_\beta}^-)}{\Delta\gamma} \right] \right\} = \int d\boldsymbol{e_\alpha} d\boldsymbol{e_\beta} S_\beta S_\alpha \left[\frac{(P(\boldsymbol{e_\alpha}^+, \boldsymbol{e_\beta}^+)\boldsymbol{e_\alpha}^+\boldsymbol{e_\beta}^+ - P(\boldsymbol{e_\alpha}^-, \boldsymbol{e_\beta}^+)\boldsymbol{e_\alpha}^-\boldsymbol{e_\beta}^+)}{(\Delta\gamma)^2} \right] + - \int d\boldsymbol{e_\alpha} d\boldsymbol{e_\beta} S_\beta S_\alpha \left[\frac{(P(\boldsymbol{e_\alpha}^+, \boldsymbol{e_\beta}^-)\boldsymbol{e_\alpha}^+\boldsymbol{e_\beta}^- + P(\boldsymbol{e_\alpha}^-, \boldsymbol{e_\beta}^-)\boldsymbol{e_\alpha}^-\boldsymbol{e_\beta}^-)}{(\Delta\gamma)^2} \right] = \frac{1}{(\Delta\gamma)^2} \left[\xi^{00}(\alpha^+, \beta^+) - \xi^{00}(\alpha^-, \beta^+) - \xi^{00}(\alpha^+, \beta^-) + \xi^{00}(\alpha^-, \beta^-) \right] \quad \text{(B.8)}$$

Putting together Eq. B.5, B.6, B.7 and B.8:

$$\begin{aligned} \langle \boldsymbol{R^{2pt}} \rangle = & \frac{1}{(\Delta\gamma)^2} \left[\xi^{++}(\alpha, \beta) - \xi^{-+}(\alpha, \beta) - \xi^{+-}(\alpha, \beta) + \xi^{--}(\alpha, \beta) \right] + \\ & \frac{1}{(\Delta\gamma)^2} \left[\xi^{0+}(\alpha^+, \beta) - \xi^{0-}(\alpha^+, \beta) - \xi^{0+}(\alpha^-, \beta) + \xi^{0-}(\alpha^-, \beta) \right] + \\ & \frac{1}{(\Delta\gamma)^2} \left[\xi^{+0}(\alpha, \beta^+) - \xi^{-0}(\alpha, \beta^+) - \xi^{+0}(\alpha, \beta^-) + \xi^{-0}(\alpha, \beta^-) \right] + \\ & \frac{1}{(\Delta\gamma)^2} \left[\xi^{00}(\alpha^+, \beta^+) - \xi^{00}(\alpha^-, \beta^+) - \xi^{00}(\alpha^+, \beta^-) + \xi^{00}(\alpha^-, \beta^-) \right] \end{aligned} \quad \text{(B.9)}$$

Ideally, the response would need to be computed shearing e_t or $e_\times$. These are the tangential and cross components of the shear along the line connecting two galaxies. We cannot do this because the shear would depend on the pair of galaxies considered. We can just shear e_1 and e_2 (which are the tangential and cross components along two arbitrary fixed axes). Let us assume in the following that the response matrix is diagonal, and let us define:

$$\langle R^{\rm 2pt}_{tt,tt} \rangle = \int de_{\alpha,t} de_{\beta,t} \frac{\partial^2 S_\alpha S_\beta P(e_{\alpha,t}, e_{\beta,t}) e_{\alpha,t} e_{\beta,t}}{\partial \gamma_{\alpha,t} \partial \gamma_{\beta,t}} \quad \text{(B.10)}$$

Analogously we can define $\langle R^{\rm 2pt}_{\times\times,\times\times}\rangle$. Under the hypothesis of isotropy, $\langle R^{\rm 2pt}_{\times\times,\times\times}\rangle = \langle R^{\rm 2pt}_{tt,tt}\rangle \equiv \langle R^{\rm 2pt}\rangle$, which would be the response needed to correct ξ_+ and ξ_-. However, these two responses are not directly accessible. Using Eq. B.9 and shearing e_1 and e_2 we obtain:

$$\langle R^{\rm 2pt}_{tt,11}\rangle + 2\langle R^{\rm 2pt}_{tt,12}\rangle + \langle R^{\rm 2pt}_{tt,22}\rangle \pm \left(\langle R^{\rm 2pt}_{\times\times,11}\rangle + 2\langle R^{\rm 2pt}_{\times\times,12}\rangle + \langle R^{\rm 2pt}_{\times\times,22}\rangle\right) \quad \text{(B.11)}$$

where now the derivatives are with respect to e_1 and e_2. The $\pm$ depends whether we chose ξ_+ or ξ_- as statistics to infer the response. Changing variables, Eq. B.11 becomes:

$$\langle R^{\rm 2pt}\rangle \left[\langle\left(\frac{\partial\gamma_t}{\partial e_1}\right)^2\rangle + 2\langle\frac{\partial\gamma_t}{\partial e_1}\frac{\partial\gamma_t}{\partial e_2}\rangle + \langle\left(\frac{\partial\gamma_t}{\partial e_2}\right)^2\rangle\right] \pm \langle R^{\rm 2pt}\rangle \left[\langle\left(\frac{\partial\gamma_\times}{\partial e_1}\right)^2\rangle + 2\langle\frac{\partial\gamma_\times}{\partial e_1}\frac{\partial\gamma_\times}{\partial e_2}\rangle + \langle\left(\frac{\partial\gamma_\times}{\partial e_2}\right)^2\rangle\right] \quad \text{(B.12)}$$

γ_t and $\gamma_\times$ are related to e_1 and e_2 by a rotation matrix; we can assume for instance

$$\frac{\partial\gamma_t}{\partial e_1} = cos\phi \quad \frac{\partial\gamma_t}{\partial e_2} = -sin\phi \quad \frac{\partial\gamma_\times}{\partial e_1} = sin\phi \quad \frac{\partial\gamma_\times}{\partial e_2} = cos\phi \quad \text{(B.13)}$$

Eq. B.12 leads to

$$\langle R^{\rm 2pt}\rangle \left[\langle cos^2\phi\rangle + \langle cos\phi sin\phi\rangle + \langle sin^2\phi\rangle\right] \pm \langle R^{\rm 2pt}\rangle \left[\langle sin^2\phi\rangle + \langle cos\phi sin\phi\rangle + \langle cos^2\phi\rangle\right] = \langle R^{\rm 2pt}\rangle \pm \langle R^{\rm 2pt}\rangle \quad \text{(B.14)}$$

Fig. B.1 shows the response obtained from Eq. B.14. We sheared e_1 and e_2 separately so as to better compare with the standard procedure implemented in the DES Y1 analysis. The shear two-point measurement has been computed in 20 bins from 2.5 to 250 arcminutes. Error bars were obtained from 100 jaccknives. We note that the values obtained from e_1 and e_2 separately show differences of the order of ~ 0.4 per cent on $\langle R^{\rm 2pt}\rangle$. This corresponds to a difference or ~ 0.2 per cent on $\langle R\rangle$, indicating that the

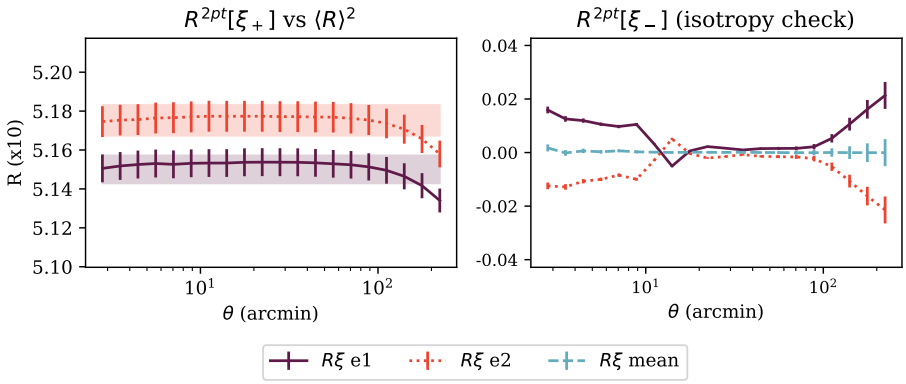

Figure B.1: *Left:* response inferred using ξ_+ (Eq. B.14, represented by the lines in plot) compared with the standard mean response squared used in the DES Y1 analysis to calibrate the shear two-point statistics (horizontal bands). *Right:* Response inferred using ξ_- (Eq. B.14). If the hypothesis of isotropy holds, this should be compatible with 0.

hypothesis of isotropy holds down to a 0.2 per cent level. The two diagonal components of the response matrix are expected to be identical if there was no preferred direction in the measurement process. In practice, this is not true, due to PSF anisotropies or mask effects with distinct orientation with respect the two shear axes (as found by Sheldon & Huff 2017). We do not expect this level of bias to impact the DES Y3 analysis, and its amplitude is within the overall calibration error budget from the image simulations. We also note that in the fiducial methodology for the DES Y1 and Y3 analyses the responses from the two components are averaged, which should mitigate this effect (see below).

Fig. B.1 also shows the comparison with the mean response implemented in DES Y1 ($\langle R\rangle^2$). The responses obtained with the two methods are in good agreement within errors for most of the angular scales probed here, except at large scales, where a small difference is measured. This large-scale discrepancy is expected to have a negligible impact for the DES Y3 analysis, given its amplitude. Such difference might be explained by the large-scale pattern of the response across the DES Y3 footprint (Fig. B.2). This pattern cannot be captured by the mean response correction implemented in the DES Y1 analysis, since the the mean response is computed over the full sample, losing any spatial/angular information. The presence of a pattern in the mean response is not unexpected and can be caused by a variety of

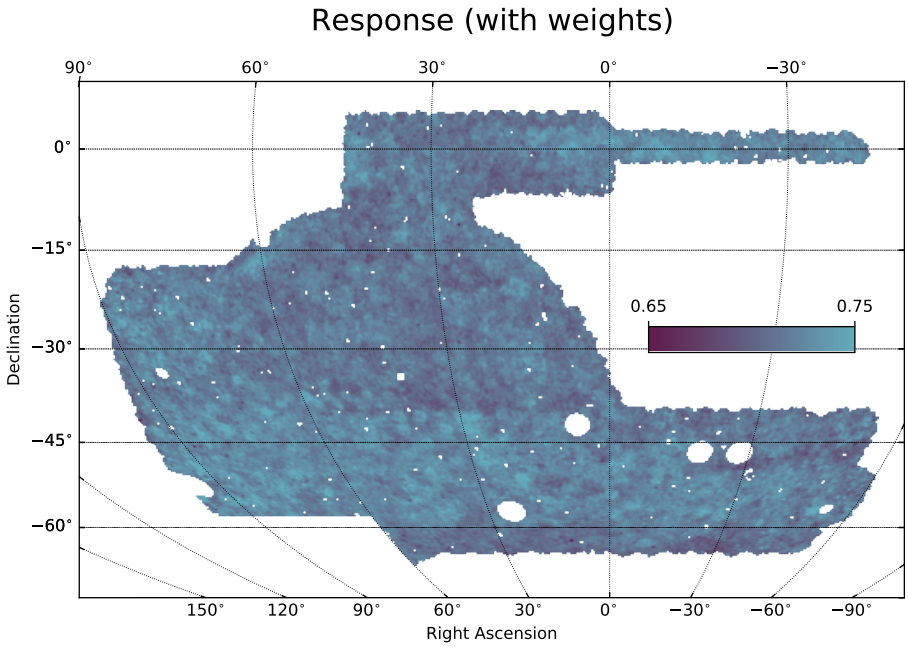

Figure B.2: Weighted mean response across the survey footprint.

factors: e.g., the mean response is expected to be correlated with imaging depth.

Finally, the right panel of Fig. B.1 tests our assumption of isotropy made before Eq. B.11: if isotropy holds for e_1 and e_2, it is not possible to estimate the response using ξ_-, since in Eq. B.14 the two terms cancel out. The response obtained for the two components separately are not compatible with zero. This again suggests that the assumption of isotropy is good only at the sub-percentage level with respect to the response computed with ξ_+, in quantitative agreement with the results shown in the left panel of of Fig. B.1. The signal vanishes when the two components are averaged, effectively erasing the bias in the estimate of the response.

B.2 Color based Star-Galaxy Separation

We made use of the star-galaxy separation at faint magnitudes using the DECam observations in *ugriz* made as part of the DES deep fields, combined with $JHKs$ bands as observed by the UltraVISTA survey, as detailed

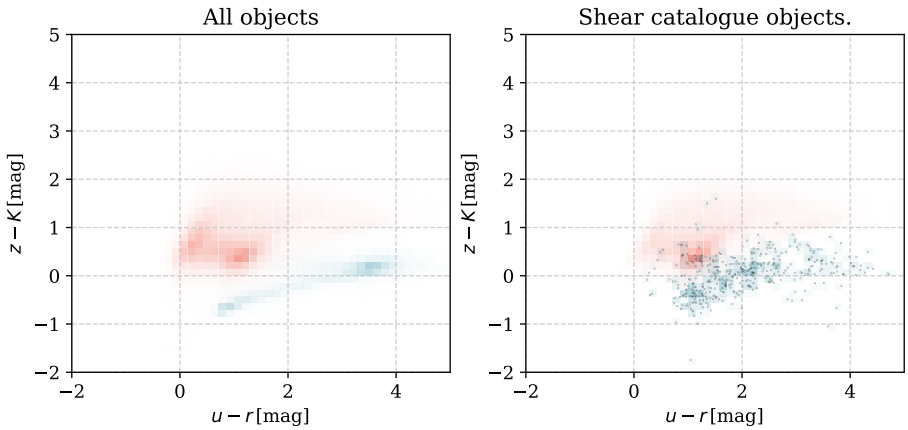

Figure B.3: Objects as separated by the kNN classifier. Blue histograms represent objects identified as galaxies, red histograms stars. The individual points in the right panel are all of the individual points. *Left* shows the color distributions for all matched objects in the DES deep fields C3, E2 and X3 regions, *right* shows color distributions for objects in this set which pass the fiducial cuts and make it into the shape catalogue.

in (Hartley et al., 2020, in particular Section 8). This star galaxy separation uses the color information as features for supervised machine learning classification. The training set for the classification comes from the HST-ACS MU_CLASS available within the COSMOS field (Leauthaud et al., 2007). MU_CLASS uses both HST-ACS color and morphololology information together. In particular, we chose the Nearest Neighbors (kNN) star-galaxy classification, as it is shown to have a the best performance in terms of stellar purity, and therefore is appropriate for assessing the contamination of stars in the shape catalogue.

The color-color plots in Fig. B.3 show the results of this classifier when applied to both all objects in the DES catalogues in the Deep Fields C3, X3 and E2 regions for which both $ugrizJHK$ colors and METACALIBRATION shape measurements are available. As can be seen, the color-based classification of shape catalogue objects (which are not selected by color) shows a small fraction of contaminating objects which have colors highly consistent with those of the stellar population. Fig. B.4 also shows the i band magnitudes of the objects in the C3, X3 and E2 regions, as classified by the color-based kNN method.

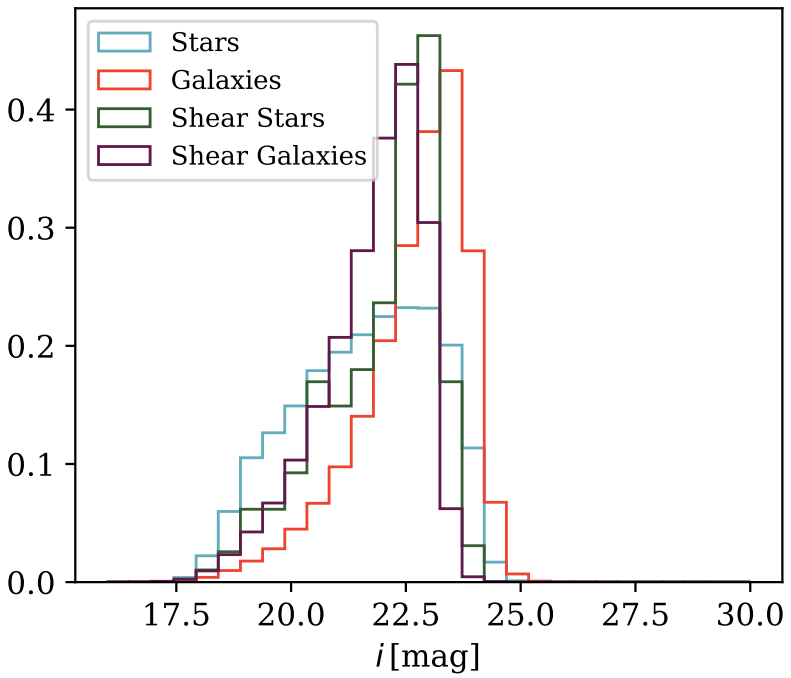

Figure B.4: i band magnitude distributions for objects as separated by the kNN classifier in the DES deep fields C3, E2 and X3 regions.

Appendix C

C.1 Skewness parameter

In perturbation theory, the Fourier space equations of motion for the matter density contrast δ and the divergence of the velocity field $\theta = \nabla \mathbf{v}$ are (Bernardeau et al., 2002):

$$\frac{\partial \delta(\mathbf{k},\tau)}{\partial \tau} + \theta(\mathbf{k},\tau) = - \int \mathrm{d}^3k_1 \mathrm{d}^3k_2 \delta_{\mathrm{D}}(\mathbf{k}-\mathbf{k}_{12}), \alpha(\mathbf{k}_1,\mathbf{k}_2)\delta(\mathbf{k}_1,\tau)\theta(\mathbf{k}_2,\tau) \equiv \alpha[\delta,\theta,\mathbf{k}], \quad \text{(C.1)}$$

$$\frac{\partial \theta(\mathbf{k},\tau)}{\partial \tau} + H\theta(\mathbf{k},\tau) + \frac{3\Omega_{\mathrm{m}}H_0^2}{2a}\delta(\mathbf{k},\tau) = - \int \mathrm{d}^3k_1 \mathrm{d}^3k_2 \delta_D(\mathbf{k}-\mathbf{k}_{12}), \beta(\mathbf{k}_1,\mathbf{k}_2)\theta(\mathbf{k}_1,\tau)\theta(\mathbf{k}_2,\tau) \equiv \beta[\delta,\theta,\mathbf{k}], \quad \text{(C.2)}$$

with τ being the conformal time, a the scale factor, $H = \frac{d}{d\tau}\ln a$, $\mathbf{k}_{12} = \mathbf{k}_1 + \mathbf{k}_2$ and α and β defined by:

$$\alpha(\mathbf{k}_1,\mathbf{k}_2) = 1 + \frac{1}{2}\frac{\mathbf{k}_1\mathbf{k}_2}{k_1k_2}(\frac{k_1}{k_2} + \frac{k_2}{k_1}), \quad \text{(C.3)}$$

$$\beta(\mathbf{k}_1,\mathbf{k}_2) = \frac{1}{2}\frac{\mathbf{k}_1\mathbf{k}_2}{k_1k_2}(\frac{k_1}{k_2} + \frac{k_2}{k_1}) + \frac{(\mathbf{k}_1\mathbf{k}_2)^2}{k_1^2k_2^2}. \quad \text{(C.4)}$$

The matter density contrast and the divergence of the velocity field can be expanded as:

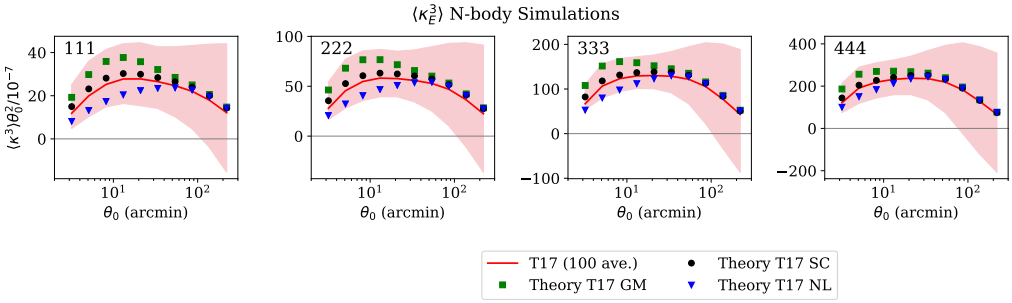

Figure C.1: Comparison between measured third moments in T17 simulations (red line) and theoretical predictions using different modelling choices for the small scales regime : SC01 fitting formulae (black points), GM12 fitting formulae (green points) and the perturbation theory prediction obtained using the non linear power spectrum (NL, blue points). The red shaded region correspond to the 1-σ uncertainty of the measurement. The grey shaded regions indicate the angular scales excluded in the main cosmological analysis when combining with second moments (i.e., a $24h^{-1}$ Mpc scale cut).

$$\delta(\mathbf{k},\tau) = \sum_{\mathrm{n}=1} \delta_n(\mathbf{k},\tau), \tag{C.5}$$

$$\theta(\mathbf{k},\tau) = -\frac{\partial \ln D_+(\tau)}{\partial \tau} \sum_{\mathrm{n}=1} \theta_{\mathrm{n}}(\mathbf{k},\tau), \tag{C.6}$$

where n indicates the order at which the fields are approximated and D_+ is the linear growth factor. At linear order, $\delta_1(\mathbf{k},\tau) = \theta_1(\mathbf{k},\tau) = D_+(\tau)\delta_1(\mathbf{k})$.

At second order the Fourier equations of motions are solved by:

$$\delta_2(\mathbf{k},\tau) = D_+^2(\tau)\alpha[\delta_1,\delta_1,\mathbf{k}] + D_2(\tau)(\beta[\delta_1,\delta_1,\mathbf{k}] - \alpha[\delta_1,\delta_1,\mathbf{k}]), \tag{C.7}$$

with D_2 the solution of the following differential equation:

$$\frac{\partial^2 D_2(\tau)}{\partial^2 \tau} + H^2\frac{(\tau)}{\partial \tau} - \frac{3\Omega_{\mathrm{m}} H_0^2}{2a} D_2(\tau) = \left(\frac{\partial D_+(\tau)}{\partial \tau}\right)^2 \tag{C.8}$$

Lastly, we define the following quantity μ, as it will enter in the modeling of the third moment:

$$\mu \equiv 1 - D_2/D_+^2 \tag{C.9}$$

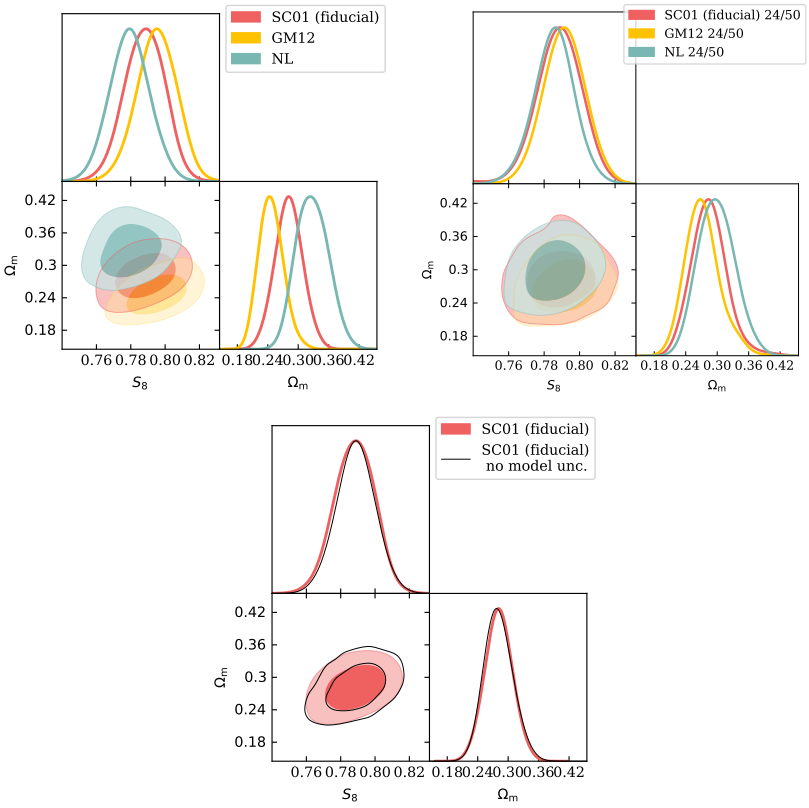

Figure C.2: *Left panel:* forecast posteriors obtained assuming three different theory data vector using different modelling choices for the third moments small scales (the SC01 and GM12 models and the simple non linear theory prediction). The three data vectors have been analysed assuming as true model the SC01 model. The data vectors include second and third moments and it assumes the fiducial scale cut (i.e., a $24h^{-1}$ Mpc scale cut). *Central panel:* same as left panel, but assuming a large scale cut ($50h^{-1}$ Mpc) for third moments. *Right panel:* comparison between forecast posteriors obtained assuming a theory data vector, a fiducial scale cut ($24h^{-1}$ Mpc) and including (or not including) third moments modelling uncertainties in the covariance.

At leading order in perturbation theory, one can compute the variance of the dark matter density field smoothed by a top hat filter as:

$$\langle\delta^2_{\theta_0,\rm lin}\rangle(\tau) = \frac{1}{2\pi}\int {\rm d}k k W(k,\theta_0)^2 P_{\rm lin}(k,\tau); \tag{C.10}$$

while the skewness will be described by the following equation:

$$\langle\delta^3_{\theta_0,\rm lin}\rangle(\tau) = \frac{6}{(2\pi)^3}\int {\rm d}^2k_1{\rm d}^2k_2 W(\mathbf{k}_1,\theta_0)W(\mathbf{k}_2,\theta_0)W(\mathbf{k}_1+\mathbf{k}_2,\theta_0) \times P_{\rm lin}(\mathbf{k}_1,\tau), P_{\rm lin}(\mathbf{k}_2,\tau)F_2(\mathbf{k}_1,\mathbf{k}_2,\tau), \tag{C.11}$$

where $P_{\rm lin}(k,\tau)$ is the linear power spectrum and $W(k,\theta_0)$ is the top hat filter described in Eq. 7.1. The term $F_2(\mathbf{k}_1,\mathbf{k}_2,\tau)$ reads:

$$F_2(\mathbf{k}_1,\mathbf{k}_2,\tau) = \frac{1}{2}[(1+\frac{k_1}{k_2}\cos\phi)+(1+\frac{k_2}{k_1}\cos\phi)]+[1-\mu(\tau)](\cos^2\phi-1). \tag{C.12}$$

We implement here a refinement of the term F_2 based on N-body simulations (while Eq. C.12 has been obtained, so far, exclusively relying on perturbation theory). The refinement we are implementing here has been first obtained by Scoccimarro & Couchman (2001) (SC01) and later on by Gil-Marín et al. (2012) (GM12) fitting an analytical formula to the non-linear evolution of the bispectrum based on a suite of cold dark matter N-body simulations. Implementing such corrections, Eq. C.12 becomes:

$$F_2(\mathbf{k}_1,\mathbf{k}_2,\tau) = \frac{1}{2}b_1b_2[(1+\frac{k_1}{k_2}\cos\phi)+(1+\frac{k_2}{k_1}\cos\phi)] + [1-\mu(\tau)]c_1c_2(\cos^2\phi-1)+[a_1a_2\mu(\tau)-b_1b_2+[1-\mu(\tau)]c_1c_2]. \tag{C.13}$$

The terms a, b, c are taken from Gil-Marín et al. (2012); their subscripts in the above equations indicate if they refer to k_1 or k_2. In particular:

$$a(n,k,\tau) = \frac{1+(\sigma_8 D_+)^{a_6}[0.7(4-2^n)/(1+2^{2n+1})]^{1/2}(qa_1)^{n+a_2}}{1+(qa_1)^{n+a_2}}, \tag{C.14}$$

$$b(n,k,\tau) = \frac{1+0.2a_3(n+3)(qa_7)^{n+3+a_8}}{1+(qa_7)^{n+3.5+a_8}}, \tag{C.15}$$

$$c(n,k,\tau) = \frac{1+4.5a_4/[1.5+(n+3)^4(qa_5)^{n+3+a_9}}{1+(qa_5)^{n+3.5+a_9}}. \tag{C.16}$$

In the above equations, n is the slope of the linear power spectrum at scale k and $q \equiv k/k_{\rm NL}$, where $k_{\rm NL}$ is the scale where non-linearities start to be important and it is defined so that $k^3_{\rm NL}P(k,\tau)/2\pi^2 = 1$. We report in table C.1 the values of the coefficients $a_1, ..., a_9$ as from Scoccimarro & Couchman (2001) and Gil-Marín et al. (2012). Implementing these corrections in Eq. C.11 leads to:

$$\langle\delta^3_{\theta_0,\rm lin}\rangle(\tau) = \frac{6}{(4\pi^2)}\int {\rm d}k_1{\rm d}k_2 W(k_1,\theta_0)W(k_2,\theta_0) \times P_{\rm lin}(k_1,\tau), P_{\rm lin}(k_2,\tau)\int {\rm d}\phi W(\sqrt{k_1^2+k_2^2+2k_1k_2{\rm cos}\phi},\theta_0) \times F_2(k_1,k_2,\phi,\tau). \quad \text{(C.17)}$$

The integral on the angle ϕ can be written as:

$$\begin{aligned}\int {\rm d}\phi W(\sqrt{k_1^2+k_2^2+2k_1K_2{\rm cos}\phi},\theta_0)F_2(k_1,k_2,\phi,\tau) \\ = \frac{1}{2}b_1b_2\int {\rm d}\phi W(\sqrt{k_1^2+k_2^2+2k_1k_2{\rm cos}\phi},\theta_0)[2+(\frac{k_1}{k_2}+\frac{k_2}{k_1}){\rm cos}\phi] \\ + \int {\rm d}\phi W(\sqrt{k_1^2+k_2^2+2k_1k_2{\rm cos}\phi},\theta_0)[(1-\mu)c_1c_2({\rm cos}^2\phi-1)] \\ + \int {\rm d}\phi W(\sqrt{k_1^2+k_2^2+2k_1k_2{\rm cos}\phi},\theta_0)[a_1a_2\mu - b_1b_2 + (1-\mu)c_1c_2]. \quad \text{(C.18)}\end{aligned}$$

For brevity, we omitted the dependence on τ from μ. The three integrals in Eq. C.18 can be solved as:

$$\begin{aligned}b_1b_2[2\pi W(k_1,\theta_0)W(k_2,\theta_0) + \frac{\pi}{2}\frac{\partial}{\partial\theta_0}(W(k_1,\theta_0)W(k_2,\theta_0))] \\ - c_1c_2[\pi(1-\mu)W(k_1,\theta_0)W(k_2,\theta_0)] \\ + 2\pi[a_1a_2\mu - b_1b_2 + (1-\mu)c_1c_2]W(k_1,\theta_0)W(k_2,\theta_0) = \\ \frac{\pi}{2}b_1b_2\frac{\partial}{\partial\theta_0}[W(k_1,\theta_0)W(k_2,\theta_0)] \\ + \pi[2a_1a_2 - (1-\mu)c_1c_2]W(k_1,\theta_0)W(k_2,\theta_0). \quad \text{(C.19)}\end{aligned}$$

After some algebra, one can express Eq. C.17 as:

$$\langle\delta^3_{\theta_0,\rm lin}\rangle(\tau) = 6\left[\int {\rm d}k k W(k,\theta_0)^2 P_{\rm lin}(k,\tau)\right]^2 - 3\left[\int {\rm d}k k(1-\mu)cW(k,\theta_0)^2 P_{\rm lin}(k,\tau)\right]^2 + \frac{3}{4}\frac{\partial}{\partial {\rm ln}\theta_{,0}}\left[\int {\rm d}k k b W(k,\theta_0)^2 P_{\rm lin}(k,\tau)\right]^2, \quad \text{(C.20)}$$

$$\langle\delta^3_{\theta_0,\rm lin}\rangle(\tau) = 3[2(\langle\delta^2_{\theta_0,{\rm lin},a}\rangle(\tau))^2 - (1-\mu)(\langle\delta^2_{\theta_0,{\rm lin},c}\rangle(\tau))^2 + \frac{3}{2}\frac{\partial\langle\delta^2_{\theta_0,{\rm lin},b}\rangle(\tau)}{\partial {\rm ln}\theta_0}. \quad \text{(C.21)}$$

In the above equation we have defined

$$\langle\delta^2_{\theta_0,{\rm lin},X}\rangle(\tau) = \frac{1}{2\pi}\int {\rm d}k k X(k,\tau) W(k,\theta_0)^2 P_{\rm lin}(k,\tau), \quad \text{(C.22)}$$

with X that can be either a, b or c. We finally define the reduced skewness parameter as

$$S_3 \equiv \frac{\langle\delta^3_{\theta_0,\rm lin}\rangle(\tau)}{\langle\delta^2_{\theta_0,\rm lin}\rangle(\tau)^2}. \quad \text{(C.23)}$$

The original perturbation theory result can be obtained noting that in the limit of $a, b, c \to 1$ we have $\delta^2_{\theta_0,{\rm lin},a}$, $\delta^2_{\theta_0,{\rm lin},b}$, $\delta^2_{\theta_0,{\rm lin},c} \to \delta^2_{\theta_0,\rm lin}$; in this case, the reduced skewness parameter assumes the following form:

$$S_3 \equiv \frac{\langle\delta^3_{\theta_0,\rm lin}\rangle(\tau)}{\langle\delta^2_{\theta_0,\rm lin}\rangle(\tau)^2} = 3(1+\mu) + \frac{3}{2}\frac{\partial {\rm ln}\langle\delta^2_{\theta_0,\rm lin}\rangle(\tau)}{\partial {\rm ln}\theta_0}. \quad \text{(C.24)}$$

The equations above for the third moments hold in the linear regime, but they are usually extrapolated to the mild non-linear regime using predictions of the non-linear power spectrum.

We note that there is up to a 30% difference between SC01 and GM12 fitting formulae at small scales (~ 5 arcmin for the first tomographic bin). This is shown in Fig. C.1, along with the predicted third moments obtained without implementing the small scales refinement (i.e., assuming the standard F_2 kernel and the non linear power spectrum). In our main analysis we used the fitting formulae from SC01 because they provide a better fit to

Table C.1: Values of the coefficients for the fitting formula described in Eqs. C.14, C.15 and C.16 from Scoccimarro & Couchman (2001) (SC01) and Gil-Marín et al. (2012) (GM12).

coefficient	SC01	GM12
α_1	0.25	0.484
α_2	3.5	3.740
α_3	2	-0.849
α_4	1	0.392
α_5	2	1.013
α_6	-0.2	-0.575
α_7	1	0.128
α_8	0	-0.722
α_9	0	-0.926

our simulations, but in order to be conservative, we included the difference between the SC01 and GM12 models in our covariance in order to grasp the small scales modelling uncertainty of the skeweness. In Fig. C.2 (left panel) we further show the level of bias we expect in the parameters posterior if the real Universe followed a model different than SC01 for the third moments (which implies the simulations we used to validate our modelling are not accurate enough for validating third moments). For this test, we used a theory data vector that combines second and third moments: it includes all the "auto" moments of different tomographic bins (e.g.,[1,1],[1,1,1],[2,2],[2,2,2]) and the "cross" moments (e.g.,[1,2],[1,1,2],[1,2,2]) and it assumes a fiducial scale cut of ($24h^{-1}$ Mpc). All the other nuisance parameters have been set to their nominal value (zero). We prepared three data vectors using the SC01, the GM12 and the standard non linear prediction for the third moments (NL). The level of bias in the parameters posterior is around $\sim 1\sigma$ when analysing the GM12 and NL data vector with the SC01 model. We note that a more conservative scale cut for the third moments ($50h^{-1}$ Mpc) would strongly decrease the bias (central panel of Fig. C.2). This would also lower the constraining power of the combined second and third moments, but the gain compared to using second moments only would still be considerable (~ 30 per cent for $\Omega_{\rm m}$, ~ 10 per cent for S_8).

Finally, the right panel of Fig. C.2 shows the change in the parameters posterior when including (or not) the third moments modelling uncertainty in the covariance; the change in the posterior obtained combining second and third moments is minimal, for the scales used in the fiducial analysis.

C.2 Mode-mode coupling matrices

We provide here mathematical recipes for the mode-mode coupling matrices $\boldsymbol{M}$ used in § 7.2.1 to account for masking effects. Such matrices are developed in the contest of pseudo power spectrum estimators (e.g, Wandelt et al. 2001; Brown et al. 2005; Hikage et al. 2011; Hikage & Oguri 2016). In particular, we strictly follow here §2.1 of Hikage et al. (2011).

In the presence of a window function (in our case, the DES Y3 footprint) $K(\theta, \phi)$, the shear field assumes the following expression:

$$\bar{\gamma}_1(\theta,\phi) + \bar{\gamma}_2(\theta,\phi) = K(\theta,\phi)(\gamma_1(\theta,\phi) + \gamma_2(\theta,\phi)). \tag{C.25}$$

When the shear field is transformed into its spherical harmonic counterpart, it obtains an additional contribution due to the convolution with the footprint mask:

$$\hat{\bar{\gamma}}_{E,\ell m} \pm i\hat{\bar{\gamma}}_{B,\ell m} = \int \mathrm{d}\Omega [K(\theta,\phi)(\gamma_1(\theta,\phi) + \gamma_2(\theta,\phi))]_{\pm 2} Y^*(\theta,\phi). \tag{C.26}$$

The quantities $\hat{\bar{\gamma}}_{E,lm}$ and $\hat{\bar{\gamma}}_{B,lm}$ are called pseudo E and B modes (as they are convolved with the footprint mask) and their relation with the true E and B modes can be written as:

$$\hat{\bar{\gamma}}_{E,\ell m} \pm i\hat{\bar{\gamma}}_{B,\ell m} = \sum_{\ell' m'} (\hat{\gamma}_{E,\ell m} \pm i\hat{\gamma}_{B,\ell m})_{\pm 2} W_{\ell\ell' m m'}, \tag{C.27}$$

where ${}_{\pm 2}W_{\ell\ell' m m'}$ is a convolution kernel

$$\begin{aligned} {}_{\pm 2}W_{\ell\ell' m m'} = \int \mathrm{d}\Omega\, {}_{\pm 2}Y_{\ell' m'}(\theta,\phi) K(\theta,\phi)\, {}_{\pm 2}Y^*_{\ell m}(\theta,\phi) = \\ \sum_{\ell'' m''} K_{\ell'' m''} (-1)^m \sqrt{\frac{(2\ell+1)(2\ell'+1)(2\ell''+1)}{4\pi}} \times \\ \begin{pmatrix} \ell & \ell' & \ell'' \\ \pm 2 & \mp 2 & 0 \end{pmatrix} \begin{pmatrix} \ell & \ell' & \ell'' \\ m & m' & m'' \end{pmatrix}, \end{aligned} \tag{C.28}$$

with $\begin{pmatrix} \ell & \ell' & \ell'' \\ m & m' & m'' \end{pmatrix}$ Wigner $3j$ symbols and $K_{\ell m} = \int \mathrm{d}\Omega K(\theta,\phi) Y^*_{\ell m}(\theta,\phi)$ the harmonic transform of the window function. Defining

$$C_\ell^{EE} = \frac{1}{2\ell+1} \sum_m |\hat{\gamma}_{E,\ell m}|^2, \tag{C.29}$$

$$C_\ell^{EB} = \frac{1}{2\ell+1}\sum_m \hat{\gamma}_{E,\ell m}\hat{\gamma}^*_{B,\ell m}, \tag{C.30}$$

$$C_\ell^{BB} = \frac{1}{2\ell+1}\sum_m |\hat{\gamma}_{B,\ell m}|^2, \tag{C.31}$$

we can write the masked (pseudo) spectra as the convolution of the true spectra with a mode-mode coupling matrix:

$$\mathbf{C}_\ell = \sum_{\ell'} \mathbf{M}_{\ell\ell'}\mathbf{C}_{\ell'}, \tag{C.32}$$

where we introduced the vector $\mathbf{C}_\ell(C_\ell^{EE}, C_\ell^{EB}, C_\ell^{BB})$. The mode-mode coupling matrix $\mathbf{M}$ is expressed in terms of $M_{\ell\ell'}^{EE,EE}$, $M_{\ell\ell'}^{BB,BB}$, $M_{\ell\ell'}^{EB,EB}$, $M_{\ell\ell'}^{EE,BB}$:

$$\begin{aligned} M_{\ell\ell'}^{EE,EE} &= M_{\ell\ell'}^{BB,BB} \\ &= \frac{2\ell'+1}{8\pi}\sum_{\ell''}(2\ell''+1)K_{\ell''}[1+(-1)^{\ell+\ell'+\ell''}]\times \\ &\qquad \begin{pmatrix} \ell & \ell' & \ell'' \\ 2 & -2 & 0 \end{pmatrix}^2, \end{aligned} \tag{C.33}$$

$$\begin{aligned} M_{\ell\ell'}^{EE,BB} &= M_{\ell\ell'}^{BB,EE} \\ &= \frac{2\ell'+1}{8\pi}\sum_{\ell''}(2\ell''+1)K_{\ell''}[1-(-1)^{\ell+\ell'+\ell''}]\times \\ &\qquad \begin{pmatrix} \ell & \ell' & \ell'' \\ 2 & -2 & 0 \end{pmatrix}^2, \end{aligned} \tag{C.34}$$

$$M_{ll'}^{EB,EB} = \frac{2\ell'+1}{4\pi}\sum_{\ell''}(2\ell'' + 1)K_{\ell''}\begin{pmatrix} \ell & \ell' & \ell'' \\ 2 & -2 & 0 \end{pmatrix}^2, \tag{C.35}$$

with $K_\ell = \frac{1}{2\ell+1}\sum_m K_{\ell m}K^*_{\ell m}$.

C.3 Constraints with data-compression

Our fiducial analysis has been carried out using a covariance matrix obtained from multiple `FLASK` realisations (see § 7.3.1). `FLASK` is a log-normal

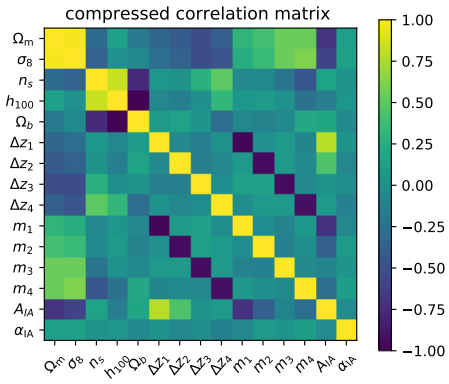

Figure C.3: Measured compressed correlation matrix of second and third moments from 1000 FLASK simulations. A $12h^{-1}$ Mpc scale cut has been applied (see § 7.6.1 for a definition of the scale cuts). The entries of the correlation matrix are shown with respect to the parameter used to compress the data vector.

simulation, where the only required inputs are the desired auto and cross power spectra of the convergence fields and the so-called log-normal shift parameters (which effectively set the skewness of the simulated fields at one scale, see e.g. Friedrich et al., 2018; Gruen et al., 2018). No additional physics is encoded in the FLASK maps. This means that our FLASK realisations reproduce the correct 2nd moments set by our ΛCDM input spectra, but has only limited accuracy in its 3rd moments. We have shown that this does not strongly bias the recovery of input cosmological parameters once applied to N-body simulations (see § 7.6.1).

In this section, we show how to obtain cosmological constraints from our pipeline using the T17 covariance and compare them to the ones obtained from the FLASK covariance, using a data compression algorithm (described in § 7.5.2). We also validate the efficiency of the data compression algorithm and show how it helps to reduce the noise in the inferred parameters caused by the paucity of simulations used to estimate the covariance matrix.

All the tests shown in this section use a theory data vector that includes all the "auto" moments of different tomographic bins (e.g.,[1,1],[1,1,1],[2,2],[2,2,2]) and the "cross" moments (e.g.,[1,2],[1,1,2],[1,2,2]), for a total of 10 combinations for second moments and 20 combinations for third moments. Depending on the test, we show results from second moments, third moments or the combination of the two. We use the fiducial scale cuts determined in § 7.7, of $20h^{-1}$ Mpc for second moments, $12h^{-1}$ Mpc for third moments, and

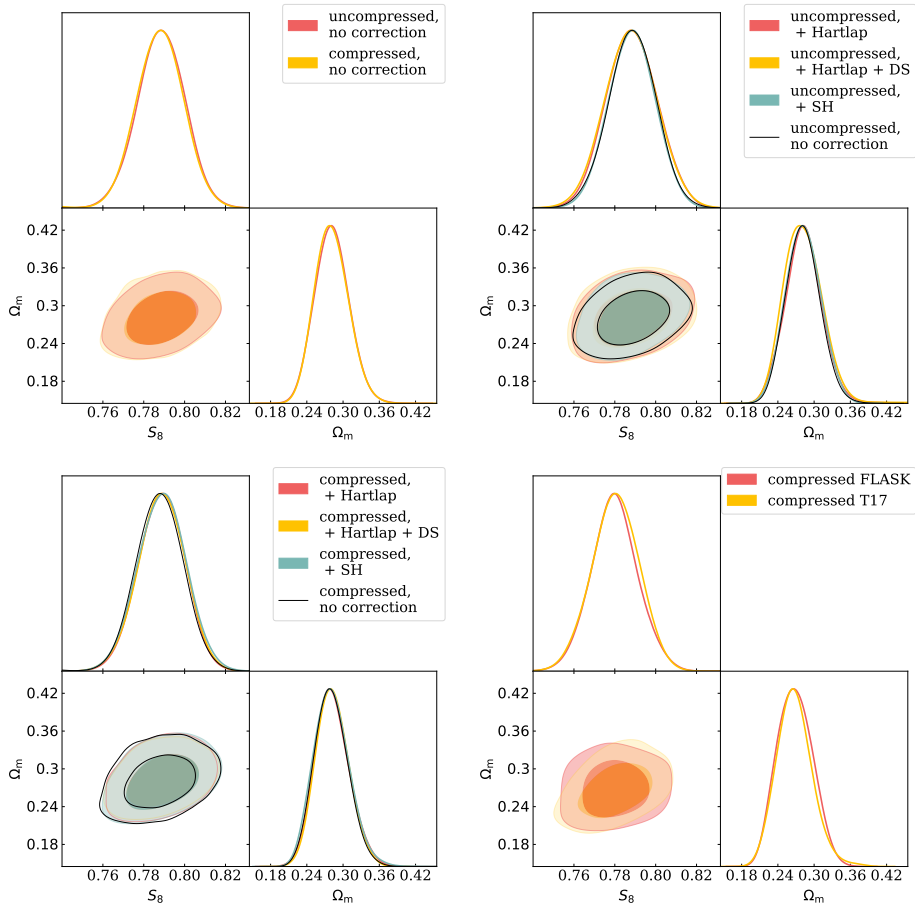

Figure C.4: Posterior of Ω_m and S_8 for four different cases. *Top left*: posteriors obtained using the uncompressed and compressed `FLASK` covariance, without applying any corrections due to the noise (Eqs. 7.37 and 7.38). *Top right*: posteriors obtained using uncompressed FLASK covariance, with a number of corrections to account for the noise in the estimated covariance matrix. "Hartlap" refers to the Hartlap et al. (2007) correction (Eq. 7.37), "DS" refers to the Dodelson & Schneider (2013) correction (Eq. 7.38), while "SH" refers to the Sellentin & Heavens (2016) likelihood (see text in Appendix C.3 for more details). *Bottom left*: same as the top right panel, but for compressed data vectors. *Bottom right*: posteriors obtained using the compressed `FLASK` and T17 covariances. 1000 `FLASK` simulations have been used for these tests.

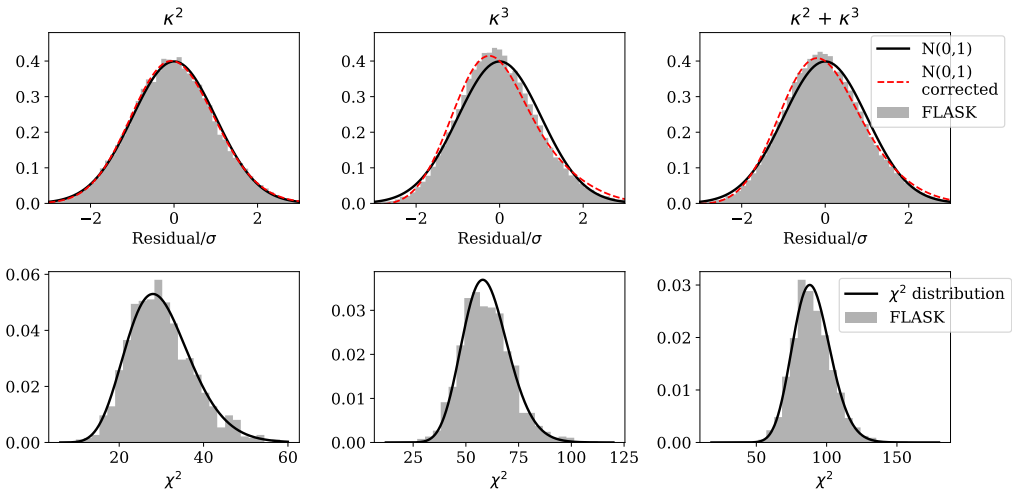

Figure C.5: This figure is the same as Fig. 7.8 but for a uncompressed data vector. *Upper panels*: residuals (i.e., the difference between the measurement signal in a `FLASK` simulation and the simulations mean value) of individual data points in units of their expected standard deviation. We compare to a Gaussian with 0 mean and unit standard deviation; we also compare to a Gaussian corrected by the first term of the Edgeworth expansion of the likelihood (see text for more details). *Bottom panels*: Distribution of the χ^2 of each realization of the `FLASK` simulations, compared to a theoretical χ^2 distribution.

$24h^{-1}$ Mpc when second and third moments are combined. For the data vector, a fiducial T17 cosmology is assumed, with nuisance and astrophysical parameters (photo-z biases, multiplicative shear biases, intrinsic alignment IA) assumed to be null, and no baryonic contamination. When estimating parameters posterior, we further marginalise over nuisance parameters as explained in § 7.2.1.

We show the compressed correlation matrix in Fig. C.3. The correlation matrix has now 15 entries, as many as as the number of parameters we constrain in our analysis. Interestingly, the correlation between the different elements of the compressed data vector reflects the correlation between parameters. For instance, $\Omega_{\rm m}$ and σ_8 show a significant correlation, as expected from Fig. 7.9. The anticorrelation between the mean shift δz and the multiplicative shear biases m is due to the fact that the amplitude of the moments depends on the mean redshift of the source distribution (see, e.g., Bernardeau et al. 1997); due to our definition, a positive δz shifts the mean of the distribution to lower redshift and lowers the amplitude of the moments, while a positive m has the opposite effect.

We next perform here several tests to validate our compression algorithm. First, we run two forecast chains using the compressed and uncompressed `FLASK` covariance and compare the contours. This is shown in the top left panel of Fig. C.4, for the $\Omega_{\rm m}$ and S_8 parameters. In this first test, we did not apply any correction for the noise in the inverse of the covariance (Eqs. 7.37 and 7.38), as we are interested in validating the compression algorithm only. The marginalised 1-D posteriors of $\Omega_{\rm m}$ and S_8 have similar width, showing that the data compression implemented is basically lossless. As a caveat, we remind the reader that we assume the likelihood to be Gaussian, which in the case of the uncompressed data vector is only an approximation (see below).

Second, we show in the top right panel of Fig. C.4 how the constraints degrade once the uncertainties in the inverse of the covariance matrix are taken into account. The Hartlap et al. (2007) and Dodelson & Schneider (2013) corrections (Eqs. 7.37 and 7.38) noticeably enlarge the contours, the net effect depending on the number of simulations used to estimate the covariance matrix. We also show, for comparison purposes, how the posteriors would look if the likelihood from Sellentin & Heavens (2016) was used. Sellentin & Heavens (2016) argue that when the covariance matrix is estimated from simulations, the likelihood is no longer Gaussian but rather is described by an adapted version of a multivariate t-distribution, a fact not taken into account by the Hartlap et al. (2007) correction. They suggest

that marginalising over the true covariance produces a tighter posterior close to the peak compared to the simple Hartlap et al. (2007) correction, which according to Sellentin & Heavens (2016) overestimates its size. This is confirmed by the top right panel of Fig. C.4. We note, however, that the additional scatter in the parameters posterior encoded by the Dodelson & Schneider (2013) correction is not accounted for in the Sellentin & Heavens (2016) framework.

The lower left panel of Fig. C.4 is the same as the top right panel but for the compressed data vector. The compression greatly reduces the noise in the estimated covariance matrix and Eqs. 7.37 and 7.38 approaches ~ 1. Also the Sellentin & Heavens (2016) likelihood approaches a multivariate Gaussian, becoming almost indistinguishable from the no correction case.

Lastly, in the lower right panel of Fig. C.4 we show the contours obtained using the compressed T17 covariance matrix. We expect the shape of the posterior to be different when using the compressed T17 covariance and the `FLASK` covariance in two ways. First, the cosmology of the T17 simulations is slightly different from `FLASK` one. Second, third moments should be more accurately modelled in the T17 simulations as `FLASK` does not contain the physics to model the third moments beyond the log-normal shift. Differences in the widths between the two compressed covariances are smaller than 2 per cent, suggesting that the two factors considered above have a modest impact.

Finally, we comment on the more Gaussian nature of the compressed data vector compared to the uncompressed one. This is shown in Fig. C.5. The residuals (i.e., the difference between the measurement signal in a `FLASK` simulation and the simulations mean value) of the uncompressed data vector appear much less Gaussian for the third moments and the combination of second and third moments compared to what we found for the compressed data vector in Fig. 7.8 (no significant difference in the distribution of the residuals is seen for when only second moments are used). We compute how the distribution of residuals would look if the likelihood were not purely Gaussian, by means of a multivariate Edgeworth expansion of the likelihood (e.g., Amendola 1996):

$$\mathcal{L} = G(x, C)[1 + \frac{1}{6} k_x^{ijk} h_{ijk} + ...], \tag{C.36}$$

with

$$h_{ijk} = (-1)^3 G^{-1}(x, C) \partial_{ijk} G(x, C), \tag{C.37}$$

where $G(x, C)$ is the Gaussian part of the likelihood, x and C are the data

vector and its covariance respectively, and $k_x^{ijk} = \langle x^i x^j x^k \rangle$ is the third order cumulant of the data vector (which can be measured in simulations). The predicted distribution of residuals in Fig. C.5 obtained with the first term of the Edgeworth expansion is in better agreement with the one measured in `FLASK` simulations.

C.4 Full data vector and signal-to-noise

We show in Fig. C.6 the full data vector, including off-diagonal terms. The total signal-to-noise ratio (defined as SNR $\equiv \sqrt{d^T C^{-1} d}$), for a $24h^{-1}$ Mpc scale cut, is 51.5, 10.4 and 66.3 for second, third and combination of second and third moments respectively. If all the scales are considered (down to 3 arcminutes), the signal-to-noise ration increases to 59.3, 15.4 and 106.0. Among the second moments bins, the 11, 22, 33 and 44 bins have signal-to-noise ratio of 8.8, 13.3, 25.2, 24.5; as for the third moments, the 111, 222, 333 and 444 bins have signal-to-noise ratio of 2.1, 2.8, 4.6, 3.9. The signal-to-noise ratio of the cross-moments is somewhat in between the values of the corresponding auto-moments.

C.5 Fast emulator theory predictions

The theory prediction described in § 7.2.1 can be quite time-consuming due to the large number of cross-correlations and integrations involved. In order to speed up this calculation, we implemented an emulator (Heitmann et al., 2006; Habib et al., 2007). Typically, emulators in the cosmology context are used when an expensive calculation is needed in a large parameter space, but the variation of the calculation over the parameter space is smooth. A primary example is predicting the dark matter power spectrum given cosmological parameters (Heitmann et al., 2009; Kwan et al., 2015). The power spectrum is computed to high accuracy at a given number of points in the cosmological parameter space and an interpolator is used to derive the power spectrum at some arbitrary point in the parameter space.

In our case, the quantities we wish to emulate are the second and third moments of the matter density field once the mask edges are accounted for, namely $\langle \delta^2_{\theta_0,\mathrm{NL}} \rangle^{EE/BB}(\chi)$ and $\langle \delta^3_{\theta_0,\mathrm{NL}} \rangle^{EE/BB}(\chi)$, as a function of the 5 cosmological parameters under study and for a large number of (fixed) redshifts. We first compute their values at specific points in our parameter space, and then we build an interpolator that provides fast prediction at

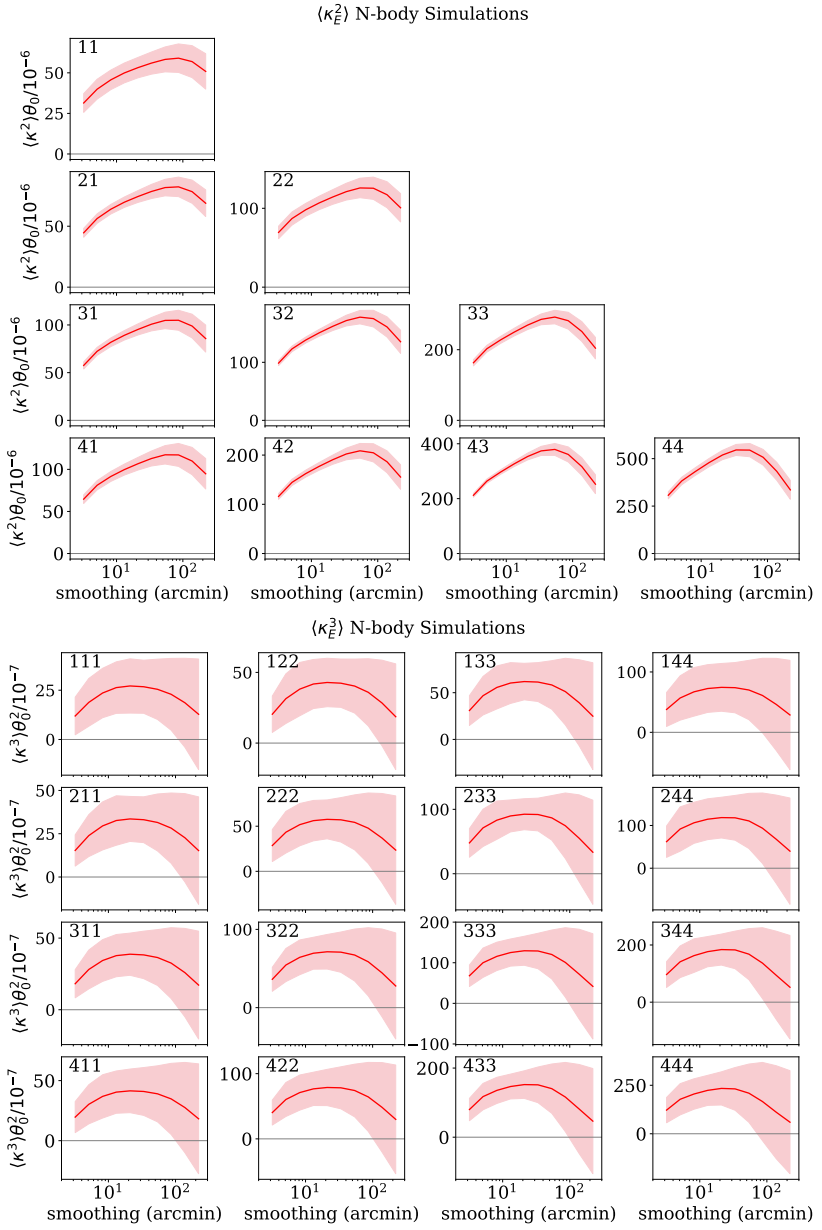

Figure C.6: Second and third moments data vector. The red line represents a theory data vector (obtained assuming the fiducial values for the nuisance parameters and a T17 cosmology) and the red shaded regions the 1-σ measurement uncertainty. Grey shaded regions show the angular scales not included in the fiducial analysis.

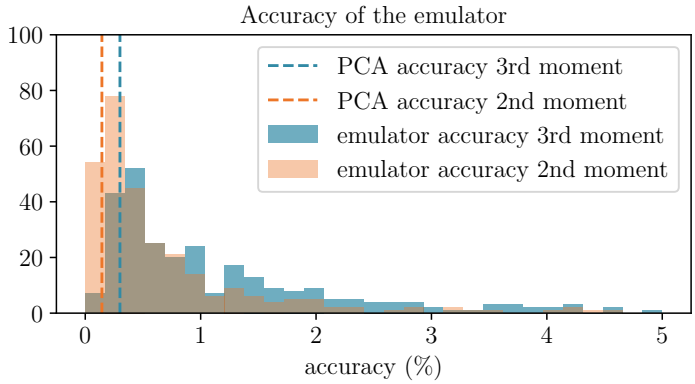

Figure C.7: Accuracy of the emulator for the second and third moments. We tested the emulator using a validation sample of 500 points. Each entry of the histogram refers to the mean relative discrepancy between the emulator predictions and the validation model over all the smoothing scales and redshifts considered. The vertical dashed lines show the error introduced by selecting only 15 principal components.

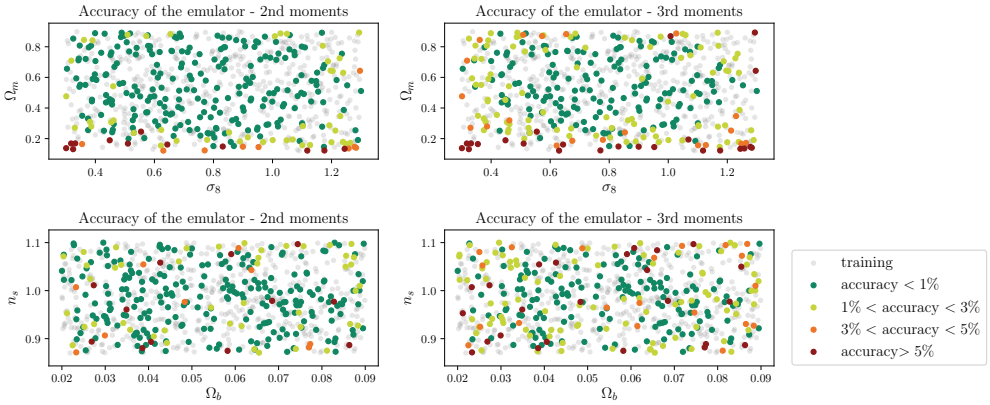

Figure C.8: Accuracy of the emulator for the second and third moments as a function of four cosmological parameters. We tested the emulator using a validation sample of 500 points. Each entry of the scatter plots refers to the mean relative discrepancy between the emulator predictions and the validation model over all the smoothing scales and redshifts considered. Training points are shown in grey.

any point of the 5-parameter space (and as a function of redshift). We also build a separate emulator for each smoothing scale considered. The fact that such quantities are emulated at a fixed range of redshifts allow us to compute the second and third moments of the convergence field for a given tomographic bin after the emulation step, by integrating over the redshifts and taking into account the lensing kernel (and other nuisance parameters).

To decide which points to use for build the interpolator, we sampled our parameter space using a Latin hypercube (McKay, 1979), which is a scheme that provides good space-filling properties. We sampled the space delimited by the priors defined in Table 7.1, and chose 500 points. For each point of the Latin hypercube, we predicted the second and third moments of the dark matter density field (Eqs. 7.2, 7.3) with a resolution of $\delta z = 0.01$ up to redshift 4, for 12 equally logarithmic spaced smoothing scales between $\theta_0 = 0$ arcmin and $\theta_0 = 220$ arcmin. For each smoothing scale, we organised the predictions of our second and third moments in a matrix of dimensionality $n_z \times n_{\rm points} = 400 \times 500$. Since interpolating a 400×500 matrix as a function of cosmological parameters would be impractical, we further reduce the dimensionality using the singular value decomposition. We define $\eta = \mathbf{UBV}^T$, where $\mathbf{U}$ has dimensionality $n_z \times n_z$ and $\mathbf{V}$ $n_z \times n_{\rm points}$. $\mathbf{B}$ is a diagonal matrix of singular values. We defined the basis vectors $\Phi = \frac{1}{\sqrt{n_z}}\mathbf{UB}$ and weights $\omega = \sqrt{n_z}\mathbf{V}^T$. Then, we kept only the first $p < n_z$ principal components of our basis vectors:

$$\langle \delta^2_{\theta_0,\rm NL} \rangle^{EE/BB}(\chi(z), \Omega_m, \Omega_b, \sigma_8, n_s, h_{100}) = \sum_{i=0}^{p} \omega_i^{\delta^2,\theta_0}(\Omega_m, \Omega_b, \sigma_8, n_s, h_{100}) \Phi_i^{\delta^2,\theta_0}(\chi(z)), \quad \text{(C.38)}$$

$$\langle \delta^3_{\theta_0,\rm NL} \rangle^{EE/BB}(\chi(z), \Omega_m, \Omega_b, \sigma_8, n_s, h_{100}) = \sum_{i=0}^{p} \omega_i^{\delta^3,\theta_0}(\Omega_m, \Omega_b, \sigma_8, n_s, h_{100}) \Phi_i^{\delta^3,\theta_0}(\chi(z)), \quad \text{(C.39)}$$

where the basis and weights are different for the second and third moments and depends on the smoothing scale. We found that setting $p = 15$ and $p = 45$ retains most of the information in the moments (99.9 per cent and 99.7 per cent for second and third moments respectively), so we can neglect the other components. The third moments require more components due to the complex dependence on cosmological parameters at small scales.

After the singular value decomposition, we are left to interpolate, as a function of five cosmological parameters, 60 weight functions in total between $\omega_i^{\delta^2,\theta_0}$ and $\omega_i^{\delta^3,\theta_0}$ measured at 500 different points in our parameter space. We opted for a Gaussian process (Rasmussen & Williams, 2006) interpolation scheme. A Gaussian process is a stochastic process where any finite subset forms a multivariate Gaussian distribution. At each reconstruction point $x = (\Omega_m, \Omega_b, \sigma_8, n_s, h_{100})$ of our parameter space, the weights $\omega_i^{\delta^2,\theta_0}$,$\omega_i^{\delta^3,\theta_0}$ are modelled as multivariate Gaussian distributions with a given mean value and Gaussian errors. The latter is determined by a covariance function $k(x; x')$ that correlates the function at different points. The covariance function depends on only two hyper-parameters (the amplitude and the typical scale of the correlation) which are fixed during the training phase.

We tested the accuracy (defined as the mean relative discrepancy between the emulator predictions and the validation model over all the smoothing scales and redshifts considered) of our interpolation scheme by training and validating over two different sets of 500 points determined using two different Latin hypercubes. The resulting accuracy is shown in Figs C.7 and C.8. The performance of the emulator is generally better than 1 per cent. The recovery gets worse close the the edges of the priors. This is particularly evident for σ_8 and Ω_m (Fig. C.8) as these two are the parameters to which our measurement is most sensitive. The emulator performs slightly worse for the third moment, due to a more complex dependence on the cosmological parameters. We note that Figs. C.7, C.8 report the mean accuracy of the emulator across smoothing scales and redshifts. While for the second moments the accuracy does not strongly depend on the smoothing scales or redshift, we found that the emulator for the third moments performs slightly worse at low redshift and intermediate scales, where the accuracy is around ~ 3 per cent, still well below observational uncertainties. The speedup achieved by using the emulator is of two orders of magnitudes.

After predicting the masked second and third moments of the dark matter density field with the emulator, we took into account the lensing kernel of the samples and the nuisance parameters as described in § 7.2.1. We checked that the emulated theory data vector causes small variations in the χ^2 with respect to a theory data vector obtained without approximations. For the fiducial cosmology, such variations are of the order of $\Delta\chi^2 \sim 0.2 - 0.4$, the exact value depending on the particular scale cut combination of second and third moments considered. We also verified that the difference between the maximum of the 1-D marginalised posterior of the cosmological parameters obtained running a MCMC chain on an emulated theory data vector and

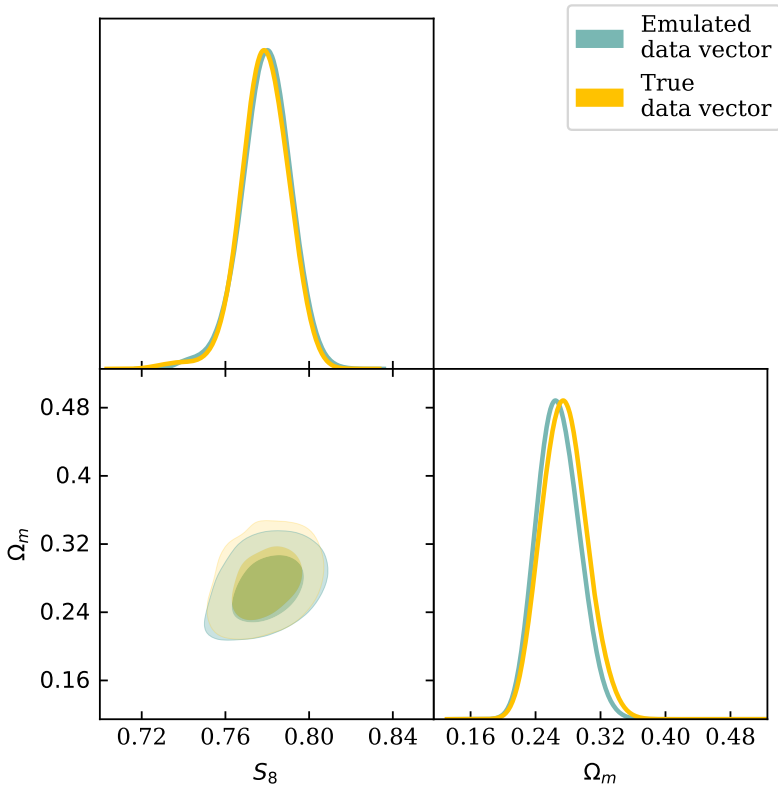

Figure C.9: Forecast posteriors for cosmological parameters, obtained with a theory data vector and an emulated data vector (see § C.5). We marginalise over nuisance parameters as explained in §7.5.3. Constraints with the second and third moments combined are shown in the $S_8 - \Omega_\mathrm{m}$ plane.

on a non-approximated one are much smaller than the parameters' 1-σ confidence intervals. This is shown in Fig. C.9, and the differences are at the level of < 1.5 per cent for Ω_m and < 0.3 per cent for $S_8 = \sigma_8(\Omega_\mathrm{m}/0.3)^{0.5}$.

Bibliography

Abbott, T. M. C., Abdalla, F. B., Allam, S., et al., 2018, , 239, 2, 18

Ahumada, R., Allende Prieto, C., Almeida, A., et al., 2019, arXiv e-prints, arXiv:1912.02905

Aihara, H., Arimoto, N., Armstrong, R., et al., 2018, , 70, S4

Alarcon, A., Sánchez, C., Bernstein, G. M., Gaztañaga, E., 2019, arXiv e-prints

Alonso, D., Sanchez, J., Slosar, A., LSST Dark Energy Science Collaboration, 2019, , 484, 3, 4127

Alsing, J., Wandelt, B., Feeney, S., 2018, , 477, 2874

Amendola, L., 1996, Astrophysical Letters and Communications, 33, 63

Amon, A., et al., 2020, in preparation

Antilogus, P., Astier, P., Doherty, P., Guyonnet, A., Regnault, N., 2014, Journal of Instrumentation, 9, C03048

Asgari, M., Heymans, C., 2019, , 484, 1, L59

Asgari, M., Heymans, C., Hildebrandt, H., et al., 2019a, , 624, A134

Asgari, M., Tröster, T., Heymans, C., et al., 2019b, arXiv e-prints

Asgari, M., Tröster, T., Heymans, C., et al., 2020, , 634, A127

Astier, P., Antilogus, P., Juramy, C., Le Breton, R., Le Guillou, L., Sepulveda, E., 2019, , 629, A36

Bartelmann, M., Schneider, P., 2001, , 340, 291

Bates, D. J., Tojeiro, R., Newman, J. A., et al., 2019, , 486, 3059

Becker, M. R., 2013, , 435, 115

Behroozi, P. S., Wechsler, R. H., Wu, H.-Y., 2013, , 762, 109

Benítez, N., 2000, , 536, 571

Bennett, C., 2015, Cosmological Constraints Using Planck 2015 and WMAP Data, NASA ADAP Proposal

Bernardeau, F., Colombi, S., Gaztañaga, E., Scoccimarro, R., 2002, , 367, 1

Bernardeau, F., van Waerbeke, L., Mellier, Y., 1997, , 322, 1

Bernstein, G. M., 2010, , 406, 2793

Bernstein, G. M., Armstrong, R., Krawiec, C., March, M. C., 2016, , 459, 4467

Bernstein, G. M., Armstrong, R., Plazas, A. A., et al., 2017, , 129, 977, 074503

Bernstein, G. M., Jarvis, M., 2002, , 123, 583

Bertin, E., 2010, SWarp: Resampling and Co-adding FITS Images Together

Bertin, E., Arnouts, S., 1996a, , 117, 393

Bertin, E., Arnouts, S., 1996b, , 117, 393

Bezanson, R., Wake, D. A., Brammer, G. B., et al., 2016, , 822, 30

Blanton, M. R., Schlegel, D. J., Strauss, M. A., et al., 2005, , 129, 2562

Blazek, J., MacCrann, N., Troxel, M. A., Fang, X., 2017, arXiv e-prints, arXiv:1708.09247

Böhm, V., Modi, C., Castorina, E., 2020, , 2020, 3, 045

Bridle, S., King, L., 2007, New Journal of Physics, 9, 444

Brown, M. L., Castro, P. G., Taylor, A. N., 2005, , 360, 1262

Bruderer, C., Chang, C., Refregier, A., Amara, A., Bergé, J., Gamper, L., 2016, , 817, 25

Buchs, R., Davis, C., Gruen, D., et al., 2019, , 489, 1, 820

Castro, P. G., Heavens, A. F., Kitching, T. D., 2005, Phys. Rev. D, 72, 023516

Cawthon, R., Davis, C., Gatti, M., et al., 2018, , 481, 2427

Chang, C., Jarvis, M., Jain, B., et al., 2013, , 434, 3, 2121

Chang, C., Pujol, A., Mawdsley, B., et al., 2018, , 475, 3165

Chang, C., Vikram, V., Jain, B., et al., 2015, , 115, 5, 051301

Chisari, N. E., Richardson, M. L. A., Devriendt, J., et al., 2018, , 480, 3962

Choi, A., Heymans, C., Blake, C., et al., 2016, , 463, 3737

Clerkin, L., Kirk, D., Manera, M., et al., 2017, , 466, 1444

Coles, P., Jones, B., 1991, , 248, 1

Conroy, C., Wechsler, R. H., Kravtsov, A. V., 2006, , 647, 201

Coulton, W. R., Armstrong, R., Smith, K. M., Lupton, R. H., Spergel, D. N., 2018, , 155, 6, 258

Crocce, M., Pueblas, S., Scoccimarro, R., 2006, , 373, 369

Das, S., Ostriker, J. P., 2006, , 645, 1

Davis, C., Gatti, M., Vielzeuf, P., et al., 2017, arXiv e-prints

Davis, C., Rozo, E., Roodman, A., et al., 2018, , 477, 2196

Davis, M., Peebles, P. J. E., 1983, , 267, 465

Dawson, K. S., Schlegel, D. J., Ahn, C. P., et al., 2013, , 145, 1, 10

de Jong, J. T. A., Kuijken, K., Applegate, D., et al., 2013, The Messenger, 154, 44

DeRose, J., Wechsler, R. H., Becker, M. R., et al., 2019, arXiv e-prints

DES, 2005, ArXiv Astrophysics e-prints

DES collaboration, 2020a, in preparation

DES collaboration, 2020b, in preparation

DES collaboration, 2020c, in preparation

DES collaboration, 2020d, in preparation

DES collaboration, 2020e, in preparation

Dietrich, J. P., Hartlap, J., 2010, , 402, 2, 1049

Dodelson, S., Schneider, M. D., 2013, , 88, 6, 063537

Einstein, A., 1936, Science, 84, 2188, 506

Elsner, F., Wandelt, B. D., 2012, arXiv e-prints, arXiv:1211.0585

Estrada, J., Alvarez, R., Abbott, T., et al., 2010, in , vol. 7735 of *Society of Photo-Optical Instrumentation Engineers (SPIE) Conference Series*, 77351R

Fixsen, D. J., 2009, , 707, 2, 916

Flaugher, B., 2005, International Journal of Modern Physics A, 20, 3121

Flaugher, B., Diehl, H. T., Honscheid, K., et al., 2015, , 150, 5, 150

Fluri, J., Kacprzak, T., Lucchi, A., et al., 2019, , 100, 6, 063514

Fluri, J., Kacprzak, T., Refregier, A., Amara, A., Lucchi, A., Hofmann, T., 2018, , 98, 12, 123518

Foreman, S., Coulton, W., Villaescusa-Navarro, F., Barreira, A., 2019, arXiv e-prints

Foreman-Mackey, D., Hogg, D. W., Lang, D., Goodman, J., 2013, , 125, 306

Fosalba, P., Gaztañaga, E., Castander, F. J., Manera, M., 2008, , 391, 435

Friedrich, O., Eifler, T., 2018, , 473, 4150

Friedrich, O., Gruen, D., DeRose, J., et al., 2018, , 98, 2, 023508

Fu, L., Kilbinger, M., Erben, T., et al., 2014, , 441, 3, 2725

Gaia Collaboration, Brown, A. G. A., Vallenari, A., et al., 2016, A&A, 595, A2

Gatti, M., Chang, C., Friedrich, O., et al., 2019, arXiv e-prints, arXiv:1911.05568

Gatti, M., Vielzeuf, P., Davis, C., et al., 2018, , 477, 1664

Gatti, M., et al., 2020, in preparation

Gaztanaga, E., Bernardeau, F., 1998, , 331, 829

Gelman, A., Rubin, D. B., 1992, Statistical Science, 7, 457

Gil-Marín, H., Noreña, J., Verde, L., et al., 2015, , 451, 1, 539

Gil-Marín, H., Wagner, C., Fragkoudi, F., Jimenez, R., Verde, L., 2012, , 2, 047

Górski, K. M., Hivon, E., Banday, A. J., et al., 2005, , 622, 759

Gruen, D., Bernstein, G. M., Jarvis, M., et al., 2015, Journal of Instrumentation, 10, C05032

Gruen, D., Friedrich, O., Krause, E., et al., 2018, , 98, 2, 023507

Gualdi, D., Manera, M., Joachimi, B., Lahav, O., 2018, , 476, 4045

Guth, A. H., 1981, , 23, 2, 347

Guyonnet, A., Astier, P., Antilogus, P., Regnault, N., Doherty, P., 2015, , 575, A41

Habib, S., Heitmann, K., Higdon, D., Nakhleh, C., Williams, B., 2007, , 76, 8, 083503

Hamana, T., Sakurai, J., Koike, M., Miller, L., 2015, , 67, 34

Hamana, T., Shirasaki, M., Miyazaki, S., et al., 2019, arXiv e-prints

Hamana, T., Shirasaki, M., Miyazaki, S., et al., 2020, , 72, 1, 16

Harnois-Déraps, J., Tröster, T., Hojjati, A., et al., 2016, , 460, 434

Hartlap, J., Simon, P., Schneider, P., 2007, , 464, 399

Hartley, W., Choi, A., et al., 2020, in preparation

Heavens, A. F., Jimenez, R., Lahav, O., 2000, , 317, 965

Heavens, A. F., Sellentin, E., de Mijolla, D., Vianello, A., 2017, , 472, 4244

Heitmann, K., Higdon, D., Nakhleh, C., Habib, S., 2006, , 646, L1

Heitmann, K., Higdon, D., White, M., et al., 2009, , 705, 156

Hellwing, W. A., Schaller, M., Frenk, C. S., et al., 2016, , 461, L11

Heymans, C., Van Waerbeke, L., Miller, L., et al., 2012, , 427, 1, 146

Hikage, C., Oguri, M., 2016, , 462, 1359

Hikage, C., Oguri, M., Hamana, T., et al., 2019, , 71, 2, 43

Hikage, C., Takada, M., Hamana, T., Spergel, D., 2011, , 412, 65

Hilbert, S., Hartlap, J., Schneider, P., 2011, , 536, A85

Hildebrandt, H., Arnouts, S., Capak, P., et al., 2010, , 523, A31

Hildebrandt, H., Erben, T., Kuijken, K., et al., 2012, , 421, 2355

Hildebrandt, H., Viola, M., Heymans, C., et al., 2017, , 465, 1454

Hinshaw, G., Larson, D., Komatsu, E., et al., 2013, , 208, 19

Hirata, C. M., Mandelbaum, R., Seljak, U., et al., 2004, , 353, 529

Hirata, C. M., Seljak, U., 2004, , 70, 6, 063526

Hoekstra, H., Jain, B., 2008, Annual Review of Nuclear and Particle Science, 58, 99

Hoekstra, H., Viola, M., Herbonnet, R., 2017, , 468, 3295

Hoyle, B., Gruen, D., Bernstein, G. M., et al., 2018, , 478, 592

Hubble, E., 1934, , 79, 8

Huff, E., Mandelbaum, R., 2017, arXiv e-prints

Huterer, D., Takada, M., Bernstein, G., Jain, B., 2006, , 366, 101

Ivezic, Z., et al., 2008, ArXiv e-prints

Jain, B., Seljak, U., 1997, , 484, 2, 560

Jarvis, M., 2015, TreeCorr: Two-point correlation functions

Jarvis, M., Sheldon, E., Zuntz, J., et al., 2016, , 460, 2, 2245

Jarvis, M., et al., 2020, in preparation

Jeffrey, N., Abdalla, F. B., Lahav, O., et al., 2018, , 479, 2871

Jeffrey, N., Lanusse, F., Lahav, O., Starck, J.-L., 2020, , 492, 4, 5023

Joachimi, B., Taylor, A. N., Kiessling, A., 2011, , 418, 145

Johnson, A., Blake, C., Amon, A., et al., 2017, , 465, 4118

Joudaki, S., Hildebrandt, H., Traykova, D., et al., 2019, arXiv e-prints

Kacprzak, T., Herbel, J., Nicola, A., et al., 2019, arXiv e-prints, arXiv:1906.01018

Kacprzak, T., Kirk, D., Friedrich, O., et al., 2016, , 463, 3653

Kaiser, N., 2000, , 537, 555

Kaiser, N., Squires, G., 1993a, , 404, 441

Kaiser, N., Squires, G., 1993b, , 404, 441

Kilbinger, M., 2015, Reports on Progress in Physics, 78, 8, 086901

Knabenhans, M., Stadel, J., Marelli, S., et al., 2019, , 484, 4, 5509

Kohonen, T., 1982, Biological Cybernetics, 43, 1, 59, ISSN 0340-1200

Kratochvil, J. M., Haiman, Z., May, M., 2010, , 81, 4, 043519

Kratochvil, J. M., Lim, E. A., Wang, S., Haiman, Z., May, M., Huffenberger, K., 2012, , 85, 10, 103513

Krause, E., Eifler, E., Zuntz, J., Friedrich, O., Troxel, M., et al., 2017, ArXiv e-prints

Krause, E., Hirata, C. M., 2010, , 523, A28

Kuijken, K., et al., 2015, , 454, 3500

Kwan, J., Heitmann, K., Habib, S., et al., 2015, , 810, 35

Lage, C., 2019, arXiv e-prints, arXiv:1911.09567

Landy, S. D., Szalay, A. S., 1993, , 412, 64

Lanusse, F., Starck, J. L., Leonard, A., Pires, S., 2016, , 591, A2

Laureijs, R., et al., 2011, ArXiv e-prints

Leauthaud, A., Massey, R., Kneib, J.-P., et al., 2007, , 172, 1, 219

Lehmann, B. V., Mao, Y.-Y., Becker, M. R., Skillman, S. W., Wechsler, R. H., 2017, , 834, 37

Leistedt, B., Mortlock, D. J., Peiris, H. V., 2016, , 460, 4258

Lima, M., Cunha, C. E., Oyaizu, H., Frieman, J., Lin, H., Sheldon, E. S., 2008, , 390, 118

Limber, D. N., 1953, , 117, 134

Liu, J., Petri, A., Haiman, Z., Hui, L., Kratochvil, J. M., May, M., 2015, , 91, 6, 063507

MacCrann, N., et al., 2020, in preparation

Mandelbaum, R., 2017, ArXiv e-prints

Mandelbaum, R., Rowe, B., Bosch, J., et al., 2014, , 212, 1, 5

Martinet, N., Schneider, P., Hildebrandt, H., et al., 2018, , 474, 1, 712

Masters, D. C., Stern, D. K., Cohen, J. G., et al., 2017, , 841, 111

Mather, J. C., 1994, Infrared Physics and Technology, 35, 2-3, 331

Mawdsley, B., Bacon, D., Chang, C., et al., 2019, arXiv e-prints

McClintock, T., Varga, T. N., Gruen, D., et al., 2019, , 482, 1, 1352

McKay, B. R. C. W., M.D., 1979

McQuinn, M., White, M., 2013, , 433, 2857

Meerburg, P. D., Green, D., Flauger, R., et al., 2019, , 51, 3, 107

Melchior, P., Böhnert, A., Lombardi, M., Bartelmann, M., 2010, , 510, A75

Melchior, P., Viola, M., 2012a, epsnoise: Pixel noise in ellipticity and shear measurements

Melchior, P., Viola, M., 2012b, , 424, 2757

Ménard, B., Scranton, R., Schmidt, S., et al., 2013, ArXiv e-prints

Meyers, J. E., Burchat, P. R., 2015, , 807, 2, 182

Mo, H. J., White, S. D. M., 1996, , 282, 2, 347

Moessner, R., Jain, B., 1998, , 294, L18

Morganson, E., Gruendl, R. A., Menanteau, F., et al., 2018, , 130, 989, 074501

Morrison, C. B., Hildebrandt, H., Schmidt, S. J., et al., 2017, , 467, 3576

Myles, J., et al., 2020, in prep.

Naidoo, K., Whiteway, L., Massara, E., et al., 2019, arXiv e-prints, arXiv:1907.00989

Narayan, R., 1989, , 339, L53

Navarro, J. F., Frenk, C. S., White, S. D. M., 1996, , 462, 563

Newman, J. A., 2008, , 684, 88-101

Newman, J. A., Abate, A., Abdalla, F. B., et al., 2015, Astroparticle Physics, 63, 81

Norberg, P., Baugh, C. M., Gaztañaga, E., Croton, D. J., 2009, , 396, 19

Oguri, M., Miyazaki, S., Hikage, C., et al., 2018, , 70, S26

Parroni, C., Cardone, V. F., Maoli, R., Scaramella, R., 2020, , 633, A71

Patton, K., Blazek, J., Honscheid, K., et al., 2016, ArXiv e-prints

Paulin-Henriksson, S., Amara, A., Voigt, L., Refregier, A., Bridle, S. L., 2008, , 484, 1, 67

Peel, A., Pettorino, V., Giocoli, C., Starck, J.-L., Baldi, M., 2018, , 619, A38

Penzias, A. A., Wilson, R. W., 1965, , 142, 419

Petri, A., Liu, J., Haiman, Z., May, M., Hui, L., Kratochvil, J. M., 2015, , 91, 10, 103511

Pieres, A., Girardi, L., Balbinot, E., et al., 2019, arXiv e-prints, arXiv:1904.04350

Pires, S., Starck, J.-L., Amara, A., Teyssier, R., Réfrégier, A., Fadili, J., 2009, , 395, 1265

Planck Collaboration, 2018, arXiv e-prints, arXiv:1807.06209

Planck Collaboration, 2019, arXiv e-prints, arXiv:1907.12875

Plazas, A., Bernstein, G., 2012, , 124, 920, 1113

Plazas, A. A., Bernstein, G. M., Sheldon, E. S., 2014a, , 126, 942, 750

Plazas, A. A., Bernstein, G. M., Sheldon, E. S., 2014b, Journal of Instrumentation, 9, 4, C04001

Prakash, A., Licquia, T. C., Newman, J. A., et al., 2016, , 224, 2, 34

Prat, J., Sánchez, C., Fang, Y., et al., 2018, , 98, 4, 042005

Pratten, G., Lewis, A., 2016, , 2016, 8, 047

Press, W. H., Schechter, P., 1974, , 187, 425

Pujol, A., Chang, C., Gaztañaga, E., et al., 2016, , 462, 35

Raichoor, A., Comparat, J., Delubac, T., et al., 2017, , 471, 4, 3955

Ramanah, D. K., Lavaux, G., Jasche, J., Wand elt, B. D., 2019, , 621, A69

Rasmussen, C. E., Williams, C. K. I., 2006, Gaussian Processes for Machine Learning

Refregier, A., Kacprzak, T., Amara, A., Bridle, S., Rowe, B., 2012a, , 425, 1951

Refregier, A., Kacprzak, T., Amara, A., Bridle, S., Rowe, B., 2012b, , 425, 1951

Reid, B., Ho, S., Padmanabhan, N., et al., 2016, , 455, 2, 1553

Rowe, B., 2010, , 404, 350

Rozo, E., Rykoff, E. S., Abate, A., et al., 2016, , 461, 1431

Rugh, S. E., Zinkernagel, H., 2010, arXiv e-prints, arXiv:1006.5848

Rykoff, E. S., Rozo, E., Keisler, R., 2015, ArXiv: 1509.00870

Samuroff, S., Blazek, J., Troxel, M. A., et al., 2019, , 489, 4, 5453

Sánchez, C., Bernstein, G. M., 2019, , 483, 2801

Sánchez, C., Carrasco Kind, M., Lin, H., et al., 2014, , 445, 1482

Schaye, J., Dalla Vecchia, C., Booth, C. M., et al., 2010, , 402, 1536

Schmidt, F., Rozo, E., Dodelson, S., Hui, L., Sheldon, E., 2009, Physical Review Letters, 103, 5, 051301

Schmidt, S. J., Ménard, B., Scranton, R., Morrison, C., McBride, C. K., 2013, , 431, 3307

Schneider, M. D., Hogg, D. W., Marshall, P. J., et al., 2015, , 807, 1, 87

Schneider, P., Ehlers, J. ., Falco, E. E., 1992, Gravitational Lenses, Gravitational Lenses, XIV, 560 pp. 112 figs.. Springer-Verlag Berlin Heidelberg New York. Also Astronomy and Astrophysics Library

Schneider, P., Eifler, T., Krause, E., 2010, , 520, A116

Schneider, P., van Waerbeke, L., Jain, B., Kruse, G., 1998, , 296, 873

Schneider, P., van Waerbeke, L., Mellier, Y., 2002, , 389, 729

Scoccimarro, R., Couchman, H. M. P., 2001, , 325, 1312

Scottez, V., Benoit-Lévy, A., Coupon, J., Ilbert, O., Mellier, Y., 2017, ArXiv e-prints

Secco, L., et al., 2020, in preparation

Seitz, C., Schneider, P., 1997, , 318, 687

Seljak, U., Zaldarriaga, M., 1996, , 469, 437

Sellentin, E., Heavens, A. F., 2016, , 456, L132

Semboloni, E., Schrabback, T., van Waerbeke, L., Vafaei, S., Hartlap, J., Hilbert, S., 2011, , 410, 1, 143

Shan, H., Liu, X., Hildebrandt, H., et al., 2018, , 474, 1, 1116

Sheldon, E., 2015, NGMIX: Gaussian mixture models for 2D images, Astrophysics Source Code Library

Sheldon, E. S., Becker, M. R., MacCrann, N., Jarvis, M., 2019, arXiv e-prints, arXiv:1911.02505

Sheldon, E. S., Huff, E. M., 2017, , 841, 24

Simon, P., Semboloni, E., van Waerbeke, L., et al., 2015, , 449, 1505

Smoot, G. F., 1992, Highlights of Astronomy, 9, 281

Spergel, D., et al., 2015, ArXiv e-prints

Springel, V., 2005, , 364, 1105

Springel, V., Pakmor, R., Pillepich, A., et al., 2018, , 475, 676

Starck, J.-L., Fadili, J., Murtagh, F., 2007, IEEE Transactions on Image Processing, 16, 2, 297

Starck, J. L., Moudden, Y., Abrial, P., Nguyen, M., 2006, , 446, 3, 1191

Takada, M., 2010, in American Institute of Physics Conference Series, edited by Kawai, N., Nagataki, S., vol. 1279 of *American Institute of Physics Conference Series*, 120–127

Takada, M., Jain, B., 2003, , 344, 3, 857

Takada, M., Jain, B., 2004, , 348, 3, 897

Takahashi, R., Hamana, T., Shirasaki, M., et al., 2017, , 850, 24

Takahashi, R., Nishimichi, T., Namikawa, T., et al., 2019, arXiv e-prints, arXiv:1911.07886

Takahashi, R., Oguri, M., Sato, M., Hamana, T., 2011, , 742, 15

Takahashi, R., Sato, M., Nishimichi, T., Taruya, A., Oguri, M., 2012, , 761, 152

Takahashi, R., Soma, S., Takada, M., Kayo, I., 2014, , 444, 3473

Taruya, A., Hamana, T., Kayo, I., 2002, in 8th Asian-Pacific Regional Meeting, Volume II, edited by Ikeuchi, S., Hearnshaw, J., Hanawa, T., 299–300

Tegmark, M., Taylor, A. N., Heavens, A. F., 1997, , 480, 22

Troxel, M. A., MacCrann, N., Zuntz, J., et al., 2018, , 98, 4, 043528

Vafaei, S., Lu, T., van Waerbeke, L., Semboloni, E., Heymans, C., Pen, U.-L., 2010, Astroparticle Physics, 32, 6, 340

van Daalen, M. P., Schaye, J., Booth, C. M., Dalla Vecchia, C., 2011, , 415, 3649

Van Waerbeke, L., Benjamin, J., Erben, T., et al., 2013, , 433, 3373

Van Waerbeke, L., Hamana, T., Scoccimarro, R., Colombi, S., Bernardeau, F., 2001, , 322, 918

Vicinanza, M., Cardone, V. F., Maoli, R., Scaramella, R., Er, X., 2016, arXiv e-prints, arXiv:1606.03892

Vicinanza, M., Cardone, V. F., Maoli, R., Scaramella, R., Er, X., 2018, , 97, 2, 023519

Vicinanza, M., Cardone, V. F., Maoli, R., Scaramella, R., Er, X., Tereno, I., 2019, , 99, 4, 043534

Vikram, V., Chang, C., Jain, B., et al., 2015, , 92, 2, 022006

Villumsen, J. V., Freudling, W., da Costa, L. N., 1997, , 481, 578

Voigt, L. M., Bridle, S. L., 2010, , 404, 1, 458

Wallis, C. G. R., McEwen, J. D., Kitching, T. D., Leistedt, B., Plouviez, A., 2017, arXiv e-prints

Walsh, D., Carswell, R. F., Weymann, R. J., 1979, , 279, 381

Wandelt, B. D., Hivon, E., Górski, K. M., 2001, , 64, 8, 083003

Wild, V., Peacock, J. A., Lahav, O., et al., 2005, , 356, 247

Wright, A. H., Hildebrandt, H., van den Busch, J. L., Heymans, C., 2019, arXiv e-prints

Xavier, H. S., Abdalla, F. B., Joachimi, B., 2016, , 459, 3693

Zuntz, J., et al., 2018, , 481, 1149